Prediction, Analysis, and Measurement of Ductile Fracture of Metals

by

Fuzuli Agri Akcay

A dissertation submitted in partial fulfillment
of the requirements for the degree of
Doctor of Philosophy
(Naval Architecture and Marine Engineering)
in the University of Michigan
2016

Doctoral Committee:

Associate Professor Dale G. Karr, Co-Chair
Professor Marc Perlin, Co-Chair
Professor Pingsha Dong
Associate Professor Veera Sundararaghavan

DEDICATION

This dissertation is dedicated to my mother for her endless care and love…

ACKNOWLEDGEMENTS

This manuscript could not have been completed without the help and support of the following:

First of all, I would like to express my gratitude to my advisors Prof. Dale G. Karr and Prof. Marc Perlin for their guidance, valuable contributions and discussions, and share of knowledge and experience. I also would like to thank them for their help and providing me an opportunity to use their resources. Moreover, I appreciate Prof. Veera Sundararaghavan and Prof. Pingsha Dong for being in the doctoral committee and for their precious suggestions.

In addition, I sincerely and greatly acknowledge the generous financial support of Turkish National Education Ministry (T.C. Milli Eğitim Bakanlığı) and American Bureau of Shipping (ABS).

Moreover, I would like to thank my BSc and MSc advisor Prof. M. Cengiz Dökmeci for his encouragement to pursue a PhD degree, and faculty and staff of Faculty of Naval Architecture and Ocean Engineering of İstanbul Technical University (İ.T.Ü.) for their priceless contribution to my undergraduate and graduate education.

Furthermore, I would like to thank Prof. Jason P. McCormick for the tensile tests conducted at the Civil Engineering Department of the University of Michigan, Brent Cragin for his help in the experiments conducted at the Marine Hydrodynamic Laboratory (MHL), Guenther Kellner for providing Nital solutions, and James Gose and Haocheng Pan for Solidworks drawings.

Finally, I would like to thank my mother, my father, my brother, and Rachel for their patience, love, and support, and all my friends for their friendships and support as well.

TABLE OF CONTENTS

DEDICATION ii

ACKNOWLEDGEMENTS iii

LIST OF TABLES vii

LIST OF FIGURES ix

ABSTRACT xx

CHAPTER 1 Introduction 1

- 1.1 Motivation for the Research 1
- 1.2 Historical Background 2
- 1.3 Outline of the Dissertation 6

CHAPTER 2 Review of Current Fracture Criteria 7

- 2.1 Griffith's Method 7
- 2.2 Orowan's Contribution 10
  - 2.2.1 Fracture Criterion for Brittle Materials 10
  - 2.2.2 Fracture Criterion for Ductile Materials 11
- 2.3 Irwin's Contribution 12
- 2.4 Rice's Contribution 14

CHAPTER 3 New Ductile Fracture Criterion: Karr-Akçay Energy Balance 16

- 3.1 Continuum Model for Ductile Fracture 16
- 3.2 Mode I (Opening Mode) Ductile Fracture 20
- 3.3 Mode II (Shear/Sliding Mode) Ductile Fracture 24

3.3.1 Mode II Shear Fracture without Sliding Friction 24
3.3.2 Mode II Shear Fracture with Sliding Friction...................................... 26
3.4 Example Applications 28
3.4.1 Mode I (Opening Mode) Fracture Example 30
3.4.1.1 Axisymmetric Stress, Opening Mode Fracture of Al 2024-T351 31
3.4.2 Mode II (Shear Mode) Fracture Example.. 34
3.4.2.1 Plane Stress, Shear Mode Fracture of Al 2024-T351 35
3.5 Results and Discussion.. 37

CHAPTER 4 Experimental Investigation 40

4.1 Summary of Past Experimental Studies on Fracture Strain Estimates............. 40
4.2 Experimental Setup 44
4.3 Digital Image Correlation (DIC) 53
4.4 Strain and Stress Triaxiality Calculation.. 55
4.4.1 Strain Calculation 55
4.4.1.1 Calculation of Forward-Plastic-Strain..................................... 58
4.4.1.2 Calculation of Effective (Fracture) Strain............................... 59
4.4.2 Stress Calculation 61
4.4.2.1 Calculation of Stress Triaxiality.. 61
4.4.2.2 Calculation of Average Stress Triaxiality............................... 64
4.4.2.3 Obtaining the State of Stress... 64
4.5 Uniaxial Test Results 66
4.5.1 Analysis of 6mm-Width Specimen without Groove 66
4.5.1.1 Test 1... 66
4.5.1.2 Test 2... 91
4.5.2 Analysis of 1in-Width Specimen with Semi-Circular Groove............ 93
4.5.3 Analysis of Shear Specimen 99
4.6 Cylindrical Indenter Test Results 116
4.6.1 Analysis of 18mm-Width Specimen without Groove 117
4.6.1.1 Test 0... 118
4.6.1.2 Test 3... 139
4.6.1.3 Test 1... 140

4.6.1.4 Test 2 ... 141
4.6.2 Analysis of 18mm-Width Specimen with 4mm Groove ... 142
4.6.2.1 Test 1 ... 143
4.6.2.2 Test 2 ... 163
4.7 Results and Discussion ... 164
4.7.1 Mask/Mesh Size Dependence ... 164
4.7.2 Strain Rate Dependence ... 167

CHAPTER 5 Comparison of Theory and Experimental Results ... 168

5.1 Toughness Stress Calculation ... 169
5.1.1 16 Pixels by 16 Pixels Mask ... 170
5.1.2 32 Pixels by 32 Pixels Mask ... 170
5.1.3 128 Pixels by 128 Pixels Mask ... 172
5.1.4 Evaluation of Toughness Stresses ... 173

CHAPTER 6 Conclusions and Suggestions for Future Work ... 177

6.1 Discussion and Conclusions ... 177
6.2 Suggestions for Future Work ... 184

References ... 186

LIST OF TABLES

Table 4-1 Summary of the average stress triaxiality (η_{ave}), the stress triaxiality at fracture (η_{frac}), and the effective strain at fracture (ε_{eff}^{f}) for the uniaxial test of 6mm-width specimen without groove with a test speed of 0.2 inch/second. 90

Table 4-2 Summary of the average stress triaxiality (η_{ave}), the stress triaxiality at fracture (η_{frac}), and the effective strain at fracture (ε_{eff}^{f}) for the uniaxial test of 6mm-width specimen without groove with a test speed of 0.4 inch/second. 92

Table 4-3 Summary of the average stress triaxiality (η_{ave}), the stress triaxiality at fracture (η_{frac}), and the effective strain at fracture (ε_{eff}^{f}) for the uniaxial test of the 1in-width specimen with semi-circular groove. 99

Table 4-4 Summary of the average stress triaxiality (η_{ave}), the stress triaxiality at fracture (η_{frac}), and the effective strain at fracture (ε_{eff}^{f}) for the uniaxial test of the shear specimen. 115

Table 4-5 Summary of the average stress triaxiality (η_{ave}), the stress triaxiality at fracture (η_{frac}), and the effective strain at fracture (ε_{eff}^{f}) for cylindrical indenter experiment of 18mm-width specimen without groove with an indentation speed of 0.6 inch/second. . 137

Table 4-6 Summary of the average stress triaxiality (η_{ave}), the stress triaxiality at fracture (η_{frac}), and the effective strain at fracture (ε_{eff}^{f}) for cylindrical indenter experiment of 18mm-width specimen without groove with an indentation speed of 0.6 inch/second. This experiment was a repetition of 'Test 0', presented in the previous sub-section. 140

Table 4-7 Summary of the average stress triaxiality (η_{ave}), the stress triaxiality at fracture (η_{frac}), and the effective strain at fracture (ε_{eff}^{f}) for cylindrical indenter experiment of 18mm-width specimen without groove with an indentation speed of 1.2 inch/second. . 141

Table 4-8 Summary of the average stress triaxiality (η_{ave}), the stress triaxiality at fracture (η_{frac}), and the effective strain at fracture (ε_{eff}^{f}) for cylindrical indenter experiment of 18mm-width specimen without groove with an indentation speed of 2.4 inch/second. . 142

Table 4-9 Summary of the average stress triaxiality (η_{ave}), the stress triaxiality at fracture (η_{frac}), and the effective strain at fracture (ε_{eff}^{f}) for the cylindrical indenter experiment of 18mm-width specimen with 4 mm groove with an indentation speed of 0.6 inch/second. 161

Table 4-10 Summary of the average stress triaxiality (η_{ave}), the stress triaxiality at fracture (η_{frac}), and the effective strain at fracture (ε_{eff}^{f}) for cylindrical indenter experiment of 18mm-width specimen without groove with an indentation speed of 1.2 inch/second. 163

Table 4-11 Summary of the average stress triaxiality (η_{ave}), the stress triaxiality at fracture (η_{frac}), and the effective strain at fracture (ε_{eff}^{f}) of all uniaxial tests – second approach. 165

Table 4-12 Summary of the average stress triaxiality (η_{ave}), the stress triaxiality at fracture (η_{frac}), and the effective strain at fracture (ε_{eff}^{f}) of all cylindrical indenter experiments – second approach. 166

LIST OF FIGURES

Figure 3-1 Representation of volume element and fracture plane 19

Figure 3-2 Effective strain to fracture versus stress triaxiality for axisymmetric loading and opening mode fracture of Al 2024-T351 cylinders. Hybrid experimental-numerical data of Al 2024-T351 were published by Bai & Wierzbicki (2010). 32

Figure 3-3 Effective strain to fracture versus stress triaxiality for axisymmetric loading and opening mode fracture of Al 2024-T351 cylinders using both the average stress triaxiality and the fracture stress triaxiality. Magenta solid line is obtained evaluating average stress triaxiality data, while cyan dashed line is obtained evaluating the stress triaxiality at fracture data. Hybrid experimental-numerical data of Al 2024-T351 were published by Bai & Wierzbicki (2010). 33

Figure 3-4 Effective strain to fracture versus stress triaxiality for plane stress loading and shear mode fracture of Al 2024-T351 bars. Blue solid curve shows the result for the critical state with no friction on the fracture planes, while the dashed lines show results of friction occuring on the fracture planes due to compressive normal stresses. Hybrid experimental-numerical data of Al 2024-T351 were published by Bai & Wierzbicki (2010). 36

Figure 3-5 Critical fracture angle versus stress triaxiality for plane stress loading and shear mode fracture of Al 2024-T351 bars. Blue solid curve shows the result for the critical state with no friction on the fracture planes, while the dashed lines show results of friction occuring on the fracture planes due to compressive normal stresses. 37

Figure 4-1 Etching process of a specimen: The specimen depicted is a 1in-width test coupon. 44

Figure 4-2 An example experimental set-up for a uniaxial test: The test specimen depicted is a shear specimen (without a groove). Note that the test specimen is adapted from Bao & Wierzbicki's (2004) specimen design for pure shear tests. 45

Figure 4-3 Another example experimental set-up for a uniaxial test using the altered indenter apparatus: The test specimen depicted is a 6mm-width specimen without groove. (Note that this specimen has been obtained by in-house machining of an 1in-width specimen). 46

Figure 4-4 Set-up for cylindrical indenter experiments: The diameter of the cylindrical indenter is 2 inches (equivalent to 50.8 mm) and the test specimen depicted is an 18mm-width specimen with a 4 mm groove. 47

Figure 4-5 The indenter set-up with camera carriage: The carriage is attached to the cylindrical indenter support system so the camera moves with the indenter and thus enables video to be captured at a constant distance from the test sample in contact with the indenter surface (Courtesy of Prof. Marc Perlin). 48

Figure 4-6 Kollmorgen AKML53L–ANCNC–00 motor with 5:1 ratio gear reducer installed. 49

Figure 4-7 Micron VT115–005–0–RM100–71 10:1 ratio gear reducer. 49

Figure 4-8 Mechanical connection (i.e., coupling) between gear reducer and the linear positioning mechanism. 50

Figure 4-9 Engineering/nominal stress versus engineering/nominal strain and true stress versus true/natural strain: The specimen used in the tensile test was an 1in-width specimen (without groove). Applied speed was 0.004 inch per second with a corresponding strain rate of approximately 0.002 s^{-1}. 51

Figure 4-10 Fractured specimens of high speed tensile tests. The specimens used in the tests were 18mm-width specimens (without groove). The specimen on the top was subjected to strain rate of 1 s^{-1}, while the one on the bottom was subjected to 2 s^{-1}. 52

Figure 4-11 True stress-strain curves obtained via an MTS machine for different strain rates. The red solid line is obtained by using the data of an 1in-width specimen (without groove), whereas the cyan dashed line and the green dotted line are obtained by using the data of 18mm-width specimens (without groove). 53

Figure 4-12 The operation list that is used to extract engineering strains within the desired 'masked region'. 56

Figure 4-13 Isometric view of the 6mm-width specimen without groove (Courtesy of James Gose and Haocheng Pan). This specimen was obtained by in-house machining of an 18mm-width specimen (without groove). 67

Figure 4-14 Technical drawing of the 6mm-width specimen without groove (Courtesy of James Gose and Haocheng Pan). This specimen was obtained by in-house machining of an 18mm-width specimen (without groove). 67

Figure 4-15 Nital etched AH32 steel 6mm-width specimen (without groove) at Frame 0; that is, in the undeformed state. 68

Figure 4-16 Nital etched AH32 steel 6mm-width specimen (without groove) at Frame 4000; a 3.387 mm end-displacement had been applied. 69

Figure 4-17 Nital etched AH32 steel 6mm-width specimen (without groove) at Frame 7000; a 5.927 mm end-displacement had been applied. 69

Figure 4-18 Nital etched AH32 steel 6mm-width specimen (without groove) at Frame 7441; a 6.300 mm end-displacement had been applied. 70

Figure 4-19 Nital etched AH32 steel 6mm-width specimen (without groove) at Frame 7443; a 6.302 mm end-displacement had been applied. 70

Figure 4-20 Nital etched AH32 steel 6mm-width specimen (without groove) at Frame 7445; a 6.303 mm end-displacement had been applied. 71

Figure 4-21 Evolution of the natural strain within the masked region during the uniaxial test – second approach. Mask size is 16 pixels by 16 pixels (0.264 mm x 0.264 mm). ... 72

Figure 4-22 Evolution of the natural strain within the masked region during the uniaxial test – second approach. Mask size is 32 pixels by 32 pixels (0.528 mm x 0.528 mm). ... 73

Figure 4-23 Evolution of the natural strain within the masked region during the uniaxial test – second approach. Mask size is 64 pixels by 64 pixels (1.056 mm x 1.056 mm). ... 73

Figure 4-24 Evolution of the natural strain within the masked region during the uniaxial test – second approach. Mask size is 128 pixels by 128 pixels (2.112 mm x 2.112 mm). 74

Figure 4-25 Evolution of the natural strain within the masked region during the uniaxial test – second approach. Mask size is 192 pixels by 192 pixels (3.168 mm x 3.168 mm). 74

Figure 4-26 Evolution of the true stress (on the left) and the stress triaxiality (on the right) within the masked region during the uniaxial test – first approach. Mask size is 16 pixels by 16 pixels (0.264 mm x 0.264 mm). 77

Figure 4-27 Evolution of the true stress (on the left) and the stress triaxiality (on the right) within the masked region during the uniaxial test – second approach. Mask size is 16 pixels by 16 pixels (0.264 mm x 0.264 mm). 77

Figure 4-28 Evolution of the true stress (on the left) and the stress triaxiality (on the right) within the masked region during the uniaxial test – first approach. Mask size is 32 pixels by 32 pixels (0.528 mm x 0.528 mm). 78

Figure 4-29 Evolution of the true stress (on the left) and the stress triaxiality (on the right) within the masked region during the uniaxial test – second approach. Mask size is 32 pixels by 32 pixels (0.528 mm x 0.528 mm). 78

Figure 4-30 Evolution of the true stress (on the left) and the stress triaxiality (on the right) within the masked region during the uniaxial test – first approach. Mask size is 64 pixels by 64 pixels (1.056 mm x 1.056 mm). 79

Figure 4-31 Evolution of the true stress (on the left) and the stress triaxiality (on the right) within the masked region during the uniaxial test – second approach. Mask size is 64 pixels by 64 pixels (1.056 mm x 1.056 mm). 79

Figure 4-32 Evolution of the true stress (on the left) and the stress triaxiality (on the right) within the masked region during the uniaxial test – first approach. Mask size is 128 pixels by 128 pixels (2.112 mm x 2.112 mm). 80

Figure 4-33 Evolution of the true stress (on the left) and the stress triaxiality (on the right) within the masked region during the uniaxial test – second approach. Mask size is 128 pixels by 128 pixels (2.112 mm x 2.112 mm). 80

Figure 4-34 Evolution of the true stress (on the left) and the stress triaxiality (on the right) within the masked region during the uniaxial test – first approach. Mask size is 192 pixels by 192 pixels (3.168 mm x 3.168 mm). 81

Figure 4-35 Evolution of the true stress (on the left) and the stress triaxiality (on the right) within the masked region during the uniaxial test – second approach. Mask size is 192 pixels by 192 pixels (3.168 mm x 3.168 mm). 81

Figure 4-36 Demonstration of mask sizes: The red square represents the 32 pixels by 32 pixels mask, whereas the blue rectangle represents the 1024 pixels by 256 pixels mask. Pixel resolution is approximately 16.5 µm/pixel. 83

Figure 4-37 Evolution of the natural strain within the masked region during the uniaxial test – second approach. Mask size is 1024 pixels by 256 pixels (16.896 mm x 4.224 mm). 84

Figure 4-38 Evolution of the true stress (on the left) and the stress triaxiality (on the right) within the masked region during the uniaxial test – first approach. Mask size is 1024 pixels by 256 pixels (16.896 mm x 4.224 mm). 85

Figure 4-39 Evolution of the true stress (on the left) and the stress triaxiality (on the right) within the masked region during the uniaxial test – second approach. Mask size is 1024 pixels by 256 pixels (16.896 mm x 4.224 mm). 85

Figure 4-40 Evolution of the longitudinal strain within the masked region during the uniaxial test for different mask sizes – second approach. Pixel resolution is approximately 16.5 µm/pixel. 87

Figure 4-41 Evolution of the transverse strain within the masked region during the uniaxial test for different mask sizes – second approach. Pixel resolution is approximately 16.5 µm/pixel. 87

Figure 4-42 Evolution of the effective strain within the masked region during the uniaxial test for different mask sizes – second approach. Pixel resolution is approximately 16.5 µm/pixel. 88

Figure 4-43 Effect of mask size on failure strain during the uniaxial test – second approach. The dashed line is a linear curve between two data points. Pixel resolution is approximately 16.5 µm/pixel. 89

Figure 4-44 True stress-strain curve of the uniaxial test for different mask sizes – second approach. Pixel resolution is approximately 16.5 µm/pixel. Solid lines with markers are obtained by digital image correlation (DIC) analysis while dashed lines are the results from the MTS machine. 91

Figure 4-45 Isometric view of the 1in-width specimen with semi-circular groove (Courtesy of James Gose). 93

Figure 4-46 Technical drawing of the 1in-width specimen with semi-circular groove (Courtesy of James Gose). 93

Figure 4-47 Nital etched AH32 steel 1in-width-specimen with semi-circular groove at Frame 0, that is, in the undeformed state. 94

Figure 4-48 Nital etched AH32 steel 1in-width-specimen with semi-circular groove at Frame 5000. 95

Figure 4-49 Nital etched AH32 steel 1in-width-specimen with semi-circular groove at Frame 10000. 95

Figure 4-50 Nital etched AH32 steel 1in-width-specimen with semi-circular groove at Frame 13000. 96

Figure 4-51 Nital etched AH32 steel 1in-width-specimen with semi-circular groove at Frame 13894. 96

Figure 4-52 Nital etched AH32 steel 1in-width-specimen with semi-circular groove at Frame 13895. 97

Figure 4-53 Nital etched AH32 steel 1in-width-specimen with semi-circular groove at Frame 13896. 97

Figure 4-54 Effect of the mask size on failure strain during the the uniaxial test of the 1in-width specimen with semi-circular groove with $y = \ln(a/x + b)$ curve fit – second approach. $a = 3.160$ and $b = 1.062$. Pixel resolution is approximately 15.3 μm/pixel. 98

Figure 4-55 Isometric view of the shear specimen (Courtesy of James Gose). This design is adapted from Bao & Wierzbicki's (2004) specimen design for pure shear tests. 100

Figure 4-56 Technical drawing of the shear specimen (Courtesy of James Gose). This design is adapted from Bao & Wierzbicki's (2004) specimen design for pure shear tests. 100

Figure 4-57 Nital etched AH32 steel shear specimen at Frame 0, that is, in the undeformed state. 101

Figure 4-58 Nital etched AH32 steel shear specimen at Frame 4000............................ 102

Figure 4-59 Nital etched AH32 steel shear specimen at Frame 7000............................ 102

Figure 4-60 Nital etched AH32 steel shear specimen at Frame 8000............................ 103

Figure 4-61 Nital etched AH32 steel shear specimen at Frame 8500............................ 103

Figure 4-62 Nital etched AH32 steel shear specimen at Frame 8600............................ 104

Figure 4-63 Nital etched AH32 steel shear specimen at Frame 8640............................ 104

Figure 4-64 Evolution of the natural strain within the masked region during the uniaxial test of the shear specimen – second approach. Mask size is 16 pixels by 16 pixels (0.219 mm x 0.219 mm). 105

Figure 4-65 Evolution of the natural strain within the masked region during the uniaxial test of the shear specimen – second approach. Mask size is 32 pixels by 32 pixels (0.438 mm x 0.438 mm). 106

Figure 4-66 Evolution of the natural strain within the masked region during the uniaxial test of the shear specimen – second approach. Mask size is 64 pixels by 64 pixels (0.877 mm x 0.877 mm). 106

Figure 4-67 Evolution of the natural strain within the masked region during the uniaxial test of the shear specimen – second approach. Mask size is 128 pixels by 128 pixels (1.754 mm x 1.754 mm). 107

Figure 4-68 Evolution of the true stress (on the left) and the stress triaxiality (on the right) within the masked region during the uniaxial test of the shear specimen – first approach. Mask size is 16 pixels by 16 pixels (0.219 mm x 0.219 mm)...................................... 108

Figure 4-69 Evolution of the true stress (on the left) and the stress triaxiality (on the right) within the masked region during the uniaxial test of the shear specimen – second approach. Mask size is 16 pixels by 16 pixels (0.219 mm x 0.219 mm). 108

Figure 4-70 Evolution of the true stress (on the left) and the stress triaxiality (on the right) within the masked region during the uniaxial test of the shear specimen – first approach. Mask size is 32 pixels by 32 pixels (0.438 mm x 0.438 mm)....................................... 109

Figure 4-71 Evolution of the true stress (on the left) and the stress triaxiality (on the right) within the masked region during the uniaxial test of shear specimen – second approach. Mask size is 32 pixels by 32 pixels (0.438 mm x 0.438 mm)....................................... 109

Figure 4-72 Evolution of the true stress (on the left) and the stress triaxiality (on the right) within the masked region during the uniaxial test of the shear specimen – first approach. Mask size is 64 pixels by 64 pixels (0.877 mm x 0.877 mm)....................................... 110

Figure 4-73 Evolution of the true stress (on the left) and the stress triaxiality (on the right) within the masked region during the uniaxial test of the shear specimen – second approach. Mask size is 64 pixels by 64 pixels (0.877 mm x 0.877 mm). 110

Figure 4-74 Evolution of the true stress (on the left) and the stress triaxiality (on the right) within the masked region during the uniaxial test of the shear specimen – first approach. Mask size is 128 pixels by 128 pixels (1.754 mm x 1.754 mm)................................... 111

Figure 4-75 Evolution of the true stress (on the left) and the stress triaxiality (on the right) within the masked region during the uniaxial test of the shear specimen – second approach. Mask size is 128 pixels by 128 pixels (1.754 mm x 1.754 mm). 111

Figure 4-76 Evolution of the shear strain within the masked region during the uniaxial test of the shear specimen for different mask sizes – second approach. Pixel resolution is approximately 13.7 µm/pixel. 112

Figure 4-77 Evolution of the effective strain within the masked region during the uniaxial test of the shear specimen for different mask sizes – second approach. Pixel resolution is approximately 13.7 µm/pixel. 113

Figure 4-78 Effect of mask size on failure strain during the uniaxial test of the shear specimen – second approach. The dashed line is a linear curve between two data points. Pixel resolution is approximately 13.7 µm/pixel. 114

Figure 4-79 True stress-strain curve of the uniaxial test of the shear specimen for different mask sizes – second approach. Pixel resolution is approximately 13.7 µm/pixel. Solid lines with markers are obtained by digital image correlation (DIC) analysis while dashed lines are the results from the MTS machine. 116

Figure 4-80 Isometric view of the 18mm-width specimen without groove (Courtesy of James Gose and Haocheng Pan). 117

Figure 4-81 Technical drawing of the 18mm-width specimen without groove (Courtesy of James Gose and Haocheng Pan). 118

Figure 4-82 Nital etched AH32 steel 18mm-width-specimen without groove at Frame 0; that is, in the undeformed state. 119

Figure 4-83 Nital etched AH32 steel 18mm-width-specimen without groove at Frame 5000; that is, a 10.160 mm indentation had been applied.. 119

Figure 4-84 Nital etched AH32 steel 18mm-width-specimen without groove at Frame 10000; that is, a 20.320 mm indentation had been applied.. 120

Figure 4-85 Nital etched AH32 steel 18mm-width-specimen without groove at Frame 15000; that is, a 30.480 mm indentation had been applied.. 120

Figure 4-86 Nital etched AH32 steel 18mm-width-specimen without groove at Frame 20000; that is, a 40.640 mm indentation had been applied.. 121

Figure 4-87 Nital etched AH32 steel 18mm-width-specimen without groove at Frame 22250; that is, a 45.212 mm indentation had been applied.. 121

Figure 4-88 Nital etched AH32 steel 18mm-width-specimen without groove at Frame 24250; that is, a 49.276 mm indentation had been applied.. 122

Figure 4-89 Nital etched AH32 steel 18mm-width-specimen without groove at Frame 24520; that is, a 49.825 mm indentation had been applied.. 122

Figure 4-90 Nital etched AH32 steel 18mm-width-specimen without groove at Frame 24526; that is, a 49.837 mm indentation had been applied.. 123

Figure 4-91 Nital etched AH32 steel 18mm-width-specimen without groove at Frame 24527; that is, a 49.839 mm indentation had been applied.. 123

Figure 4-92 Evolution of the natural strain within the masked region during the cylindrical indentation – first approach. Mask size is 16 pixels by 16 pixels (0.219 mm x 0.219 mm).. 125

Figure 4-93 Evolution of the natural strain within the masked region during the cylindrical indentation – second approach. Mask size is 16 pixels by 16 pixels (0.219 mm x 0.219 mm).. 125

Figure 4-94 Evolution of the natural strain within the masked region during the cylindrical indentation – second approach. Mask size is 32 pixels by 32 pixels (0.438 mm x 0.438 mm).. 126

Figure 4-95 Evolution of the natural strain within the masked region during the cylindrical indentation – second approach. Mask size is 64 pixels by 64 pixels (0.877 mm x 0.877 mm).. 126

Figure 4-96 Evolution of the natural strain within the masked region during the cylindrical indentation – second approach. Mask size is 128 pixels by 128 pixels (1.754 mm x 1.754 mm).. 127

Figure 4-97 Evolution of the natural total strain within the masked region during the cylindrical indentation – second approach. Mask size is 192 pixels by 192 pixels (2.630 mm x 2.630 mm).. 127

Figure 4-98 Evolution of the true stress (on the left) and the stress triaxiality (on the right) within the masked region during the cylindrical indentation – first approach. Mask size is 16 pixels by 16 pixels (0.219 mm x 0.219 mm). 129

Figure 4-99 Evolution of the true stress (on the left) and the stress triaxiality (on the right) within the masked region during the cylindrical indentation – second approach. Mask size is 16 pixels by 16 pixels (0.219 mm x 0.219 mm)... 129

Figure 4-100 Evolution of the true stress (on the left) and the stress triaxiality (on the right) within the masked region during the cylindrical indentation – first approach. Mask size is 32 pixels by 32 pixels (0.438 mm x 0.438 mm). 130

Figure 4-101 Evolution of the true stress (on the left) and the stress triaxiality (on the right) within the masked region during the cylindrical indentation – second approach. Mask size is 32 pixels by 32 pixels (0.438 mm x 0.438 mm)....................................... 130

Figure 4-102 Evolution of the true stress (on the left) and the stress triaxiality (on the right) within the masked region during the cylindrical indentation – first approach. Mask size is 64 pixels by 64 pixels (0.877 mm x 0.877 mm). 131

Figure 4-103 Evolution of the true stress (on the left) and the stress triaxiality (on the right) within the masked region during the cylindrical indentation – second approach. Mask size is 64 pixels by 64 pixels (0.877 mm x 0.877 mm)....................................... 131

Figure 4-104 Evolution of the true stress (on the left) and the stress triaxiality (on the right) within the masked region during the cylindrical indentation – first approach. Mask size is 128 pixels by 128 pixels (1.754 mm x 1.754 mm). 132

Figure 4-105 Evolution of the true stress (on the left) and the stress triaxiality (on the right) within the masked region during the cylindrical indentation – second approach. Mask size is 128 pixels by 128 pixels (1.754 mm x 1.754 mm).................................. 132

Figure 4-106 Evolution of the true stress (on the left) and the stress triaxiality (on the right) within the masked region during the cylindrical indentation – first approach. Mask size is 192 pixels by 192 pixels (2.630 mm x 2.630 mm). 133

Figure 4-107 Evolution of the true stress (on the left) and the stress triaxiality (on the right) within the masked region during the cylindrical indentation – second approach. Mask size is 192 pixels by 192 pixels (2.630 mm x 2.630 mm).................................. 133

Figure 4-108 Evolution of the effective strain within the masked region the during cylindrical indentation for different mask sizes – second approach. Pixel resolution is approximately 13.7 µm/pixel... 135

Figure 4-109 Effect of the mask size on failure strain during the cylindrical indention with $y = \ln(a/x + b)$ curve fit – second approach. $a = 2.209$ and $b = 1.026$. Pixel resolution is approximately 13.7 µm/pixel. 136

Figure 4-110 True stress-strain curve of the cylindrical indenter test for different mask sizes – second approach. Pixel resolution is approximately 13.7 µm/pixel. Solid lines with markers are obtained by digital image correlation (DIC) analysis while dashed lines are the results from the MTS machine. 138

Figure 4-111 Isometric view of the 18mm-width specimen with 4mm groove (Courtesy of James Gose and Haocheng Pan). 142

Figure 4-112 Technical drawing of the 18mm-width specimen with 4mm groove (Courtesy of James Gose and Haocheng Pan). 143

Figure 4-113 Nital etched AH32 steel 18mm-width-specimen with 4mm groove at Frame 0, that is, in the undeformed state. 144

Figure 4-114 Nital etched AH32 steel 18mm-width-specimen with 4mm groove at Frame 7500, that is, a 15.240 mm indentation had been applied.. 144

Figure 4-115 Nital etched AH32 steel 18mm-width-specimen with 4mm groove at Frame 13000, that is, a 26.416 mm indentation had been applied.. 145

Figure 4-116 Nital etched AH32 steel 18mm-width-specimen with 4mm groove at Frame 13500, that is, a 27.432 mm indentation had been applied.. 145

Figure 4-117 Nital etched AH32 steel 18mm-width-specimen with 4mm groove at Frame 13800, that is, a 28.042 mm indentation had been applied.. 146

Figure 4-118 Nital etched AH32 steel 18mm-width-specimen with 4mm groove at Frame 13880, that is, a 28.204 mm indentation had been applied.. 146

Figure 4-119 Nital etched AH32 steel 18mm-width-specimen with 4mm groove at Frame 13883, that is, a 28.210 mm indentation had been applied.. 147

Figure 4-120 Nital etched AH32 steel 18mm-width-specimen with 4mm groove at Frame 13884, that is, a 28.212 mm indentation had been applied.. 147

Figure 4-121 Evolution of the natural strain within the masked region during the cylindrical indentation – first approach. Mask size is 16 pixels by 16 pixels (0.219 mm x 0.219 mm)... 149

Figure 4-122 Evolution of the natural strain within the masked region during the cylindrical indentation – second approach. Mask size is 16 pixels by 16 pixels (0.219 mm x 0.219 mm).. 149

Figure 4-123 Evolution of the natural strain within the masked region during the cylindrical indentation – second approach. Mask size is 32 pixels by 32 pixels (0.438 mm x 0.438 mm).. 150

Figure 4-124 Evolution of the natural strain within the masked region during the cylindrical indentation – second approach. Mask size is 64 pixels by 64 pixels (0.877 mm x 0.877 mm).. 150

Figure 4-125 Evolution of the natural strain within the masked region during the cylindrical indentation – second approach. Mask size is 128 pixels by 128 pixels (1.754 mm x 1.754 mm).. 151

Figure 4-126 Evolution of the true stress (on the left) and the stress triaxiality (on the right) within the masked region during the cylindrical indentation – first approach. Mask size is 16 pixels by 16 pixels (0.219 mm x 0.219 mm). 152

Figure 4-127 Evolution of the true stress (on the left) and the stress triaxiality (on the right) within the masked region during the cylindrical indentation – second approach. Mask size is 16 pixels by 16 pixels (0.219 mm x 0.219 mm)....................................... 153

Figure 4-128 Evolution of the true stress (on the left) and the stress triaxiality (on the right) within the masked region during the cylindrical indentation – first approach. Mask size is 32 pixels by 32 pixels (0.438 mm x 0.438 mm). 153

Figure 4-129 Evolution of the true stress (on the left) and the stress triaxiality (on the right) within the masked region during the cylindrical indentation – second approach. Mask size is 32 pixels by 32 pixels (0.438 mm x 0.438 mm)....................................... 154

Figure 4-130 Evolution of the true stress (on the left) and the stress triaxiality (on the right) within the masked region during the cylindrical indentation – first approach. Mask size is 64 pixels by 64 pixels (0.877 mm x 0.877 mm). 154

Figure 4-131 Evolution of the true stress (on the left) and the stress triaxiality (on the right) within the masked region during the cylindrical indentation – second approach. Mask size is 64 pixels by 64 pixels (0.877 mm x 0.877 mm)....................................... 155

Figure 4-132 Evolution of the true stress (on the left) and the stress triaxiality (on the right) within the masked region during the cylindrical indentation – first approach. Mask size is 128 pixels by 128 pixels (1.754 mm x 1.754 mm). 155

Figure 4-133 Evolution of the true stress (on the left) and the stress triaxiality (on the right) within the masked region during the cylindrical indentation – second approach. Mask size is 128 pixels by 128 pixels (1.754 mm x 1.754 mm).................................... 156

Figure 4-134 Evolution of the longitudinal strain within the masked region during the cylindrical indentation for different mask sizes – second approach. Pixel resolution is approximately 13.7 µm/pixel.. 157

Figure 4-135 Evolution of the transverse strain within the masked region during the cylindrical indentation for different mask sizes – second approach. Pixel resolution is approximately 13.7 µm/pixel.. 158

Figure 4-136 Evolution of the effective strain within the masked region during the cylindrical indentation for different mask sizes – second approach. Pixel resolution is approximately 13.7 µm/pixel.. 159

Figure 4-137 Effect of the mask size on failure strain during the cylindrical indention with $y = \ln(a/x + b)$ curve fit – second approach. $a = 1.246$ and $b = 1.111$. Pixel resolution is approximately 13.7 µm/pixel.. 160

Figure 4-138 True stress-strain curve of the cylindrical indenter test for different mask sizes – second approach. Pixel resolution is approximately 13.7 µm/pixel. Solid lines with markers are obtained by digital image correlation (DIC) analysis while dashed lines are the results from the MTS machine.. 162

Figure 5-1 Effective strain to fracture versus stress triaxiality for the plane stress condition for the 16 pixels by 16 pixels mask. Two toughness stress results are shown for the opening mode fracture (cyan solid curve and green solid curve), whereas the results of only one toughness stress are presented for the shear mode fracture. For the shear mode fracture, the blue solid curve shows the result for the critical state with no friction on the fracture planes, while the dotted dashed line shows the results of friction occuring on the fracture planes due to compressive normal stresses... 171

Figure 5-2 Effective strain to fracture versus stress triaxiality for the plane stress condition for the 32 pixels by 32 pixels mask. Two toughness stress results are shown for the opening mode fracture (cyan solid curve and green solid curve), whereas the results of only one toughness stress are presented for the shear mode fracture. For the shear mode fracture, the blue solid curve shows the result for the critical state with no friction on the fracture planes, while the dotted dashed line shows the results of friction occuring on the fracture planes due to compressive normal stresses.. 172

Figure 5-3 Effective strain to fracture versus stress triaxiality for the plane stress condition for the 128 pixels by 128 pixels mask. Two toughness stress results are shown for the opening mode fracture (cyan solid curve and green solid curve), whereas the results of one toughness stress is presented for the shear mode fracture. For the shear mode fracture, the blue solid curve shows the result for the critical state with no friction on the fracture planes, while the dotted dashed line shows the results of friction occuring on the fracture planes due to compressive normal stresses.. 173

Figure 5-4 Effective strain to fracture versus toughness stress for Mode I fracture for the uniaxial test of the 6mm-width specimen without groove with a test speed of 0.2 inch/second. 174

Figure 5-5 Effective strain to fracture versus characteristic length for the uniaxial test of the 6mm-width specimen without groove with a test speed of 0.2 inch/second. Pixel resolution is approximately 16.5 µm/pixel. 175

ABSTRACT

A new method of predicting ductile fracture initiation is presented based on comparison of the energy dissipation rates of the bulk continuum system to the fractured medium. A fracture criterion is posited for plastic materials with no pre-existing cracks as a critical state being reached when the energy release rate of the bulk system is balanced by the energy release rate associated with the fractured medium. The energy dissipation of the continuum system includes that of plastic work while that of the fractured system includes the surface energy of the crack formation, plastic work, and frictional losses (if any) at the instant of crack initiation. Two fracture modes are considered which are commonly addressed in fracture mechanics: Mode I crack opening perpendicular to the fracture plane and Mode II shear rupture tangential to the fracture plane. The theory introduces a length scale and a new material constant which we call toughness stress. The toughness stress is defined as the surface energy release rate divided by the micro-structural characteristic length of the material. A study of the use of the criterion for a plastic material with power-law hardening is examined and compared with published experimental data for aluminum.

Furthermore, a series of uniaxial tests and cylindrical indenter experiments on AH32 steel, a mild steel, were conducted to investigate fracture initiation states and the scale/mesh size effect. Strains at fracture are obtained using digital image correlation (DIC) analysis, and the corresponding states of stress are obtained via the constitutive relationships and the stress-strain relationships using the measured strains. The strain fields are calculated to the point of fracture initiation where we define the fracture initiation as the condition when the first visible crack appears in the digital image of the test specimen.

The toughness stress of AH32 steel for the two fracture modes are calculated using the current experimental results. It is shown that the surface energy release rates for both the aluminum alloy and the AH32 steel calculated from the new theory for ductile fracture compare well with the surface energy release rates used in traditional fracture mechanics.

CHAPTER 1

Introduction

1.1 Motivation for the Research

Mechanical failure is of particular interest to humankind for designing and constructing large expensive transportation structures such as ships, offshore structures, airplanes and automobiles. These structures may become damaged due to collision with a similar structure or due to an impact with icebergs, floating or flying debris, etc.

Material failure, which may be categorized as 'brittle fracture' or 'ductile fracture', is a mechanical failure mode among several possible modes, which include buckling, fatigue, creep, and plastic collapse. Brittle fracture can be catastrophic as it happens very rapidly due to lack of plastic deformation[1] whereas extensive plastic deformation takes place in a ductile fracture[2] process. Due to its catastrophic nature, brittle fracture has been a subject of interest for many years and it has been more extensively studied and better understood than ductile fracture. However, ductile fracture began receiving more attention from researchers with the development and growth of the naval, aerospace and automobile industries, whose usage of high strength metals has become common.

The safety of such structures depends in large part on the system's ability to withstand extreme loading events such as collision, accidental impact from other objects, and in some cases, explosions. In other words, these mobile structures require safe operational

---

[1] It is worth noting that notch-brittleness might occur after considerable plastic deformation. Hence, by 'brittle fracture' the author means fracture occurring during or immediately after elastic loading; that is, there is no or very little plastic deformation.

[2] By ductile fracture, we mean the occurrence of fracture in materials which undergo large deformations before the fracture is complete.

requirements during their life span, not only because they are expensive but also because their failure may cause loss of human life. The duty of designers and engineers is to provide maximum safety with minimum weight and cost while satisfying design requirements. Therefore, prediction of material failure initiation is crucial for a safe design.

The objective of the research presented here is to develop, through combined experimental and analytical studies, a thorough understanding of the evolution of the non-linear stress and strain states leading to ductile fracture. Moreover, this study is to provide key parameters for predicting fracture of ductile materials in general, and thus assist in the guidance of criteria development for materials other than those specifically addressed. The goals are to obtain and compare analytical and experimental results, and to define an appropriate criterion for the onset of ductile fracture at the continuum scale.

1.2 Historical Background

Although human interest in fracture started a very long time ago, most of the effort to understand and explain the mechanisms behind it has been advanced over the past several decades. This sub-section provides an overview of only the most influential studies and developments; a comprehensive historical development of fracture mechanics is discussed by Erdogan (2000) and Cotterel (2002).

Griffith (1921) developed a fracture criterion for a (brittle) material with a pre-existing elliptical crack by using an energy balance approach. In the derivation of his fracture criterion, Griffith considered only the elastic strain energy of the system and validated his formulation by conducting experiments with glass, which is a brittle material. However, the application of the criterion did not provide satisfying results for ductile materials. Later, it was shown by Orowan (1945, 1949) and Irwin (1948) that Griffith's fracture criterion can be applicable only to brittle fracture; i.e., it cannot be directly applied to ductile fracture where the fracture mechanism is different and plastic deformation plays an essential role.

Orowan (1949) derived an expression – similar to Griffith's expression – for fracture of brittle materials by approaching the problem at the micro-scale, and he suggested a fracture criterion for brittle fracture of ductile materials by making a small but important modification (i.e., adding the plastic work contribution) to Griffith's formula.

In a related effort, Irwin (1957) showed that the stress distribution near the crack tip can be determined by a so-called 'crack-extension-force' and he generalized Griffith's formulation for arbitrary crack geometries and loading conditions. This was accomplished by developing the 'stress intensity factor' concept in addition to the 'crack-extension-force' concept.

A criterion for brittle fracture usually requires the current state of stress, whereas ductile fracture depends on the history of the state of stress and strain. Moreover, the underlying mechanisms of ductile fracture are very complex. The fracture process can be divided into three stages: i) void nucleation, ii) void growth, iii) void coalescence[3]. The simulation of the deformation and eventual fracture of structural materials are fundamentally important and have received considerable attention. The modeling efforts are often based on the pioneering works of McClintock (1968), Rice & Tracey (1969), Needleman (1972) and Gurson (1977) for modelling of void growth and coalescence.

Roughly half a century ago, McClintock (1968) developed an expression for void growth and coalescence of long cylindrical holes (i.e., using the plane-strain assumption) of elliptical cross section in an infinite plastic medium under an equiaxial stress state. He assumed that most of the strain occurs while the holes are still small and neglected their interactions. He developed the criterion by combining and modifying the solution of the growth of circular holes in a plastic medium and the Berg (1962) solution of change in size and shape of elliptical holes in a viscous medium. Moreover, he used his solution for void growth and coalescence to develop a ductile fracture criterion of pre-existing holes in a plastic material. Note that, as he pointed out, his criterion overpredicts the fracture strain.

---

[3] Garrison & Moody (1987) provided a detailed summary of experimental observations and mathematical models on each stage of the ductile fracture process in their review paper. In addition, the paper includes research studies and results of stress states and strain distributions of tensile tests on smooth and notched specimens. Finally, the authors conclude the paper with a thorough discussion on fracture toughness and crack-tip-opening displacement predictions.

Rice & Tracey (1969) explored the contribution of the volume change and the shape change parts in the growth of an isolated spherical void (i.e., they neglected the interactions of neighboring voids) in a non-hardening infinite rigid-plastic medium under uniform far-field stress and strain. The solution was obtained by establishing a variational principle and applying it through the Rayleigh-Ritz method. Moreover, as a complement to McClintock's (1968) analysis, they also applied the established variational principle to McClintock's study of cylindrical voids (for a non-hardening material).

Needleman (1972) studied void growth and coalescence of doubly-periodic square arrays of circular cylindrical voids in an elastic-plastic medium under uniaxial deformation. His numerical solution was obtained by a variational principle for the plane-strain condition. He extrapolated his solution to predict the strain at void coalescence.

Gurson (1977) developed a general yield criterion and flow rule for porous ductile materials[4] by using a unit cube model having random void shapes and orientations. The matrix material is assumed to be homogeneous, incompressible, rigid-plastic and sufficiently large to statistically represent the properties of the aggregate. Moreover, he applied his general formulation to two different void geometries (a long circular cylinder and a sphere) by simplifying his model as a single void that is located in the center of the cell and geometrically similar to the outer cell wall. A few years later, Tvergaard (1981) introduced three parameters into the (original) Gurson model to account for realistic values.

However, original and the modified Gurson models are based on the void growth mechanics of axisymmetric stress states and predict zero void growth rate under zero mean stress, except when voids are nucleated (Nahshon & Hutchinson, 2008). Nahshon & Hutchinson (2008) introduced a new term into the void growth rate (see/compare Equation (9) and Equation (10) of the cited reference) that accounts for the shear-dominated stress states. As they pointed out, this modification leaves the growth rate unaltered for the axisymmetric stress states.

---

[4] *"... a porous material (aggregate of voids and ductile matrix) rather than a polycrystalline aggregate."* (Gurson, 1977). In other words, his analyses focused on microscopic scale rather than macroscopic scale.

Macro-scale studies have been conducted as well in addition to micro-scale studies discussed above. At the macro-scale, the most popular approach for the initiation of ductile fracture of metals is to establish the limiting effective strain to material failure based on the stress state. The state of stress may be expressed in terms of the mean stress and the second deviatoric stress invariant (e.g., stress triaxiality) for two dimensional state of stress conditions and the third deviatoric stress invariant (e.g., Lode parameter) as well for three dimensional state of stress conditions. Such proposals for characterizing ductile failure have been studied extensively.

Over a decade ago, Bao & Wierzbicki (2004) developed a fracture locus for 2024-T351 aluminum alloy by introducing three empirical relations for three different regions: void sheeting (i.e., shear fracture), internal necking (i.e., opening mode fracture), and the combination of void sheeting and internal necking[5]. The most important result was that the fracture locus has a slope discontinuity, which they define as the point of transition of the fracture mechanisms. A decade later, Papasidero et al. (2015) performed experiments on 2024-T351 aluminum alloy tubular specimens to revisit the results of Bao & Wierzbicki (2004) and investigate the effects of non-proportional loading on fracture strain. Although they have qualitatively similar results as Bao & Wieazbicki (2004) for high stress triaxialities, Papasidero et al. (2015) obtained different qualitative results in the low stress triaxiality region. Possible reasons for this are discussed in the 'Discussion section' of Papasidero et al. (2015). As they pointed out, this may be due to differences in the microstructures of the Al 2024-T351 specimens used. However, the author believes that the differences in the numerical modeling (element type, for example) may contribute as well.

Recently, Li & Karr (2009) predicted the onset of ductile fracture in tension from the stability point of view. Small dynamic perturbations were introduced near static equilibrium to assess the static stability. An idealized three-piece-model, addressed by Hart (1967), was used to represent the 'homogenous' and 'imperfect' parts of the material. The onset of fracture was interpreted as the result of a supercritical pitchfork bifurcation of homogeneous deformation. They also developed an analytical expression that accounts

---

[5] Figure 3 of Besson (2010) shows the difference between internal necking and void sheeting.

for the length scale in fracture strain (see "Equation 22" of the cited reference). Moreover, they explored the effect of an 'imperfection parameter' on the evolution of strains of 'homogenous' and 'imperfect' parts (see Figure 8 of the cited reference) and the effect of length scale on the evolution of total strain (see Figure 9 of the cited reference).

Most of the past studies have been focused on void growth and coalescence; that is, numerous researchers have focused on establishing a criterion for crack propagation (i.e., extension of pre-existing cracks). Moreover, there is presently no generally-accepted criterion for ductile fracture. Therefore, the objective of the current study is the development of a closed-form theoretical solution and the presentation of experimental results on the ***initiation*** of ductile fracture at the continuum scale. Ductile fracture at the atomistic level is discussed elsewhere (see e.g., Baskes & Ortiz, 2015).

1.3 Outline of the Dissertation

This dissertation consists of six chapters. An overview of the most influential fracture criteria is presented in the second chapter, while a new fracture criterion on the initiation of ductile fracture is presented in the third chapter. The fourth chapter provides the process, analyses, and the results of the experiments on a mild steel. Finally, the experimental and the theoretical results are compared in the fifth chapter, and conclusions and suggested future work are presented in the sixth chapter.

CHAPTER 2

Review of Current Fracture Criteria

2.1 Griffith's Method

Griffith's (1921) study was the first published work that considered the energy balance approach to define a fracture criterion. He called this approach the 'extended theorem of minimum energy'. He stated that:

"The total decrease in potential energy due to formation of a crack is equal to the increase in strain energy less the increase in surface energy[6]*."*

Griffith believed that the difference between the theoretical and practical strength of a material was due to existing small cracks in the material. He then developed a fracture criterion (for brittle materials) by minimizing the 'change in potential energy', which represents an unstable equilibrium[7]; i.e., the condition for a crack to propagate. He considered a large flat plate (under biaxial stress state) with a pre-existing small crack (the crack length should be small compared to the plate dimension but large compared to 'radius of molecular action') for plane-stress and plane-strain conditions. His derivation was obtained by using the linear elasticity relationships and assuming that the plate is homogenous, isotropic and has a uniform thickness.

---

[6] The surface energy which occurs during the formation of new surfaces.

[7] The second derivative of ΔU with respect to c equals "$-\frac{2\pi\sigma^2}{E^*}$" (see Equation (2-5)). As the second derivative of "change in potential energy, ΔU" is negative, it represents an unstable equilibrium.

The increase in elastic strain energy of a plate per unit thickness due to an existing elliptical crack of length[8] $2c$ is[9]

$$U_e = -\frac{\pi\sigma^2 c^2}{E^*} \tag{2-1}$$

where $E^* = E$ for plane-stress and $E^* = E/(1-\nu^2)$ for plane-strain conditions. σ is the applied in-plane stress, c is half the crack length, υ is Poisson's ratio, and E is the modulus of elasticity. The negative sign represents the decrease of elastic strain energy (due to formation of the crack); that is, the crack releases elastic strain energy.

The surface energy of the crack per unit thickness is

$$U_s = 4c\alpha \tag{2-2}$$

where α is the specific surface energy.

The total change in potential energy per unit thickness (due to formation of the crack) is then

$$\Delta U = U_s + U_e \tag{2-3}$$

According to Griffith's 'extended theorem of minimum energy', if an infinitesimal increase in crack length produces no change in the total potential energy of the system under constant applied load, then the existing crack will propagate (Dieter, 1986). This is due to the system seeking the minimum potential energy state.

Using this notion, the necessary condition for crack propagation can be expressed mathematically in the form:

$$\frac{d}{dc}(\Delta U) = \frac{d}{dc}(U_s + U_e) = 0 \tag{2-4}$$

---

[8] An internal crack of length $2c$ is equivalent to a surface crack of depth c (Orowan, 1945) and edge crack of length c (Dieter, 1986).

[9] The expressions given in the original paper (Griffith, 1921) were erroneous due to miscalculation of the elastic strain energy. The expression above (i.e., Equation (2-1)) is the correct formulation of the elastic strain energy, however.

and

$$\Delta U = 4c\alpha - \frac{\pi\sigma^2 c^2}{E^*} \tag{2-5}$$

Hence, substitution yields

$$\frac{d}{dc}\left(4c\alpha - \frac{\pi\sigma^2 c^2}{E^*}\right) = 0 \tag{2-6}$$

Simplifying this yields the expression for the critical applied in-plane stress at fracture

$$\sigma^f = \sqrt{\frac{2\alpha E^*}{\pi c}} \tag{2-7}$$

where again $E^* = E$ for plane-stress and $E^* = E/(1-\nu^2)$ for plane-strain conditions.

As can be seen from the expressions above, and as Griffith (1921) stated, $\sigma^f\sqrt{c}$ is a constant for a specific material; that is, it is a material constant. Here σ^f is the critical applied in-plane stress (required for 'fracture' for a given crack length) and c is the crack half-length.

As a validation, Griffith performed (plane-stress) experiments with glass. As the loading and annealing of large glass flat plates were difficult, he decided to use thin round tubes and spherical bulbs for his experiments (Griffith, 1921). His experiments with various sizes of cracks were in fairly good agreement with his expression for the plane-stress condition.

However, glass is a brittle material and the plastic strain energy, which has an important role in ductile facture, was not included in Griffith’s (1921) formulation. Later, it was shown by Orowan (1945; 1949) and Irwin (1948) that Griffith’s (1921) fracture criterion is applicable only to brittle fracture; i.e., it cannot be directly applied to ductile fracture as the fracture mechanism[10] of ductile fracture is different than that of the brittle fracture. It turns out that plastic deformation plays an essential role, and furthermore, strain hardening is an additional important factor. However, Griffith's idea and approach made a considerable contribution to the field, in general, and also has had a major influence on the progress of modeling ductile fracture.

2.2 Orowan's Contribution

Orowan derived an expression – similar to Griffith's (1921) expression – for fracture of brittle materials by approaching the problem at the micro-scale and he suggested a fracture criterion for brittle fracture of ductile materials by making a small modification to Griffith's formula.

2.2.1 Fracture Criterion for Brittle Materials

By equating the elastic strain energy per unit volume between two neighboring atomic planes of distance a_0 to the specific surface energy α, Orowan (1949) obtained

$$a_0 \frac{\sigma_{ms}^2}{2E} = \alpha \tag{2-8}$$

Rearranging Equation (2-8) yields

$$\sigma_{ms} = \sqrt{\frac{2\alpha E}{a_0}} \tag{2-9}$$

where σ_{ms} is the order of magnitude of maximum theoretical molecular strength and E is the modulus of elasticity.

---

[10] In brittle fracture, the crack propagates suddenly following the initiation of facture. In the case of ductile fracture, however, the specimen undergoes a considerable amount of extension – this amount varies depending on the geometrical shape, ductility of the material, and the loading condition – between the initiation and completion of fracture, and this involves large plastic deformations (Orowan, 1945).

The maximum tensile stress of a plate containing a flat elliptical hole of length $2c$, which occurs at the corners, is (Griffith, 1921)

$$\sigma_{max} = 2\sigma\sqrt{\frac{c}{\rho}} \tag{2-10}$$

where c is the crack half-length, ρ is the radius of curvature at the corners of the elliptical crack, and σ is the applied in-plane stress.

Orowan (1949) assumed that the radius of curvature of the sharpest crack cannot be less than the order of the atomic distance magnitude a_0. Then, the maximum tensile stress at the sharpest crack is

$$\sigma_{max} = 2\sigma\sqrt{\frac{c}{a_0}} \tag{2-11}$$

As the brittle fracture starts at the point of maximum stress, Orowan (1949) obtained an expression for the critical applied in-plane stress for a given crack length (for fracture of a brittle material) by equating the microscopic stress at the sharpest crack (i.e., σ_{max}) to the value of maximum molecular cohesion (i.e., σ_{ms}). Hence, $\sigma_{ms} = \sigma_{max}$ and he obtained

$$\sigma^f = \sqrt{\frac{\alpha E}{2c}} \tag{2-12}$$

Note that this expression differs from Griffith's (1921) expression (for the plane-stress condition) only by a factor of $\sqrt{\pi/4}$.

2.2.2 Fracture Criterion for Ductile Materials

Orowan (1945) observed a considerable amount of plastic deformation in X-ray photos of low carbon steel 0.5 mm beneath the surface (see Fig 11b of Orowan, 1945). Hence, he (Orowan, 1949) proposed that plastic work should be added to the surface energy term in Griffith's (1921) expression (for brittle fracture of ductile materials), which yields

$$\sigma^f = \sqrt{\frac{(2\alpha + p)E^*}{\pi c}} \qquad (2\text{-}13)$$

where again $E^* = E$ for plane-stress and $E^* = E/(1-\nu^2)$ for plane-strain conditions. Also, p is the amount of plastic work per unit area, c is half the crack length, and σ^f is the critical applied in-plane stress (required for 'fracture' for a given crack length)[11].

As the magnitude of the plastic work would be much larger than the specific surface energy, the specific surface energy can be neglected (Orowan, 1949). Hence, the order of critical applied in-plane stress for a given crack length (for brittle fracture of a ductile material) is

$$\sigma^f \approx \sqrt{\frac{pE^*}{\pi c}} \qquad (2\text{-}14)$$

2.3 Irwin's Contribution

Irwin (1957) generalized Griffith's formulation for arbitrary crack geometries and loading conditions by developing the 'crack-extension-force' and the 'stress intensity factor' concepts.

Irwin (1957) obtained the stress distribution near the crack tip in a large plate containing a straight crack (a single crack or a collinear series of such cracks) along the x-axis. The crack length is assumed to be small compared to the plate dimensions. Moreover, the plastic zone around the crack tip is assumed small[12] compared to the crack length such that linear elasticity solutions can be applied near the crack tip. The formulation was derived for the opening mode (i.e., Mode I) fracture of an arbitrary shape of crack and

---

[11] Note that in the notation and formulation in Chapter 3, the corresponding values are $2\alpha = \Gamma \times A$ and $p = l_3 . dW^*$ or $p = l_2 . dW^*$, depending on which direction is the thickness direction. Note that dW^* is the plastic work per unit volume of the fractured element.

[12] *"... a region of large plastic deformations may exist close to the crack but does not extend away from the crack by more than a small fraction of the crack length"* (Irwin, 1957).

loading condition with the aid of the linear elastic solutions obtained by Westergaard (1939)

$$\sigma_{xx} = \left(\frac{\mathcal{G}_I E^*}{\pi}\right)^{1/2} \frac{1}{\sqrt{2r}} \cos\left(\frac{\theta}{2}\right)\left[1 - \sin\left(\frac{\theta}{2}\right)\sin\left(\frac{3\theta}{2}\right)\right] \tag{2-15}$$

$$\sigma_{yy} = \left(\frac{\mathcal{G}_I E^*}{\pi}\right)^{1/2} \frac{1}{\sqrt{2r}} \cos\left(\frac{\theta}{2}\right)\left[1 + \sin\left(\frac{\theta}{2}\right)\sin\left(\frac{3\theta}{2}\right)\right] \tag{2-16}$$

where σ_{xx} and σ_{yy} are the components of the stress tensor. Moreover, $\mathcal{G}$ is independent of r and θ and it is called 'fixed-grip strain energy release rate' (loss/release of strain energy due to unit crack extension[13]) and can also be interpreted as the 'crack-extension-force' (Irwin, 1957). r is the radial distance from the crack tip and the upper range of r is limited to distances small compared to crack dimensions. θ is the angle measured from the x-axis in the counter-clockwise direction and the Roman subscript I (of $\mathcal{G}$) refers to the opening mode (i.e., Mode I). $E^* = E$ for plane-stress and $E^* = E/(1-\nu^2)$ for plane-strain conditions.

As can be seen from the expressions above (see Equation (2-15) and Equation (2-16)), Irwin (1957) showed that stress distribution near the crack tip can be determined by the 'crack-extension-force'.

These expressions (i.e., Equation (2-15) and Equation (2-16)) can be generalized to all three fracture modes, that is, the opening mode (called 'Mode I'), the shear/sliding-mode (called 'Mode II'), and the tearing-mode (called 'Mode III') in the following form

$$\sigma_{ij} = \frac{K}{\sqrt{2r}} f_{ij}(\theta) \tag{2-17}$$

---

[13] *"The strain-energy loss rate associated with the extension of the fracture accompanied only by plastic strains local to the crack surfaces"* (Irwin, 1957).

Here, $f_{ij}(\theta)$ is associated with the fracture mode and it is independent of the crack geometry and the loading conditions. K is called the 'stress intensity factor'[14] and it varies with the crack geometry and the loading conditions. The stress intensity factor can be expressed as[15]

$$K = \sqrt{\frac{\mathcal{G}E^*}{\pi}} \tag{2-18}$$

The necessary condition for crack propagation is satisfied when the crack-extension-force reaches a critical value, called the critical-crack-extension-force, $\mathcal{G}_c$. The critical crack-extension-force for a particular fracture mode is a material constant and the corresponding critical stress intensity factor is called the 'fracture toughness'.

Theoretical calculations of the stress intensity factors of the opening mode (K_I) for different crack geometries and loading conditions can be found on p. 563–565 of Irwin (1960). In addition, the experimental measurement procedure of the crack-extension-force for the opening mode ($\mathcal{G}_I$) by strain-gauge is explained on p. 364 of Irwin (1957), while that based on the change of the spring constant is explained on p. 565–567 of Irwin (1960).

2.4 Rice's Contribution

Just over a decade after the development of the stress intensity factor and the crack-extension force (i.e., the strain energy release rate) concepts by Irwin (1957), a new method on the calculation of the crack-extension-force $\mathcal{G}$ was developed by Rice

---

[14] The notation/formulation here is adapted from the original references, that is, Irwin (1957, 1960). However, it is worth noting that recent references may use the following notation/formulation:
$\sigma_{ij} = \frac{K}{\sqrt{2\pi r}} f_{ij}(\theta)$ where $K = \sqrt{\mathcal{G}E^*}$.

[15] Note that this expression is the generalization of Griffith's (1921) expression for various crack geometries and loading conditions. For instance, the stress intensity factor (of the opening mode) for Griffith's (1921) specific case is $K_I = \sigma\sqrt{c}$ (Irwin, 1960).

(1968)[16]. This method consists of evaluating a path-independent line integral called the J integral (Rice, 1968):

$$J = \oint_S \left(W dy - t_i \frac{\partial u_i}{\partial x} ds \right) \tag{2-19}$$

where W is the strain-energy density (i.e., strain energy per unit volume), t_i is the traction vector, and u_i is the displacement vector. The integral is evaluated along the closed curve S surrounding the crack tip in the counterclockwise direction.

The criteria presented in this Chapter cannot be directly applied to ductile fracture, which consists of large plastic deformations. As mentioned, there is currently no generally-accepted criterion for ductile fracture. Therefore, a criterion which relates the formation of macro-scale ductile fracture to a critical state is presented in the following chapter.

---

[16] *"Another way of calculating $\mathcal{G}$ is by way of the path-independent integral, a new concept developed by Rice"* (Hahn et al., 1972).

CHAPTER 3

New Ductile Fracture Criterion: Karr-Akçay Energy Balance

A general criterion for ductile fracture[17] has been sought for several decades. The common, widely used approach is establishing the effective failure strain (i.e., the material failure occurs when a critical level of effective strain is reached), which depends on the state of stress[18]. However, there is presently no generally-accepted criterion for ductile fracture. This is an extremely important issue as crashworthiness assessment, energy absorption capacity and damage survivability depend on the accurate prediction of fracture initiation, which limits the structure's performance.

A criterion which relates the formation of macro-scale ductile fracture to a critical state, in which the rate of mechanical work done on the continuum system reaches the energy release rate of the fractured system, is presented in the following (Karr & Akçay, 2016).

3.1 Continuum Model for Ductile Fracture

When a material is exposed to external forces[19], the external work done is exchanged with the internal energy of the system assuming that the system is in equilibrium and quasi-static conditions apply (i.e., the kinetic energy of the whole system is neglected). In

---

[17] See Footnote 2.

[18] As mentioned previously, note that the state of stress may be expressed in terms of the mean stress and the second deviatoric stress invariant (e.g., stress triaxiality) for two dimensional state of stress conditions and the third deviatoric stress invariant (e.g., Lode parameter) as well for three dimensional state of stress conditions.

[19] External forces may be categorized as surface tractions and body forces.

addition, temperature changes[20] are neglected and the plastic work dissipates through heat.

We presume that the effective surface energy density is a macroscopic constant for a particular fracture mode and that there are no pre-existing cracks at the macroscale. Moreover, we presume that the stress and strain fields are stable such that any localization of the deformation (shear bands, for example) is included. Hence, the application of the proposed fracture criteria may be appropriate for pre-localization and/or post-localization.

As discussed by Griffith (1921), work must be done on a continuous medium in order to overcome cohesive forces on either side of a fracture. The range of the molecular forces is small, and although the molecular force-displacement relations may not be known at this level, it is presumed that the net work of the debonding mechanism equals the surface energy of the material. Later, this concept was extended by Orowan (1945, 1949) and Irwin (1948) to include additional plastic work.

In the following, we consider the continuum manifestation of micro-scale and molecular scale debonding mechanisms as the release of surface energy when a cracks forms on a local plane. We use the modified or effective surface energy in association with the fracture energy release and presume that the effective surface energy density is a macroscopic constant quantity for a particular fracture mode of a material.

As the system maintains the minimum energy state, the rate of energy change of the intact system is initially less than the fractured state. In other words, the system, seeking a minimum energy state, will fracture if the rate of energy change for the system in the fracture mode becomes less than the un-fractured continuum system. Therefore, the critical state is reached when the energy release rate of the bulk system is balanced by the energy release rate of the fractured medium.

---

[20] Note that Mirza et al. (1996) observed rapid temperature rise in the material at high rates of loading (i.e., above ~10^2 s^{-1}) in their numerical simulations of experiments (on pure iron and aluminum alloy) in which the material constitutive relation takes thermal softening into account (see "Discussion" part of the cited reference for more details). However, here it is presumed that quasi-static conditions apply, that is, small rates of loading.

For ductile materials, fracture is usually associated with large strains in which the plastic strains are much greater than the elastic strains; hence, elastic deformation can be ignored, $\varepsilon_{ij}^{e} \approx 0$. The total work increment per unit volume, dW, then consists of only plastic strain increments and can be expressed as[21]

$$dW = \sigma_{ij} d\varepsilon_{ij} = \sigma_{ij}\left(d\varepsilon_{ij}^{e} + d\varepsilon_{ij}^{p}\right) \approx \sigma_{ij} d\varepsilon_{ij}^{p} \tag{3-1}$$

where $d\varepsilon_{ij}^{e}$, $d\varepsilon_{ij}^{p}$, and $d\varepsilon_{ij}$ are the components of the elastic strain increment tensor, the plastic strain increment tensor, and the total strain increment tensor, respectively. Also, σ_{ij} are the components of the true stress tensor. Note that the superscript for the plastic deformation is dropped in the following, and again the total strain is assumed to be composed of only plastic strains.

Now, consider a continuous medium with current dimensions l_I x l_{II} x l_{III} (in the directions of x_I, x_{II}, and x_{III} respectively) subjected to a uniform state of stress before fracture. Assume x_I is in the direction of maximum principal stress/strain and x_{III} is in the direction of minimum principal stress/strain. Hence, the total work increment per unit volume can be written in terms of principal stresses and the strains as

$$dW = \sigma_I d\varepsilon_I + \sigma_{II} d\varepsilon_{II} + \sigma_{III} d\varepsilon_{III} \tag{3-2}$$

where $\sigma_I \geq \sigma_{II} \geq \sigma_{III}$.

Multiplying both sides of the equation by the current volume yields the total/plastic work increment of the volume element, $d\mathfrak{W}$, before fracture

$$d\mathfrak{W} = l_I l_{II} l_{III}(\sigma_I d\varepsilon_I + \sigma_{II} d\varepsilon_{II} + \sigma_{III} d\varepsilon_{III}) \tag{3-3}$$

Using the flow rule for the material, the strain increments $d\varepsilon_{II}$ and $d\varepsilon_{III}$ can be written in terms of $d\varepsilon_I$ for a given stress state.

---

[21] $dW = \sigma_{ij} d\varepsilon_{ij} + \frac{1}{2} d\sigma_{ij} d\varepsilon_{ij} = \sigma_{ij} d\varepsilon_{ij}\left(1 + \frac{1}{2}\frac{d\sigma_{ij}}{\sigma_{ij}}\right) \cong \sigma_{ij} d\varepsilon_{ij}$. In other words, the increment in stress is assumed to be very small compared to the current stress itself; therefore, the second term is neglected.

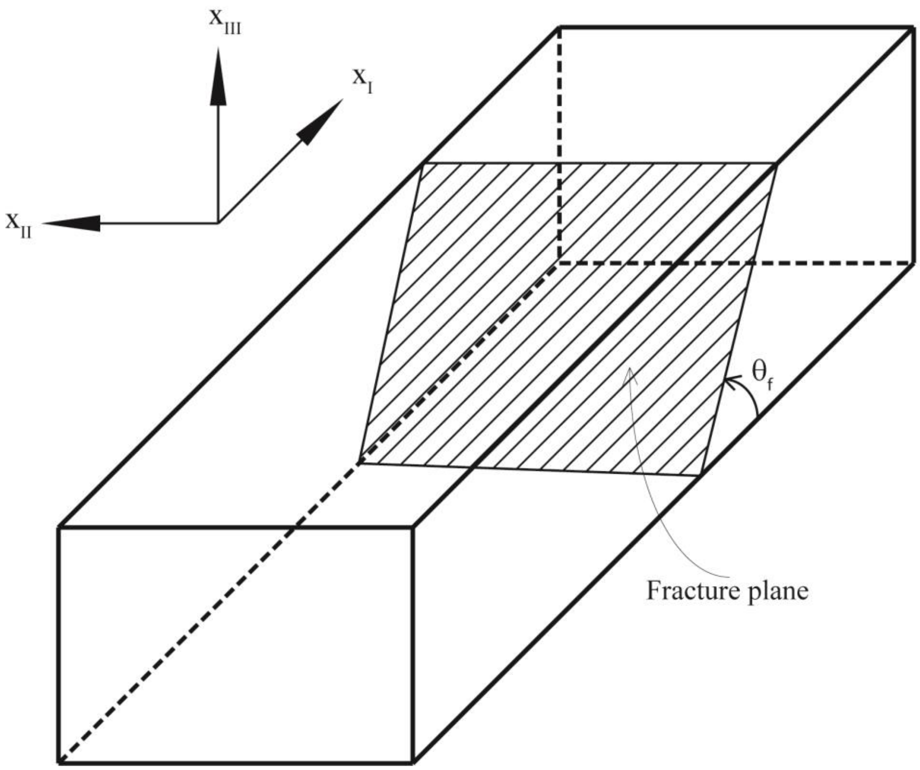

Figure 3-1 Representation of volume element and fracture plane

The energy release rate of the fractured medium can be associated with the total/plastic work increment of the fractured volume element, $d\mathfrak{W}^*$, the effective surface energy release rate per unit surface area, Γ, and the frictional energy losses per unit area, $\mathcal{F}$, if any[22].

The flat fracture plane depicted in Figure 3-1 has area, A,

$$A = \frac{l_{II} l_{III}}{\sin(\theta_f)} \tag{3-4}$$

where θ_f is the angle from the longitudinal, x_I, direction to the plane of fracture.

---

[22] It's worth noting that this representation is very similar to Irwin's following statement for ductile fracture. Note that we added a term for frictional losses, which depends on the mode of fracture under consideration.
"The term equivalent to $4\alpha c$ may be approximately represented by two terms, one proportional to area of fracture, and one proportional to volume of metal affected by plastic flow" Irwin (1948).
Note that $4\alpha c$ represents the surface energy term; see Section 2.1 and/or Equation (2-2).

The fracture plane disrupts the continuity of the element with the release of debonding energy of the fracture. Denoting the effective surface energy release rate (per increment) per unit surface area of the fracture as Γ, the surface energy release of the fracture medium is ΓxA. Moreover, other considerations are the change of stress state of the fractured element from σ_{ij} to say σ_{ij}^*, and the frictional energy losses per unit area, $\mathcal{F}$, due to contact and sliding of the fracture surfaces.

The total/plastic work increment per unit volume associated with the fractured element may be expressed as

$$dW^* = \sigma_I^* d\varepsilon_I^* + \sigma_{II}^* d\varepsilon_{II}^* + \sigma_{III}^* d\varepsilon_{III}^* \tag{3-5}$$

Note that the development of the frictional losses, if any, depends on the mode of fracture under consideration.

3.2 Mode I (Opening Mode) Ductile Fracture

Consider the application of the proposed fracture criterion to crack formation with the plane of fracture having a normal in the direction of the maximum principal strain. Referring to Figure 3-1, the angle of inclination to the x_I axis is $\pi/2$. Therefore, the initiation of the crack results in no tangential motion of the crack surfaces, and no frictional forces develop at the crack surface interface.

Applying the fracture criterion by equating the energy release of the un-fractured and fractured systems, we obtain:

$$l_I l_{II} l_{III} dW = (\Gamma_I \text{x} A) d\varepsilon_I + l_I l_{II} l_{III} dW^* \tag{3-6}$$

where dW^* is the increment in plastic work per unit volume associated with the fractured element.

Note that the rate of change of plastic work is assumed constant over a small continuum interval $d\varepsilon_I$. This increment interval for the (discontinuous) fracture mode with the overall strain increment remains $d\varepsilon_I$; however, the increment in strain is concentrated in the fracture zone.

We then consider that the effective surface energy release to be concentrated in this very small zone is similar to what Griffith (1921) referred as the 'radius of molecular action'. However, this zone must be generalized to include plastic work consistent with the effective surface energy release. In this sense, Γ is interpreted as the rate of change of surface energy; that is, the change in surface energy per macro-scale strain increment, $d\varepsilon_I$, per unit area. Hence, it is assumed that the plastic work component $\sigma_I^* d\varepsilon_I^*$ of the fractured volume vanishes as $d\varepsilon_I^*$ drops suddenly zero as the increment in strain is concentrated in the fracture zone (and σ_I^* suddenly decreases to zero at the completion of fracture).

Equation (3-6) defines a necessary condition for the onset of ductile fracture; that is, the fractured energy state is higher than the homogeneous, continuous state until Equation (3-6) is satisfied. The fractured energy state is presumably the lower state thereafter. We also presume that the surrounding material has not reached this critical state yet. Hence, it is at this point that fracture is imminent within the element of consideration. Nevertheless, once the fracture actually develops within the element, one would then of course examine the consequence of its formation and growth and its effects on the neighboring elements. Here however, we are only establishing a condition for the onset of crack formation in an un-cracked plastic medium.

Substituting Equation (3-4) into Equation (3-6), dividing by the incremental strain $d\varepsilon_I$ and simplifying it yields

$$l_I\left(\frac{dW}{d\varepsilon_I} - \frac{dW^*}{d\varepsilon_I}\right) = \Gamma_I \tag{3-7}$$

The natural strain component in the x_I direction is defined as

$$d\varepsilon_I = dl_I / l_I \tag{3-8}$$

Hence, the current length of the element l_I will be proportional to the original unstressed, unstrained element length $l_{I,0}$

$$l_I = e^{\varepsilon_I} l_{I,0} \tag{3-9}$$

Substituting Equation (3-9) into Equation (3-7) yields

$$e^{\varepsilon_I} l_{I,0} \left(\frac{dW}{d\varepsilon_I} - \frac{dW^*}{d\varepsilon_I} \right) = \mathit{\Gamma}_I \tag{3-10}$$

Note that the work done on the volume element is dependent on the length of the element; that is, doubling the length of the element doubles the plastic work of the element yet we presume only one fracture plane. We consider $\mathit{\Gamma}_I$ as a constant for a particular material, but there is evidently a characteristic length associated with $l_{I,0}$ such that a limited portion of the material near the crack itself provides work to the formation of the fracture.

Equation (3-10) is then rewritten in the following form for the critical state

$$e^{\varepsilon_I} \left(\frac{dW}{d\varepsilon_I} - \frac{dW^*}{d\varepsilon_I} \right) = C_I \tag{3-11}$$

where

$$C_I = \Gamma_I / l_{I,0} \tag{3-12}$$

The constant C_I is the specific surface energy density (surface energy per unit area per unit length) for the material, having same dimensions as stress.

The characteristic length $l_{I,0}$ can be associated with averaged spacing of micro-structural inclusions and void defects as presented in Xia & Shih (1995)[23]. Xia & Shih also discussed the use of such a physical length scale and applied it in simulating crack growth resistance under small scale yielding using 2D computational cells. This model was developed further by Gao et al. (1998) using 3D computational cell elements having representative volume elements of size compatible with the micro-structural length

---

[23] *"It must be emphasized that the cell size D should not be regarded as a length that can be adjusted for computational convenience, and neither should it be changed to accommodate different crack sizes and/or geometries. Rather, D is related to the microstructural dimension relevant to the fracture mechanism, i.e., it has a microstructural basis.*

...

... the length D should be interpreted as the mean spacing between the voids nucleated from large inclusions. Microvoids nucleated from small inclusions assist the process of hole link-up with the crack tip and can be taken into account in the coalescence phase" (p. 236 of Xia & Shih, 1995).

scale[24] in simulating ductile crack growth. Afterward, Gullerud et al. (2000) explored the computational issues of computational cell methodology and discussed the guidelines and algorithms that lead an efficient analysis.

Both the effective surface energy (Γ) and the characteristic length ($l_{I,0}$) are thus material specific. As an example, as presented in Section 3.4.1.1, we find a characteristic length for Al 2024 on the order of 10 µm. This is consistent with the micro-structural length scale dominant in aluminum alloys as discussed by Hahn & Rosenfield (1975).

Furthermore, we presume the fracture renders a complete loss of the axial component of work, $\sigma_I^* d\varepsilon_I^* = 0$, as mentioned.

$$e^{\varepsilon_I}\left(\frac{\sigma_I d\varepsilon_I + \sigma_{II} d\varepsilon_{II} + \sigma_{III} d\varepsilon_{III}}{d\varepsilon_I} - \frac{0 + \sigma_{II}^* d\varepsilon_{II}^* + \sigma_{III}^* d\varepsilon_{III}^*}{d\varepsilon_I}\right) = C_I \tag{3-13}$$

However, the other principal stresses and strains are maintained consistent with the boundary conditions; therefore, we have $\sigma_{II} d\varepsilon_{II} = \sigma_{II}^* d\varepsilon_{II}^*$ and $\sigma_{III} d\varepsilon_{III} = \sigma_{III}^* d\varepsilon_{III}^*$. This mode of fracture is then predicted by the critical state

$$e^{\varepsilon_I}\sigma_I = C_I \tag{3-14}$$

The stress-strain relations must be established for the material, in addition to value for C_I, in order to predict the occurrence of fracture.

Finally, note that the Equation (3-14) is not limited to uniaxial stress conditions. Rather the relationship between σ_I and ε_I will depend upon the complete state of stress and the stress history. This is addressed further in Section 3.4, where example applications are presented.

---

[24] *"The layer height, denoted D, introduces a characteristic length scale over which damage occurs and is associated with the mean spacing of the larger, void initiating inclusions"* (p. 762 of Gao et al., 1998).

3.3 Mode II (Shear/Sliding Mode) Ductile Fracture

The underlying micromechanical mechanisms leading to shear-dominated ductile fracture differ substantially from those which are dominant in high stress triaxiality states (Nahshon & Hutchinson, 2008). This distinction is also made in linear elastic fracture mechanics where the modes for crack opening, sliding, and tearing are distinguished. In this section we presume a mode of ductile fracture initiation associated with a shearing mode. Note that mixed-mode fracture, in which one should also consider the change in energy dissipation from the component of the tensile stress acting normal to the potential crack, is not addressed here.

Returning to attention to Figure 3-1, we presume the crack formation occurs as tangential sliding along the fracture plane. Also, we now presume a surface energy density constant C_{II} for the material which generally differs from the opening mode (Mode I) constant. Presently, the precise relationship among ductile fracture modes and energy release rates warrants further attention.

In the following, we assume there is no directional dependency of the surface energy; hence, anisotropy of the material is neglected.

3.3.1 Mode II Shear Fracture without Sliding Friction

We examine the initiation of fracture referring to Figure 3-1 with normal to the fracture plane oriented in the $x_I - x_{III}$ plane. We first change the coordinate system to x_1, x_2 and x_3 directions where x_1 is oriented in the $x_I - x_{III}$ plane in the direction tangent to the fracture plane. Note that x_2 direction is overlapped with the x_{II} direction.

The plastic work in the bulk, intact system is given by

$$dW = \tau d\gamma + \sigma_{11} d\varepsilon_{11} + \sigma_{22} d\varepsilon_{22} + \sigma_{33} d\varepsilon_{33} \tag{3-15}$$

Note that in Equation (3-15) the stress and the strain components are written in the new defined coordinate system rather than the principal directions and we let the shear strain $\gamma = \gamma_{31}$ and the shear stress $\tau = \tau_{31}$. Then, for the fractured system $d\gamma^* = 0$. Hence,

$$dW^* = \sigma_{11}^* d\varepsilon_{11}^* + \sigma_{22}^* d\varepsilon_{22}^* + \sigma_{33}^* d\varepsilon_{33}^* \qquad (3\text{-}16)$$

Applying the fracture criterion by equating the energy release rates of the un-fractured and the fractured systems,

$$l_I l_{II} l_{III} dW = (\mathit{\Gamma}_{II} \mathrm{x} A) d\gamma + l_I l_{II} l_{III} dW^* \qquad (3\text{-}17)$$

Substitution of A (see Equation (3-4)) and further simplification yields

$$l_I \left(\frac{dW}{d\gamma} - \frac{dW^*}{d\gamma} \right) = \frac{\mathit{\Gamma}_{II}}{\sin \theta_f} \qquad (3\text{-}18)$$

Substituting Equation (3-15) and Equation (3-16) into Equation (3-18) and applying the same procedure as in the previous section, the necessary condition for the onset of shear fracture with no frictional losses on the fracture plane is obtained

$$e^{\varepsilon_I} \tau = \frac{C_{II}}{\sin \theta_f} \qquad (3\text{-}19)$$

Hence, C_{II} is the specific surface energy density for the shear-mode and is defined as

$$C_{II} = \frac{\mathit{\Gamma}_{II}}{l_{I,0}} \qquad (3\text{-}20)$$

As discussed in the previous sub-section, we presume the normal stresses for that orientation are unchanged from the un-cracked to the fractured medium. Moreover, this formulation (i.e., Equation (3-19)) is valid only up to the instant of fracture, after which the formation of the fracture would affect the surrounding media.

The shear stress (in the $x_I - x_{III}$ plane) in terms of principal stresses is

$$\tau = \left(\frac{\sigma_I - \sigma_{III}}{2} \right) \sin 2\theta \qquad (3\text{-}21)$$

Substituting Equation (3-21) into Equation (3-19) yields the shear mode failure condition without sliding friction:

$$e^{\varepsilon_I}\left(\frac{\sigma_I - \sigma_{III}}{2}\right)\sin 2\theta_f \sin\theta_f = C_{II} \tag{3-22}$$

In the examples, it is convenient to let $\sigma_{III} = \beta_{WS}\sigma_I$. Then, the state for the shear fracture without sliding friction can be expressed as

$$\sigma_I e^{\varepsilon_I}(1 - \beta_{WS})\sin 2\theta_f \sin\theta_f = 2C_{II} \tag{3-23}$$

The minimum, critical strain occurs when the product of $\sin 2\theta_f \sin\theta_f$reaches a maximum which occurs at a fracture angle of

$$\theta_f = \cos^{-1}\left(\frac{1}{\sqrt{3}}\right) \cong 54.7^0 \tag{3-24}$$

3.3.2 Mode II Shear Fracture with Sliding Friction

If there is compressive normal stress σ_N acting on the interfaces of the fracture surfaces, then frictional energy loss per unit area, $\mathcal{F}$, due to contact and sliding must also be included. The tangential force is then given by the product of the coefficient of friction and the normal force, $\mu\sigma_N$. The specific frictional dissipation rate is then

$$\mathcal{F} = \mu\sigma_N l_{I,0} \tag{3-25}$$

The resulting critical state is then

$$e^{\varepsilon_I}\tau = \frac{C_{II} + \mu\sigma_N}{\sin\theta_f} \tag{3-26}$$

The compressive normal stress acting on the shear plane in terms of principal stresses is

$$\sigma_N = \frac{|\sigma_I + \sigma_{III}|}{2} + \frac{\sigma_I - \sigma_{III}}{2}\cos 2\theta \tag{3-27}$$

Note that $\sigma_{III} < -2\sigma_I$ for shear fracture with sliding friction to occur; hence, $\sigma_I + \sigma_{III} < 0$. Then, Equation (3-27) can be written as

$$e^{\varepsilon_I}(\sigma_I - \sigma_{III}) \sin 2\theta_f \sin \theta_f + \mu\big[(\sigma_I + \sigma_{III}) + (\sigma_{III} - \sigma_I) \cos 2\theta_f\big] = 2C_{II} \qquad \text{(3-28)}$$

Let θ_n denote the angle for the fracture plane such that the normal compressive stress vanishes. Then, the friction term on the left hand-side disappears when $\theta_f \geq \theta_n$.

In the examples, it is convenient to let $\sigma_I = \beta_S \sigma_{III}$. Then, the state for the shear fracture with sliding friction can be expressed as

$$\sigma_{III}\big\{e^{\varepsilon_I}(\beta_S - 1) \sin 2\theta_f \sin \theta_f + \mu\big[(\beta_S + 1) + (1 - \beta_S) \cos 2\theta_f\big]\big\} = 2C_{II} \qquad \text{(3-29)}$$

Finally, the corresponding (fracture) angle for minimum, critical strain can be obtained by differentiating Equation (3-28) or Equation (3-29)

$$\begin{aligned} &e^{\varepsilon_I} \sin 2\theta_f \sin \theta_f \, d\varepsilon_I \\ &+ \big[2 \cos 2\theta_f \sin \theta_f \, e^{\varepsilon_I} + \sin 2\theta_f \cos \theta_f \, e^{\varepsilon_I} + 2\mu \sin 2\theta_f\big] d\theta_f = 0 \end{aligned} \qquad \text{(3-30)}$$

This can be written as

$$\frac{d\varepsilon_I}{d\theta_f} = \frac{2 \cos 2\theta_f \sin \theta_f \, e^{\varepsilon_I} + \sin 2\theta_f \cos \theta_f \, e^{\varepsilon_I} + 2\mu \sin 2\theta_f}{e^{\varepsilon_I} \sin 2\theta_f \sin \theta_f} \qquad \text{(3-31)}$$

The strain takes its minimum value when $d\varepsilon_I / d\theta_f = 0$ (local minimum). This gives

$$2 \cos 2\theta_f \sin \theta_f \, e^{\varepsilon_I} + \sin 2\theta_f \cos \theta_f \, e^{\varepsilon_I} + 2\mu \sin 2\theta_f = 0 \qquad \text{(3-32)}$$

Further simplification yields

$$\big[e^{\varepsilon_I}\big(3 \cos^2 \theta_f - 1\big) + 2\mu \cos \theta_f\big] \sin \theta_f = 0 \qquad \text{(3-33)}$$

Therefore, the relation between the critical strain and the fracture angle is

$$e^{\varepsilon_I} = \frac{2\mu \cos \theta_f}{1 - 3 \cos^2 \theta_f} \qquad \text{(3-34)}$$

The fracture angle is thus

$$\theta_f = \cos^{-1}\left(\frac{-\mu \mp \sqrt{\mu^2 + 3(e^{\varepsilon_I})^2}}{3e^{\varepsilon_I}}\right) \tag{3-35}$$

Note that Equation (3-35) reduces to Equation (3-24) for no friction (i.e., $\mu = 0$) or when $\theta_f \geq \theta_n$.

3.4 Example Applications

The direction of the plastic strain vectors is defined through a flow rule by assuming the existence of a plastic potential function, to which the incremental strain vectors are orthogonal (Desai & Siriwardane, 1984). Then, the plastic strain increments are given by the flow/normality rule:

$$d\varepsilon_{ij}^p = \lambda \frac{\partial f}{\partial \sigma_{ij}} \tag{3-36}$$

where f is the plastic potential function and λ is a non-negative scalar factor and may vary throughout the loading history.

Employing J_2 incremental plasticity with the Von-Mises yield function $f = J_2 - k^2 = 0$, the strain increments can be written in terms of the principal stress components, for example,

$$\varepsilon_I^p = \frac{2}{3}\lambda\left[\sigma_I - \frac{1}{2}(\sigma_{II} + \sigma_{III})\right] \tag{3-37}$$

A power-law hardening relationship is applied in the following

$$\sigma_{eff} = \Omega\left(\varepsilon_{eff}^p\right)^n \tag{3-38}$$

where Ω is the strength coefficient, n is the hardening exponent, and the ε_{eff}^p is the effective plastic strain.

The Von-Mises effective stress for the plane-stress condition is defined as

$$\sigma_{eff} = \sqrt{\frac{1}{2}[(\sigma_I - \sigma_{II})^2 + (\sigma_{II} - \sigma_{III})^2 + (\sigma_{III} - \sigma_I)^2]} \tag{3-39}$$

The effective strain increment is defined as

$$d\varepsilon_{eff}^p = \sqrt{\frac{2}{3}\left(d\varepsilon_{ij}^p\right)_D \left(d\varepsilon_{ij}^p\right)_D} \tag{3-40}$$

where $\left(d\varepsilon_{ij}^p\right)_D$ is the deviatoric part of the plastic strain increment tensor[25]. Note that the deviatoric part of the plastic strain increment tensor is equal to the plastic strain increment tensor due to incompressibility; i.e., $d\varepsilon_{ii}^p = 0$ (Hill, 2009). Hence,

$$d\varepsilon_{eff}^p = \sqrt{\frac{2}{3} d\varepsilon_{ij}^p d\varepsilon_{ij}^p} \tag{3-41}$$

where $d\varepsilon_{ij}^p$ are the components of the plastic strain increment tensor. This expression can be integrated when the principal axes of strain increments do not rotate relative to the element and when the loading is proportional (p. 31 of Hill, 2009). The integration yields (in terms of principal strains)

$$\varepsilon_{eff}^p = \sqrt{\frac{2}{3}\left[\left(\varepsilon_I^p\right)^2 + \left(\varepsilon_{II}^p\right)^2 + \left(\varepsilon_{III}^p\right)^2\right]} \tag{3-42}$$

As the plastic strains are much greater than the elastic strain, the elastic part of the total strain can be neglected; that is,

$$\varepsilon_{ij} \approx \varepsilon_{ij}^p \tag{3-43}$$

Also, the effective strain can be expressed in terms of the maximum principal strain for proportional loading:

---

[25] Note that: $d\varepsilon_{ij}^p = \left(d\varepsilon_{ij}^p\right)_D + \frac{1}{3} d\varepsilon_{ii}^p$

$$\varepsilon_{eff} = \zeta_I \varepsilon_I \tag{3-44}$$

Finally, stress triaxiality is defined as

$$\eta = \frac{\sigma_m}{\sigma_{eff}} \tag{3-45}$$

where σ_{eff} is the Von-Mises effective stress (see Equation (3-39)) and σ_m is the mean stress:

$$\sigma_m = \frac{\sigma_I + \sigma_{II} + \sigma_{III}}{3} \tag{3-46}$$

In the following examples, we use the hybrid experimental-numerical data published by Wierzbicki and his research group (Bao & Wierzbicki, 2004; Wierzbicki et al., 2005; Bai & Wierzbicki, 2010).

3.4.1 Mode I (Opening Mode) Fracture Example

For a given stress state, it is convenient to express the effective stress in terms of the maximum principal stress:

$$\sigma_{eff} = \xi_I \sigma_I \tag{3-47}$$

Substituting Equation (3-38), Equation (3-44), and Equation (3-47) into Equation (3-14) with using Equation (3-43) yields

$$\frac{\Omega}{\xi_I} \varepsilon_{eff}^n e^{\varepsilon_{eff}/\zeta_I} = C_I \tag{3-48}$$

The solution to Equation (3-48) is then

$$\varepsilon_{eff}^f = \zeta_I n \cdot \mathrm{W}\left(\frac{1}{n\zeta_I}\left(\frac{\xi_I C_I}{\Omega}\right)^{1/n}\right) \tag{3-49}$$

where W represents the Lambert W function.

3.4.1.1 Axisymmetric Stress, Opening Mode Fracture of Al 2024-T351

For the axisymmetric case, one can obtain the following using Equation (3-39), Equation (3-45), Equation (3-46), and Equation (3-47)

$$\xi_I = \frac{3}{2 + 3\eta} \tag{3-50}$$

and from Equation (3-37), Equation (3-42), Equation (3-43), Equation (3-44)

$$\zeta_I = 1 \tag{3-51}$$

Substituting Equation (3-50) and Equation (3-51) into Equation (3-49) yields

$$\varepsilon_{eff}^{f} = n \cdot \mathrm{W}\left(\frac{1}{n}\left(\frac{3C_I}{\Omega(3\eta + 2)}\right)^{1/n}\right) \tag{3-52}$$

Results obtained using Equation (3-52) are shown in Figure 3-2 along with the three data points published by Bai & Wierzbicki (2010).

Bao & Wierzbicki (2004) performed a series of experiments (tensile tests, shear tests, combined tensile and shear tests, conventional upsetting tests, and new compression tests) with 2024-T351 aluminum alloy to explore the effect of stress triaxiality on fracture strain. They used finite element analyses to determine the state of stress and strain at fracture locations. Their approach was to model the test specimen and the loading conditions based on the corresponding physical experiment and calculate, via finite element analysis, the strain at the critical point in the specimen at the time of fracture found in the physical experiment. The data of all test results re-processed by Bai & Wierzbicki (2010), and the results and the corresponding test specimens are provided in Table 1 and Figure 21 of the cited reference, respectively.

Equation (3-14) involves the current strain and the current stress state. However, current strain cannot generally be determined from the current stress using the plastic material’s constitutive relationships because the strain is history dependent. If we assume monotonically increasing, proportional loading however the strain levels can be determined from the stress state. Thus, although there is no one-to-one comparison of the results of Bai & Wierzbicki (2010) with our analysis results, we can be consistent in our approach for comparison purposes by using a proportional stress state based on the reported average stress triaxiality.

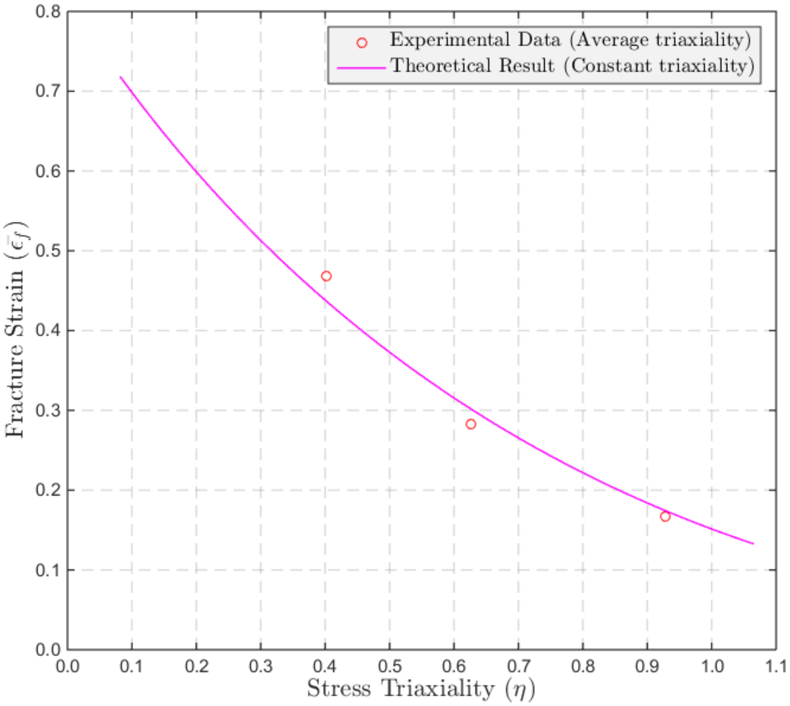

Figure 3-2 Effective strain to fracture versus stress triaxiality for axisymmetric loading and opening mode fracture of Al 2024-T351 cylinders. Hybrid experimental-numerical data of Al 2024-T351 were published by Bai & Wierzbicki (2010).

In their studies of Al 2024-T351, Bai & Wierzbicki (2010) found the specific values for the strength coefficient $\Omega = 740$ MPa, and for the hardening exponent $n = 0.15$. Using a best-fit for their data from round bars in tension, we calculate a toughness stress of $C_I = 1081$ MPa. Hahn et al. (1972) provided energy release rates[26] of aluminum-base alloys (ductile fracture) in the range of 7-16 KJ/m^2. Taking a mid-range value of 11 KJ/m^2 and applying Equation (3-12) with the calculated value of 1081 MPa for C_I, we find a characteristic length of 10 μm. This is the same order of magnitude of average spacing of large dimples[27], center-to-center spacing of inclusions, and the critical crack-

---

[26] See Table 3 of Hahn et al. (1972) for details.
"$\mathcal{G}$ is the energy per unit area given up by the system during an incremental extension of the crack … It is common practice to measure $\mathcal{G}_c$, which is the minimum value of $\mathcal{G}$ at which crack extension is observed experimentally" (p. 381 of Hahn et al., 1972).

[27] *" … spacing of cracked particles (dimple spacing) …"* (p. 658 of Hahn & Rosenfield, 1975).

tip opening displacement (CTOD) provided in Table I of Hahn & Rosenfield (1975) for various aluminum alloys.

There could presumably be a different effective strain to failure if the actual stress/strain history was used over the course of loading. However, the history of the stress states for each experiment is not available. To get an idea of the range of variations one might expect, we present the results obtained using the average stress triaxiality and the stress triaxiality at fracture together in Figure 3-3. Even though there is an obvious difference (the value of C_I changes from 1081 MPa to 1144 MPa), we feel that the use of average stress triaxiality is more appropriate because the average stress triaxiality reflects the state of stress history better.

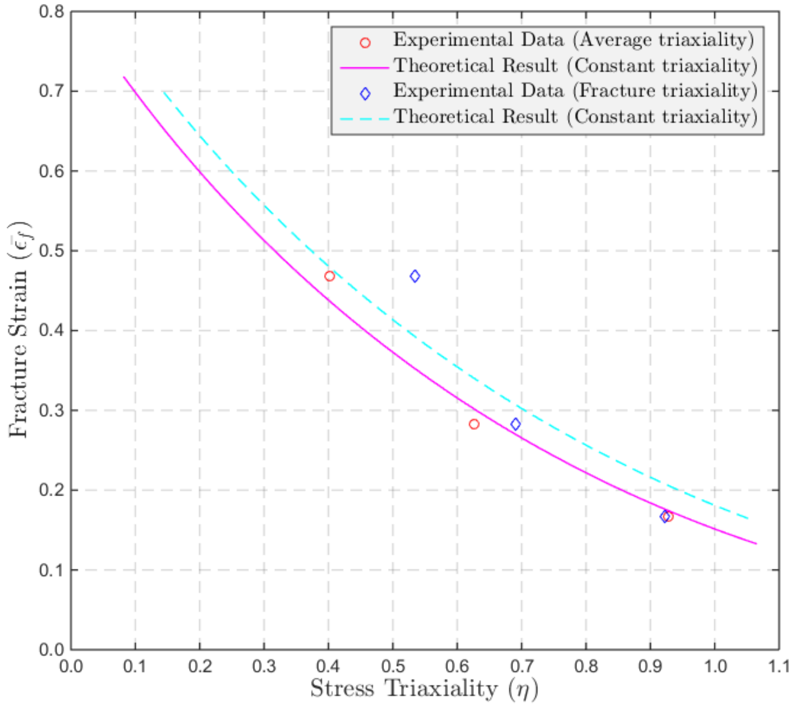

Figure 3-3 Effective strain to fracture versus stress triaxiality for axisymmetric loading and opening mode fracture of Al 2024-T351 cylinders using both the average stress triaxiality and the fracture stress triaxiality. Magenta solid line is obtained evaluating average stress triaxiality data, while cyan dashed line is obtained evaluating the stress triaxiality at fracture data. Hybrid experimental-numerical data of Al 2024-T351 were published by Bai & Wierzbicki (2010).

The general approach for non-proportional loading would be to check Equation (3-14) throughout the loading history with the critical state being reached when Equation (3-14) is first satisfied as the loading is applied. Therefore, proportional loading is not required for its usage.

3.4.2 Mode II (Shear Mode) Fracture Example

For tensile stress states (i.e., $\sigma_{III} \geq -2\sigma_I$), there is no compression on the fracture plane and the critical fracture state is found from Equation (3-23); and it is convenient to express the effective stress in terms of the maximum principal stress as in Equation (3-47). Substituting Equation (3-38), Equation (3-44), and Equation (3-47) into Equation (3-23) using Equation (3-43) yields

$$\frac{\Omega}{\xi_I} \varepsilon_{eff}^{n} e^{\varepsilon_{eff}/\zeta_I} (1-\beta_{WS}) \sin 2\theta_f \sin\theta_f = 2C_{II} \tag{3-53}$$

The solution to Equation (3-53) is then

$$\varepsilon_{eff}^{f} = \zeta_I n \cdot \mathrm{W}\left(\frac{1}{n\zeta_I}\left(\frac{2\xi_I C_{II}}{\Omega(1-\beta_{WS})\sin 2\theta_f \sin\theta_f}\right)^{1/n}\right) \tag{3-54}$$

where W represents the Lambert W function.

On the other hand, for compressive stress states, it is convenient to express the effective stress in terms of the minimum principal stress (i.e., the compressive stress)

$$\sigma_{eff} = \xi_{III}\sigma_{III} \tag{3-55}$$

Substituting Equation (3-38), Equation (3-44), and Equation (3-55) into Equation (3-29) with using Equation (3-43) yields

$$\begin{aligned}\frac{\Omega}{\xi_{III}} \varepsilon_{eff}^{n} \left\{ e^{\varepsilon_{eff}/\zeta_I} (\beta_S - 1) \sin 2\theta_f \sin\theta_f + \mu\left[(\beta_S + 1) + (1-\beta_S)\cos 2\theta_f\right]\right\} \\ = 2C_{II}\end{aligned} \tag{3-56}$$

For no friction (i.e., $\mu = 0$) or when $\theta_f \geq \theta_n$, Equation (3-56) simplifies to

$$\frac{\Omega}{\xi_{III}}\varepsilon_{eff}^{n}e^{\varepsilon_{eff}/\zeta_I}(\beta_S-1)\sin 2\theta_f \sin\theta_f = 2C_{II} \tag{3-57}$$

The solution to Equation (3-57) is then

$$\varepsilon_{eff}^{f} = \zeta_I n\cdot \mathrm{W}\left(\frac{1}{n\zeta_I}\left(\frac{2\xi_{III}C_{II}}{\Omega(\beta_S-1)\sin 2\theta_f\sin\theta_f}\right)^{1/n}\right) \tag{3-58}$$

3.4.2.1 Plane Stress, Shear Mode Fracture of Al 2024-T351

Bao & Wierzbicki (2004) also examined fracture under plane-stress conditions in their studies of Al 2024-T351. These data are also re-processed and the results are summarized in Table 1 of Bai & Wierzbicki (2010).

The same power-law constitutive relationships with the same coefficients (i.e., the strength coefficient of $\Omega = 740$ MPa and the hardening exponent of $n = 0.15$) is used here as for the Mode I case, presented in Section 3.4.1.1. Using a best fit for the (tensile stress states) data from the plane-stress condition, we calculate a toughness stress of $C_{II} = 344$ MPa. Assuming a characteristic length of say 10 μm, the energy release rate for Mode II is approximately 3.5 KJ/m^2. This is about one third of the Mode I energy release rate found in Chapter 3.4.1.1.

Results obtained using Equation (3-54) and Equation (3-58) are shown by blue solid curve[28] in Figure 3-4 along with the data points reported by Wierzbicki and his research group. We note that this curve is qualitatively very similar to the extended Mohr-Coulomb criterion presented in Figure 23 of Bai & Wierzbicki (2010). Moreover, the effect of friction is obtained by solving Equation (3-56). Figure 3-4 also shows the effect of including energy dissipation due to friction forces on the critical plane using values of friction coefficient $\mu = 0.5$ and $\mu = 1.0$. Increased frictional forces tend to increase the effective strain to fracture as more energy is required to induce the fracture mode. However, again, care should be taken with the comparison (of the hybrid experimental-

---

[28] Equation (3-54) is used to obtain the right part of the curve, where tensile stress is dominant. On the other hand, Equation (3-58) is used to obtained left part of the curve, where compressive stress is dominant.

numerical data) here as we use a constant stress ratio in determining the critical strains to fracture, whereas experimental results may involve non-proportional loading histories.

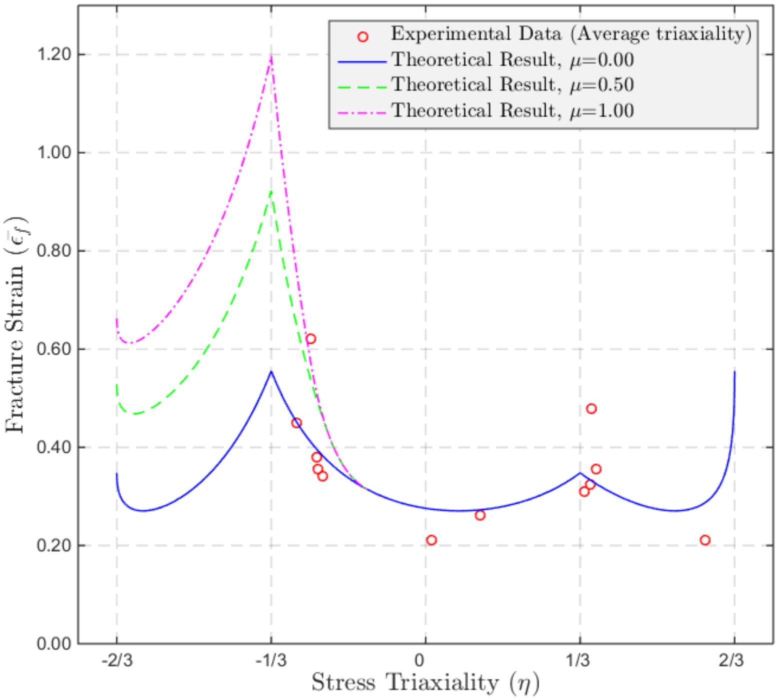

Figure 3-4 Effective strain to fracture versus stress triaxiality for plane stress loading and shear mode fracture of Al 2024-T351 bars. Blue solid curve shows the result for the critical state with no friction on the fracture planes, while the dashed lines show results of friction occuring on the fracture planes due to compressive normal stresses. Hybrid experimental-numerical data of Al 2024-T351 were published by Bai & Wierzbicki (2010).

Application of Equation (3-56) requires a search for the critical angle which yields the minimum strain to failure. Differentiating Equation (3-56) with respect to ε_{eff} (or ε_I) and θ_f and setting the result equal to zero (for a local minimum) yield Equation (3-34). One can substitute this relation into Equation (3-56) for a single unknown in terms of θ_f. Instead, we found the most convenient approach for solving Equation (3-56) for the minimum strain to failure was to step the angle θ_f in increments and solve for ε_{eff} (or ε_I) using Newton-Raphson's method. Equation (3-34) serves then as a check on our solution. Results for the critical fracture angle are shown in Figure 3-5 for various stress triaxialities. Also, shown in the figure is the curve for θ_n, the angle for the fracture plane such that the normal compressive stress vanishes.

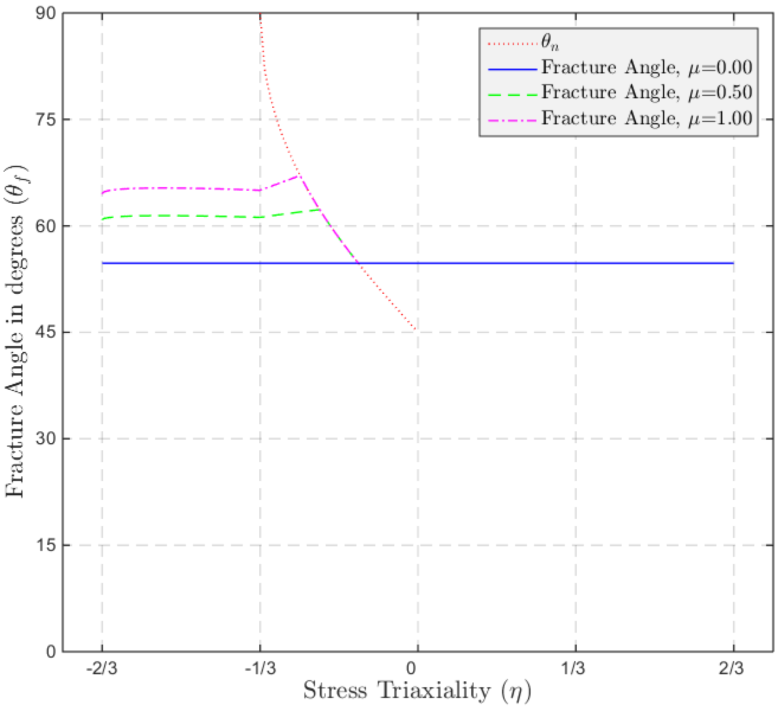

Figure 3-5 Critical fracture angle versus stress triaxiality for plane stress loading and shear mode fracture of Al 2024-T351 bars. Blue solid curve shows the result for the critical state with no friction on the fracture planes, while the dashed lines show results of friction occuring on the fracture planes due to compressive normal stresses.

3.5 Results and Discussion

A new method of predicting ductile fracture is presented based on comparison of the dissipation rates of the bulk continuum system to the fractured medium. The dissipation of the continuum system includes that of plastic work while that of the fractured system includes the surface energy of the crack formation, plastic work and frictional losses at the instant of crack initiation. Two mechanisms were considered, that of mode I which accounts for a crack-opening displacement field and a mode II shear crack initiation. The shear crack was addressed with and without frictional dissipation of the crack surfaces.

We believe that, as noted by Hancock & Mackenzie (1976) earlier[29], a failure criterion must involve the 'characteristic scale of the physical event' and the introduction of the characteristic length, $l_{I,0}$, is a point of further consideration. In this chapter we note that the strain field reported by Wierzbicki and his research group (Bao & Wierzbicki, 2004; Wierzbicki et al, 2005; Bai & Wierzbicki, 2010) were determined from finite element models and were not mesh size dependent. It seems appropriate for such cases to use a single characteristic length which reflects the length of medium which contributes to the fracture energy release; i.e., the micro-structural length scale as discussed in Section 3.2. Often times, however, finite element simulations to failure do show mesh size dependency of strain to failure. In these cases, choice of an appropriate description of the effects of the element length scale is crucial and this is discussed further in Chapter 5.

In this study, the micro-scale deformation mechanisms for the power-law plastic material are accounted for only in the constitutive equations. A further refinement of this approach would be the application of Gurson's model or variations of it to account for void growth in the parent material[30]. This also affects the stress and strain field within the parent material which differs from the averaged state. It seems appropriate that the approach provided here could then be applied to the parent material surrounding the voids.

Another avenue of continuing the study to more general loading would be to consider further the mixed mode failure of the material in an effort to better understand the effects of combined tensile and shear stress states. To this point, only two mechanisms have been considered and these two modes are considered to occur independently.

The presented approach offers a critical condition which can be assessed as the stress or strain history of the systems evolves and can thus account for non-proportional loading. Although there is considerable agreement with published hybrid experimental-numerical data, there is not at this point a set of published data which can be considered directly

---

[29] *"In order to predict failure initiation in non-uniform stress fields, such as those ahead of cracks and flaws, it is not a sufficient condition for failure initiation that a strain which is a function of stress-state is exceeded at a point. Failure initiation must involve a minimum amount of material which is characteristic of the scale of physical events involved"* (Hancock & Mackenzie, 1976).

[30] Void growth is considered as crack propagation at the micro-scale. However, growth and/or coalescence of micro voids may be considered as fracture initiation at the macro/continuum scale, where the proposed theory can be applied.

comparable to the solutions presented. This is because the published data may offer only an averaged stress history for the experiments or in some cases variable triaxiality is provided but not the actual stress histories in component form. Therefore, the digital image correlation (DIC) study was undertaken as reported in Chapter 4.

CHAPTER 4

Experimental Investigation

4.1 Summary of Past Experimental Studies on Fracture Strain Estimates

Over half a century ago, the experimental work of Bridgman on large plastic flow and fracture was collected in Bridgman (1964). The book was first published in 1952 and it encompasses numerous experiments with ductile materials as well as brittle materials.

Hancock & Mackenzie (1976) conducted tensile tests on un-notched and various circumferentially notched cylindrical specimens using three different steels (Q1, HY130, and an electro slag re-melted version of HY130) to investigate the effect of the state of stress and machining direction (of the specimen) with respect to the rolling direction (i.e., long transverse and short transverse direction) on failure strain. The logarithmic ratio between the initial and final diameters of the minimum cross section, which was measured by a strain-gauge extensometer, was used to calculate the failure strain. The corresponding state of stress was computed using the geometry of the specimen; that is, they used Bridgman triaxiality[31]. Note that the strain at which the average stress (load divided by instantaneous cross-sectional area) decreases dramatically is defined as the

---

[31] The Bridgman triaxiality is defined as (Bao & Wierzbicki, 2004)

$$\eta_{Bridgman} = \frac{1}{3} + \ln\left(1 + \frac{R_{CS}}{2R_N}\right)$$

assuming that effective strain is constant across the neck. Here, R_{CS} is the radius of the minimum cross section and R_N is the profile radius of neck/notch.

material failure initiation[32]. Moreover, the paper includes the study of the metallographic features leading to failure initiation and a detailed discussion of void nucleation, void growth, and void coalescence.

Johnson & Cook (1985) performed a series of quasi-static tensile tests with un-notched and various circumferentially notched specimens. These experiments include (tensile) Hopkinson bar[33] (over a range of temperatures) and torsion tests (over a range of strain rates) using three different metals (OFHC copper, Armco iron, and 4340 steel) to determine the effect of strain rate, temperature and pressure on fracture strain. Fracture strains of the Hopkinson bar tests were obtained by measuring the cross-sectional area of the fractured specimen. Although it was not clearly stated how the material failure initiation and the fracture strains of the quasi-static tensile tests were established, the corresponding state of stress was computed by numerical simulation with a code known as EPIC-2[34]. Moreover, fracture strains also were obtained by using the developed cumulative-damage fracture model (see Equation (3) of the cited reference).

Mirza et al. (1996) conducted tensile tests on circumferentially notched cylindrical specimens using three different metals (pure iron, mild steel, and aluminum alloy BS1474) to explore the effect of the state of stress and the strain-rate on fracture strain. Fracture strain was established by measuring the minimum diameter of the fractured specimen from at least ten positions and the corresponding state of stress was obtained by finite element simulation. Note that the main issue here is that the fracture strain measurement may not represent the correct measure of fracture initiation as the material may continue to deform a considerable amount (between the initiation of fracture and complete fracture) depending on the level of ductility.

---

[32] *"In specimens examined after the drop in average stress, there was a large central crack as shown in Fig.6 and a loss in load-bearing cross-section: in specimens examined before a drop in average stress, there were discrete holes. ... The linking-up of the larger holes and the subsequent sudden loss in load-bearing cross-section is considered to be a distinct event in the failure process which we have termed failure initiation"* (p. 153 of Hancock & Mackenzie, 1976).

[33] Split-Hopkinson bar (also called 'Kolsky bar') is an apparatus that is used to obtain dynamic stress-strain behavior of a material.

[34] EPIC-2 (Elastic-Plastic Impact Computations in two dimensions plus spin) was an explicit finite element code for obtaining solutions for axisymmetric solids. The formulation was given for axisymmetric triangular elements which can account for large deformations (in the radial, axial, and angular direction), elastic-plastic solution, and wave propagation (Johnson, 1979).

Over a decade ago, Bao & Wierzbicki (2004) performed a series of experiments (tensile tests, shear tests, combined tensile and shear tests, conventional upsetting tests, and new compression tests) with 2024-T351 aluminum alloy to explore the effect of stress triaxiality on fracture strain. They used various specimen geometries (i.e., un-notched and notched cylindrical specimens, pure shear specimen, and plate with a circular hole) to measure the ductility over a wide stress triaxiality range. The point at which the load decreases dramatically was designated as the fracture initiation. Both the fracture strain and the stress triaxiality were obtained by finite element simulation using the experimental results of displacement to fracture. Moreover, they developed a fracture locus for this specific aluminum alloy by introducing three empirical relations for three different regions: void sheeting (i.e., shear mode fracture), internal necking (opening mode fracture), and the combination of void sheeting and internal necking.

Barsoum & Faleskog (2007a) conducted experiments under combined tension and shear loads on circumferentially notched tubular specimens using two different steels (a medium strength steel: Weldox 420, and a high strength steel: Weldox 460) to explore the effect of stress triaxiality and Lode parameter on the failure strain and the failure mechanism (i.e., internal necking and void sheeting[35]). Although it was not clearly stated how the material failure initiation was established, the failure strain was calculated by inserting the measured axial displacement and rotation into the derived mathematical formulation. The corresponding state of stress was obtained by finite element simulation. Note that measured axial displacement and rotation represents the global deformation; hence, they evaluated the displacement and rotation over the notched region through a mathematical expression (see Equation (8) of the cited reference). However, these may not be an accurate representation of the deformation over the notched region as the derived mathematical expression (for the displacement and rotation over the notched region) relies on assumptions.

---

[35] The micromechanics of the failure mechanisms observed in their experimental study is investigated and modeled (the model consists of a 3D unit-cell containing a single void) in a different paper; that is, in Barsoum & Faleskog (2007b).
Moreover, note that Figure 3 of Besson (2010) shows the difference between internal necking and void sheeting mechanisms.

Recently, Haltom et al. (2013) conducted experiments on aluminum alloy (Al-6061-T6) tubular specimens under combined shear and tension for various proportional loading ratios to explore the fracture strain including grain-level strain estimates. The point at which the load decreases dramatically was designated as the material failure and fracture strain was computed by monitoring digital images of square grids (on the test specimen) drawn by electro-etching. The corresponding state of stress was evaluated by inserting the measured force and torque into the mathematical expression for stresses. Note that they used the 'principal stretch ratios', which were obtained through the non-linear strain-displacement relationships, for the calculation of the logarithmic principal strains and effective strain rather than using the 'principal engineering strains'[36].

Papasidero et al. (2015) performed experiments on 2024-T351 aluminum alloy tubular specimens to revisit the results of Bao & Wierzbicki (2004) and investigate the effects of non-proportional loading on fracture strain. A wide range of stress triaxiality was accomplished by conducting the experiments under combined tension and torsion. The point at which the load decreases dramatically was designated as the fracture initiation, and fracture strain and the corresponding state of stress were obtained by finite element simulation using the experimental results of displacement to fracture and/or rotation to fracture as Bao & Wierzbicki (2004) did. However, they used axisymmetric elements in the finite element simulations, whereas Bao & Wierzbicki used shell elements or solid elements for modeling the low stress triaxiality experiments, and axisymmetric elements for modeling the high stress triaxiality experiments (i.e., round specimens). Moreover, in the finite element simulations of Papasidero et al. (2015), the yield surface is defined by the Hosford model (rather than the von-Mises model), and a linear combination of Swift and Voce laws was used as constitutive equations. Although they have qualitatively similar results as Bao & Wierzbicki (2004) for high stress triaxialities, Papasidero et al. (2015) obtained different qualitative results in the low stress triaxiality region. Possible reasons for this are discussed in the 'Discussion section' of Papasidero et al. (2015). As they pointed out, this may be due to differences in the microstructures of the Al 2024-

---

[36] Note that 'principal stretch ratios' and 'principal strains' have the same principal directions and their values are related (see p. 107 of Wineman (2010)). The relationship between 'principal stretch ratios' and 'principal strains' can be seen in equation (A.4) of Haltom et al. (2013) as well.

T351 specimens used. However, the author believes that the differences in the numerical modeling (element type, for example) may contribute as well.

In the following descriptions of our experimental work, fracture strain is established by digital image correlation (DIC) analysis via DaVis LaVision particle image velocimetry (PIV) software (DaVis LaVision, 2015). In addition, the corresponding state of stress is obtained using the power-law hardening relationship, the flow rule, and the measured strains. We define fracture initiation as the condition when the first visible crack appears in the digital picture of the test specimen.

4.2 Experimental Setup

All experiments were conducted at room temperature with AH32 steel, which is commonly used in ship hull structures, and results presented here are the initial results. Test specimens were machined by Northwest Tool of Jackson, MI.

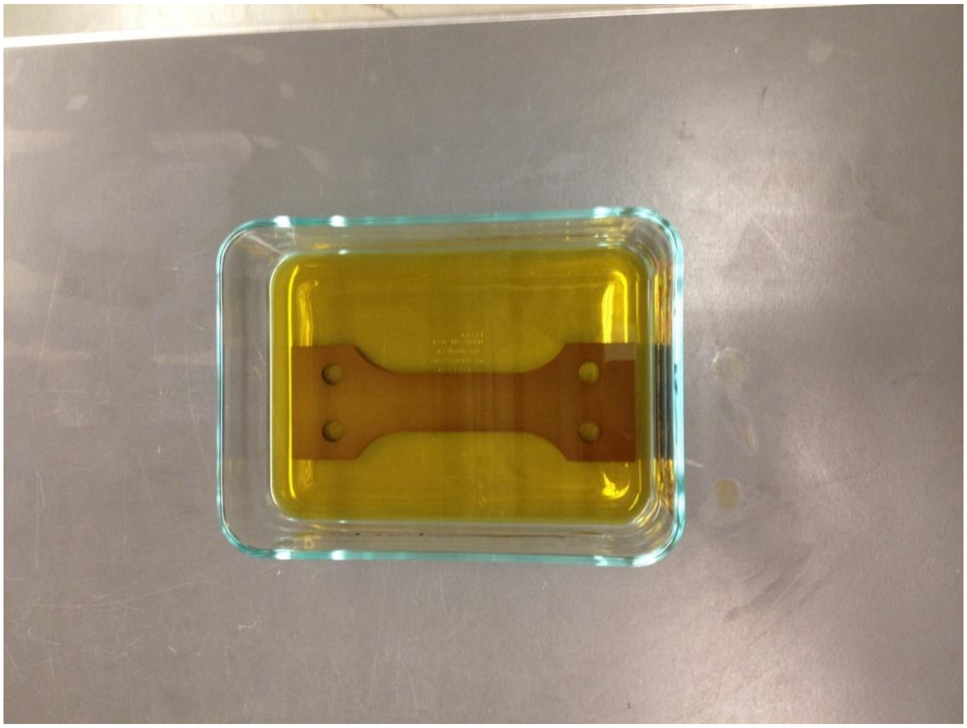

Figure 4-1 Etching process of a specimen: The specimen depicted is a 1in-width test coupon.

All specimens have been etched to create a random surface pattern for the digital image correlation (DIC) analysis. The etching process is depicted in Figure 4-1. Specimens were immersed into a 2% Nital solution for a few hours to reveal the substructure of the material. A mixture of methanol and nitric acid was used as a mixture of ethanol and nitric acid is potentially explosive.

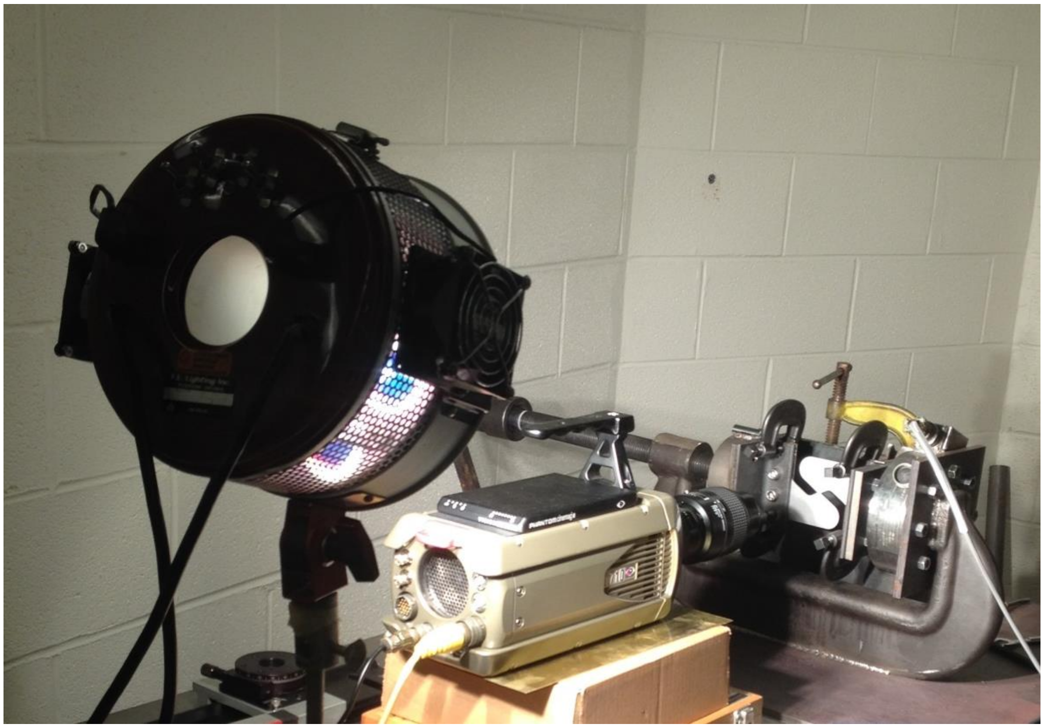

Figure 4-2 An example experimental set-up for a uniaxial test: The test specimen depicted is a shear specimen (without a groove). Note that the test specimen is adapted from Bao & Wierzbicki’s (2004) specimen design for pure shear tests.

Some uniaxial tests[37] (i.e., the uniaxial tests of the shear specimen and the 1in-width-specimen with semi-circular groove) were performed using a custom designed and built C-clamp mechanism, which is depicted in Figure 4-2. The C-clamp is capable of experiencing a 7000 lbs load exert via its 7:1 lead screw. The test specimen seen in Figure 4-2 is a shear specimen. Note that the shear specimen is adapted from Bao & Wierzbicki’s (2004) design for pure shear tests.

---

[37] Note that two different set-ups have been used for uniaxial tests.

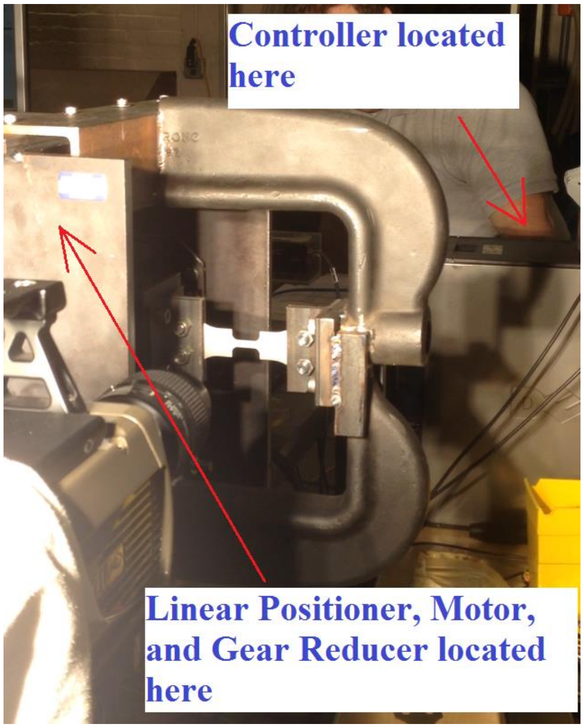

Figure 4-3 Another example experimental set-up for a uniaxial test using the altered indenter apparatus: The test specimen depicted is a 6mm-width specimen without groove. (Note that this specimen has been obtained by in-house machining of an 1in-width specimen).

A LinTech Corporation custom-designed linear positioning mechanism RS150025–S5–N3–W1–F4–M00–C000–E00–B00–L15.0 has been used to perform cylindrical indenter experiments and the rest of the uniaxial tests (i.e., the low and the high speed uniaxial tests of the 6mm-width specimen). An example set-up for these uniaxial tests and a cylindrical indenter experiment can be seen in Figure 4-3 and Figure 4-4, respectively. The test specimens seen in Figure 4-3 and Figure 4-4 are a 6mm-width specimen without groove[38] and an 18mm-width specimen with 4 mm groove, respectively.

The linear positioning mechanism is capable of exerting 11700 lbs via its 4:1 lead screw. Its overall length is 24 inches with 6 inches maximum travel range and it consists of the following assembled parts: LinTech HRC25 bearing blocks/rails, custom base/carriage/end stops, and rigid-rigid thrust load capacity. In addition, a 2-inch-diameter stainless steel cylinder, from McMaster-Carr, has been used as an indenter. The indenter set-up also includes a carriage for the high speed video camera as depicted in Figure 4-5. The carriage is attached to the cylindrical indenter support system so that the

---

[38] This specimen has been obtained by in-house machining of an 1"-width specimen.

camera moves with the indenter and thus enables digital video to be captured at a constant distance from the test sample in contact with the indenter surface. This helps maintain the focus of the magnified image and minimizes possible strain errors caused by out-of-plane motion.

The friction at the cylinder-specimen interface may affect the stress state, and the fracture mode and position. Figure 4-4 shows the specimen where friction is reduced by using teflon sheet and graphite particles at the interface. The distance from the camera lens to the test specimens is approximately 8 inches, equivalent to about 203 mm.

A high speed camera operating at 6000 frame per second (fps) or 7500 fps has been used to record digital images of the specimen during experiments. The frame rate was chosen according to the imposed indenter displacement speed. The imager is a Phantom v710 (by Vision Research/Ametek) with full 1200 pixels by 800 pixels frame recording at 7500 fps. The total memory in the imager (44.5 GB) is such that it can record 22,253 frames when recording at 1200 pixels x 800 pixels. The lens is a Nikkor with a 105 mm focal distance and an f-stop aperture of 2.8.

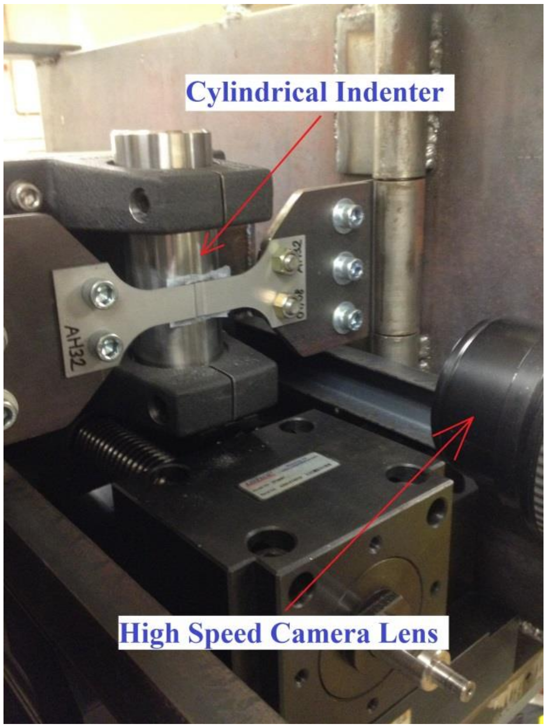

Figure 4-4 Set-up for cylindrical indenter experiments: The diameter of the cylindrical indenter is 2 inches (equivalent to 50.8 mm) and the test specimen depicted is an 18mm-width specimen with a 4 mm groove.

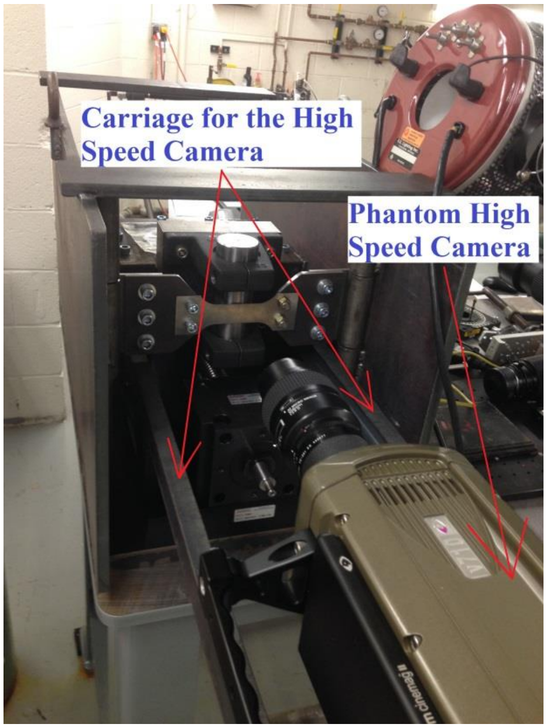

Figure 4-5 The indenter set-up with camera carriage: The carriage is attached to the cylindrical indenter support system so the camera moves with the indenter and thus enables video to be captured at a constant distance from the test sample in contact with the indenter surface (Courtesy of Prof. Marc Perlin).

The pixel resolution range of the experiments varied between 13.7 μm and 16.5 μm. This range was chosen to obtain digital images having pixel resolutions of approximately one grain size such that approximate grain-to-grain strain variations can be observed. Jia et al. (2013) and Zhou et al. (2016) provided average grain sizes of AH32 steels they used in their experimental investigation, and these published data suggests that the average grain size of AH32 steel ranges from ~5 μm to ~25 μm depending on the cooling process/system used. Therefore, the pixel resolution range of the experiments is on the order of the grain size.

The drive mechanism is comprised of a Kollmorgen AKML53L–ANCNC–00 motor, shown in Figure 4-6, and a Kollmorgen AKD–P01205–NBAN–0000 controller. They can drive the indenter mechanism at constant speeds following the initial acceleration period. In addition, a Micron VT115–005–0–RM100–71 gear reducer with 5:1 or 10:1 ratio was installed between the motor and the linear positioning mechanism to obtain the desired speeds. The 10:1 ratio gear reducer and the mechanical connection between the gear reducer and the linear positioning mechanism are depicted in Figure 4-7 and Figure 4-8, respectively.

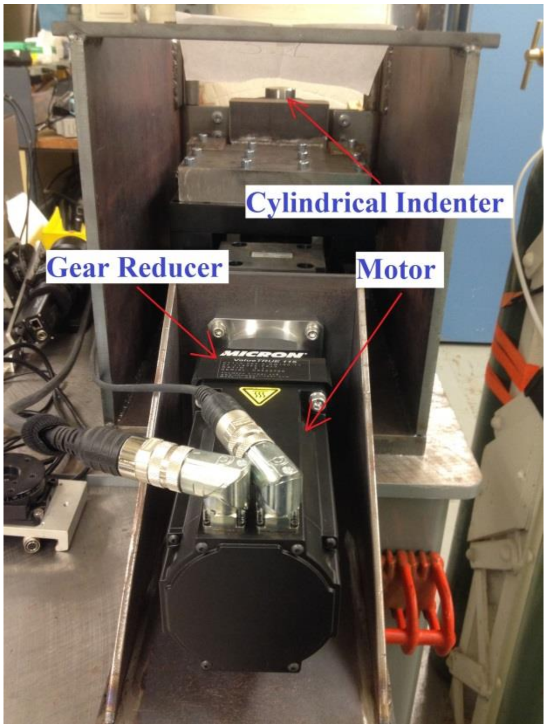

Figure 4-6 Kollmorgen AKML53L–ANCNC–00 motor with 5:1 ratio gear reducer installed.

Figure 4-7 Micron VT115–005–0–RM100–71 10:1 ratio gear reducer.

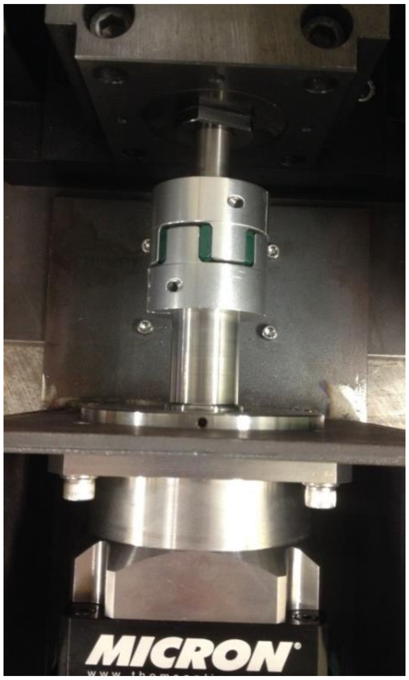

Figure 4-8 Mechanical connection (i.e., coupling) between gear reducer and the linear positioning mechanism.

Various displacement speeds have been applied to various specimen geometries for both uniaxial tests (0.20 inch/second and 0.40 inch/second) and cylindrical indenter experiments (0.60 inch/second, 1.20 inch/second, and 2.40 inch/second).

Strain components of the deformed specimen have been obtained via DaVis LaVision Particle Image Velocimetry (PIV) software (DaVis LaVision, 2015). This process is explained in detail in Section 4.4.1. A listing of the brief program required to obtain the strain is presented in Figure 4-12.

A number of researchers observed strong grain level strain heterogeneity (see e.g., Raabe et al., 2001; Haltom et al., 2013; Banerjee et al., 2016) in their experimental work and numerical analysis, meaning that the localization occurs at a scale much smaller than the thickness scale. Therefore, the current research will also present an investigation of the scale effect; however, smaller scales than the continuum scale are beyond the scope of the present investigation.

Although he focused on quasi-brittle materials (e.g., concrete, rock, sea ice, etc.), Bažant (2000) provides a general discussion on the 'size effect' phenomenon. The paper also outlines the historical evolution of the ideas on the 'size effect'. In addition, de Borst

(2001) discusses the underlying mathematical reason and some possible solutions of the mesh sensitivity in numerical analysis. The manuscript also encompasses cohesive zone models, and stationary and propagative instabilities.

A typical engineering/nominal stress-strain curve and the true stress-strain curve of a uniaxial test for AH32 steel are presented in Figure 4-9. The test was conducted using an MTS machine located in the Civil Engineering Department of the University of Michigan. The gauge length of the extensometer was 1 inch. The specimen used in the tensile test was an 1in-width specimen. The initial tensile yield stress and the ultimate tensile strength of the material are obtained as 436 MPa and 585 MPa, respectively. A comprehensive discussion of the true stress-strain curve and other experiments are presented later in this chapter.

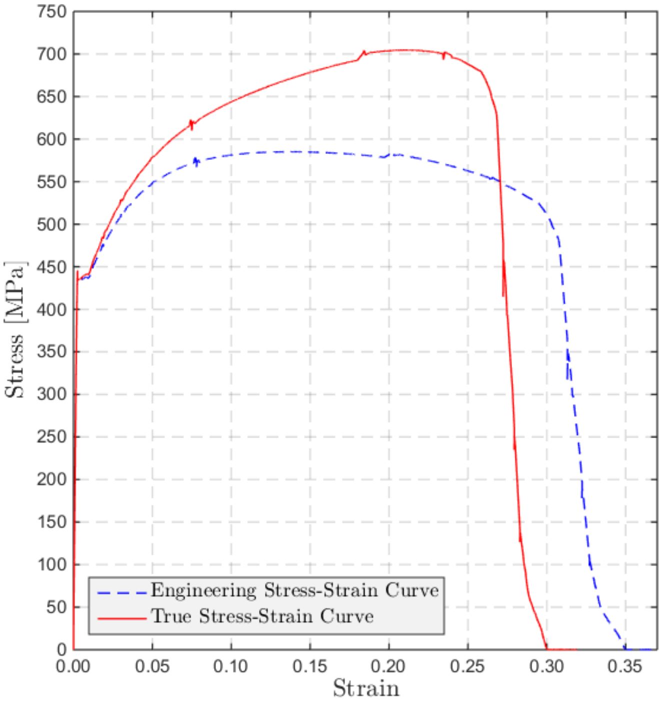

Figure 4-9 Engineering/nominal stress versus engineering/nominal strain and true stress versus true/natural strain: The specimen used in the tensile test was an 1in-width specimen (without groove). Applied speed was 0.004 inch per second with a corresponding strain rate of approximately 0.002 s^{-1}.

Two more uniaxial tests with higher strain rates were conducted. These tests were also conducted using the MTS machine located in the Civil Engineering Department of the University of Michigan. The specimens used in the high speed tensile tests were 18mm-width specimens (without groove) and the fractured specimens are exhibited in Figure 4-10.

The true stress-strain curve of all three tests is presented together in Figure 4-11. The red solid line is obtained by using the data of 1in-width specimen. The applied speed was 0.004 inch per second with a corresponding strain rate of approximately 0.002 s^{-1}. On the other hand, the cyan dashed line and the green dotted line are obtained by using the data of 18mm-width specimens. Applied speed for the cyan dashed line was approximately 1.5 inch/second with a corresponding strain rate of 1 s^{-1}, whereas the speed for the green dotted line was approximately 3.0 inch/second with a corresponding strain rate of 2 s^{-1}.

Figure 4-10 Fractured specimens of high speed tensile tests. The specimens used in the tests were 18mm-width specimens (without groove). The specimen on the top was subjected to strain rate of 1 s^{-1}, while the one on the bottom was subjected to 2 s^{-1}.

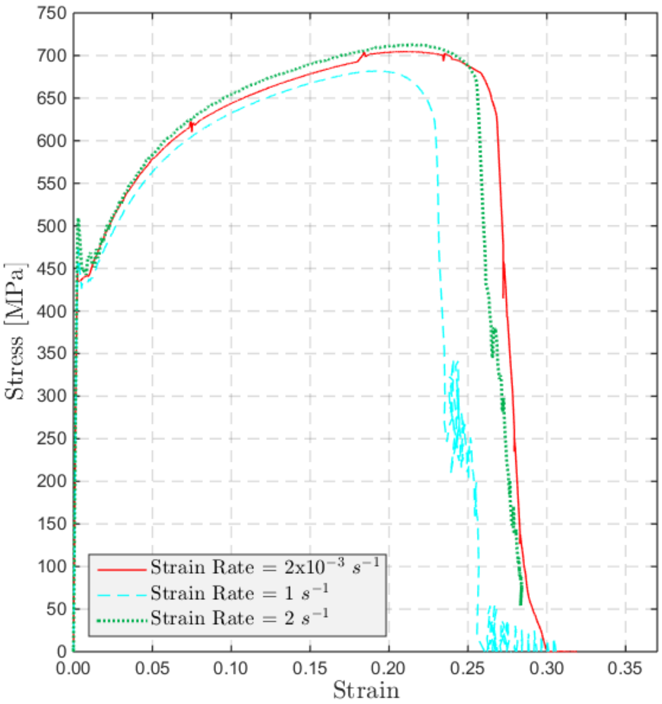

Figure 4-11 True stress-strain curves obtained via an MTS machine for different strain rates. The red solid line is obtained by using the data of an 1in-width specimen (without groove), whereas the cyan dashed line and the green dotted line are obtained by using the data of 18mm-width specimens (without groove).

The primary aim of the experimental program is to provide data for researchers needing data for validation and verification of fracture models, and to provide the data with which to evaluate the constants (i.e., toughness stresses) in the analytical formulation presented in Chapter 3. Another aim of the experimental investigation is to explore the effects of the state of stress and the element size on the fracture behavior of metals, particularly AH32 steel. The tertiary objective is to investigate the effects of strain rate on fracture initiation.

4.3 Digital Image Correlation (DIC)

Digital image correlation (DIC) is an optical image processing technique that uses mathematical tools to capture the difference between two digital images, a (possibly un-deformed) reference state image and a deformed state image, for example. The digital image correlation technique was developed at the University of South Carolina in the early 1980s (Jin et al., 2008; Pan et al., 2009). However, it is worth noting that the fundamental notions were based on Particle Image Velocimetry (PIV), developed for fluid mechanics research.

Although in–plane interferometric methods have better strain measurement accuracy, 2D–DIC has the following advantages compared to in–plane interferometric methods (Pan et al., 2009):

i) Experimental setup is relatively simple; that is, only one fixed CCD camera is sufficient

ii) Surface pattern creation is simple or even might be unnecessary if the surface already has a natural texture

iii) A white light source is sufficient; i.e., no laser source is required

iv) Using digital images allow a wide resolution range

The restriction to in–plane deformation measurement is the main disadvantage of 2D–DIC compared to 3D–DIC (also called Stereo DIC) and DVC (Digital Volume Correlation). However, having easier experimental set up and faster recording and processing times (i.e., less cost) still make 2D–DIC practical and useful. This is the method used throughout.

The error of 2D–DIC due to out-of-plane motion (both out-of-plane translation and out-of-plane rotation) has been formulated and examined experimentally by Sutton et al. (2008). In the experiments presented here, these errors are very small compared to large plastic (fracture) strains and neglect of them affects the fracture strain calculation little; hence, they are neglected.

Moreover, the impact of lens distortion on strain measurements has been studied by Lava et al. (2013). In addition to their study of the influence of lens distortion on rigid body translation, rigid body rotation, and uniaxial tensile test of a textile composite at low strain levels, Lava et al. (2013) also investigated the influence of lens distortion at large strain levels on a uniaxial tensile test of SS304 steel. As can clearly be seen from Figure 13 of the cited reference, the impact of lens distortion on strain measurement loses its importance and becomes negligible after approximately 1.5%–2.0% of strain. In the fracture experiments presented here, the strains are much larger and therefore such adverse effects of lens distortion are negligible.

Finally, it is worth noting that electronic speckle photography (ESP), texture correlation, computer-aided speckle interferometry (CASI), and digital speckle correlation method (DSCM) are other names attributed to DIC in the literature (Pan et al., 2009).

4.4 Strain and Stress Triaxiality Calculation

4.4.1 Strain Calculation

One way of obtaining the failure strain is measuring the diameter (or thickness) of the fractured specimen (see e.g., Hancock & Mackenzie, 1976; Mirza et al., 1996). Another method of obtaining the failure strain is using the experimental load-deformation record substituted into the derived mathematical formulation of strain (see e.g., Barsoum & Faleskog, 2007a).

Currently, a common, widely used approach to post-process experimental results is extracting stress and strain fields from the corresponding finite element models, that is, hybrid experimental-numerical analysis (see e.g., Bao & Wierzbicki, 2004; Bai & Wierzbicki, 2010; Papasidero et al., 2015). In this approach, both stress and strain depend on the results of the finite element analyses and are not measured during tests. An accurate measurement of strain can be obtained by use of an electrical strain-gauge. However, this method cannot be used for large strain measurements (e.g., failure/fracture strain) as its range is generally limited to strain of 0.02 (Zhu et al., 2015). Therefore, in this study, a direct measure of strain has been obtained by DIC. Strains have been obtained by analyzing digital images that were recorded during the experiments with a Phantom v710 high speed camera, via DaVis LaVision (2015) software. The state of stress has been calculated directly (rather than through a numerical simulation) by using the DIC results via power-law relationship and flow rule.

The operations that lead to extracting the engineering/nominal strains are depicted in Figure 4-12. The first two operations in the list import the desired digital images into

DaVis LaVision software. In the first operation, the time interval has been chosen as one second so that the velocity field obtained by the third operation is equivalent to determining the displacement field. In the second operation, the pixel dimensions of the digital images are defined and the third operation, as already noted, provides the displacement field. The fourth operation in the list sums the displacement field in a Lagrangian manner, while the fifth operation provides strain calculations. In this manner, the surface engineering strain components e_{11}^{BW}, e_{22}^{BW}, and e_{12}^{BW} are determined. The sixth operation in the list provides an opportunity to define a region the user is to examine. Therefore, a sub-region of interest, which is called a 'geometric mask', is introduced in the sixth operation such that this 'masked region' can be used to investigate a specific sub-region of the imaged surface. Finally, in the seventh operation a constant value (which has been chosen as 9999) is prescribed to delineate the region outside the mask so that the results within the masked region can be extracted. Fluctuations in the strain field due to polycrystalline microstructure and the noise of the DIC measurements can be reduced by averaging (Papasidero et al, 2014). Therefore, average strains within the masked region are obtained. An average of all numbers less than 9999 provides the average strain within the masked region.

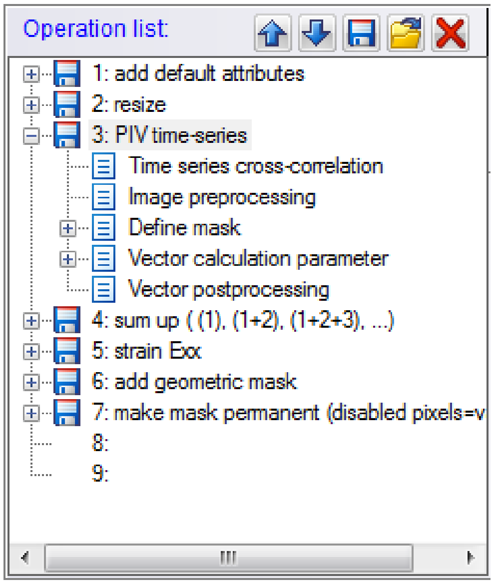

Operation list:

- 1: add default attributes
- 2: resize
- 3: PIV time-series
  - Time series cross-correlation
  - Image preprocessing
  - Define mask
  - Vector calculation parameter
  - Vector postprocessing
- 4: sum up ((1), (1+2), (1+2+3), ...)
- 5: strain Exx
- 6: add geometric mask
- 7: make mask permanent (disabled pixels=v
- 8:
- 9:

Figure 4-12 The operation list that is used to extract engineering strains within the desired 'masked region'.

Strains have been calculated to the point of fracture initiation. We define the fracture initiation as the condition when the first visible crack appears in the digital picture of the test specimen. Moreover, as the continuum scale is the subject of interest, the initiation of fracture has been established by observing the digital images of the test specimen.

Not all the digital images are used in the analysis. The lower-bound step intervals have been chosen such that the effect of noise on the strain values is relatively small. Upper-bound intervals have been chosen such that the average correlation value between any two digital images is sufficiently high (e.g., higher than 0.80). In addition, obtained displacement fields are visually evaluated to confirm whether the results are reasonable.

Strains have been calculated in a backward-stepping manner; that is, the last frame (which is the digital image of the specimen at the point of fracture initiation) has been taken as the first step and from there, time is reversed by using a previous image, and so forth (that is, the first frame is the last step). The difference between forward steps ('forward-strain-calculation') and backward steps ('backward-strain-calculation') is only the sign of displacement vector. The primary reason for doing 'backward-strain-calculation' is that it was much easier to define the crack/fracture region more precisely. In other words, the exact material position of the fracture region is known in the last frame, and can then be traced (by DaVis LaVision software) backwards in time to its location before loading. On the other hand, if the 'forward-strain-calculation' was used, the material position of the fracture in the first frame would be based on an estimate and it would likely not be precise.

This procedure is repeated for various mask sizes. The minimum mask size, which is 16x16 pixels, was chosen such that the 'masked region' is still on the continuum scale. The number of grains required to develop a continuum scale occurs when the grains have random orientations in a macroscopic manner[39]. This number for polycrystalline aggregates (e.g., steel, aluminum, etc.) is approximately twenty[40] (Leis et al., 1985; Tegart, 1966).

---

[39] *"The number of grains required to develop such continuum behavior (homogeneous grain-to-grain compability) ..."* (p. 326 of Leis et al, 1985).

[40] *"... polycrystalline aggregates with >20 grains per cross section where we have essentially random orientations of the grains ..."* (p. 166 of Tegart, 1966).

4.4.1.1 Calculation of Forward-Plastic-Strain

Let the backward-engineering-strain and forward-engineering-strain tensors of the last frame (which is the digital image of the specimen at the point of fracture initiation) be denoted as $\left(e_{ij}^{BW}\right)_1$ and $\left(e_{ij}^{FW}\right)_N$, respectively. Similarly, let the backward-engineering-strain and forward-engineering-strain tensors of the first frame (which is the digital image of the unstrained specimen) be denoted as $\left(e_{ij}^{BW}\right)_N$ and $\left(e_{ij}^{FW}\right)_1$, respectively. Obviously, $\left(e_{ij}^{BW}\right)_1 = 0$ (as this is the first step in the backward sense), $\left(e_{ij}^{FW}\right)_1 = 0$ (as this is the first step in the forward sense), and $\left(e_{ij}^{FW}\right)_N \neq -\left(e_{ij}^{BW}\right)_N$.

Therefore, the forward-engineering-strain components are calculated in the following manner:

$$\left(e_{ij}^{FW}\right)_1 = 0 \tag{4-1}$$

$$\left(e_{ij}^{FW}\right)_2 = \begin{cases} \dfrac{1+\left(e_{ij}^{BW}\right)_{N-1}}{1+\left(e_{ij}^{BW}\right)_N} - 1 \; if \; i = j \\ \left(e_{ij}^{BW}\right)_{N-1} - \left(e_{ij}^{BW}\right)_N \; if \; i \neq j \end{cases} \tag{4-2}$$

$$\left(e_{ij}^{FW}\right)_3 = \begin{cases} \dfrac{1+\left(e_{ij}^{BW}\right)_{N-2}}{1+\left(e_{ij}^{BW}\right)_N} - 1 \; if \; i = j \\ \left(e_{ij}^{BW}\right)_{N-2} - \left(e_{ij}^{BW}\right)_N \; if \; i \neq j \end{cases} \tag{4-3}$$

…

$$\left(e_{ij}^{FW}\right)_{N-1} = \begin{cases} \dfrac{1+\left(e_{ij}^{BW}\right)_2}{1+\left(e_{ij}^{BW}\right)_N} - 1 \; if \; i = j \\ \left(e_{ij}^{BW}\right)_2 - \left(e_{ij}^{BW}\right)_N \; if \; i \neq j \end{cases} \tag{4-4}$$

$$\left(e_{ij}^{FW}\right)_N = \begin{cases} \dfrac{1+\left(e_{ij}^{BW}\right)_1}{1+\left(e_{ij}^{BW}\right)_N} - 1 \; if \; i = j \\ \left(e_{ij}^{BW}\right)_1 - \left(e_{ij}^{BW}\right)_N \; if \; i \neq j \end{cases} \tag{4-5}$$

This can be generalized as

$$\left(e_{ij}^{FW}\right)_k = \begin{cases} \dfrac{1+\left(e_{ij}^{BW}\right)_{N-k+1}}{1+\left(e_{ij}^{BW}\right)_N} - 1 \; if \; i = j \\ \left(e_{ij}^{BW}\right)_{N-k+1} - \left(e_{ij}^{BW}\right)_N \; if \; i \neq j \end{cases} \tag{4-6}$$

where $k = 1,2, \dots, N$.

Finally, forward-natural-strains at any step can be obtained by the following relationship

$$\varepsilon_{ij}^{FW} = \begin{cases} \ln\left(1 + e_{ij}^{FW}\right) \; if \; i = j \\ \left(e_{ij}^{FW}\right)_N \; if \; i \neq j \end{cases} \tag{4-7}$$

where e_{ij}^{FW} are the components of the forward-engineering strain tensor and ε_{ij}^{FW} are the forward-natural-strain components[41].

4.4.1.2 Calculation of Effective (Fracture) Strain

The effective strain increment can be obtained by substituting forward-natural-strain increments into the expression

$$d\varepsilon_{eff}^{p} = \sqrt{\frac{2}{3}\left(d\varepsilon_{ij}^{p}\right)_D \left(d\varepsilon_{ij}^{p}\right)_D} \tag{4-8}$$

where $\left(d\varepsilon_{ij}^{p}\right)_D$ is the deviatoric part of the plastic strain increment tensor[42]. Note that the deviatoric part of the plastic strain increment tensor is equal to the plastic strain increment tensor due to incompressibility; i.e., $d\varepsilon_{ii}^{p} = 0$ (Hill, 2009). Hence,

$$d\varepsilon_{eff}^{p} = \sqrt{\frac{2}{3} d\varepsilon_{ij}^{p} d\varepsilon_{ij}^{p}} \tag{4-9}$$

---

[41] Note that the natural strain increments ($d\varepsilon_{ij}$) are components of a tensor; hence, transformation rules/formulas/laws can be applied. On the other hand, natural strains (ε_{ij}) are not components of a tensor (p. 152 of Malvern, 1969); hence, transformation rules/formulas/laws cannot be applied.

[42] Note that: $d\varepsilon_{ij}^{p} = \left(d\varepsilon_{ij}^{p}\right)_D + \frac{1}{3} d\varepsilon_{ii}^{p}$

where $d\varepsilon_{ij}^{p}$ are the components of the plastic strain increment tensor.

As the surface (that has been considered in DIC analysis) is free of stress, a state of plane-stress is established; hence, $\sigma_{33} = \sigma_{13} = \sigma_{23} = 0$. Using the flow rule yields $d\varepsilon_{13}^{p} = d\varepsilon_{23}^{p} = 0$. Therefore, the effective plastic strain increment yields the form

$$d\varepsilon_{eff}^{p} = \sqrt{\frac{2}{3}\left[\left(d\varepsilon_{11}^{p}\right)^{2} + \left(d\varepsilon_{22}^{p}\right)^{2} + \left(d\varepsilon_{33}^{p}\right)^{2} + 2\left(d\varepsilon_{12}^{p}\right)^{2}\right]} \tag{4-10}$$

where $d\varepsilon_{11}^{p}$, $d\varepsilon_{22}^{p}$, and $d\varepsilon_{33}^{p}$ are the normal strain increments and $d\varepsilon_{12}^{p}$ is the shear strain increment.

Plastic strain increments on the surface (or in-plane strain increments), that is, $d\varepsilon_{11}^{p}$, $d\varepsilon_{22}^{p}$, and $d\varepsilon_{12}^{p}$ are computed by using the result of the DIC analysis and the engineering-natural strain relationship given by Equation (4-7). Nevertheless, the plastic strain increment in the third direction (the thickness direction in our case) is obtained by using the incompressibility ($d\varepsilon_{11}^{p} + d\varepsilon_{22}^{p} + d\varepsilon_{33}^{p} = 0$); that is,

$$d\varepsilon_{33}^{p} = -\left(d\varepsilon_{11}^{p} + d\varepsilon_{22}^{p}\right) \tag{4-11}$$

As the plastic strains are much greater than the elastic strains, the elastic part of the total strain (and the total strain increment) can be neglected; that is,

$$d\varepsilon_{ij} \approx d\varepsilon_{ij}^{p} \text{ and } \varepsilon_{ij} \approx \varepsilon_{ij}^{p} \tag{4-12}$$

Hence, the total strain increment ($d\varepsilon_{ij}$) obtained by DIC analysis can be taken as the plastic strain increment ($d\varepsilon_{ij}^{p}$) in the above formulation (i.e., in Equation (4-10) and Equation (4-11)).

Two different strain increment approaches are applied in the calculation of effective strain, the state of stress, and the stress triaxiality; i.e., each approach provides a set of figures for a specific mask size. In the first approach, the strain increments are from the un-deformed state to the current state, while the second set of figures are obtained by taking strain increments from the previous state to the current state.

1st approach: $$\varepsilon_{eff}(k) = \varepsilon_{eff}(1) + d\varepsilon_{eff}(k,1) = d\varepsilon_{eff}(k,1) \tag{4-13}$$

2nd approach: $$\varepsilon_{eff}(k) = \varepsilon_{eff}(k-1) + d\varepsilon_{eff}(k,k-1) \tag{4-14}$$

where k is the step number; i.e., $k = 1,2,\dots,N$. Moreover, $d\varepsilon_{eff}(q,s)$ represents the effective strain increment from step s to step q.

The only difference between the two approaches is the amount of strain increment considered. As the stress-strain relationships (i.e., the flow rule) are based on the linear incremental relationships, use of smaller strain increments (that is, the second approach) is believed to provide more reliable results. However, results of both approaches will be presented for comparison purposes.

4.4.2 Stress Calculation

4.4.2.1 Calculation of Stress Triaxiality

Applying the flow rule for a plastic material (Desai & Siriwardane, 1984), the plastic strain increments are related to the true stress components:

$$d\varepsilon_{11}^{p} = \frac{2}{3}\lambda\left[\sigma_{11} - \frac{1}{2}(\sigma_{22} + \sigma_{33})\right] \tag{4-15}$$

$$d\varepsilon_{22}^{p} = \frac{2}{3}\lambda\left[\sigma_{22} - \frac{1}{2}(\sigma_{11} + \sigma_{33})\right] \tag{4-16}$$

$$d\varepsilon_{12}^{p} = \lambda\sigma_{12} \tag{4-17}$$

where λ is a non-negative scalar factor and may vary throughout the loading history.

Define ψ_1 and ψ_2 as the ratios of the plastic strain increments, i.e.,

$$d\varepsilon_{22}^{p} = \psi_1 d\varepsilon_{11}^{p} \tag{4-18}$$

$$d\varepsilon_{12}^{p} = \psi_2 d\varepsilon_{11}^{p} \tag{4-19}$$

By using the flow rule expressions above, these expressions can be written

$$\psi_1 = \frac{\sigma_{22} - \frac{1}{2}(\sigma_{11} + \sigma_{33})}{\sigma_{11} - \frac{1}{2}(\sigma_{22} + \sigma_{33})} \tag{4-20}$$

$$\psi_2 = \frac{\sigma_{12}}{\frac{2}{3}\left[\sigma_{11} - \frac{1}{2}(\sigma_{22} + \sigma_{33})\right]} \tag{4-21}$$

Simplifying the equalities yields

$$\sigma_{11}(1 + 2\psi_1) - \sigma_{22}(2 + \psi_1) + \sigma_{33}(1 - \psi_1) = 0 \tag{4-22}$$

$$2\sigma_{11}\psi_2 - \sigma_{22}\psi_2 - \sigma_{33}\psi_2 - 3\sigma_{12} = 0 \tag{4-23}$$

Again, as the surface (that has been considered in DIC analysis) is free of stress, a state of plane-stress is established. Therefore, in the case of the plane-stress condition (i.e., $\sigma_{33} = \sigma_{13} = \sigma_{23} = 0$), Equation (4-22) and Equation (4-23) reduce to

$$\sigma_{11}(1 + 2\psi_1) - \sigma_{22}(2 + \psi_1) = 0 \tag{4-24}$$

$$2\sigma_{11}\psi_2 - \sigma_{22}\psi_2 - 3\sigma_{12} = 0 \tag{4-25}$$

These expressions may also be written as,

$$\sigma_{22} = \frac{1 + 2\psi_1}{2 + \psi_1}\sigma_{11} \tag{4-26}$$

$$\sigma_{12} = \frac{1}{3}(2\sigma_{11}\psi_2 - \sigma_{22}\psi_2) \tag{4-27}$$

Substituting the expression for σ_{22} (Equation (4-26)) into the expression for σ_{12} (Equation (4-27)) gives

$$\sigma_{12} = \frac{\psi_2}{2 + \psi_1}\sigma_{11} \tag{4-28}$$

The Von-Mises effective stress for the plane-stress condition is defined as

$$\sigma_{eff} = \sqrt{\sigma_{11}^2 - \sigma_{11}\sigma_{22} + \sigma_{22}^2 + 3\sigma_{12}^2} \tag{4-29}$$

Substituting expressions for σ_{22} (Equation (4-26)) and σ_{12} (Equation (4-27)) into σ_{eff} (Equation (4-29)) yields

$$\sigma_{eff} = \sqrt{\sigma_{11}^2 - \sigma_{11}\left[\frac{(1+2\psi_1)}{(2+\psi_1)}\sigma_{11}\right] + \left[\frac{(1+2\psi_1)}{(2+\psi_1)}\sigma_{11}\right]^2 + 3\left[\frac{\psi_2}{(2+\psi_1)}\sigma_{11}\right]^2} \tag{4-30}$$

Further simplification yields

$$\sigma_{eff} = \psi_{eff\_tensile}\sigma_{11} \tag{4-31}$$

where

$$\psi_{eff\_tensile} = \sqrt{\frac{3(1+\psi_1+\psi_1^2+\psi_2^2)}{(2+\psi_1)^2}} \tag{4-32}$$

Note that as the components of the stress state are expressed in terms of σ_{11} and the sign of $\psi_{eff\_tensile}$ is chosen positive (i.e., tension in 11 direction), 11 direction should be chosen in the direction of positive loading to prevent possible unrealistic stress states (negative longitudinal stress under tension, for example).

However, the state of stress should be expressed in terms of σ_{12} for the shear test as the loading is dominated in the 12 direction.

$$\sigma_{eff} = \sqrt{\left[\frac{(2+\psi_1)}{\psi_2}\sigma_{12}\right]^2 - \left[\frac{(2+\psi_1)}{\psi_2}\sigma_{12}\right]\left[\frac{(1+2\psi_1)}{\psi_2}\sigma_{12}\right] + \left[\frac{(1+2\psi_1)}{\psi_2}\sigma_{12}\right]^2 + 3\sigma_{12}^2} \tag{4-33}$$

Further simplification yields

$$\sigma_{eff} = \psi_{eff\_shear}\sigma_{12} \tag{4-34}$$

where

$$\psi_{eff\_shear} = \sqrt{\frac{3(1+\psi_1+\psi_1^2+\psi_2^2)}{{\psi_2}^2}} \tag{4-35}$$

In addition, the mean stress for the plane-stress condition is

$$\sigma_m = \frac{\sigma_{11}+\sigma_{22}+0}{3} = \frac{\sigma_{11}+\sigma_{22}}{3} \tag{4-36}$$

Inserting the expressions for σ_{22} and σ_{11} into the expression for the mean stress (Eq. (4-36)), one obtains σ_m in the form

$$\sigma_m = \frac{\frac{3(1+\psi_1)}{(2+\psi_1)}}{3}\sigma_{11} \quad \text{or} \quad \sigma_m = \frac{\frac{3(1+\psi_1)}{\psi_2}}{3}\sigma_{12} \tag{4-37}$$

Finally, the stress triaxiality can then be calculated as

$$\eta = \frac{\sigma_m}{\sigma_{eff}} = \frac{1+\psi_1}{\sqrt{3(1+\psi_1+\psi_1^2+\psi_2^2)}} \tag{4-38}$$

4.4.2.2 Calculation of Average Stress Triaxiality

The average stress triaxiality is obtained by dividing the area under the effective strain – stress triaxiality curve to effective strain at fracture; that is,

$$\eta_{ave} = \frac{1}{\varepsilon_{eff}^f}\int_0^{\varepsilon_{eff}^f} \eta d\varepsilon_{eff} \tag{4-39}$$

This integration is carried out numerically by using the trapezoidal rule. Note that as the stress triaxiality is not defined for the unloaded condition, calculations and figures for the stress triaxiality are provided after the first loading point.

4.4.2.3 Obtaining the State of Stress

Recall the power-law hardening relationship

$$\sigma_{eff} = \Omega\left(\varepsilon_{eff}^p\right)^n \tag{4-40}$$

where Ω is the strength coefficient, n is the hardening exponent, and the ε_{eff}^{p} is the effective plastic strain. The effective stress can be written in the form (see Equation (4-31))

$$\sigma_{eff} = \psi_{eff\_tensile}\sigma_{11} \tag{4-41}$$

$\psi_{eff\_tensile}$, ψ_1, and ψ_2 can be obtained by Equation (4-32), Equation (4-18), and Equation (4-19), respectively.

Therefore, the power-law hardening relationship can be written as

$$\psi_{eff\_tensile}\sigma_{11} = \Omega\left(\varepsilon_{eff}^{p}\right)^{n} \tag{4-42}$$

Rearranging it yields

$$\sigma_{11} = \frac{1}{\psi_{eff\_tensile}}\Omega\left(\varepsilon_{eff}^{p}\right)^{n} \tag{4-43}$$

The other two components of the true stress tensor (i.e., σ_{22} and σ_{12}) can be obtained from Equation (4-26) and Equation (4-28), respectively.

However, the following relationship is used when the effective stress is expressed in terms of the shear stress (σ_{12}); that is, only for the shear test

$$\sigma_{12} = \frac{1}{\psi_{eff\_shear}}\Omega\left(\varepsilon_{eff}^{p}\right)^{n} \tag{4-44}$$

Similarly, the other two components of the stress tensor (i.e., σ_{11} and σ_{22}) can be obtained from Equation (4-28) and Equation (4-26), respectively.

Note that $\sigma_{33} = \sigma_{13} = \sigma_{23} = 0$ due to the plane-stress condition.

Finally, the power-law hardening parameters are computed as $\Omega = 868.4$ MPa and $n = 0.128$ by using the stress-strain data from the uniaxial test (see Figure 4-9).

4.5 Uniaxial Test Results

Uniaxial tests have been conducted for three different specimen geometries. Two different strain increment approaches are applied in the calculation of effective strain, the state of stress, and the stress triaxiality; i.e., each approach provides a set of figures for a specific mask size. In the first approach, the strain increments have been determined from the un-deformed state to the current state, while the second set of figures have been obtained by taking strain increments from the previous state to the current state. For the strain analysis only the data of the second approach are presented unless the effective strain of the two approaches have different qualitative behavior, whereas data of both approaches are provided for the stress analysis.

All stresses presented in this section (i.e., Uniaxial Test Results) are the true stresses and all strains are the natural/true strains unless otherwise stated. Moreover, the subscript *11* corresponds to the longitudinal direction of the specimen and the subscript *22* corresponds to the width direction.

4.5.1 Analysis of 6mm-Width Specimen without Groove

DIC analyses are conducted for two different test speeds for this particular specimen and presented in the following sequential sub-sections.

4.5.1.1 Test 1

This specimen was obtained by in-house machining of an 18mm-width specimen (without groove). The width of the specimen was reduced to capture the entire mid-region (during imaging) with a similar pixel resolution to the other specimens. The isometric view and technical drawing of the specimen are depicted in Figure 4-13 and Figure 4-14, respectively.

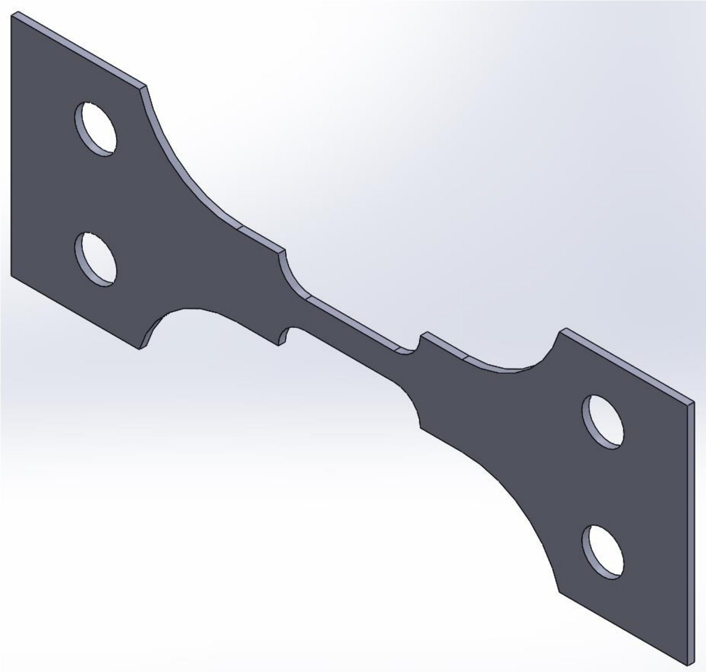

Figure 4-13 Isometric view of the 6mm-width specimen without groove (Courtesy of James Gose and Haocheng Pan). This specimen was obtained by in-house machining of an 18mm-width specimen (without groove).

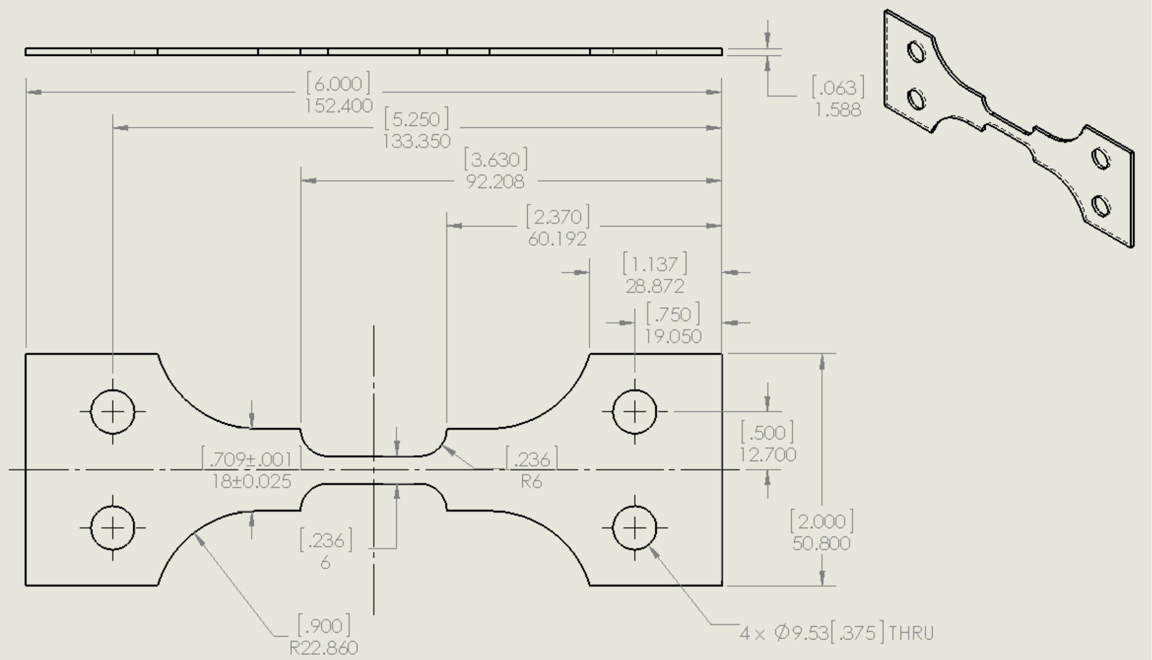

Figure 4-14 Technical drawing of the 6mm-width specimen without groove (Courtesy of James Gose and Haocheng Pan). This specimen was obtained by in-house machining of an 18mm-width specimen (without groove).

A test speed of 0.2 inch/second was applied to the end of the test specimen with 6000 digital images recorded per second for this experiment. The pixel resolution is approximately 16.5 microns per pixel. Note that the high speed camera and the experimental device were snychronized in this experiment.

Frames from the video recording are presented in Figure 4-15, Figure 4-16, Figure 4-17, Figure 4-18, Figure 4-19, and Figure 4-20. The vertical direction and the horizontal direction are the width direction and the longitudinal direction of the specimen, respectively. The regions depicted are the exploded views and their dimensions are approximately 645–665 pixels by 370–390 pixels.

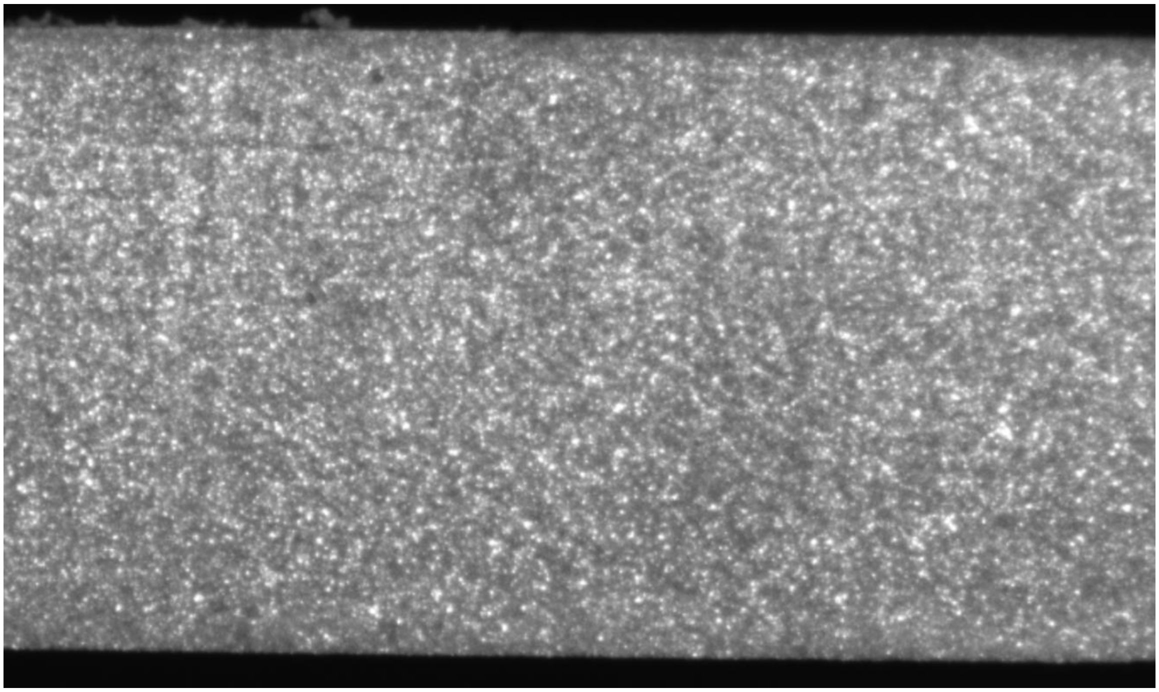

Figure 4-15 Nital etched AH32 steel 6mm-width specimen (without groove) at Frame 0; that is, in the undeformed state.

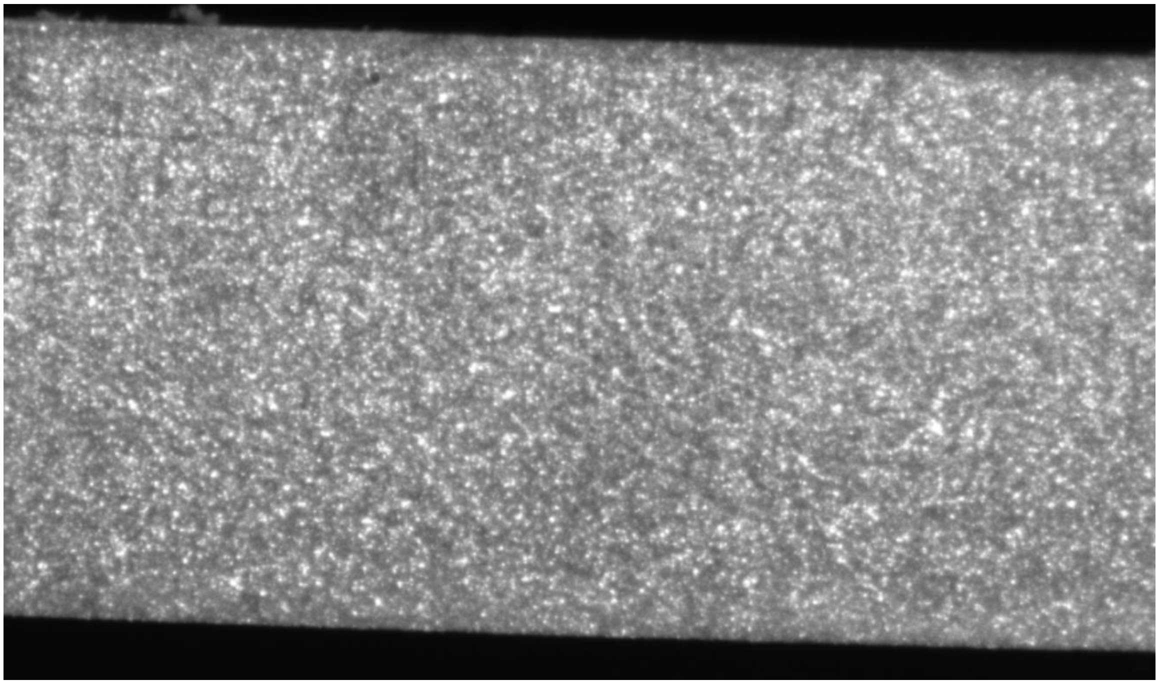

Figure 4-16 Nital etched AH32 steel 6mm-width specimen (without groove) at Frame 4000; a 3.387 mm end-displacement had been applied.

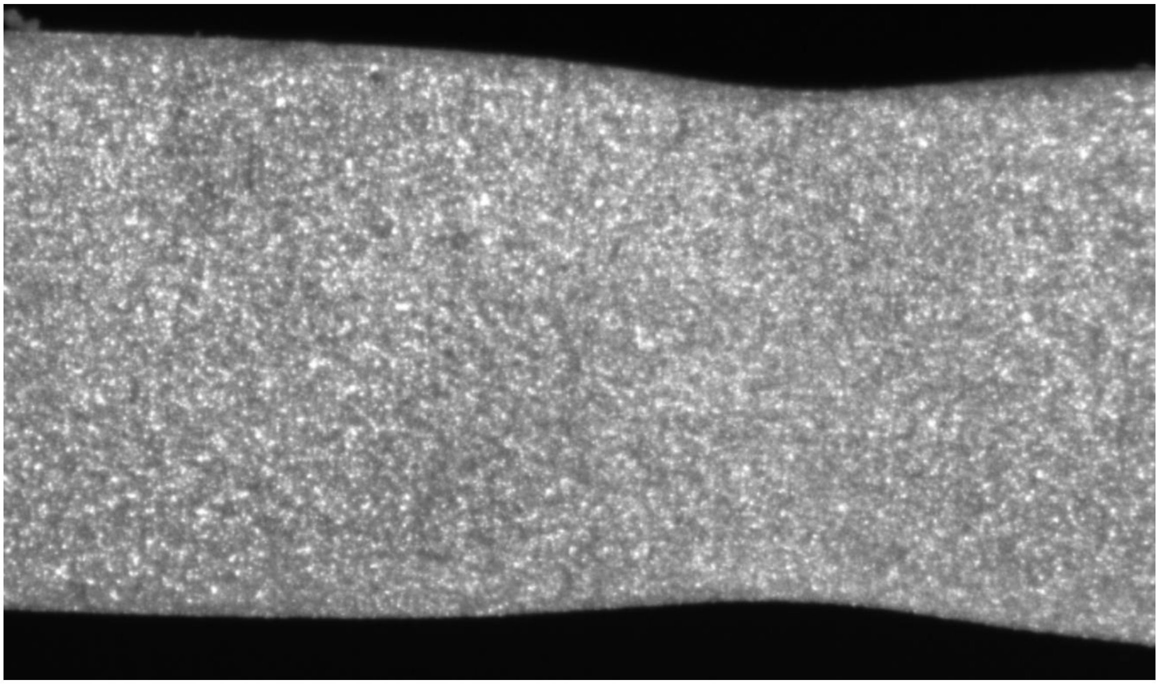

Figure 4-17 Nital etched AH32 steel 6mm-width specimen (without groove) at Frame 7000; a 5.927 mm end-displacement had been applied.

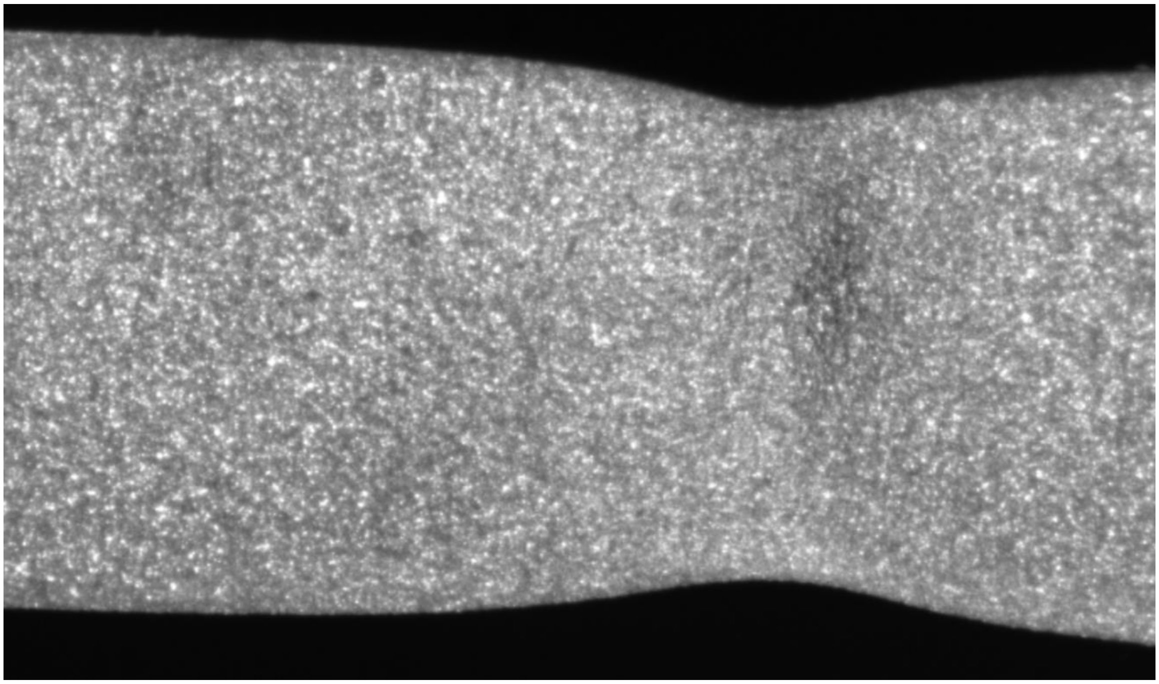

Figure 4-18 Nital etched AH32 steel 6mm-width specimen (without groove) at Frame 7441; a 6.300 mm end-displacement had been applied.

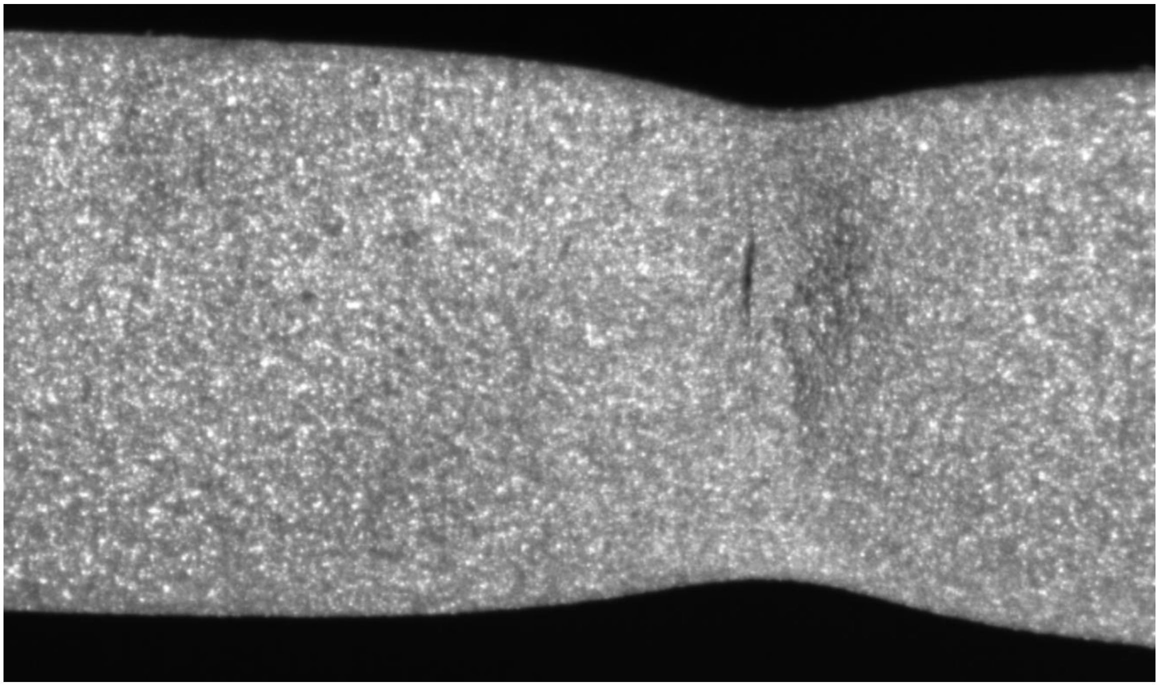

Figure 4-19 Nital etched AH32 steel 6mm-width specimen (without groove) at Frame 7443; a 6.302 mm end-displacement had been applied.

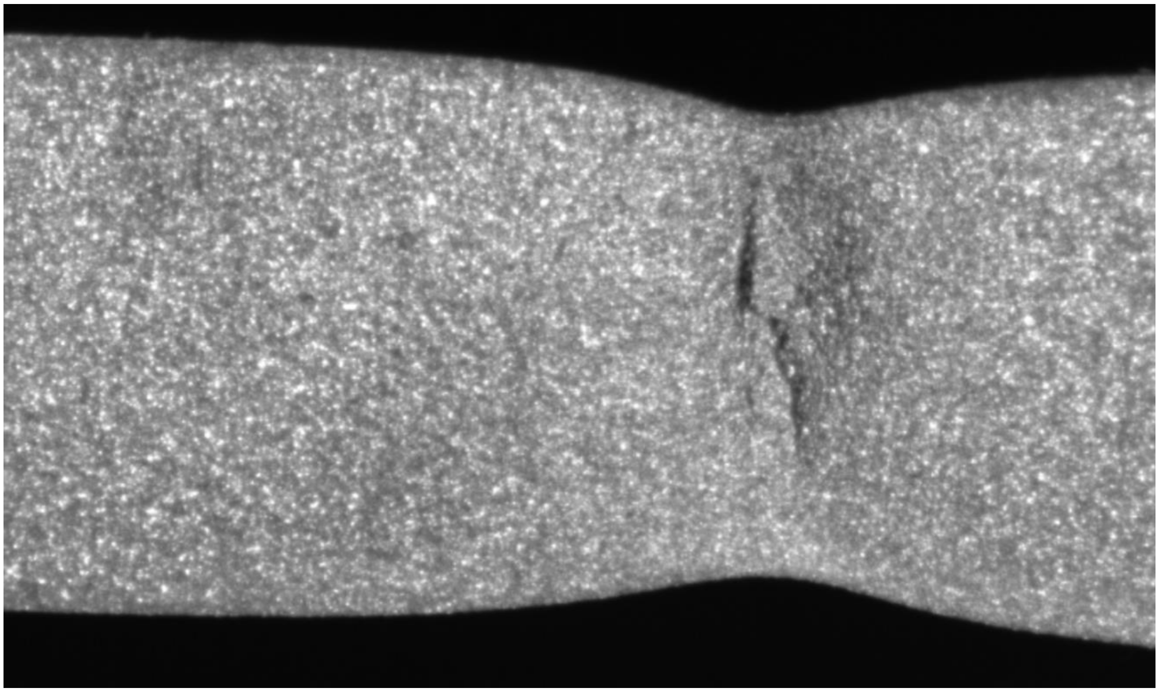

Figure 4-20 Nital etched AH32 steel 6mm-width specimen (without groove) at Frame 7445; a 6.303 mm end-displacement had been applied.

Diffuse necking starts around Frame 5500 and is clearly visible in Frame 7000, depicted in Figure 4-17. Moreover, fracture initiates around Frame 7200 (that is, following an approximately 6.096 mm horizontal displacement) and cracks are clearly visible in Frame 7441 as presented in Figure 4-18. Interestingly, however, as can be seen from Frame 4443 and Frame 7445, which are shown in Figure 4-19 and Figure 4-20, respectively, fracture progresses rapidly in a different region than where the first macroscopic cracks are seen. Moreover, Frame 7445 reveals that the fracture may be a combination of the opening mode and the shear mode as fracture progresses.

The evolution of the natural strain and the effective strain within the masked region during the uniaxial test for different mask sizes are presented in Figure 4-21, Figure 4-22, Figure 4-23, Figure 4-24, and Figure 4-25.

The shear strain is zero or nearly zero for all mask sizes until the initiation of fracture (i.e., Frame 7200), where the analysis was curtailed. Assuming that the material is incompressible, when the ratio of the transverse strain increment to the longitudinal strain increment is -0.50, the strain increment in the longitudinal direction and the effective strain increment exactly overlap if the shear strain increment is zero. This overlap can be identified approximately in all mask sizes of the current analysis as the ratio of the transverse strain increment to the longitudinal strain increment is close to -0.50.

Moreover, both the transverse strain (ε_{22}) and the longitudinal strain (ε_{11}) have relatively smaller slope until Frame 1000. The reason for this behavior is that the specimen is likely still in the elastic region and/or the elastic-plastic transition region. Considering that the Poisson’s ratio of mild steel is around 0.30, and having transverse to longitudinal strain ratios of -0.27 for 16 pixels by 16 pixels mask, -0.33 for 32 pixels by 32 pixels mask, -0.39 for 64 pixels by 64 pixels mask, -0.35 for 128 pixels by 128 pixels mask, and -0.24 for 192 pixels by 192 pixels mask, support this view. In fact, as can be seen in the stress-strain curve presented in Figure 4-44, the corresponding point of Frame 1000 lies on the elastic-plastic transition region. Furthermore, the longitudinal strain and the effective strain have nearly constant slope between Frame 1000 and Frame 5000 while the slope begins increasing around Frame 5500, where diffuse necking starts. Finally, it is worth noting the progressively increasing transverse strains. For example, for the 16 pixels by 16 pixels mask, the transverse strain at Frame 5500 is -0.099 and it reaches -0.258 at Frame 7200, where fracture initiates.

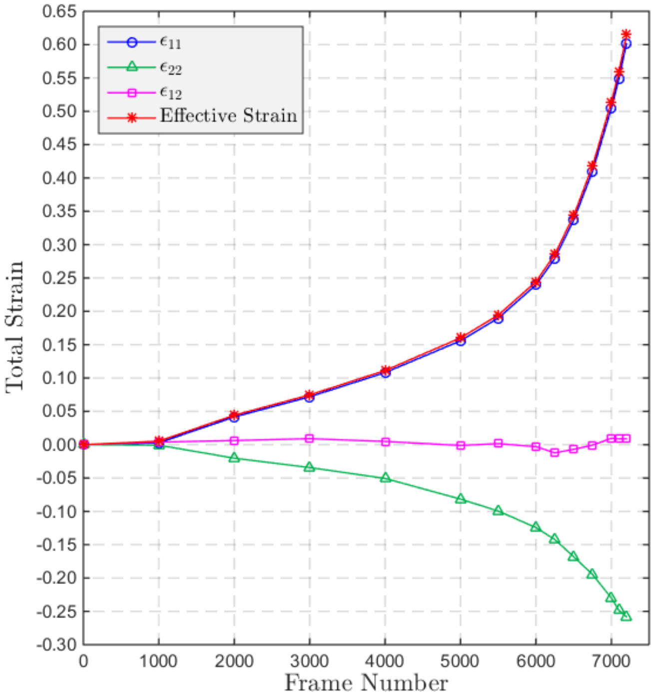

Figure 4-21 Evolution of the natural strain within the masked region during the uniaxial test – second approach. Mask size is 16 pixels by 16 pixels (0.264 mm x 0.264 mm).

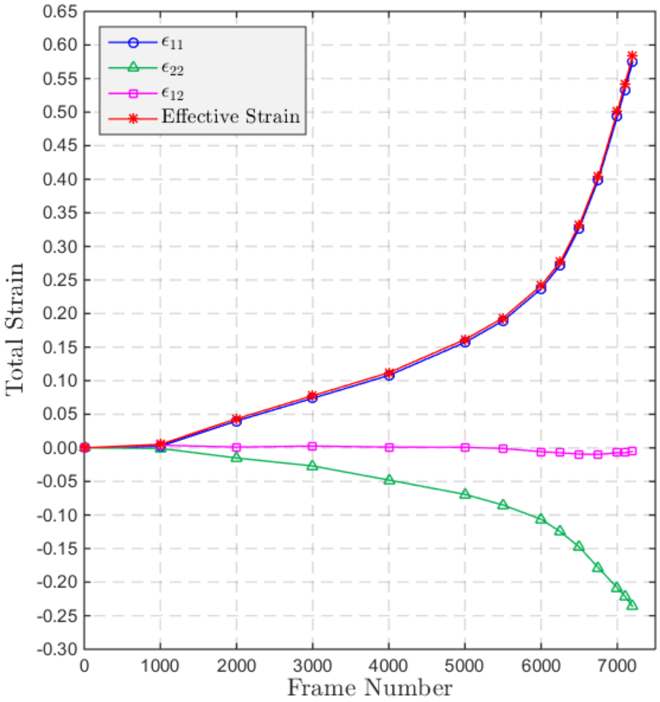

Figure 4-22 Evolution of the natural strain within the masked region during the uniaxial test – second approach. Mask size is 32 pixels by 32 pixels (0.528 mm x 0.528 mm).

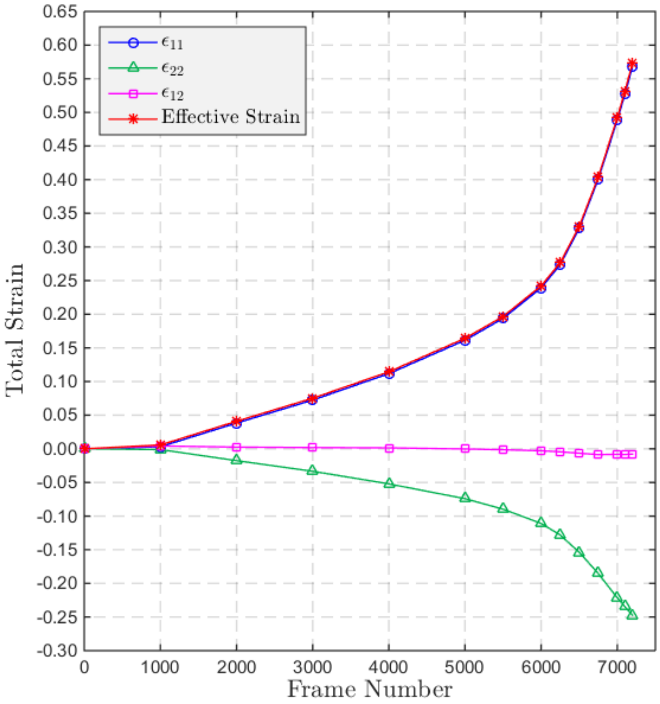

Figure 4-23 Evolution of the natural strain within the masked region during the uniaxial test – second approach. Mask size is 64 pixels by 64 pixels (1.056 mm x 1.056 mm).

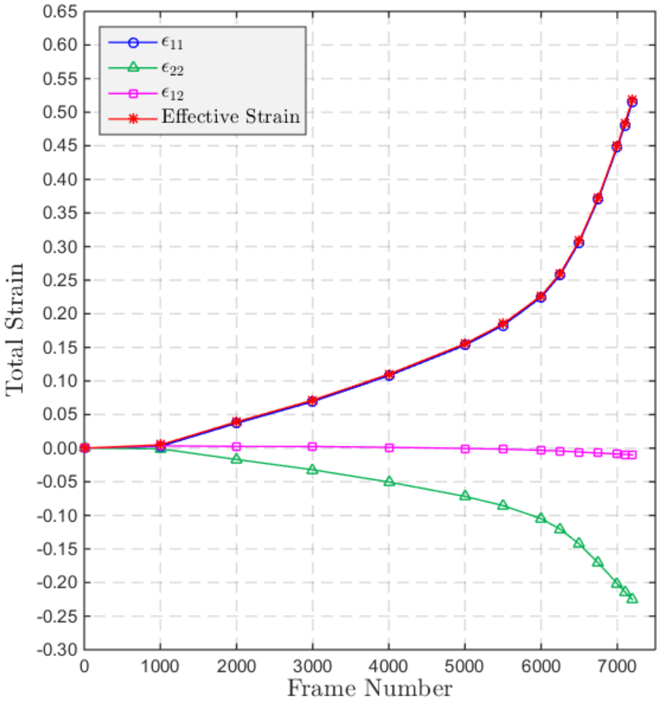

Figure 4-24 Evolution of the natural strain within the masked region during the uniaxial test – second approach. Mask size is 128 pixels by 128 pixels (2.112 mm x 2.112 mm).

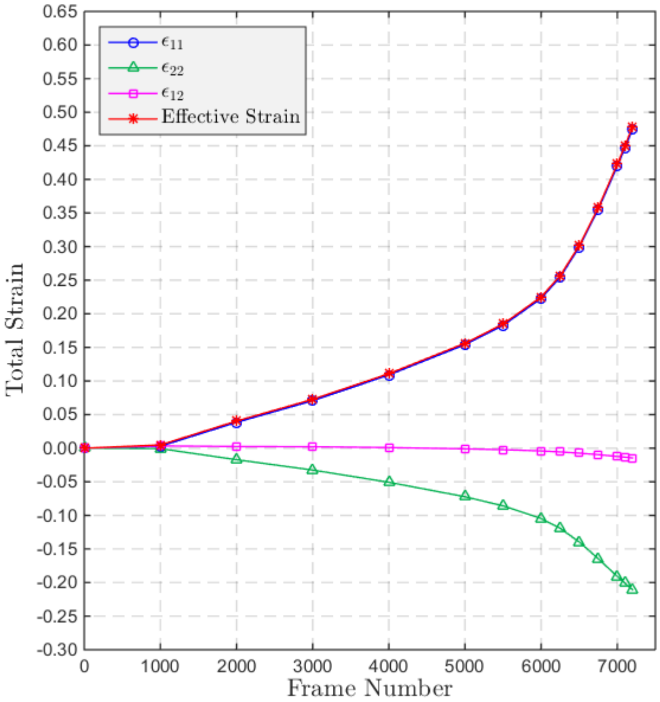

Figure 4-25 Evolution of the natural strain within the masked region during the uniaxial test – second approach. Mask size is 192 pixels by 192 pixels (3.168 mm x 3.168 mm).

The evolution of the true stress (on the left) and the stress triaxiality (on the right) within the masked region during the uniaxial test for different mask sizes are depicted in Figure 4-26, Figure 4-27, Figure 4-28, Figure 4-29, Figure 4-30, Figure 4-31, Figure 4-32, Figure 4-33, Figure 4-34, and Figure 4-35. Note that the state of stress is obtained by assuming that the stress in the longitudinal direction (σ_{11}) remains positive during the entire loading (see Section 4.4.2 for details).

The average stress triaxiality ranges between 0.34 and 0.37, and the stress triaxiality at fracture is higher than the theoretical stress triaxiality value of the purely uniaxial state, which is 1/3, for all mask sizes. However, the stress triaxiality at the initiation of the test is lower than the theoretical stress triaxiality value of the uniaxial test. The low stress triaxiality at the initiation of the test (i.e. at Frame 1000) is the result of high shear stress (which is ~200 MPa). This high shear may have developed for three reasons: the region being in the elastic-plastic transition zone, and/or the inclination of the test specimen[43], and/or as a consequence of unknown local behavior. Part of the high shear stress may be due to the region being in the elastic-plastic transition zone (as the plasticity is shear dominated) as all of the investigated regions are in the elastic-plastic transition zone (see Figure 4-44). Some part of the high shear stress may be due to the inclination of the test specimen as the 1024 pixels by 256 pixels mask (this analysis is presented in the following pages), which represents global behavior, has a considerable amount of shear stress. Moreover, it is believed that some part of the (localized) high shear stress possibly is a consequence of unknown more local behavior.

The shear stress is zero or nearly zero for the larger mask sizes (which represent more global behavior) after Frame 2000. Moreover, the true stress curve of the first and the second approach has nearly the same quantitative behavior until Frame 3000 for smaller mask sizes (16 pixels by 16 pixels mask and 32 pixels by 32 pixels mask, for example) and until Frame 6000 for larger mask sizes (128 pixels by 128 pixels mask and 192 pixels

---

[43] Note that the test specimen rotates approximately two degrees in the clock-wise direction immediately after the experiment started.

by 192 pixels mask, for example), meaning that the loading remains proportional[44] both locally (represented by smaller mask sizes) and more globally (represented by larger mask sizes) at the beginning of the test. However, they start differing immediately thereafter. This difference between the two approaches demonstrates that the loading does not remain proportional after around Frame 3000 for smaller length scales and after around Frame 6000 for larger length scales. In other words, if the loading remained proportional, the first and the second approach would have similar, or the same, stress states. In fact, mathematically, this difference is caused by the instantaneous changes of ψ_1 and ψ_2 (see Equation (4-18), Equation (4-19), Equation (4-26), and Equation (4-28)) in the second approach due to non-proportional loading of the strain history. This difference occurs as fluctuations in the cases of smaller mask sizes, while the fluctuations disappear as the mask sizes are increased and are overtaken by differences in magnitude although the qualitative behavior remains similar. It is worth noting that the sign of stress and stress triaxiality fluctuations first appear for the 64 pixels by 64 pixels mask and that the magnitude of the fluctuations increases as the mask size is decreased. Note that the Von-Mises stress has the same quantitative behavior both locally (smaller mask sizes) and more globally (larger mask sizes), as expected, as the plastic constitutive and stress-strain relationships that are used (the hardening-law and the flow rule) are independent of a length scale.

---

[44] Proportional loading (or strain history) satisfies the following state of strain:
$d\varepsilon_{22} = \Psi_1 d\varepsilon_{11}$ and $d\varepsilon_{12} = \Psi_2 d\varepsilon_{11}$
where Ψ_1 and Ψ_2 are constants, and remains the same during the entire loading process.

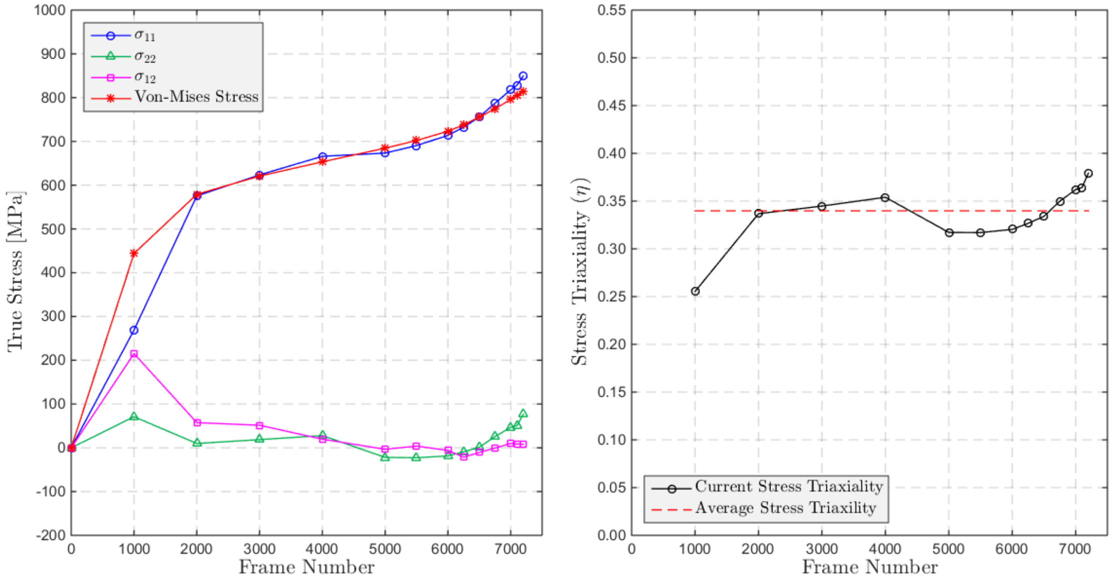

Figure 4-26 Evolution of the true stress (on the left) and the stress triaxiality (on the right) within the masked region during the uniaxial test – first approach. Mask size is 16 pixels by 16 pixels (0.264 mm x 0.264 mm).

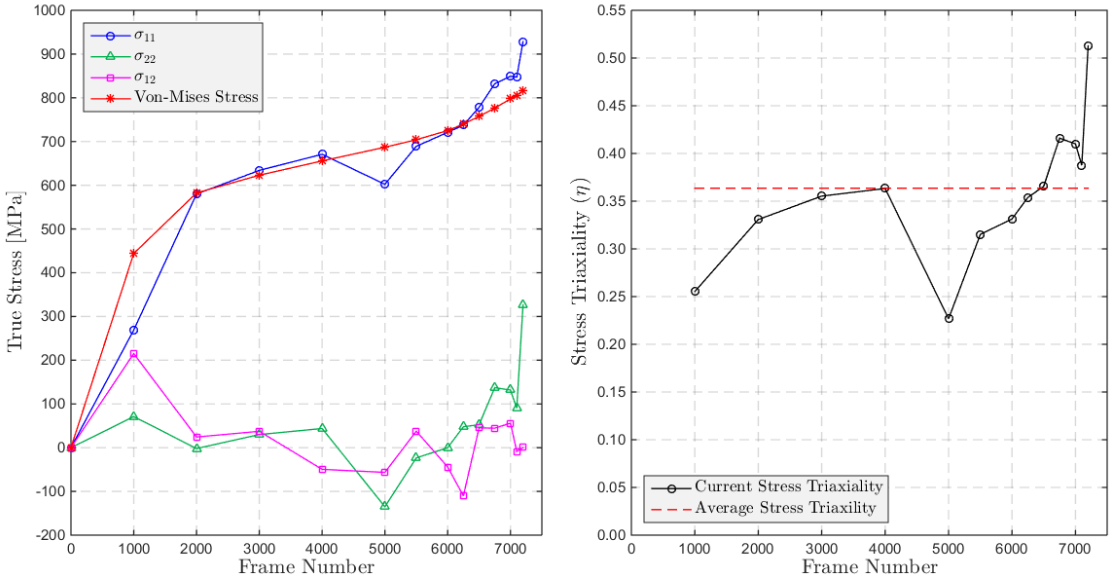

Figure 4-27 Evolution of the true stress (on the left) and the stress triaxiality (on the right) within the masked region during the uniaxial test – second approach. Mask size is 16 pixels by 16 pixels (0.264 mm x 0.264 mm).

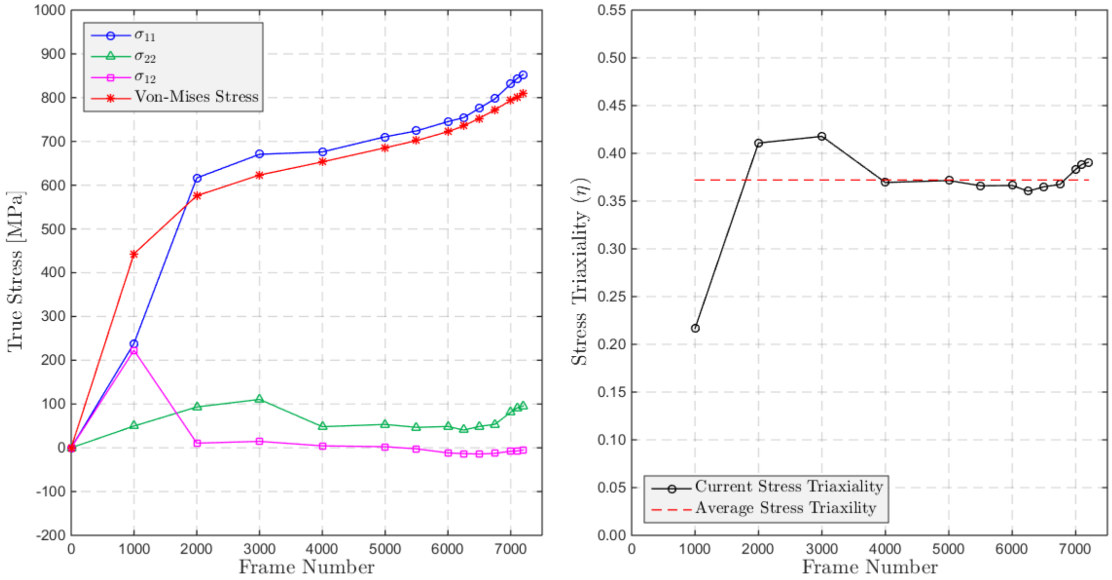

Figure 4-28 Evolution of the true stress (on the left) and the stress triaxiality (on the right) within the masked region during the uniaxial test – first approach. Mask size is 32 pixels by 32 pixels (0.528 mm x 0.528 mm).

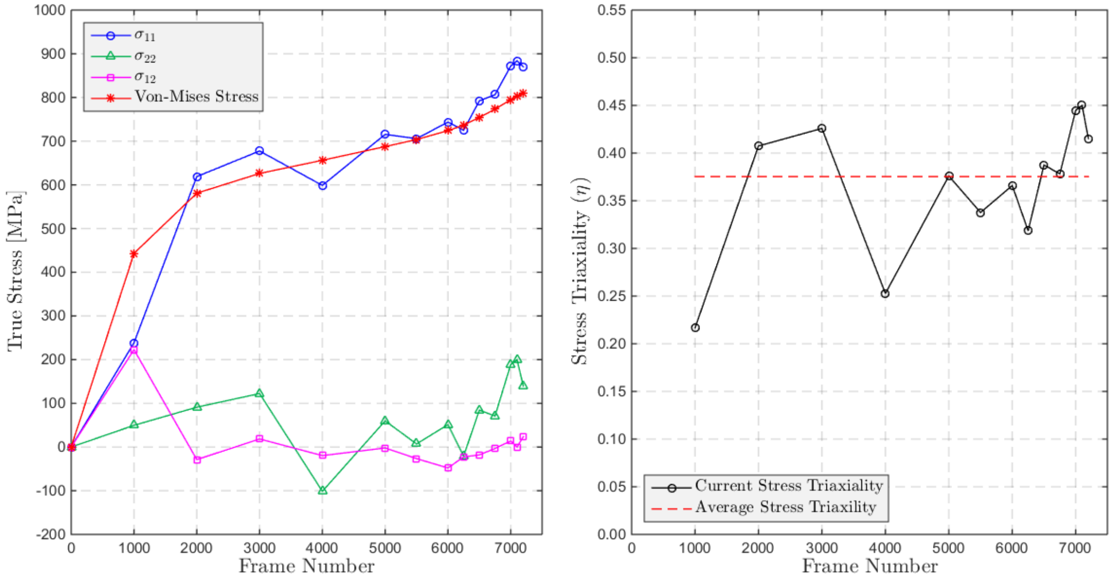

Figure 4-29 Evolution of the true stress (on the left) and the stress triaxiality (on the right) within the masked region during the uniaxial test – second approach. Mask size is 32 pixels by 32 pixels (0.528 mm x 0.528 mm).

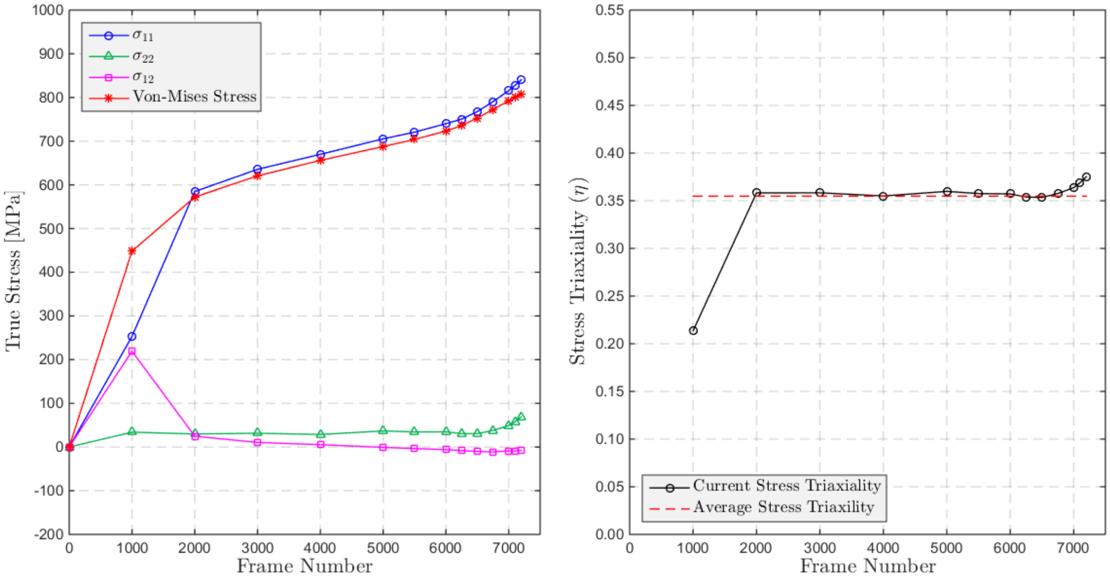

Figure 4-30 Evolution of the true stress (on the left) and the stress triaxiality (on the right) within the masked region during the uniaxial test – first approach. Mask size is 64 pixels by 64 pixels (1.056 mm x 1.056 mm).

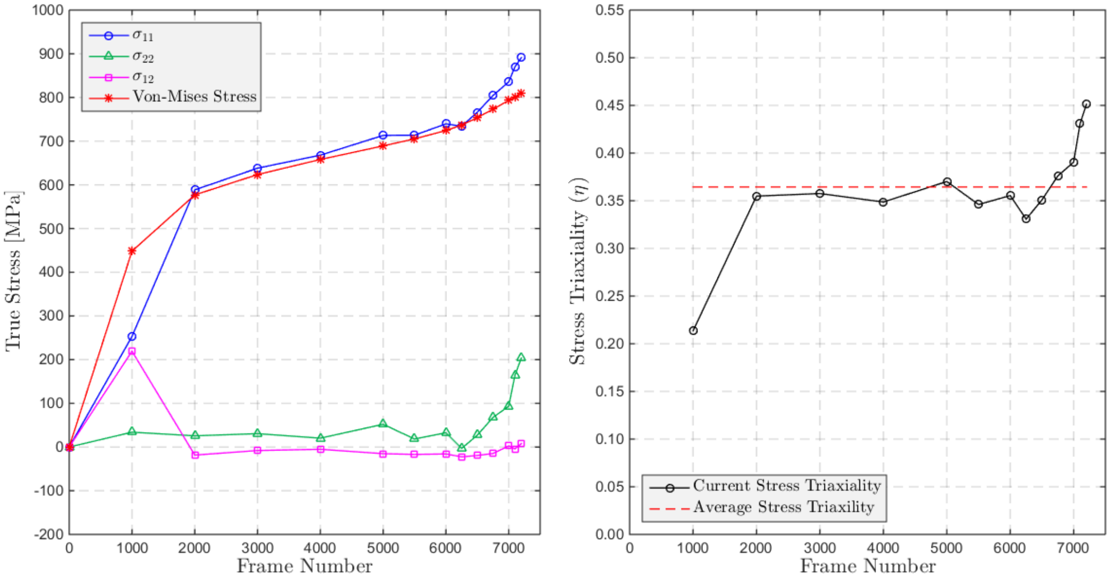

Figure 4-31 Evolution of the true stress (on the left) and the stress triaxiality (on the right) within the masked region during the uniaxial test – second approach. Mask size is 64 pixels by 64 pixels (1.056 mm x 1.056 mm).

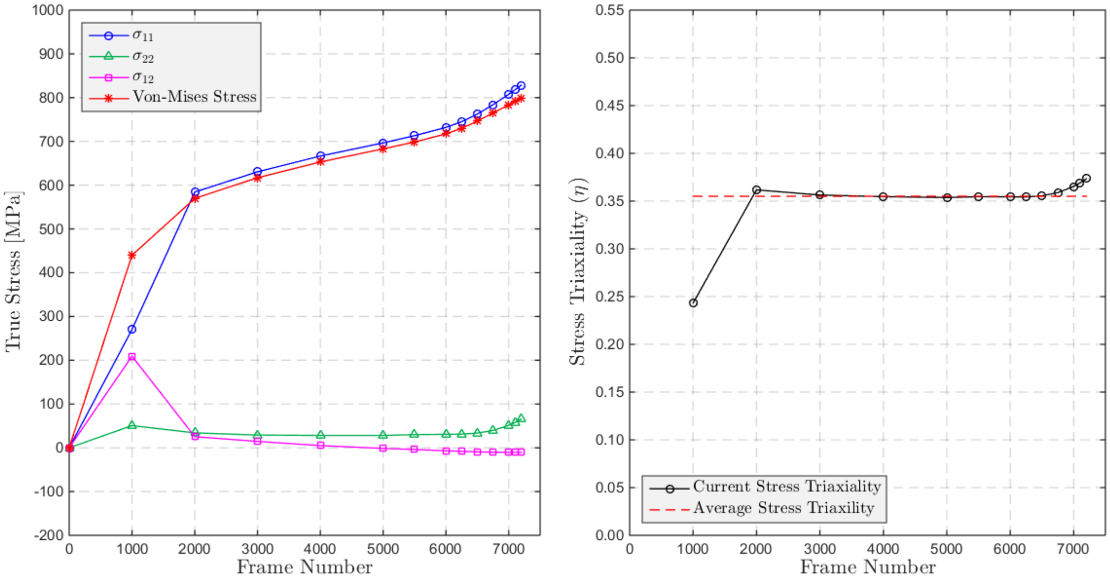

Figure 4-32 Evolution of the true stress (on the left) and the stress triaxiality (on the right) within the masked region during the uniaxial test – first approach. Mask size is 128 pixels by 128 pixels (2.112 mm x 2.112 mm).

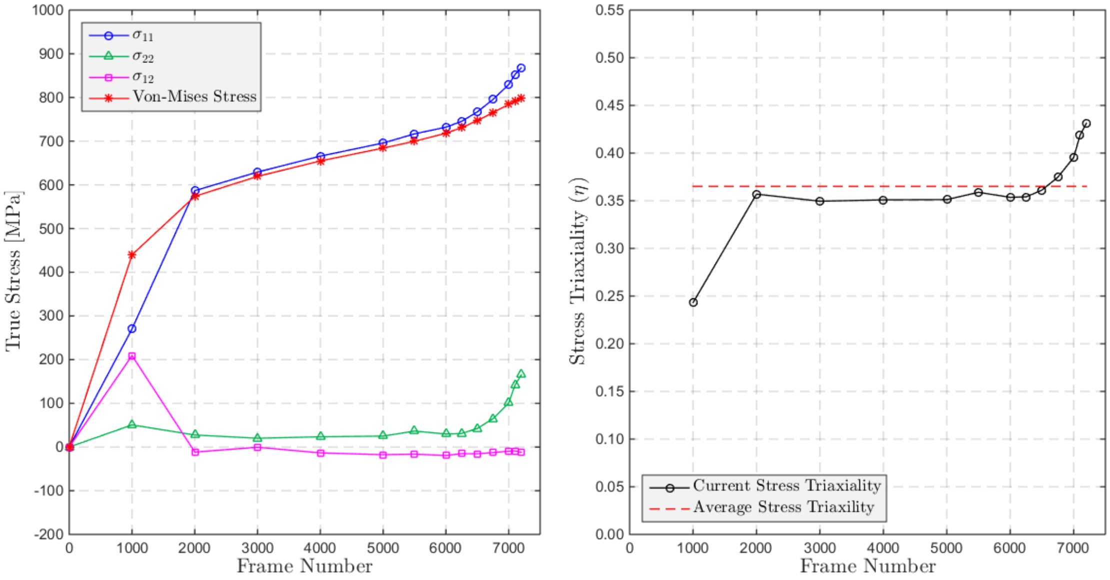

Figure 4-33 Evolution of the true stress (on the left) and the stress triaxiality (on the right) within the masked region during the uniaxial test – second approach. Mask size is 128 pixels by 128 pixels (2.112 mm x 2.112 mm).

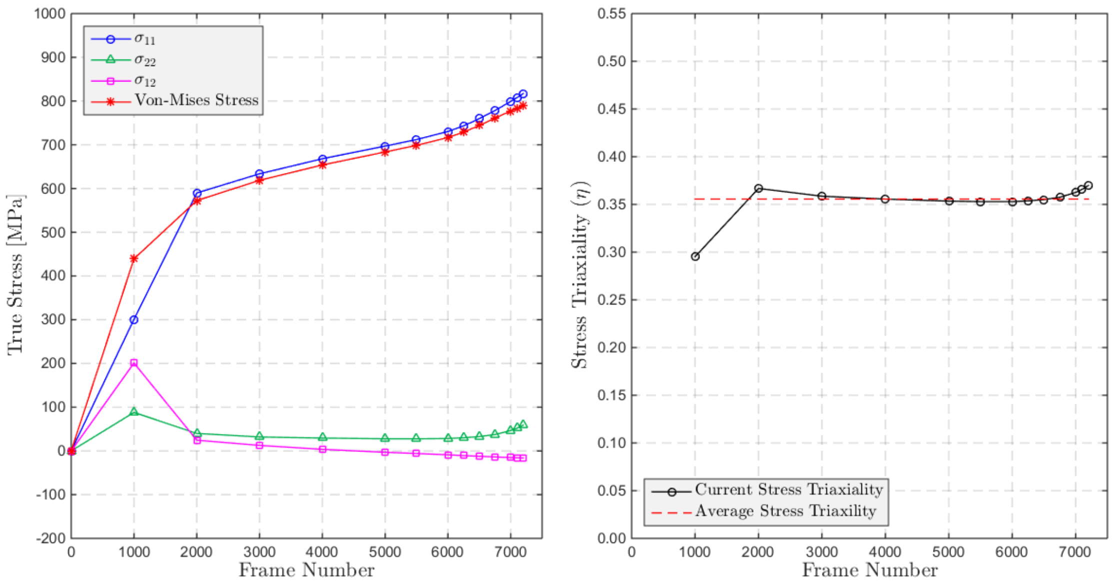

Figure 4-34 Evolution of the true stress (on the left) and the stress triaxiality (on the right) within the masked region during the uniaxial test – first approach. Mask size is 192 pixels by 192 pixels (3.168 mm x 3.168 mm).

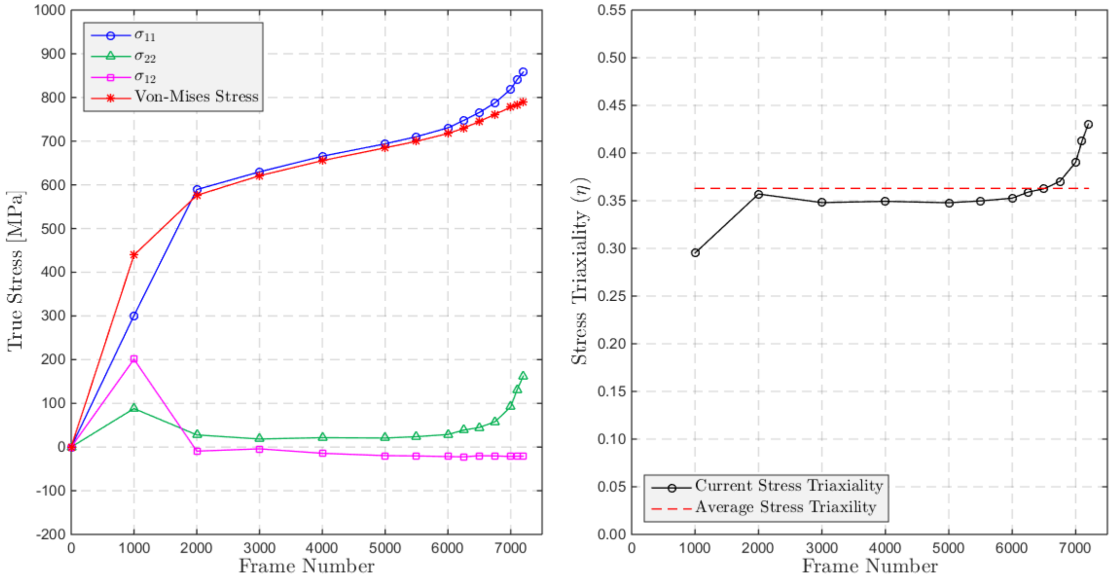

Figure 4-35 Evolution of the true stress (on the left) and the stress triaxiality (on the right) within the masked region during the uniaxial test – second approach. Mask size is 192 pixels by 192 pixels (3.168 mm x 3.168 mm).

It is interesting to note the stress fluctuations in the second approach at smaller mask sizes, which represent more local behavior. On the other hand, stress fluctuations vanish as more global behavior is followed; i.e., larger mask sizes. These fluctuations may be due to two occurrences: noise effects and/or plastic flow localization.

One cause for the stress fluctuations in the second approach may be due to very small strain increments[45], which might be influenced by the noise. However, the author does not believe that the noise plays a primary role in these fluctuations. If it were the case, the stress fluctuation in the second approach for larger mask sizes (128 pixels by 128 pixels and/or 192 pixels by 192 pixels, for example), where the strain increments are even smaller (compared to small mask sizes) as the strains are smaller, would be more pronounced. However, there is no fluctuation in the stress state (for the mask size of 128 pixels by 128 pixels and 192 pixels by 192 pixels) as can be seen in Figure 4-33 and Figure 4-35. On the other hand, a counter argument is that the noise is eliminated when the average of a larger area (i.e., larger mask sizes) is considered. If this were the case, there should have been fluctuations in the smaller mask sizes of the first approach as well. However, there are no fluctuations in the stress state (for the mask size of 16 pixels by 16 pixels and 32 pixels by 32 pixels) as can be seen in Figure 4-26 and Figure 4-28.

Therefore, the author believes that the stress fluctuations are primarily due to plastic flow localization[46] at the small scales/mask sizes. Having small or no stress and stress triaxiality deviations at larger mask sizes (see Figure 4-33 and Figure 4-35, for example), which are the representations of more global behavior, support this view. The reason that these fluctuations do not appear in the first approach is that the first approach is based on the current strain state; hence, the strain increments are sufficiently large such that small, instantaneous changes in the loading (especially at later stages) are not captured.

In addition to the analysis above, a very large mask size, 1024 pixels by 256 pixels (16.896 mm x 4.224 mm), is investigated to explore the behavior of the entire region. The size of the mask with respect to the specimen can be seen in Figure 4-36. The red square represents the 32 pixels by 32 pixels mask, whereas the blue rectangle represents the

---

[45] As the second approach is based on the increments from the previous state to the current state, the strain increments in this approach are much smaller compared to the first approach.

[46] The author's inference is inspired by the following quotation:
"Our calculations indicate that, as long as deviations from a constant triaxiality history are not too great, the onset of failure, when represented in a plot of stress triaxiality vs effective strain, is approximately represented by a single curve. However, significant deviations from this behavior can occur for nonproportional histories, with plastic flow localization playing an important role in this regard." (Needleman & Tvergaard, 1984)

1024 pixels by 256 pixels mask. The color difference within the specimen is due to the variation of lightning intensity and is obtained by DaVis LaVision software.

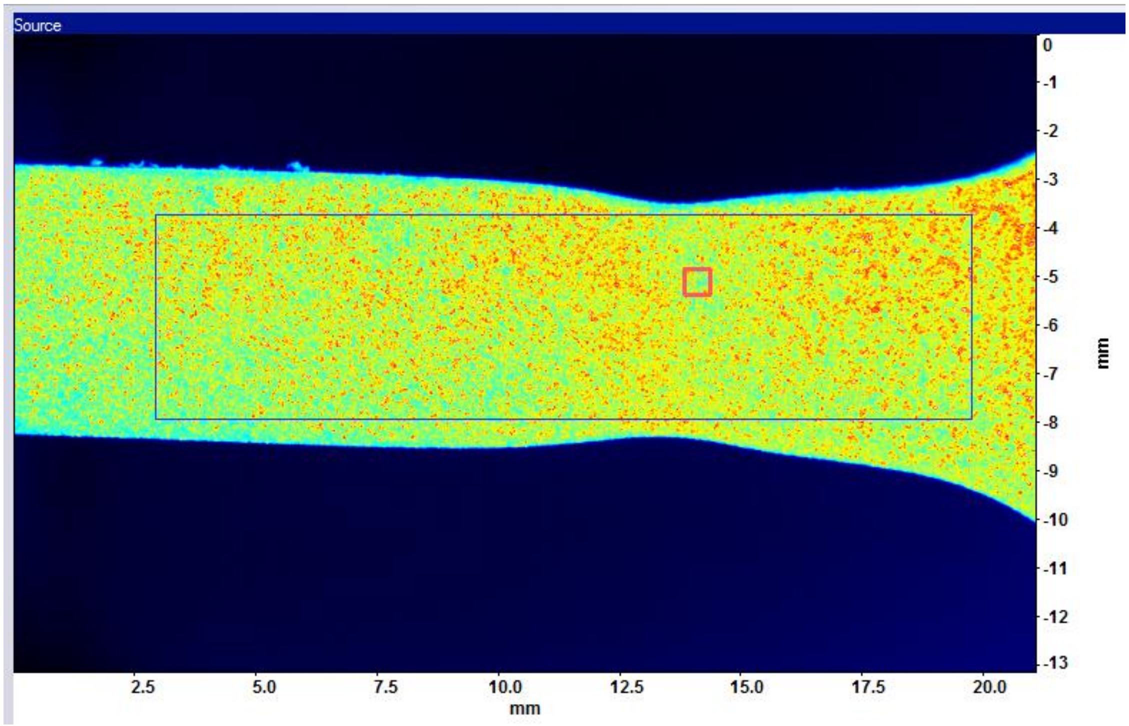

Figure 4-36 Demonstration of mask sizes: The red square represents the 32 pixels by 32 pixels mask, whereas the blue rectangle represents the 1024 pixels by 256 pixels mask. Pixel resolution is approximately 16.5 µm/pixel.

The evolution of the natural strain and the effective strain within the masked region during the uniaxial test for 1024 pixels by 256 pixel mask is presented in Figure 4-37. The shear strain remains zero or nearly zero until the initiation of fracture (i.e., Frame 7200), where the analysis was curtailed. Moreover, as the ratio of the strain increment in the transverse direction to the longitudinal direction is around -0.5 except for Frame 1000 and after Frame 7000 (i.e., it ranges between -0.51 and -0.46 between Frame 1000 and Frame 6750) the strain in the longitudinal direction overlaps the effective strain. Furthermore, it is worth noting that, beginning with Frame 1000, the slope of the strain curves in the longitudinal direction (ε_{11}) and those of the transverse direction (ε_{22}) remains nearly constant until Frame 5500, where it starts increasing slightly due to the onset of diffuse necking. The reason for this different behavior until Frame 1000 is that the specimen may still be in the elastic region and/or the elastic-plastic transition region. Considering that the Poisson's ratio of mild steel is around 0.30, and having a transverse strain to longitudinal strain ratio for different mask sizes varying between -0.39 and -0.25 (as provided in previous pages) supports this view. In fact, as can be seen in the stress-strain curve shown in Figure 4-44, the corresponding point of Frame 1000 lies on the elastic-plastic transition region.

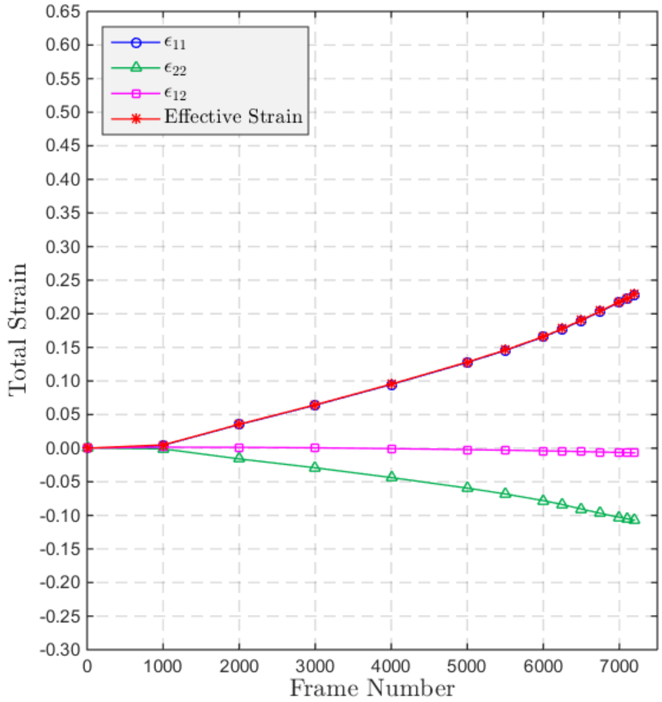

Figure 4-37 Evolution of the natural strain within the masked region during the uniaxial test – second approach. Mask size is 1024 pixels by 256 pixels (16.896 mm x 4.224 mm).

The evolution of the true stress (on the left) and the stress triaxiality (on the right) within the masked region for 1024 pixels by 256 pixels mask are shown in Figure 4-38 and Figure 4-39. The stress triaxiality at the initiation of the test (i.e., at Frame 1000) is higher than the theoretical stress triaxiality value of the uniaxial test, which is 1/3. Thereafter, it experiences a sudden decrease at Frame 2000 and remains nearly constant between Frame 2000 and Frame 6500, where it starts increasing, in the second approach. On the other hand, in the first approach, the stress triaxiality remains nearly constant until the initiation of fracture (i.e., Frame 7200). Note that the shear stress remains zero or nearly zero after Frame 2000. Moreover, the true stress curve of the first and the second approach have nearly the same quantitative behavior until Frame 6500, meaning that the global loading remains nearly proportional until the later stages of the test.

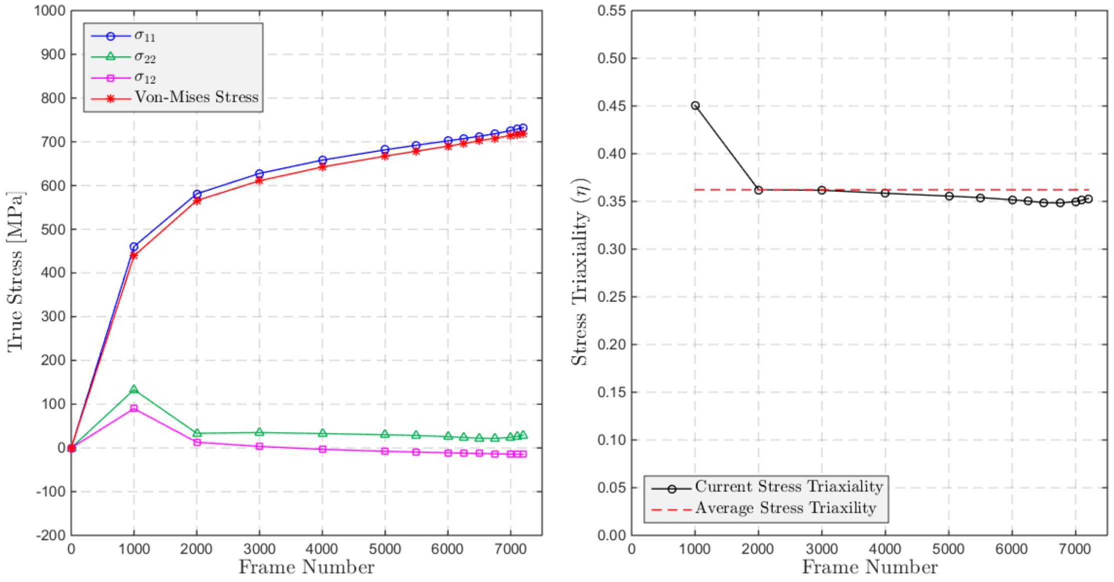

Figure 4-38 Evolution of the true stress (on the left) and the stress triaxiality (on the right) within the masked region during the uniaxial test – first approach. Mask size is 1024 pixels by 256 pixels (16.896 mm x 4.224 mm).

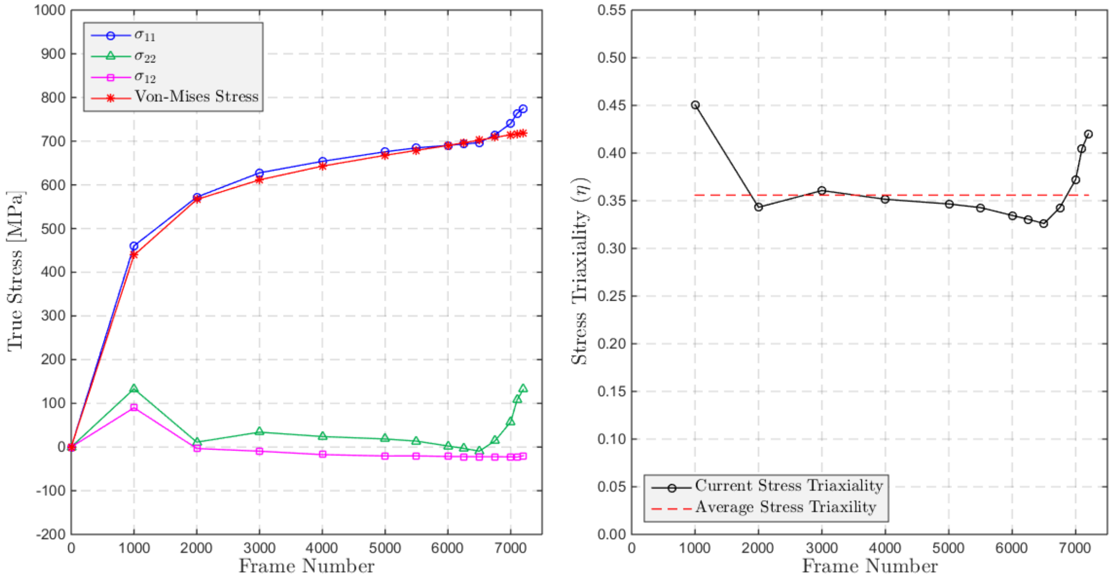

Figure 4-39 Evolution of the true stress (on the left) and the stress triaxiality (on the right) within the masked region during the uniaxial test – second approach. Mask size is 1024 pixels by 256 pixels (16.896 mm x 4.224 mm).

The uni-directional stress-strain curve (σ_{11} curve) nearly overlaps the effective stress-strain curve (Von-Mises stress curve) until the initiation of fracture (i.e., Frame 7200) in the first approach, whereas this overlap remains only until the later stages of the test (i.e., until Frame 6500) in the second approach due to the development of the transverse stress

(σ_{22}). The maximum difference (with respect to uni-directional stress) in the first approach is 4.7% (which occurs at Frame1000), while it is 7.2% in the second approach (which occurs at Frame 7200). In other words, the uni-directional stress-strain curve is in fairly good agreement with the effective stress-strain curve in both approaches. Therefore, a global uni-directional stress-strain curve may be a fairly good representation of the global effective stress-strain curve, which is a general assumption in obtaining stress-strain curves of materials (through a conventional uniaxial test), when the gauge length is sufficiently large compared to the localization zone. Nevertheless, it is worth noting that global strains obtained by a conventional uniaxial test may not represent the actual strains in the localized zone, as presented in the following pages.

The evolution of the longitudinal strain (ε_{11}) and the transverse strain (ε_{22}) for different mask sizes are presented in Figure 4-40 and Figure 4-41, respectively. Both the transverse strain and the longitudinal strain are moderately affected by the mask size and the effect of mask size is more pronounced especially at later stages of the experiment. For example, the strain difference between the smallest and the largest mask size (with respect to the largest mask size) at the initiation of fracture (i.e., at Frame 7200) is 22.5% for the transverse strain, whereas it is 26.7% for the longitudinal strain. Thus, having different longitudinal and transverse strains for different mask sizes demonstrates that the strain is not exactly uniform within the neck region at the initiation of fracture. However, it is worth noting that the percentages mentioned above are the maximum differences and that they are lower in the previous stages of the experiment. Hence, uniform longitudinal strain and/or uniform transverse strain assumptions may be reasonable depending on what stage of the uniaxial test is under consideration.

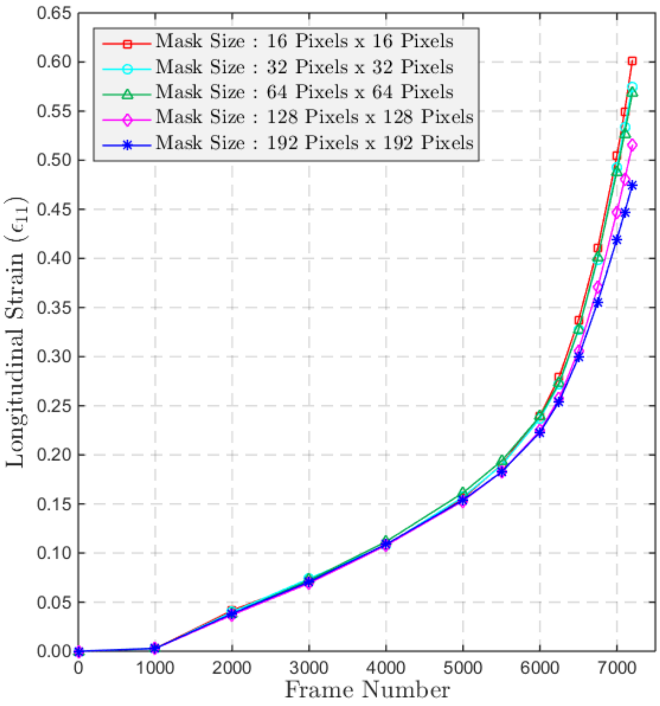

Figure 4-40 Evolution of the longitudinal strain within the masked region during the uniaxial test for different mask sizes – second approach. Pixel resolution is approximately 16.5 µm/pixel.

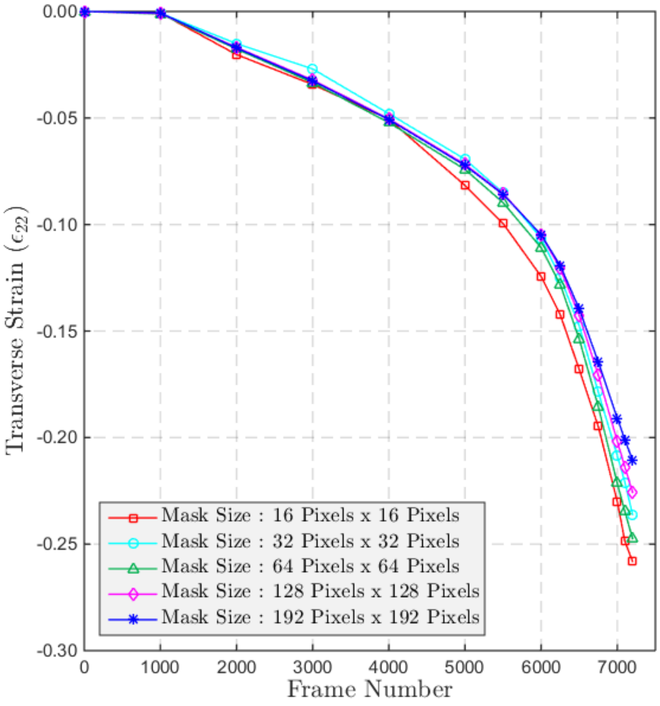

Figure 4-41 Evolution of the transverse strain within the masked region during the uniaxial test for different mask sizes – second approach. Pixel resolution is approximately 16.5 µm/pixel.

The evolution of the effective strain for the six scales studied from the results of this particular experiment is presented in Figure 4-42. Effective strains for all mask sizes (except 1024 pixels by 256 pixels) nearly overlap until about Frame 5000 and then separation becomes clearer around Frame 5500, where diffuse necking starts. The most prominent feature of the figure as the experiment progresses is the increasing difference between the 1024 pixels by 256 pixels mask and the rest of the mask sizes. This difference (with respect to 1024 pixels by 256 pixels) at the initiation of fracture (i.e., at Frame 7200) reaches 109% for the 192 pixels by 192 pixels mask and 168% for the 16 pixels by 16 pixels mask. Therefore, global strains obtained by a conventional uniaxial test may not represent the actual strains in the localized zone, as expected. Moreover, it is worth noting that as the 64 pixels by 64 pixels mask and the 32 pixels by 32 pixels mask nearly overlap, a false convergence behavior would be interpreted if 16 pixels by 16 pixels mask were not analyzed.

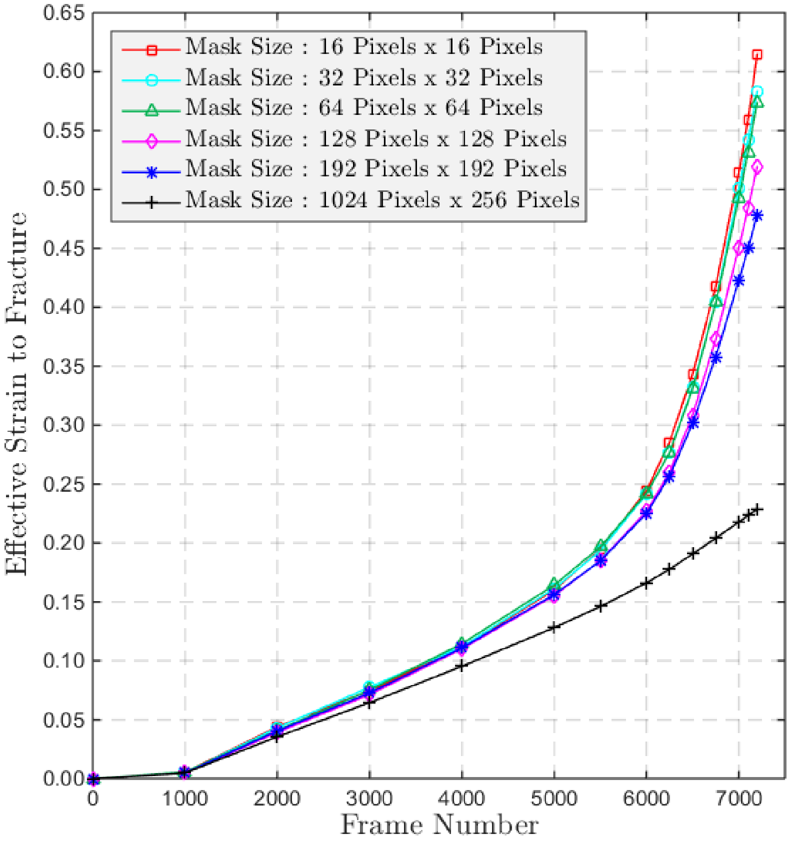

Figure 4-42 Evolution of the effective strain within the masked region during the uniaxial test for different mask sizes – second approach. Pixel resolution is approximately 16.5 μm/pixel.

The effect of mask size on failure strain is shown in Figure 4-43. As it was not a square mask, the result of the 1024 pixels by 256 pixels mask is not included in the figure. Interestingly, if the result of the 32 pixels by 32 pixels mask were excluded, the other four points nearly fit a linear curve. Moreover, as can be seen in the figure and as mentioned above, a false convergence would be interpreted if the analyses were limited to a minimum of 32 pixels by 32 pixels. Therefore, convergence behavior likely needs to be verified by multiple mask sizes.

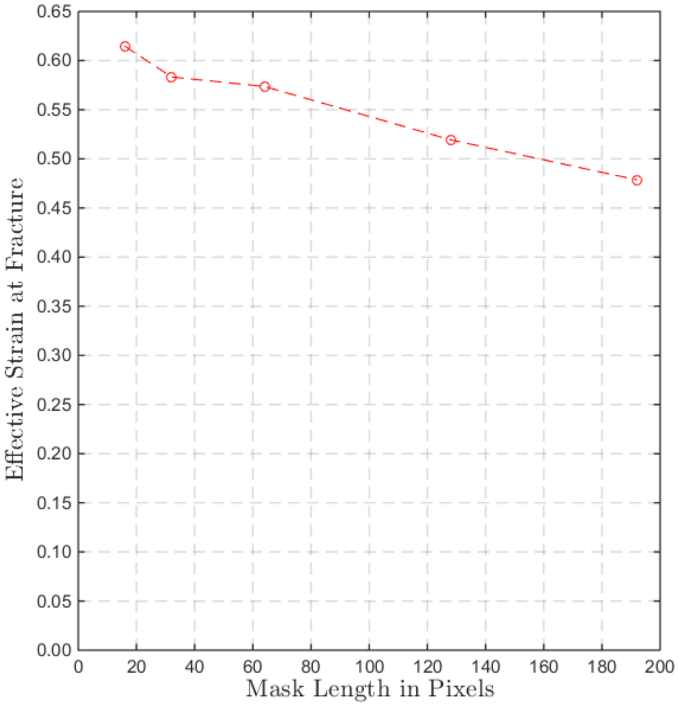

Figure 4-43 Effect of mask size on failure strain during the uniaxial test – second approach. The dashed line is a linear curve between two data points. Pixel resolution is approximately 16.5 µm/pixel.

The average stress triaxiality (η_{ave}), the stress triaxiality at fracture (η_{frac}), and the effective strain at fracture (ε_{eff}^{f}) for both approaches are summarized in Table 4-1. The effective strain at fracture increases as the mask size is decreased, a sign of localization. Moreover, while the stress triaxiality at fracture increases as the mask size is decreased (with the exception of 32 pixels by 32 pixels mask), the average stress triaxiality exhibits no particular order regarding the mask size.

Table 4-1 Summary of the average stress triaxiality (η_{ave}), the stress triaxiality at fracture (η_{frac}), and the effective strain at fracture (ε_{eff}^{f}) for the uniaxial test of 6mm-width specimen without groove with a test speed of 0.2 inch/second.

	Mask size [pixels]	η_{ave}	η_{frac}	ε_{eff}^{f}
First approach	16x16	0.340	0.379	0.603
	32x32	0.372	0.391	0.577
	64x64	0.355	0.375	0.570
	128x128	0.355	0.373	0.516
	192x192	0.356	0.370	0.476
	1024x256	0.362	0.353	0.228
Second approach	16x16	0.364	0.513	0.615
	32x32	0.375	0.415	0.583
	64x64	0.364	0.451	0.574
	128x128	0.365	0.431	0.519
	192x192	0.363	0.430	0.479
	1024x256	0.356	0.420	0.229

As can be seen from Table 4-1, the maximum difference between the effective strain at fracture for two different approaches is 2.0%, which occurs on the smallest mask size.

Finally, the true stress-strain curves for different mask sizes are presented together in Figure 4-44. Note that the flow rule and the power-law hardening relationship (with $\Omega = 868.4$ MPa and $n = 0.128$) are used to obtain the components of the stress tensor (see Section 4.4.2 for details) of the DIC analysis. In addition, the stress-strain curve obtained via the MTS machine is superposed on the same figure for comparison purposes[47]. Solid lines with markers are obtained by the digital image correlation analysis, while dashed lines are the results of the uniaxial test with the MTS machine. Note that the DIC analyses are conducted to the point of fracture initiation. Therefore, the last marker of each color represents the fracture initiation point for different mask sizes.

---

[47] The author is aware that although a uni-directional stress-strain curve (i.e., the stress-strain curve obtained via an MTS machine) may be the correct representation of the effective stress-strain curve in a global manner (when the gauge length is sufficiently large compared to the localization zone), it may not correctly reflect the actual strains in the localized zone as can be seen in Figure 4-42. A uniaxial test with a strain-gauge extensometer and a high speed camera recording simultaneously would provide better comparative results; however, that experiment was not conducted.

Fairly good agreement between the hardening part of the MTS uniaxial test result and the DIC analysis demonstrates that the power-law hardening relationship with calculated hardening parameters $\Omega = 868.4\, MPa$ and $n = 0.128$ fits reasonably well for this specific material. However, as the power-law hardening relationship is used to obtain the stress state in the DIC analysis, stress-strain curves of the DIC analysis cannot capture the softening. Finally, it is worth noting that the effective stress-strain curve is independent of the mask size, as expected, as the plastic constitutive and stress-strain relationships that are used (the hardening-law and the flow rule) are independent of a length scale.

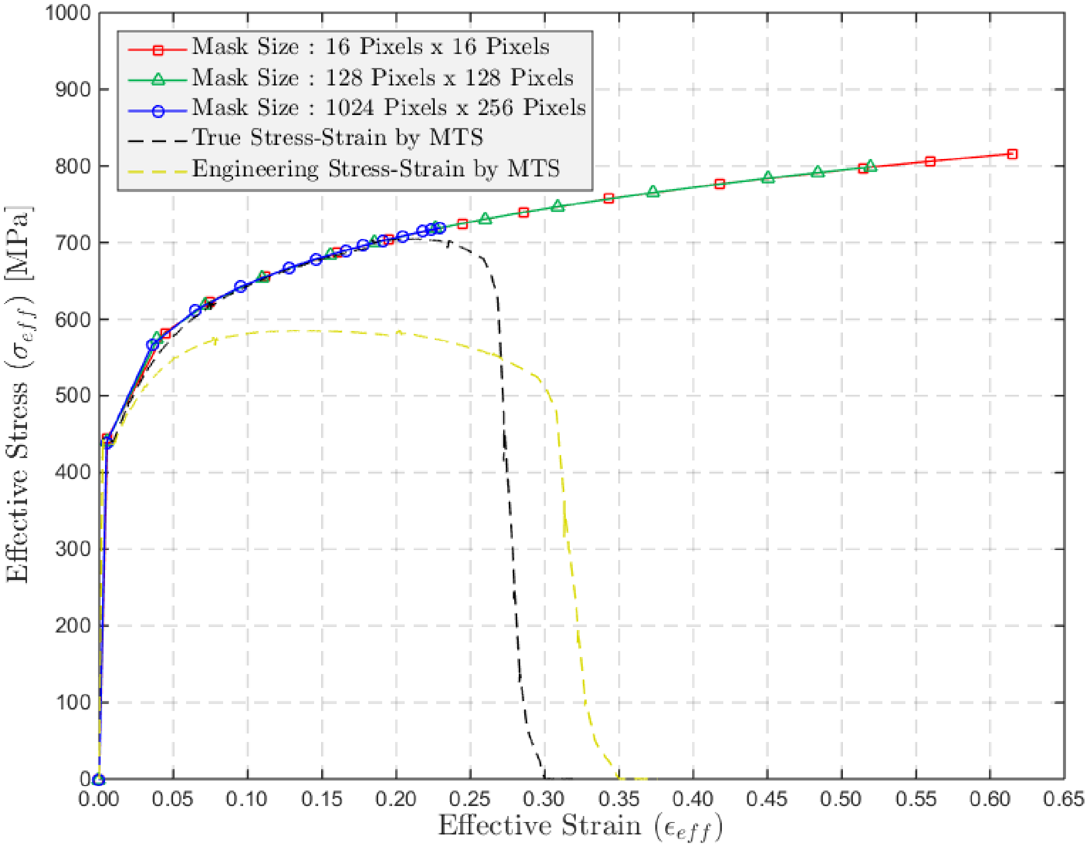

Figure 4-44 True stress-strain curve of the uniaxial test for different mask sizes – second approach. Pixel resolution is approximately 16.5 µm/pixel. Solid lines with markers are obtained by digital image correlation (DIC) analysis while dashed lines are the results from the MTS machine.

4.5.1.2 Test 2

This specimen has the same mid-region geometry as the one presented in the previous sub-section (see Figure 4-13 and Figure 4-14). The only difference is that this test specimen was obtained by in-house machining of a 1in-width specimen (without groove), while the one presented in the previous sub-section was obtained by in-house machining of a 18mm-width specimen (without groove). This test specimen with the experimental set-up can be seen in Figure 4-3. The width of the specimen was reduced to capture the entire mid-region (during imaging) with a similar pixel resolution as the other specimens.

A test speed of 0.4 inch/second was applied to the end of the test specimen with 6000 digital images recorded per second for this experiment. The pixel resolution is approximately 16.3 microns per pixel. Note that the high speed camera and the experimental device were snychronized in this experiment.

Fracture initiates around Frame 3350; that is, following an approximately 5.673 mm horizontal displacement. Note that this displacement is slightly lower than the one obtained for the low speed test, presented in the previous sub-section.

DIC analyses are conducted for three different mask sizes, that is, the 16 pixel by 16 pixel mask (the smallest mask size), the 32 pixels by 32 pixels mask and the 128 pixels by 128 pixels mask. Results are summarized in Table 4-2.

Table 4-2 Summary of the average stress triaxiality (η_{ave}), the stress triaxiality at fracture (η_{frac}), and the effective strain at fracture (ε_{eff}^{f}) for the uniaxial test of 6mm-width specimen without groove with a test speed of 0.4 inch/second.

	Mask size [pixels]	η_{ave}	η_{frac}	ε_{eff}^{f}
First approach	16x16	0.360	0.390	0.520
	32x32	0.353	0.357	0.458
	128x128	0.346	0.361	0.454
Second approach	16x16	0.371	0.420	0.533
	32x32	0.344	0.404	0.466
	128x128	0.354	0.424	0.458

As can be seen from Table 4-1 and Table 4-2, the fracture strain is lower at the high strain rate test for both mask sizes investigated. Although more data are required to reach a more solid conclusive trend, one of the reasons for the smaller fracture strain is that the test specimen at high strain rate has a slightly lower displacement to fracture.

4.5.2 Analysis of 1in-Width Specimen with Semi-Circular Groove

The isometric view and technical drawing of the test specimen are depicted in Figure 4-45 and Figure 4-46, respectively.

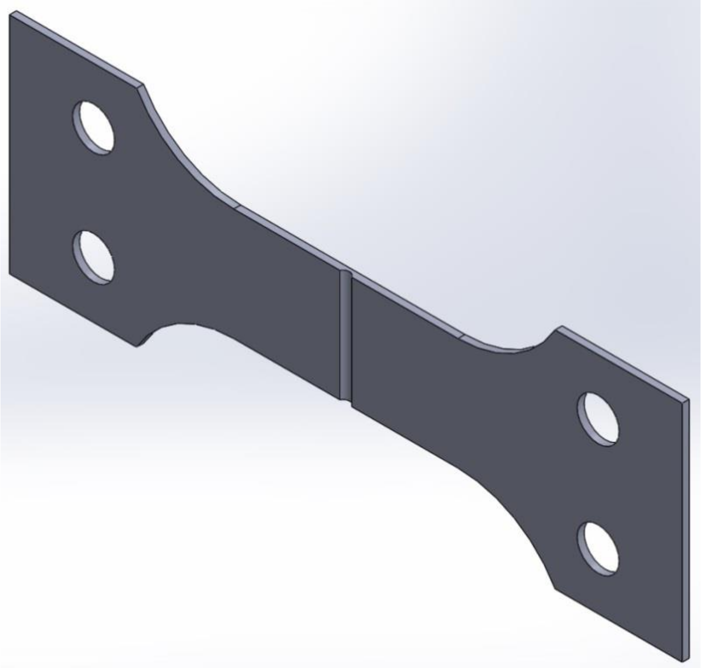

Figure 4-45 Isometric view of the 1in-width specimen with semi-circular groove (Courtesy of James Gose).

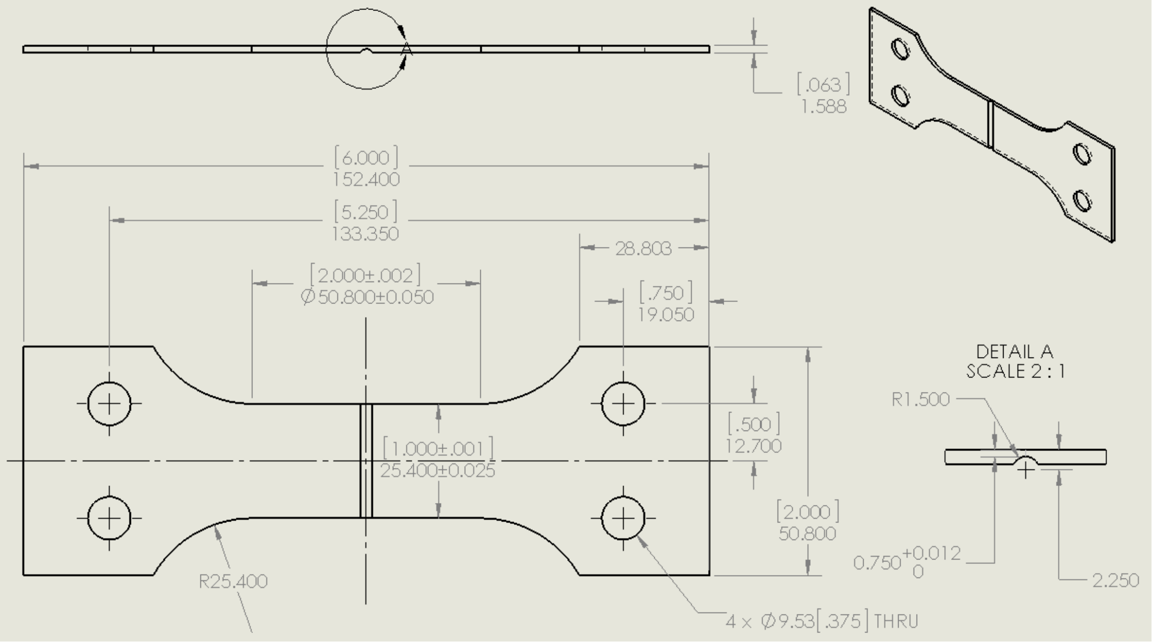

Figure 4-46 Technical drawing of the 1in-width specimen with semi-circular groove (Courtesy of James Gose).

The load/displacement was applied rapidly by hand with 7500 digital images recorded per second for this experiment. The test speed may not be constant as the load was applied by hand. The back side of the specimen was the recorded region because the groove and non-groove regions on the front side were not able to be captured simultaneously due to depth of field constraint of the camera-lens system. The pixel resolution is approximately 15.3 microns per pixel. Note that the high speed camera and the experimental device were not snychronized in this experiment. A very small lag in the recording might thus be possible.

Frames from the video recording are presented in Figure 4-47, Figure 4-48, Figure 4-49, Figure 4-50, Figure 4-51, Figure 4-52, and Figure 4-53. The vertical direction and the horizontal direction are the width direction and the longitudinal direction of the specimen, respectively. The regions depicted are the exploded views and their dimensions are approximately 895–925 pixels by 520–550 pixels.

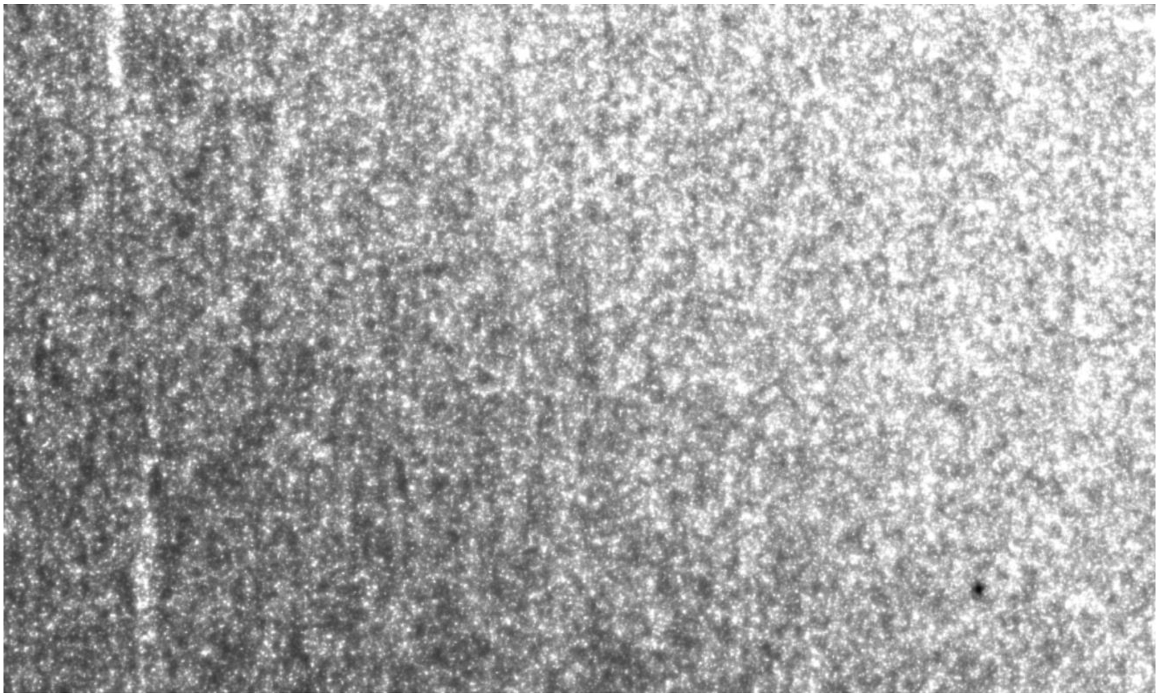

Figure 4-47 Nital etched AH32 steel 1in-width-specimen with semi-circular groove at Frame 0, that is, in the undeformed state.

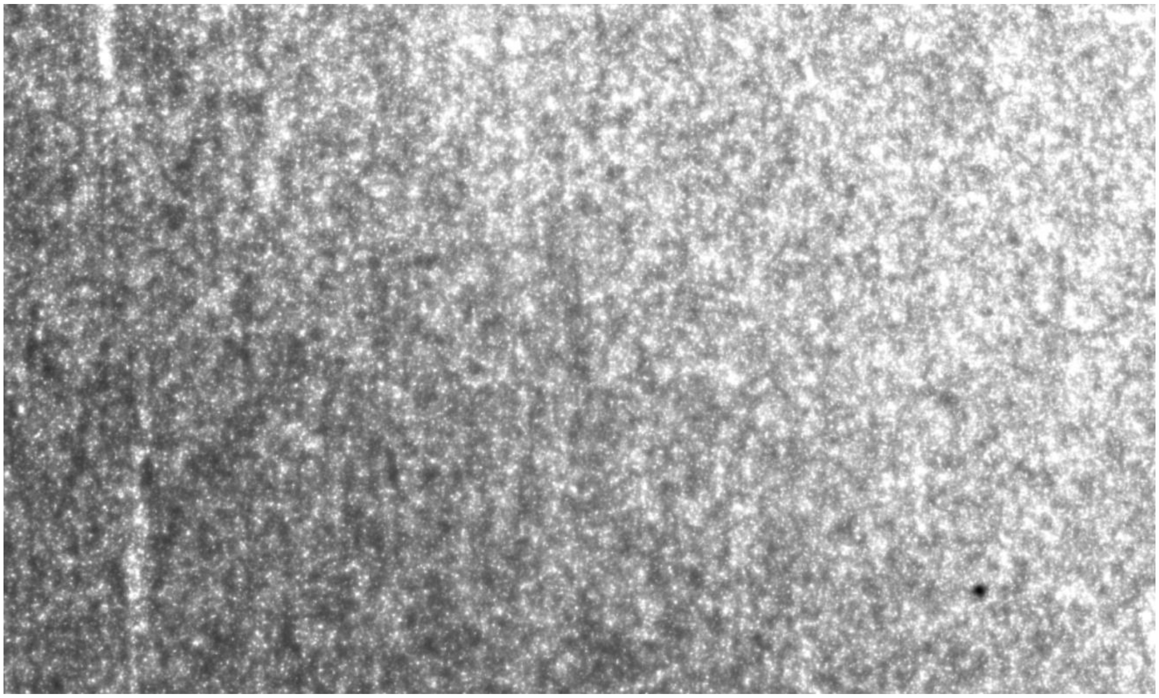

Figure 4-48 Nital etched AH32 steel 1in-width-specimen with semi-circular groove at Frame 5000.

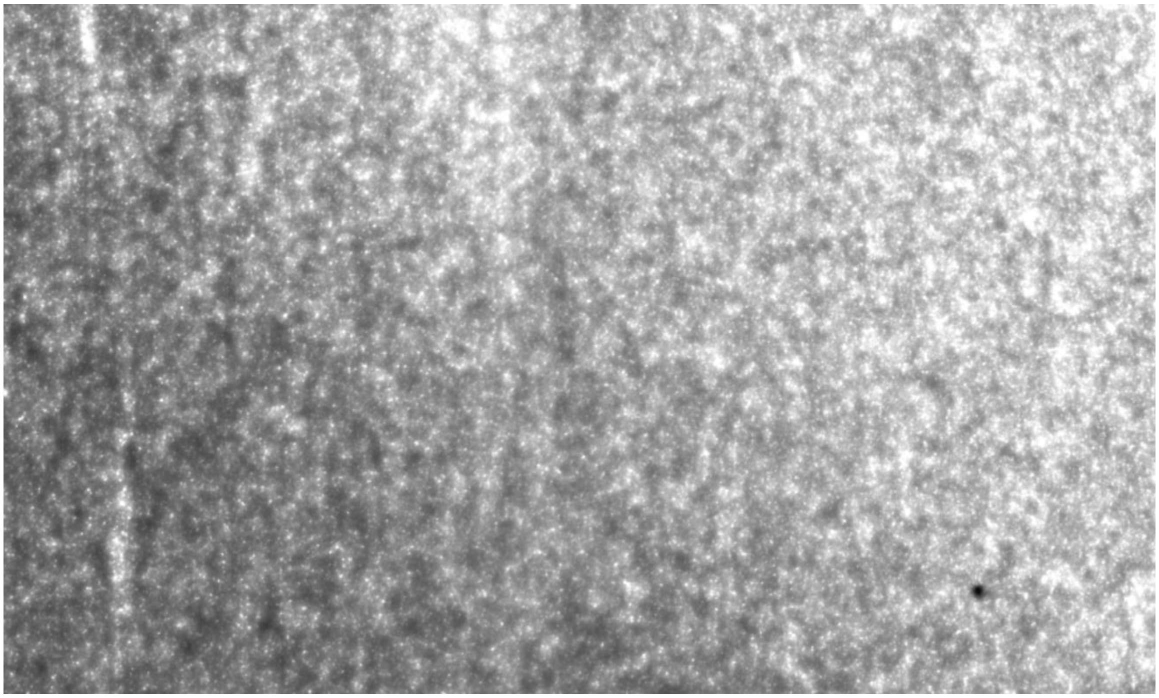

Figure 4-49 Nital etched AH32 steel 1in-width-specimen with semi-circular groove at Frame 10000.

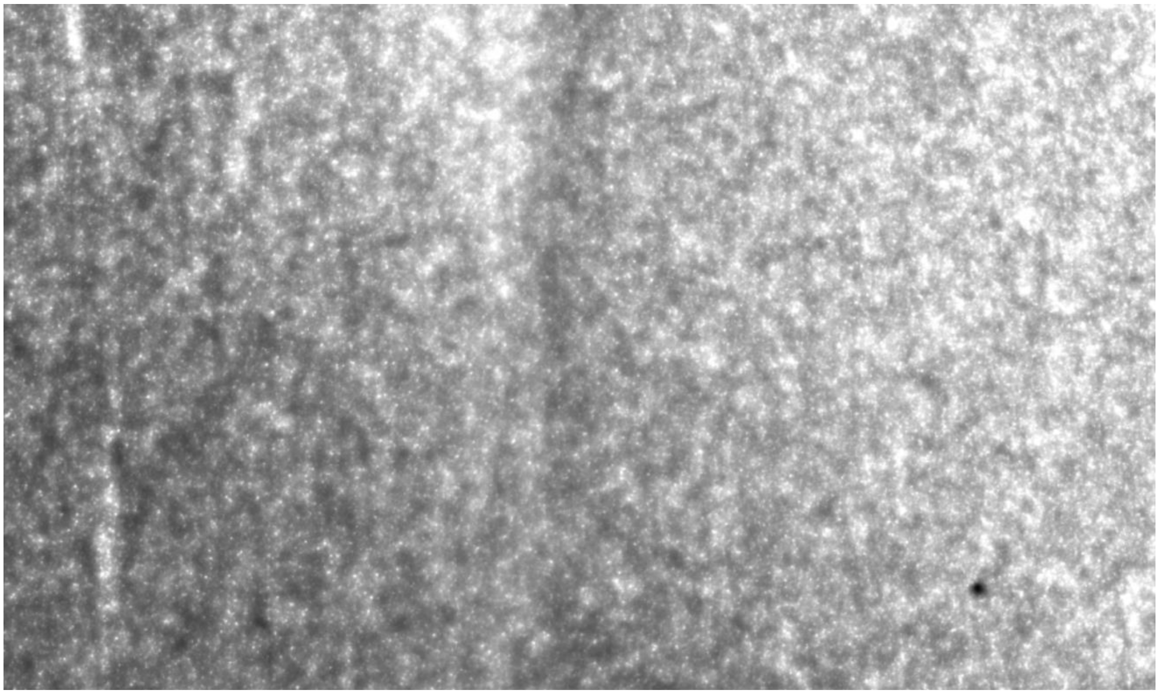

Figure 4-50 Nital etched AH32 steel 1in-width-specimen with semi-circular groove at Frame 13000.

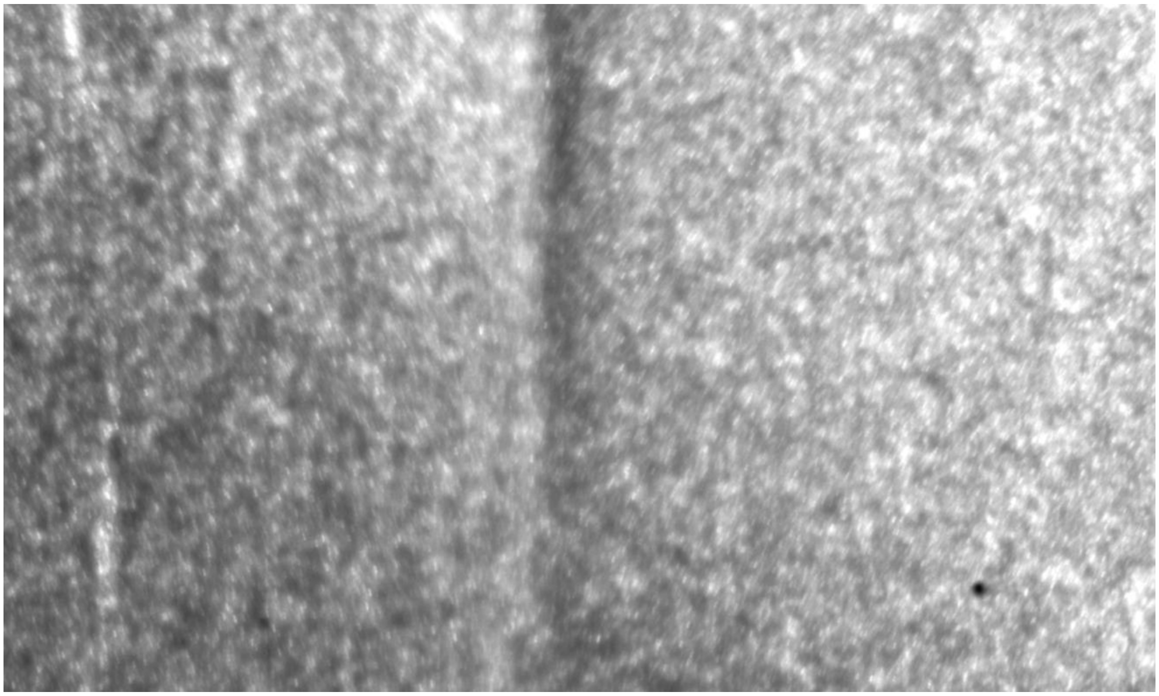

Figure 4-51 Nital etched AH32 steel 1in-width-specimen with semi-circular groove at Frame 13894.

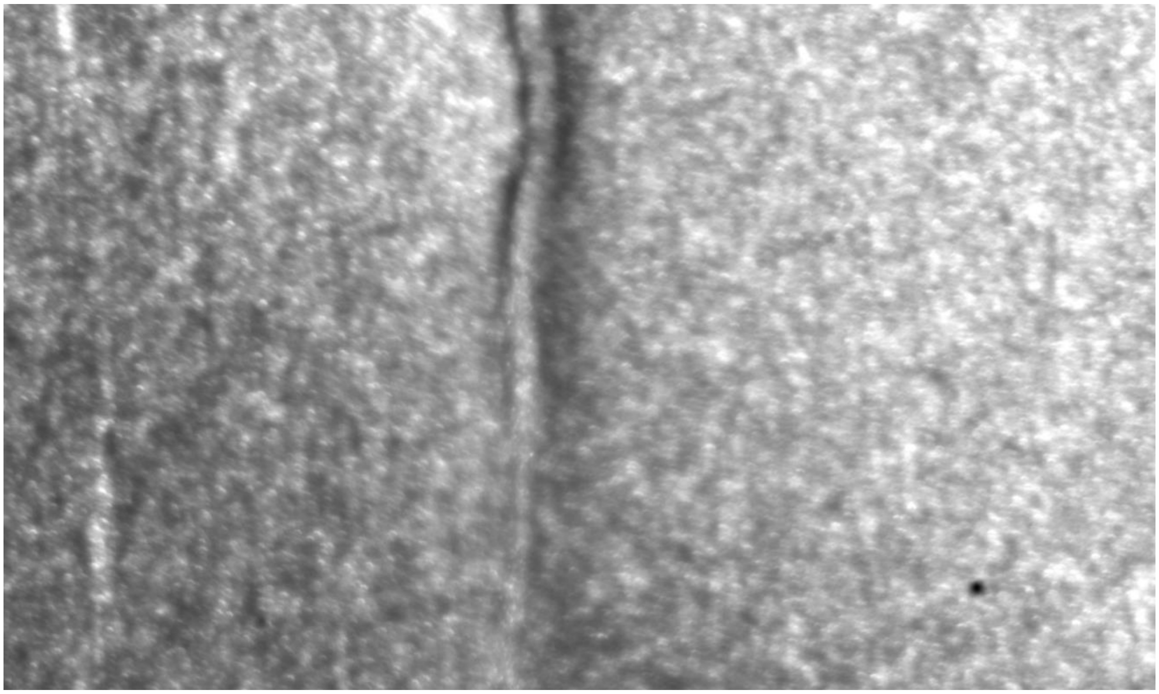

Figure 4-52 Nital etched AH32 steel 1in-width-specimen with semi-circular groove at Frame 13895.

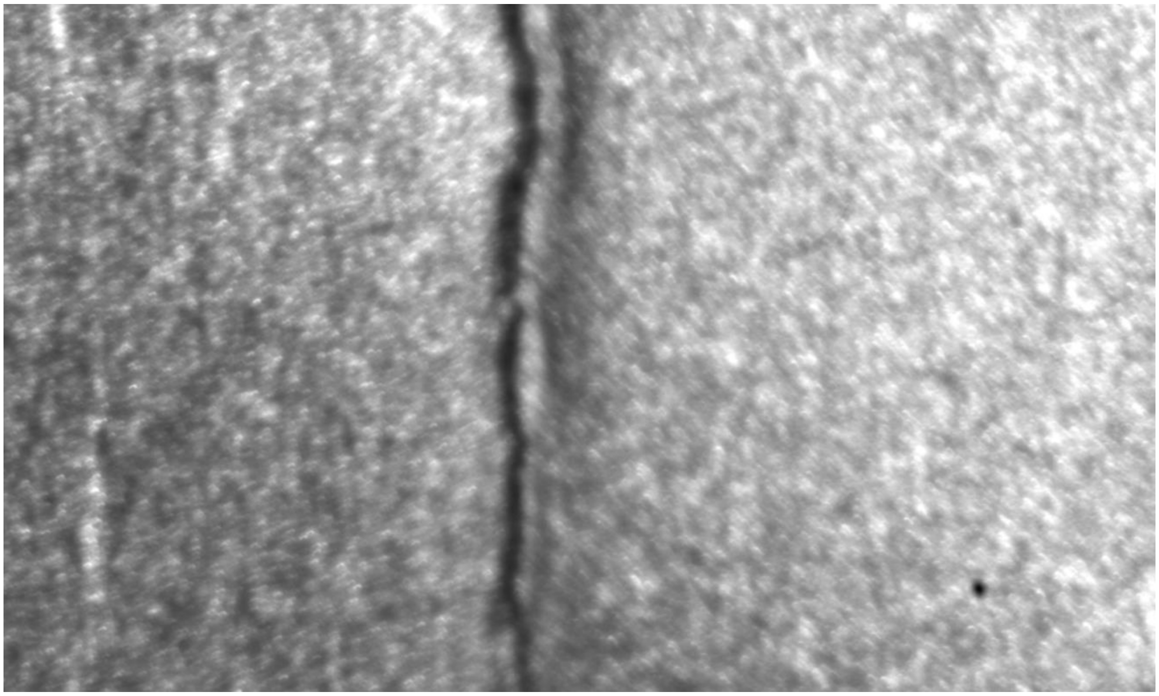

Figure 4-53 Nital etched AH32 steel 1in-width-specimen with semi-circular groove at Frame 13896.

Fracture initiates around Frame 13893 and the initial crack can clearly be seen at Frame 13894, depicted in Figure 4-51. Moreover, final stages of the crack propagation are presented in Figure 4-52 and Figure 4-53.

The effect of mask size on failure strain is presented in Figure 4-54. The analytical relationship depicted in the figure was proposed by Li & Karr (2009). They found the effect of length scale on the fracture strain to be of the form[48]:

$$y = \ln(a/x + b) \tag{4-45}$$

where x represents the length scale and y represents the fracture strain. Note that the material parameters a and b were determined by a best fit of the experimental results[49]. As can be seen from the figure, there was no sign of convergence of the results as the length scales were reduced.

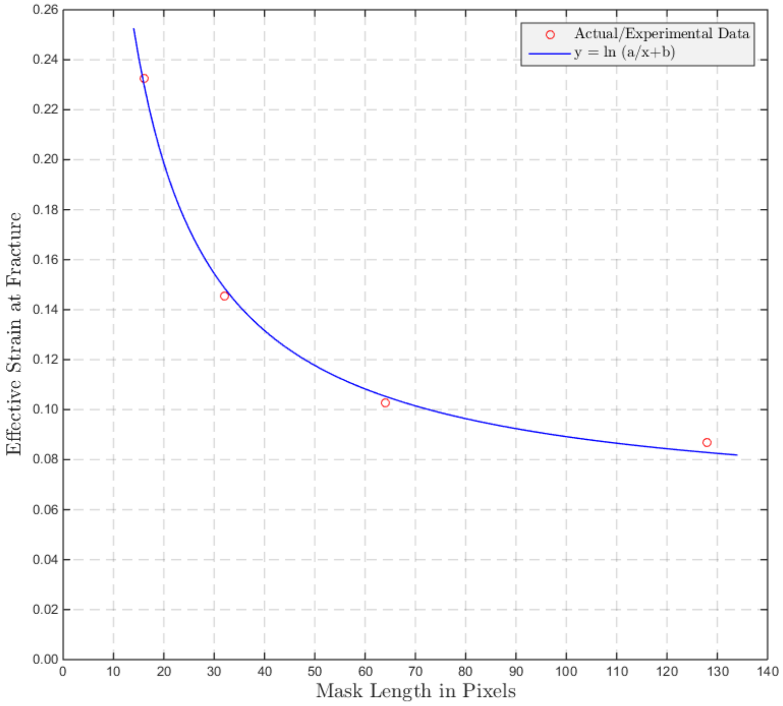

Figure 4-54 Effect of the mask size on failure strain during the the uniaxial test of the 1in-width specimen with semi-circular groove with $y = \ln(a/x + b)$ curve fit – second approach. $a = 3.160$ and $b = 1.062$. Pixel resolution is approximately 15.3 μm/pixel.

---

[48] They obtained this expression by modeling the uniaxial tension test as an 'idealized three-piece-model' (see Figure 1 of Li & Karr, 2009) and by assuming that the fracture occurs at the bifurcation point (see "Equation 22" of the cited reference). Note that the bifurcation of a uniaxial tension test occurs at the onset of diffuse necking. However, as the authors pointed out:
"Eq. (22), derived from the three piece model in section 3, is also evidently applicable to continuum plasticity finite element models of structural elements"

[49] See "Equation 23" and "Equation 24" of Li & Karr (2009) for the definition of parameters a and b.

The average stress triaxiality (η_{ave}), the stress triaxiality at fracture (η_{frac}), and the effective strain at fracture (ε_{eff}^{f}) for both approaches are summarized in Table 4-3.

Table 4-3 Summary of the average stress triaxiality (η_{ave}), the stress triaxiality at fracture (η_{frac}), and the effective strain at fracture (ε_{eff}^{f}) for the uniaxial test of the 1in-width specimen with semi-circular groove.

	Mask size [pixels]	η_{ave}	η_{frac}	ε_{eff}^{f}
First approach	16x16	0.512	0.474	0.172
	32x32	0.557	0.590	0.123
	64x64	0.424	0.539	0.094
	128x128	0.477	0.547	0.085
Second approach	16x16	0.369	0.327	0.233
	32x32	0.521	0.622	0.145
	64x64	0.519	0.577	0.103
	128x128	0.530	0.584	0.087

As can be seen from Table 4-3, the maximum difference between the effective strain at fracture for the two different approaches is 26.2%, which occurs on the smallest mask size.

4.5.3 Analysis of Shear Specimen

The isometric view and technical drawing of the shear test specimen are depicted in Figure 4-55 and Figure 4-56, respectively. Note that this design is adapted from Bao & Wierzbicki's (2004) specimen design for pure shear tests.

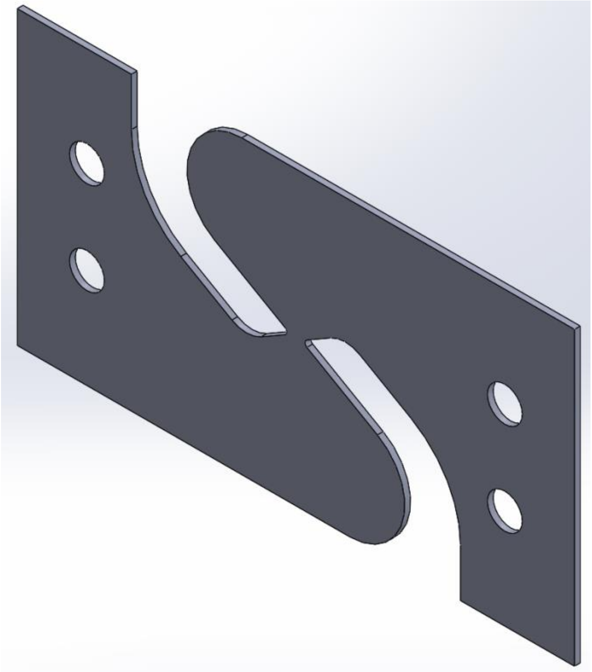

Figure 4-55 Isometric view of the shear specimen (Courtesy of James Gose). This design is adapted from Bao & Wierzbicki's (2004) specimen design for pure shear tests.

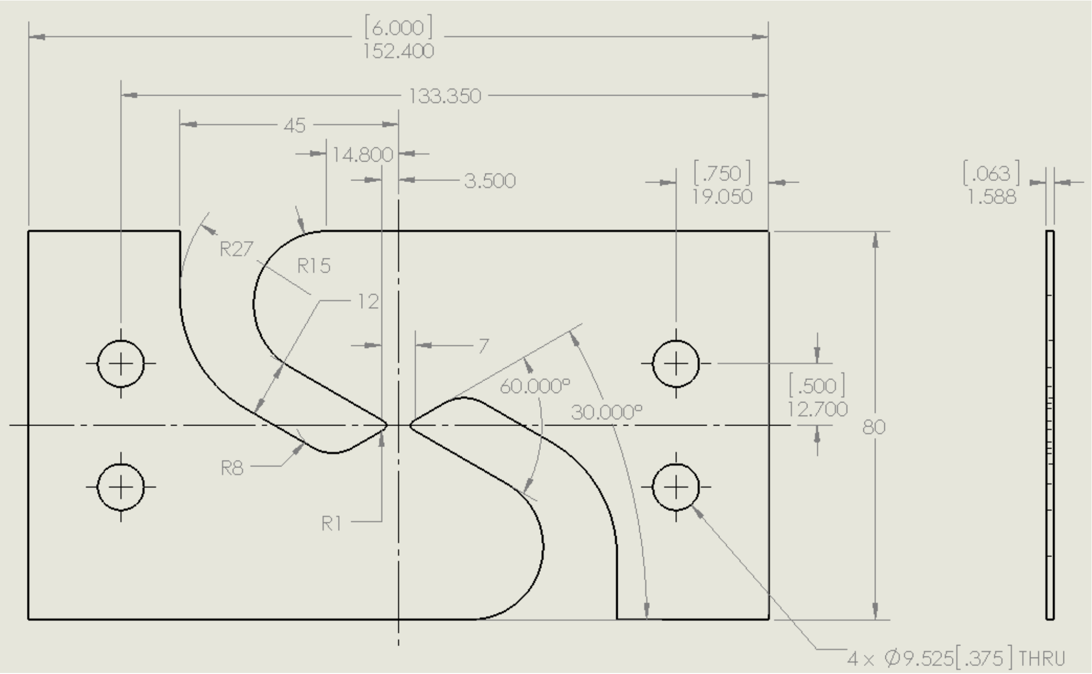

Figure 4-56 Technical drawing of the shear specimen (Courtesy of James Gose). This design is adapted from Bao & Wierzbicki's (2004) specimen design for pure shear tests.

The load/displacement was applied rapidly by hand with 7500 digital images recorded per second for this experiment. The test speed may not be constant as the load was applied by hand. The experimental set-up for the shear test can be seen in Figure 4-2. The pixel resolution is approximately 13.7 microns per pixel. Note that the high speed camera and the experimental device were not snychronized in this experiment. A very small lag in the recording might thus be possible.

Frames from the video recording are presented in Figure 4-57, Figure 4-58, Figure 4-59, Figure 4-60, Figure 4-61, Figure 4-62, and Figure 4-63. The vertical direction and the horizontal direction are the width direction and the longitudinal direction of the specimen, respectively. The regions depicted are the exploded views and their dimensions are approximately 890–920 pixels by 520–550 pixels.

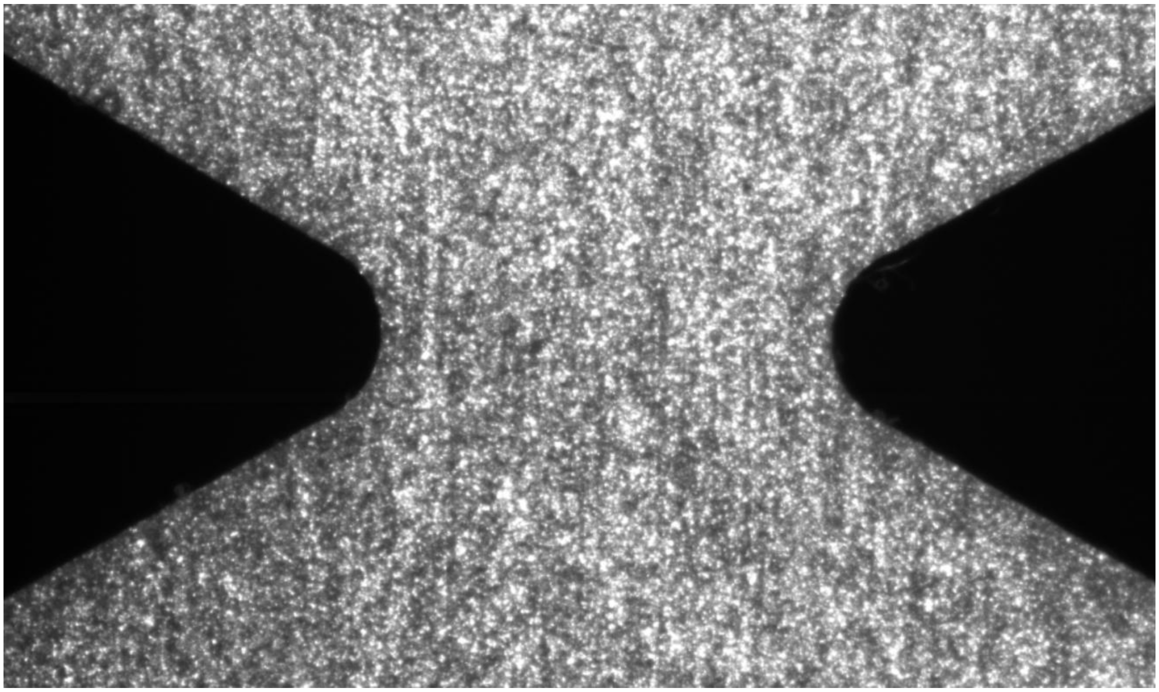

Figure 4-57 Nital etched AH32 steel shear specimen at Frame 0, that is, in the undeformed state.

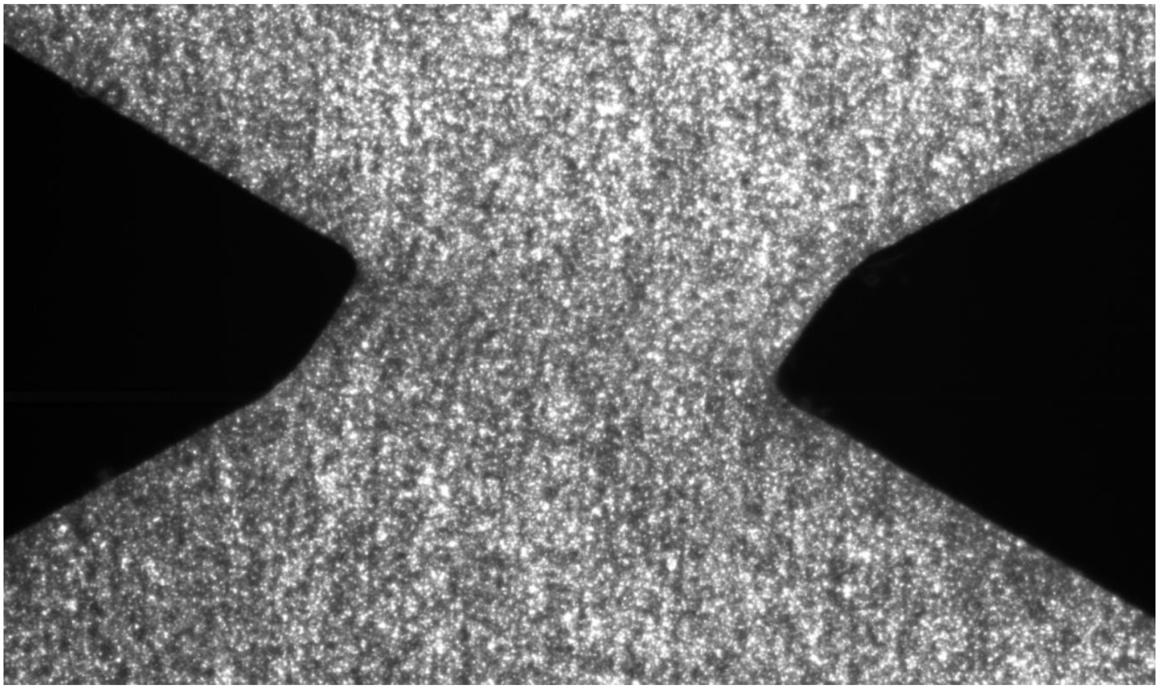

Figure 4-58 Nital etched AH32 steel shear specimen at Frame 4000.

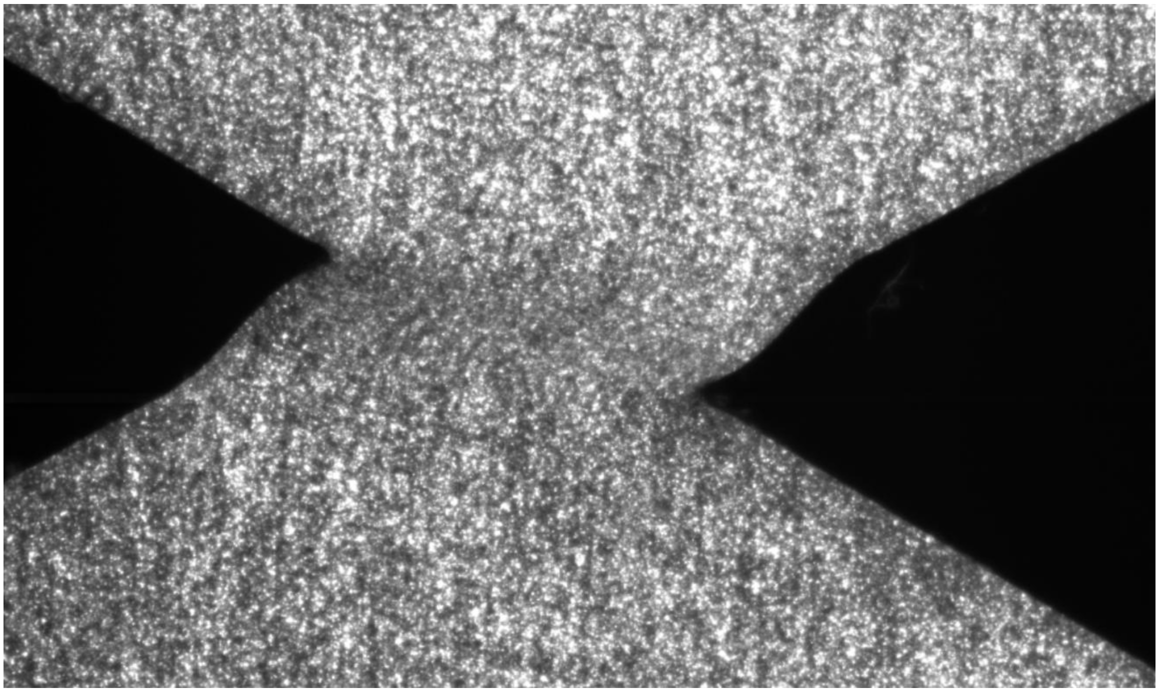

Figure 4-59 Nital etched AH32 steel shear specimen at Frame 7000.

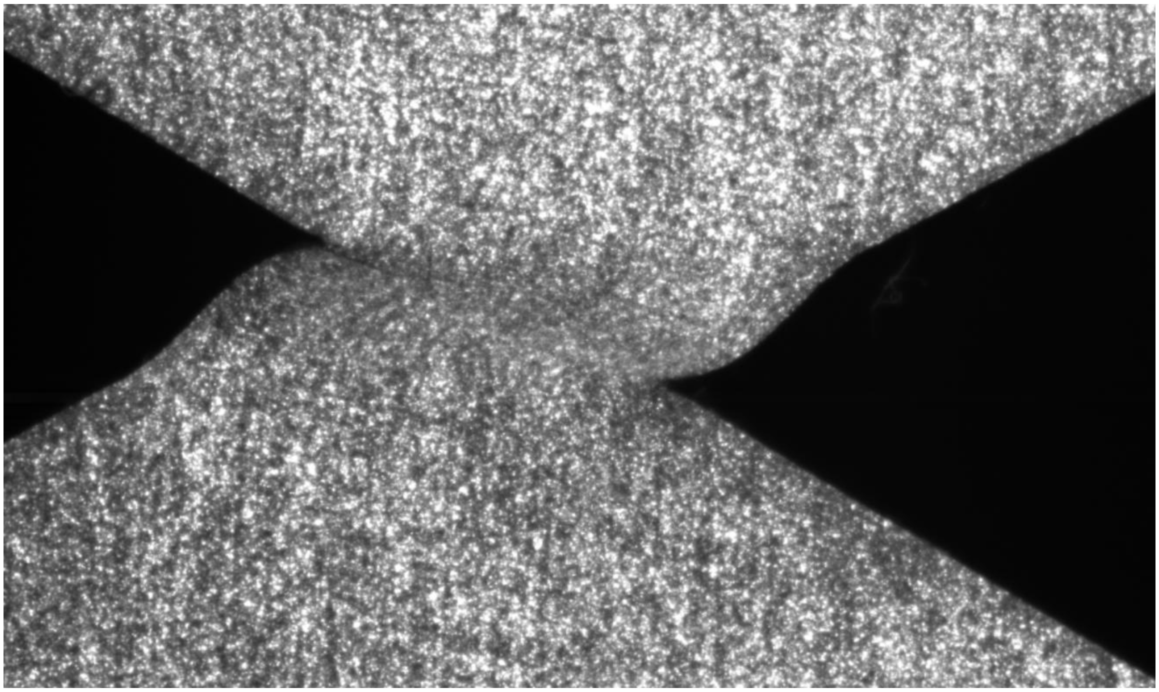

Figure 4-60 Nital etched AH32 steel shear specimen at Frame 8000.

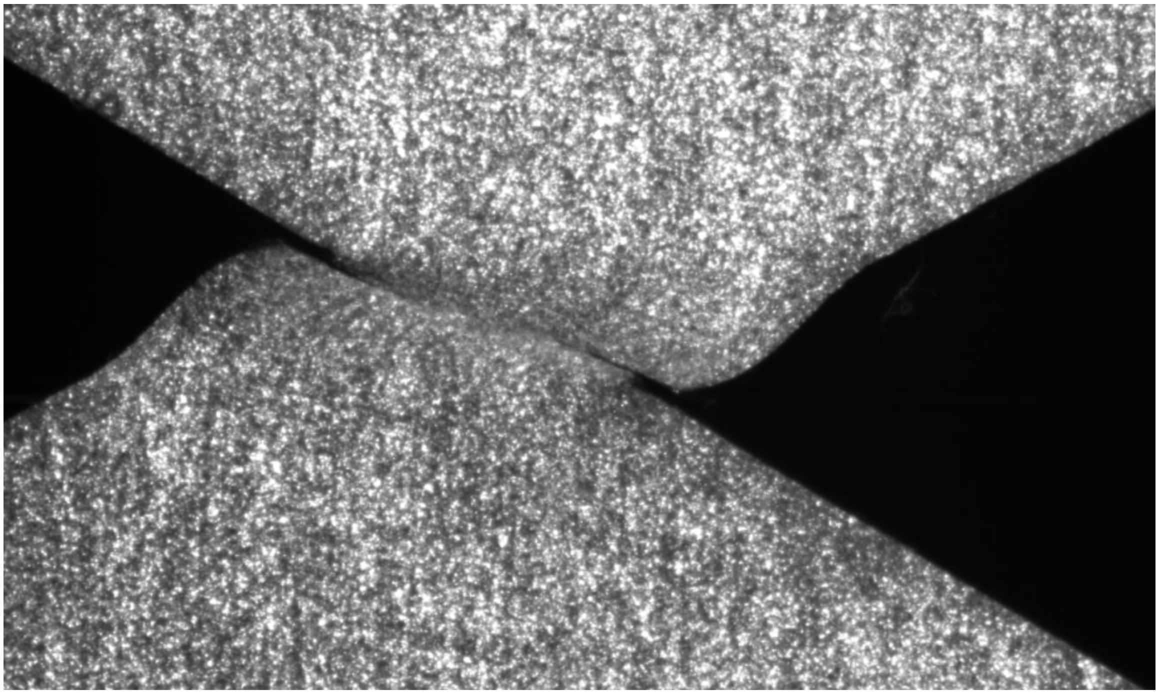

Figure 4-61 Nital etched AH32 steel shear specimen at Frame 8500.

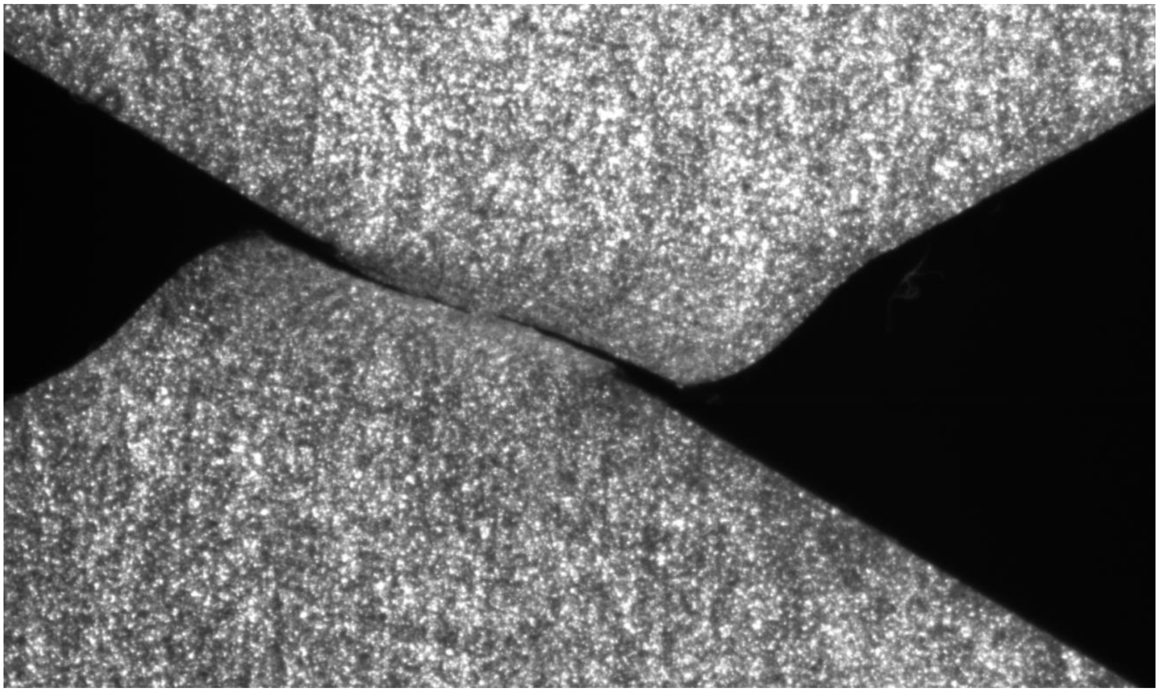

Figure 4-62 Nital etched AH32 steel shear specimen at Frame 8600.

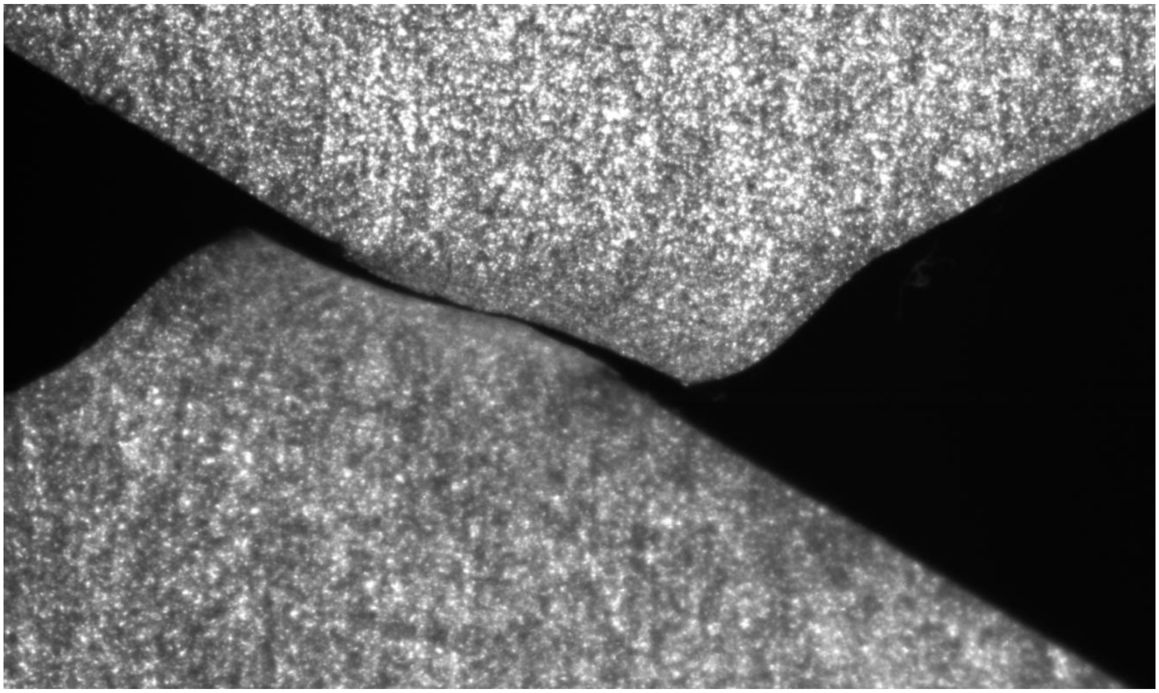

Figure 4-63 Nital etched AH32 steel shear specimen at Frame 8640.

Fracture initiates around Frame 6000 and the initial crack can clearly be seen at Frame 7000, depicted in Figure 4-59. Moreover, final stages of the crack propagation are presented in Figure 4-61, Figure 4-62, and Figure 4-63 with Figure 4-63 showing the completely fractured specimen.

The evolution of the natural strain and the effective strain within the masked region during the uniaxial test of the shear specimen for different mask sizes are presented in Figure 4-64, Figure 4-65, Figure 4-66, and Figure 4-67.

The dominant strain component is the shear strain (ε_{12}), as expected, due to the specimen geometry (see Figure 4-56). The shear strain is around 0.45 for the smallest two mask sizes (i.e., 16 pixels by 16 pixels and 32 pixels by pixels) and it decreases as the mask size is increased. Nevertheless, the other two strain components, that is, the longitudinal strain (ε_{11}) and the transverse strain (ε_{22}) remain small until the initiation of fracture, i.e., Frame 6000. Moreover, it is worth noting that these two strain components are nearly equal to each other but have the opposite sign, meaning that the strain in the thickness direction (ε_{33}) remains nearly zero. Strain convergence is discussed in the following pages, where the evolution of the strain for different mask sizes is presented (see Figure 4-76 and Figure 4-77).

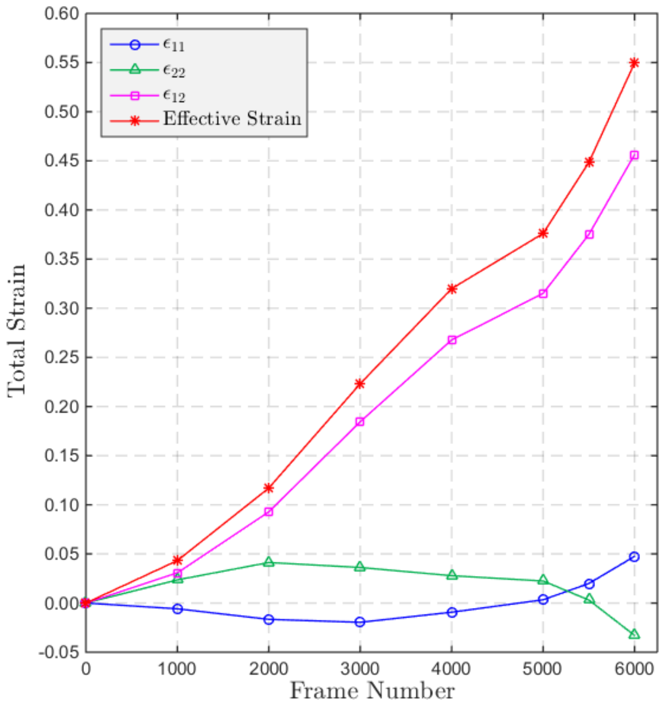

Figure 4-64 Evolution of the natural strain within the masked region during the uniaxial test of the shear specimen – second approach. Mask size is 16 pixels by 16 pixels (0.219 mm x 0.219 mm).

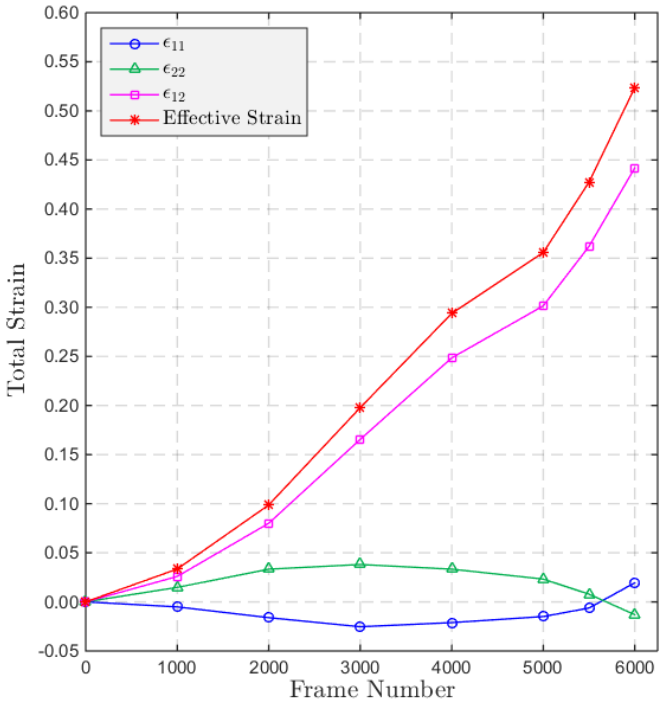

Figure 4-65 Evolution of the natural strain within the masked region during the uniaxial test of the shear specimen – second approach. Mask size is 32 pixels by 32 pixels (0.438 mm x 0.438 mm).

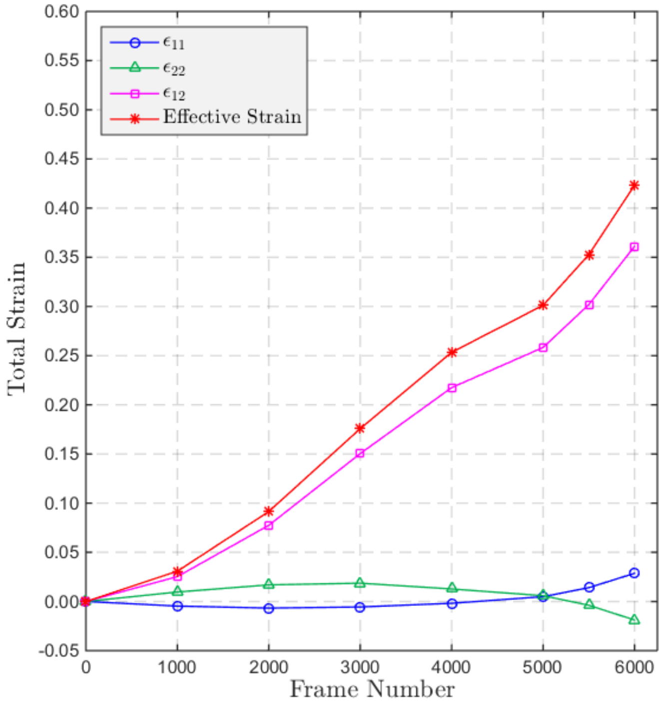

Figure 4-66 Evolution of the natural strain within the masked region during the uniaxial test of the shear specimen – second approach. Mask size is 64 pixels by 64 pixels (0.877 mm x 0.877 mm).

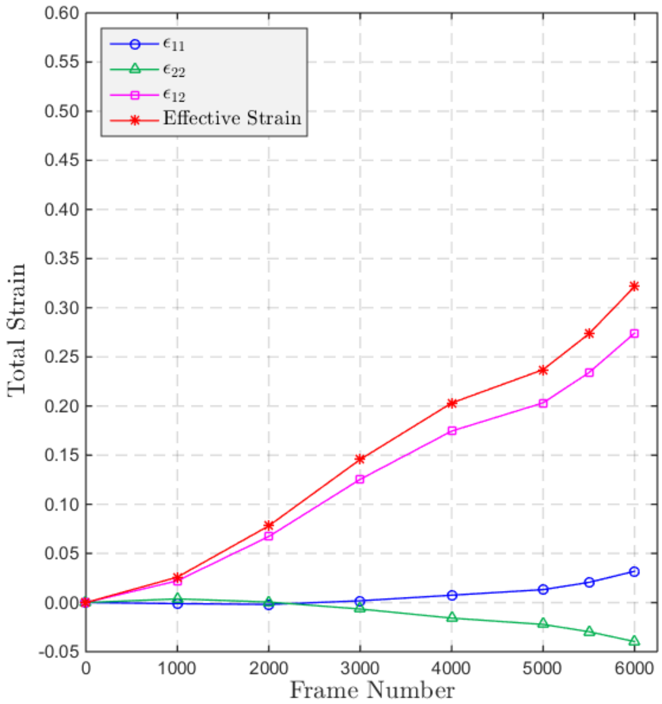

Figure 4-67 Evolution of the natural strain within the masked region during the uniaxial test of the shear specimen – second approach. Mask size is 128 pixels by 128 pixels (1.754 mm x 1.754 mm).

The evolution of the true stress (on the left) and the stress triaxiality (on the right) within the masked region during the uniaxial test of the shear specimen for different mask sizes are depicted in Figure 4-68, Figure 4-69, Figure 4-70, Figure 4-71, Figure 4-72, Figure 4-73, Figure 4-74, and Figure 4-75. Note that the state of stress is obtained by assuming that the shear stress (σ_{12}) remains positive during the entire loading (see Section 4.4.2 for details).

The stress triaxiality at the initiation of the test (i.e., at Frame 1000) varies between 0.27 and 0.07 with the largest value in the smallest mask size and the smallest value in the largest mask size. On the other hand, the stress triaxiality at fracture varies between -0.02 and 0.02 for the first approach, whereas it varies between -0.06 and 0.02 for the second approach. In addition, the average stress triaxiality varies between -0.01 and 0.08 for the first approach, while it varies between -0.02 and 0.02 for the second approach. Note that the variations of the stress triaxiality at fracture and the average stress triaxiality exhibit no particular order regarding the mask size. Finally, it is worth noting that the theoretical stress triaxiality for the pure shear state is zero.

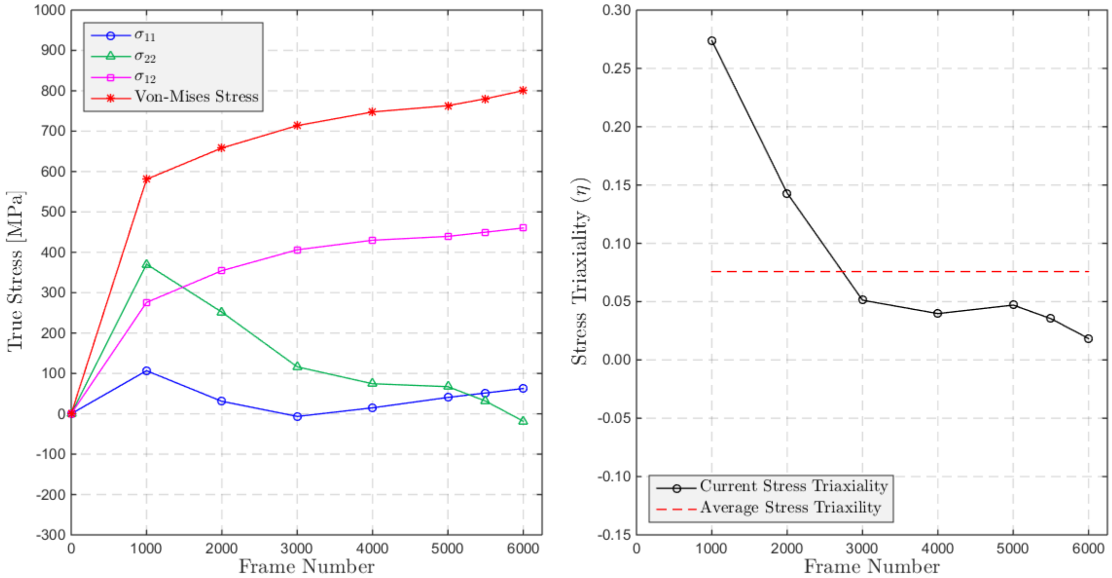

Figure 4-68 Evolution of the true stress (on the left) and the stress triaxiality (on the right) within the masked region during the uniaxial test of the shear specimen – first approach. Mask size is 16 pixels by 16 pixels (0.219 mm x 0.219 mm).

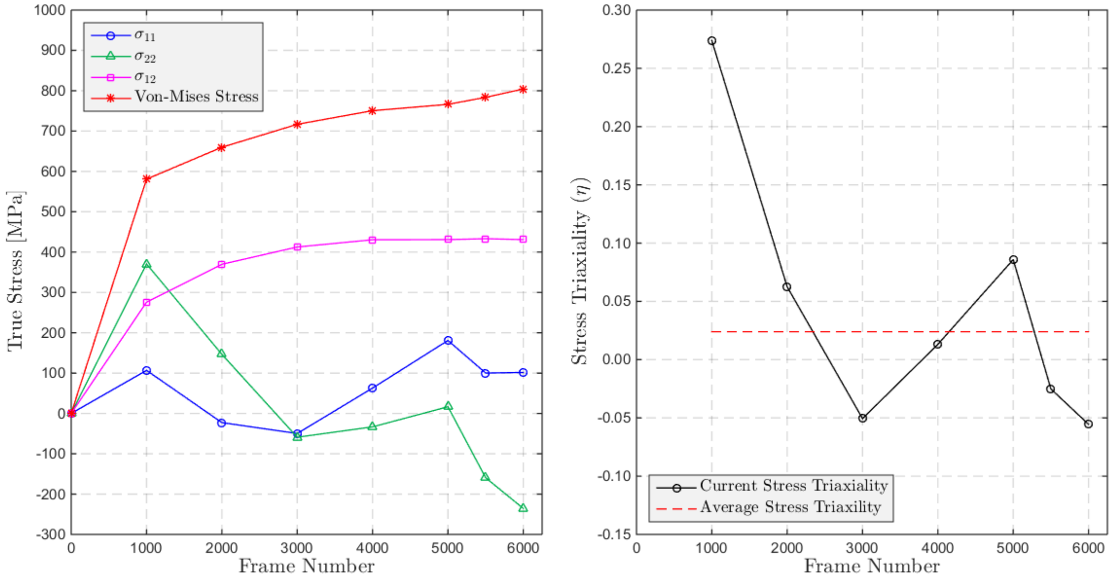

Figure 4-69 Evolution of the true stress (on the left) and the stress triaxiality (on the right) within the masked region during the uniaxial test of the shear specimen – second approach. Mask size is 16 pixels by 16 pixels (0.219 mm x 0.219 mm).

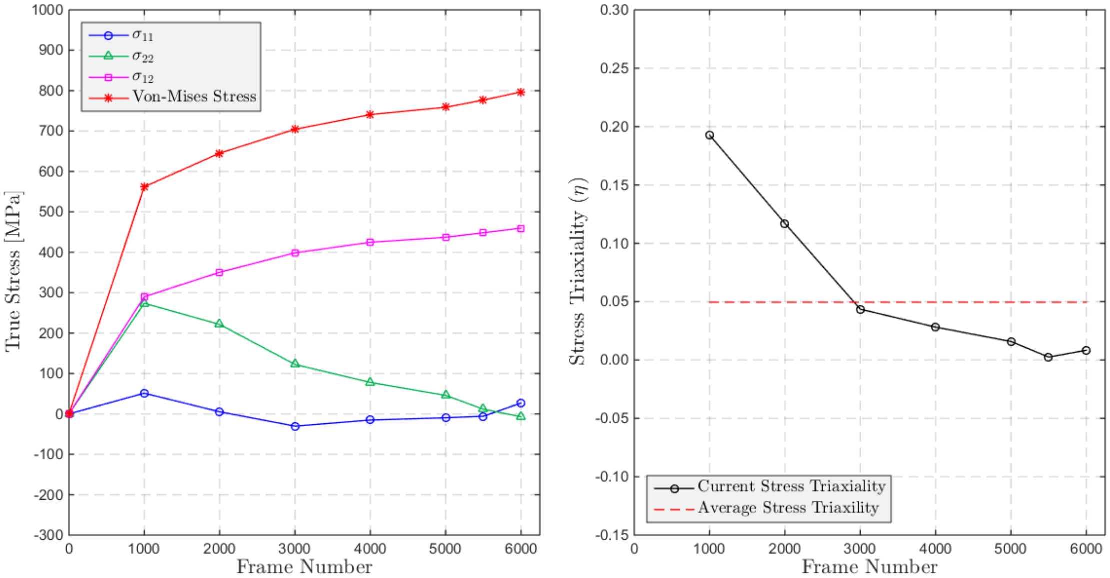

Figure 4-70 Evolution of the true stress (on the left) and the stress triaxiality (on the right) within the masked region during the uniaxial test of the shear specimen – first approach. Mask size is 32 pixels by 32 pixels (0.438 mm x 0.438 mm).

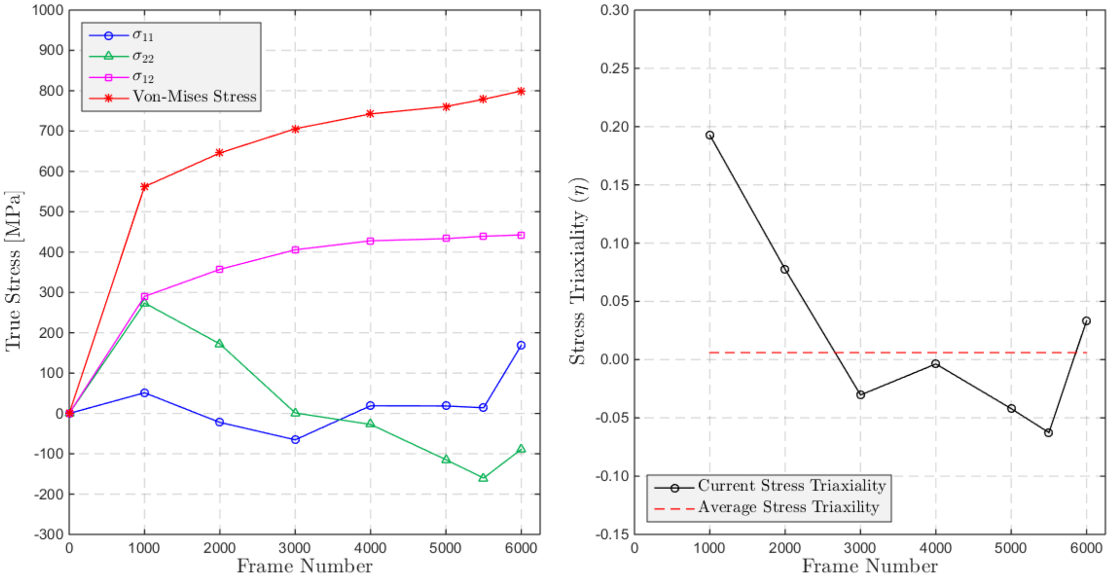

Figure 4-71 Evolution of the true stress (on the left) and the stress triaxiality (on the right) within the masked region during the uniaxial test of shear specimen – second approach. Mask size is 32 pixels by 32 pixels (0.438 mm x 0.438 mm).

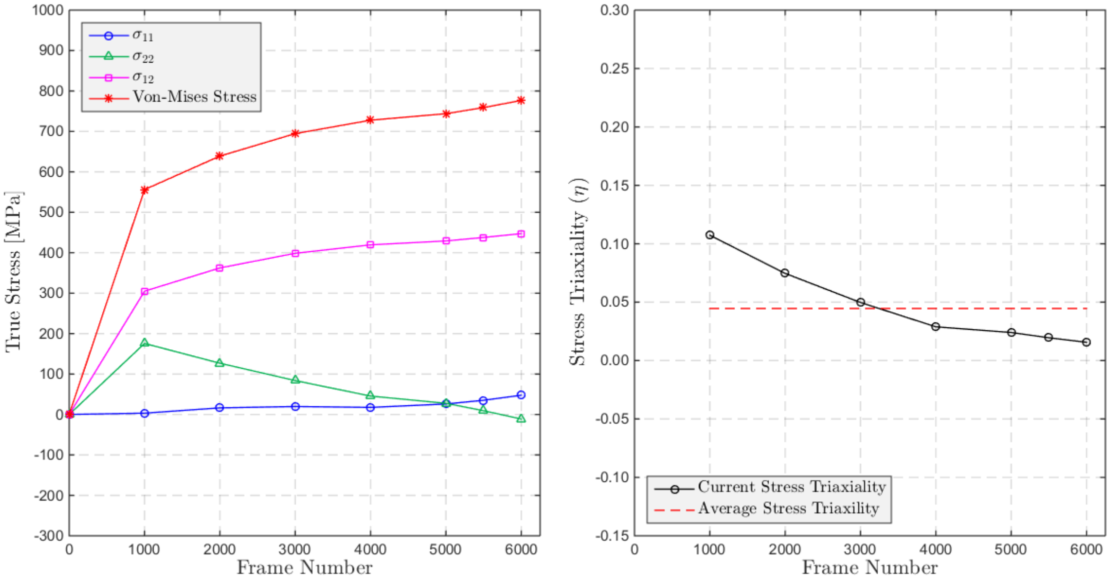

Figure 4-72 Evolution of the true stress (on the left) and the stress triaxiality (on the right) within the masked region during the uniaxial test of the shear specimen – first approach. Mask size is 64 pixels by 64 pixels (0.877 mm x 0.877 mm).

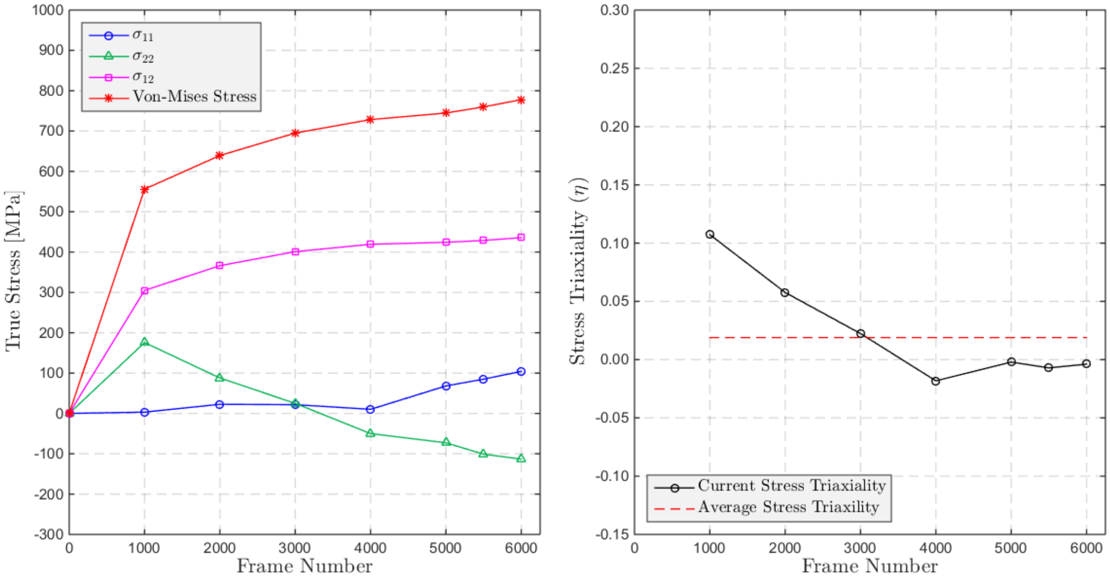

Figure 4-73 Evolution of the true stress (on the left) and the stress triaxiality (on the right) within the masked region during the uniaxial test of the shear specimen – second approach. Mask size is 64 pixels by 64 pixels (0.877 mm x 0.877 mm).

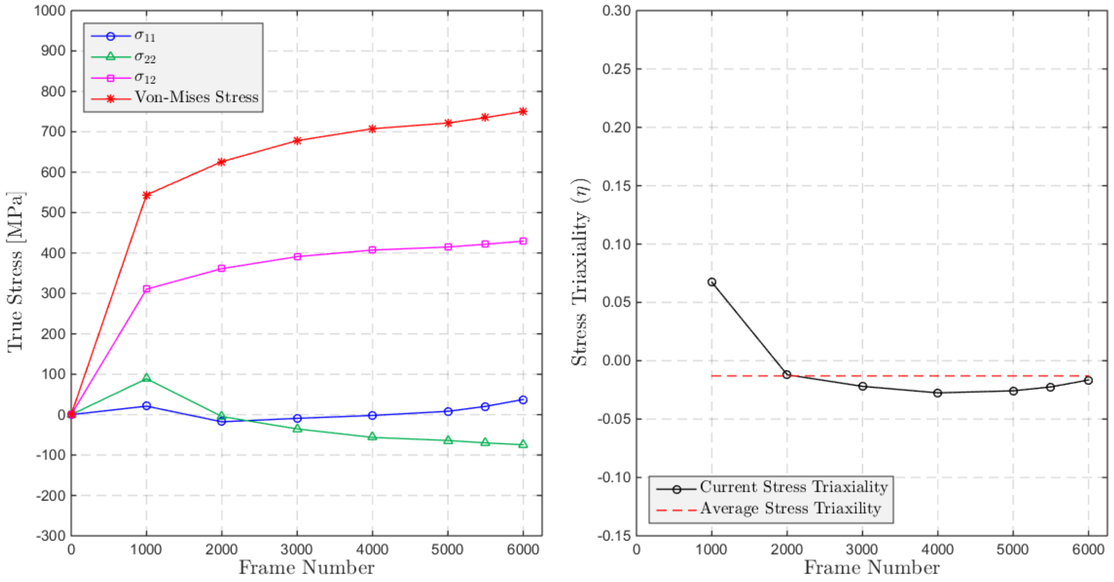

Figure 4-74 Evolution of the true stress (on the left) and the stress triaxiality (on the right) within the masked region during the uniaxial test of the shear specimen – first approach. Mask size is 128 pixels by 128 pixels (1.754 mm x 1.754 mm).

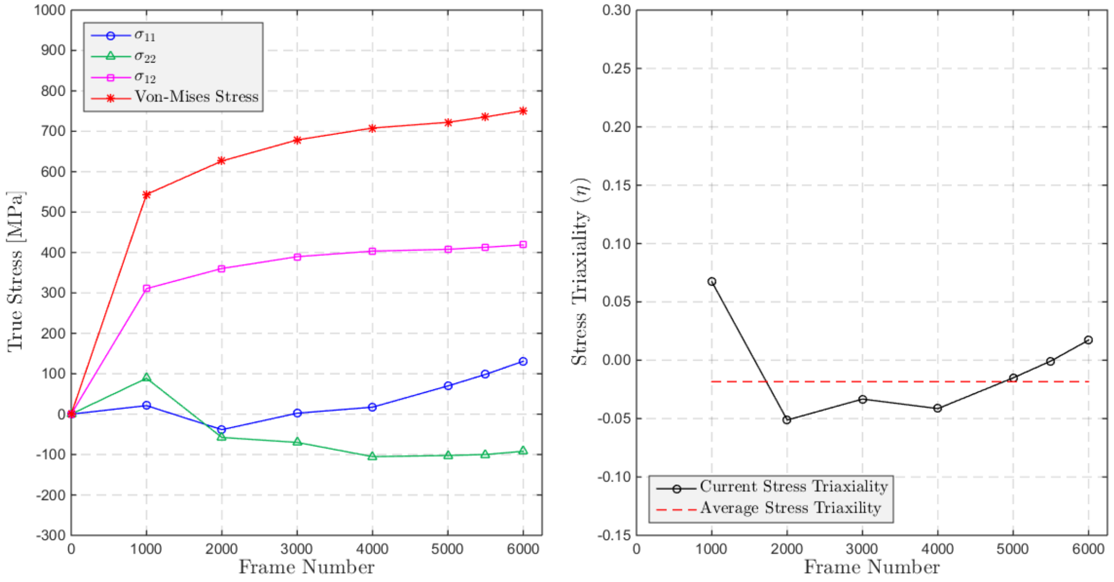

Figure 4-75 Evolution of the true stress (on the left) and the stress triaxiality (on the right) within the masked region during the uniaxial test of the shear specimen – second approach. Mask size is 128 pixels by 128 pixels (1.754 mm x 1.754 mm).

The evolution of the shear stress for the two different approaches shows nearly the same quantitative behavior and the shear stress remains very stable even for the smaller mask sizes. Moreover, the longitudinal stress (σ_{11}) and the transverse stress (σ_{22}) remain nearly stable as well; i.e., there are no noteworthy fluctuations. This stable behavior of the stress field suggests that the loading remains nearly proportional[50]. Finally, the development of the longitudinal stress and the transverse stress shows that the exact pure shear condition was not achieved and this suggests that the geometry of the specimen may be improved to satisfy a pure shear stress state.

The evolution of the shear strain for different mask sizes is presented in Figure 4-76. Shear strain increases as the mask size is decreased and it ranges between 0.27 and 0.46. Note that the discussion on the strain convergence is explained together with the evolution of the effective strain (depicted in Figure 4-77) as they exhibit similar behavior.

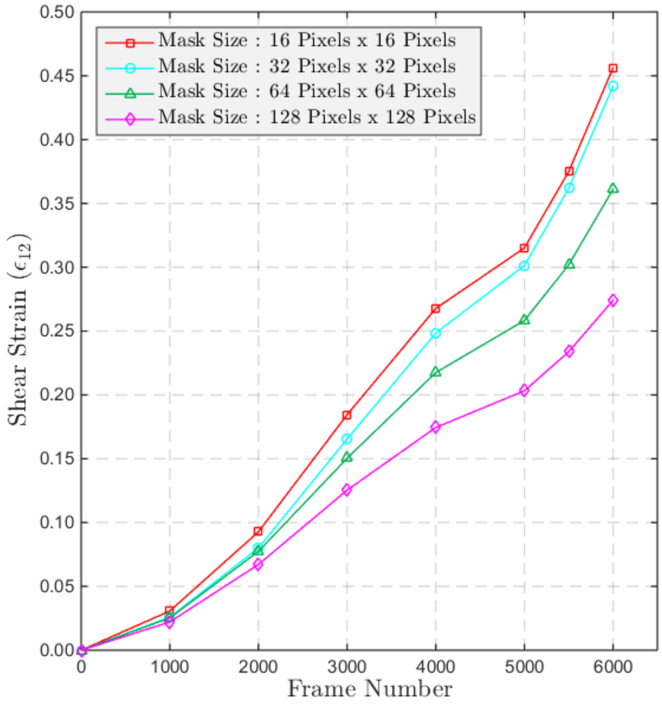

Figure 4-76 Evolution of the shear strain within the masked region during the uniaxial test of the shear specimen for different mask sizes – second approach. Pixel resolution is approximately 13.7 μm/pixel.

The evolution of the effective strain for the four scales studied from the results of this particular experiment is presented in Figure 4-77. The evolution of the strain exhibits the same qualitative behavior for all mask sizes investigated. Moreover, an indication of convergence of the result appears as the length scales were reduced. Nevertheless, this is not sufficient to draw a 'strain convergence' conclusion as convergence behavior likely needs to be verified by multiple mask sizes.

---

[50] See Footnote 44.

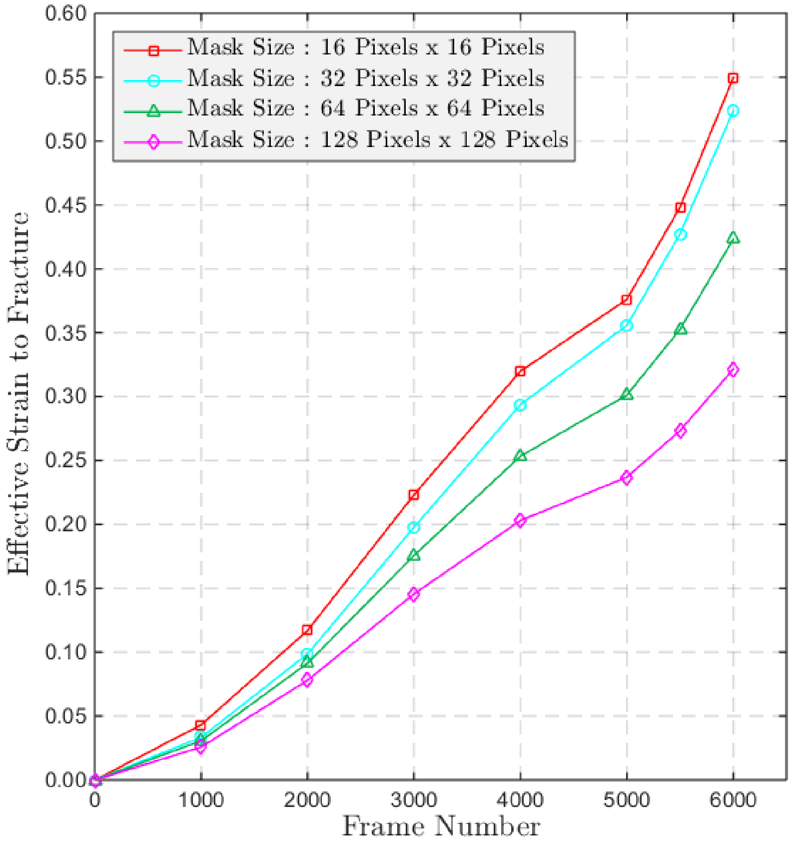

Figure 4-77 Evolution of the effective strain within the masked region during the uniaxial test of the shear specimen for different mask sizes – second approach. Pixel resolution is approximately 13.7 µm/pixel.

The effect of mask size on failure strain is shown in Figure 4-78. There may be strain convergence as the mask size is decreased; however, this can be affected by the arrangement choice of the masked regions. Therefore, we investigated the effect of mask position on fracture strain as well. For instance, the 8 pixels by 8 pixels mask can be arranged in nine different ways with all the arrangements remaining within the 16 pixels by 16 pixels mask. As an example, two of these calculations are shown in Figure 4-78. Similar fluctuations can be observed for the other mask sizes as well; however, the author believes that these fluctuations should not be as large as the one observed for the 8 pixels by 8 pixels mask. The reason for the large differences observed in using various 8 pixels by 8 pixels masks is that this mask size is very small such that micro-structural variations are likely present and only four strain values are averaged to obtain the average strain within the mask region. This mask size is apparently at the transition of micro-scale and continuum scale.

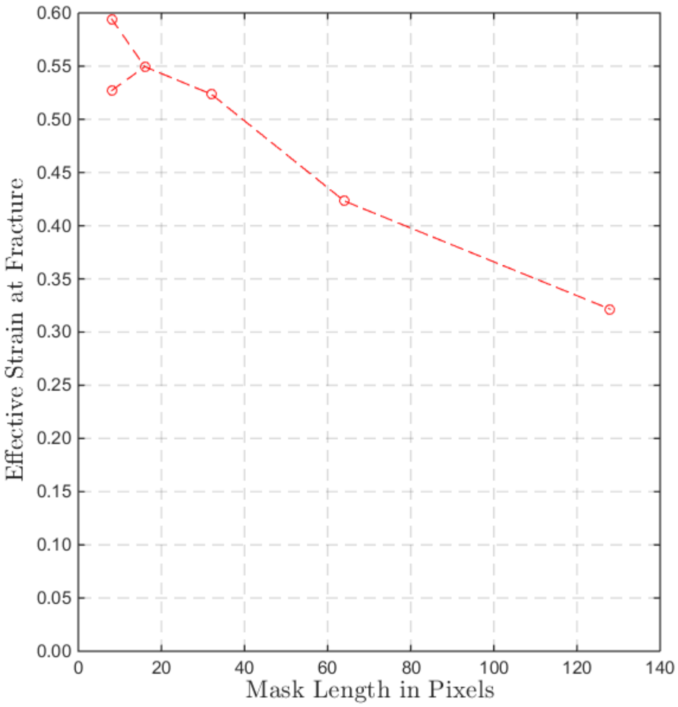

Figure 4-78 Effect of mask size on failure strain during the uniaxial test of the shear specimen – second approach. The dashed line is a linear curve between two data points. Pixel resolution is approximately 13.7 μm/pixel.

The average stress triaxiality (η_{ave}), the stress triaxiality at fracture (η_{frac}), and the effective strain at fracture (ε_{eff}^{f}) for both approaches are summarized in Table 4-4. The effective strain at fracture increases as the mask size is decreased, a sign of localization. However, the stress triaxiality at fracture and the average stress triaxiality exhibit no particular order regarding the mask size for the second approach, while they decrease as the mask size is increased for the first approach. Finally, as can be seen from Table 4-4, the maximum difference between the effective strain at fracture for two different approaches is 3.6%, which occurs on the smallest mask size.

Table 4-4 Summary of the average stress triaxiality (η_{ave}), the stress triaxiality at fracture (η_{frac}), and the effective strain at fracture (ε_{eff}^{f}) for the uniaxial test of the shear specimen.

	Mask size [pixels]	η_{ave}	η_{frac}	ε_{eff}^{f}
First approach	16x16	0.076	0.018	0.529
	32x32	0.049	0.001	0.511
	64x64	0.045	0.001	0.418
	128x128	-0.013	-0.016	0.319
Second approach	16x16	0.024	-0.055	0.549
	32x32	0.006	-0.001	0.524
	64x64	0.019	-0.004	0.423
	128x128	-0.018	0.017	0.321

Finally, the true stress-strain curves for different mask sizes are presented together in Figure 4-79. Note that the flow rule and the same power-law hardening relationship with the same coefficients (i.e., $\Omega = 868.4$ MPa and $n = 0.128$) are used here as for the uniaxial test of the 6mm-width specimen, presented in Section 4.5.1, to obtain the components of the stress tensor (see Section 4.4.2 for details) of the DIC analysis. Moreover, the stress-strain curve obtained via the MTS machine is superposed on the same figure for comparison purposes[51]. Solid lines with markers are obtained by the digital image correlation analysis, while dashed lines are the results of the uniaxial test with the MTS machine. Note that as the DIC analyses are conducted to the point of fracture initiation the last marker of each color represents the fracture initiation point for different mask sizes. Finally, it is worth noting that the effective stress-strain curve is independent of the mask size, as expected, as the plastic constitutive and stress-strain relationships that are used (the hardening-law and the flow rule) are independent of a length scale.

---

[51] As also mentioned in the analysis of the uniaxial test (see Chapter 4.5.1), the author is aware that although a uni-directional stress-strain curve (i.e., the stress-strain curve obtained via an MTS machine) may be the correct representation of the effective stress-strain curve in a global manner (when the gauge length is sufficiently large compared to the localization zone), it may not correctly reflect the actual strains in the localized zone as can be seen in Figure 4-42. Therefore, the stress-strain curve obtained via the MTS machine is superposed on the same figure for comparison purposes.

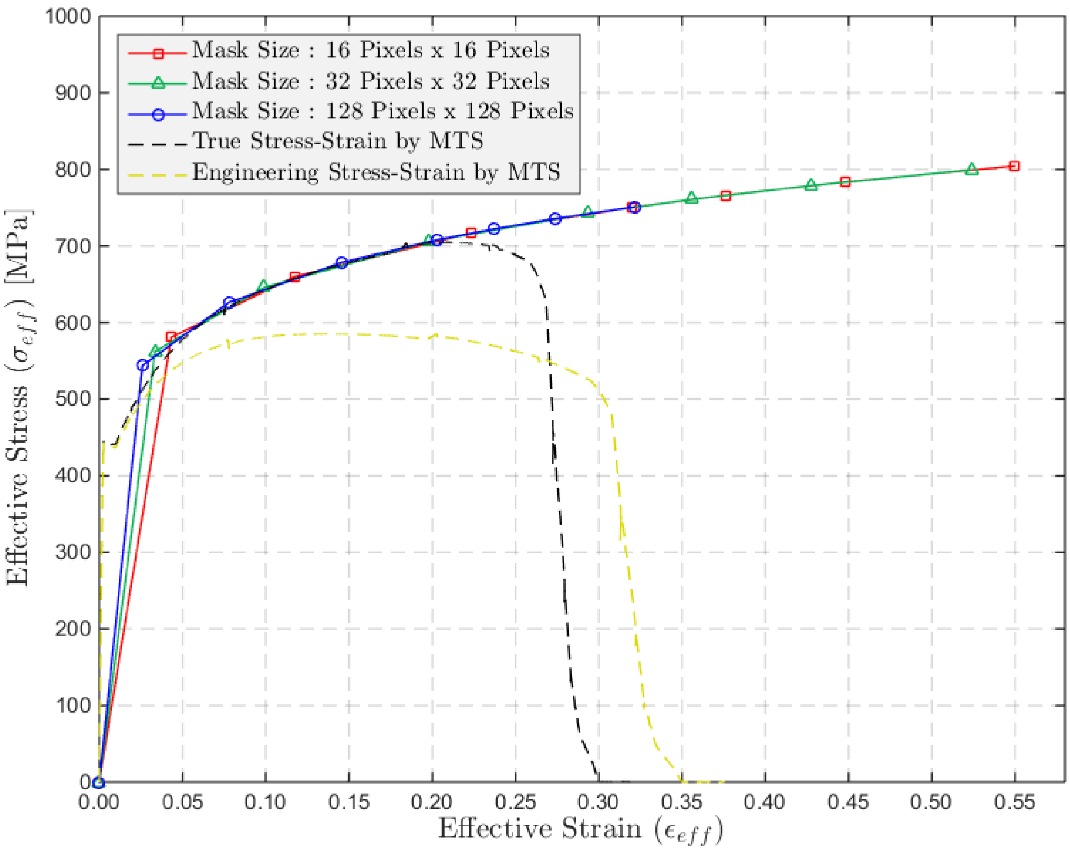

Figure 4-79 True stress-strain curve of the uniaxial test of the shear specimen for different mask sizes – second approach. Pixel resolution is approximately 13.7 μm/pixel. Solid lines with markers are obtained by digital image correlation (DIC) analysis while dashed lines are the results from the MTS machine.

4.6 Cylindrical Indenter Test Results

The friction at the cylinder/specimen interface may affect the stress state, and the fracture mode and position. All cylindrical indenter experiments presented here are conducted using teflon sheet and graphite particles at the interface to reduce friction and help provide a frictionless state.

Two different specimen geometries have been used in the cylindrical indenter experiments with a 2-inch-diameter stainless steel circular cylinder, from McMaster-Carr, used as an indenter.

Two different strain increment approaches are applied in the calculation of effective strain, the state of stress, and the stress triaxiality; i.e., each approach provides a set of figures for a specific mask size. In the first approach, the strain increments have been determined from the un-deformed state to the current state, while the second set of figures have been obtained by taking strain increments from the previous state to the current state. For strain analysis only the data of the second approach are presented unless the effective strain of the two approaches have different qualitative behavior, whereas data of both approaches are provided for the stress analysis.

All stresses presented in this section (i.e., Cylindrical Indenter Test Results) are the true stresses and all strains are the natural/true strains unless otherwise stated. Moreover, the subscript *11* corresponds to the longitudinal direction of the specimen and the subscript *22* corresponds to the width direction.

4.6.1 Analysis of 18mm-Width Specimen without Groove

The isometric view and technical drawing of the test specimen are depicted in Figure 4-80 and Figure 4-81, respectively.

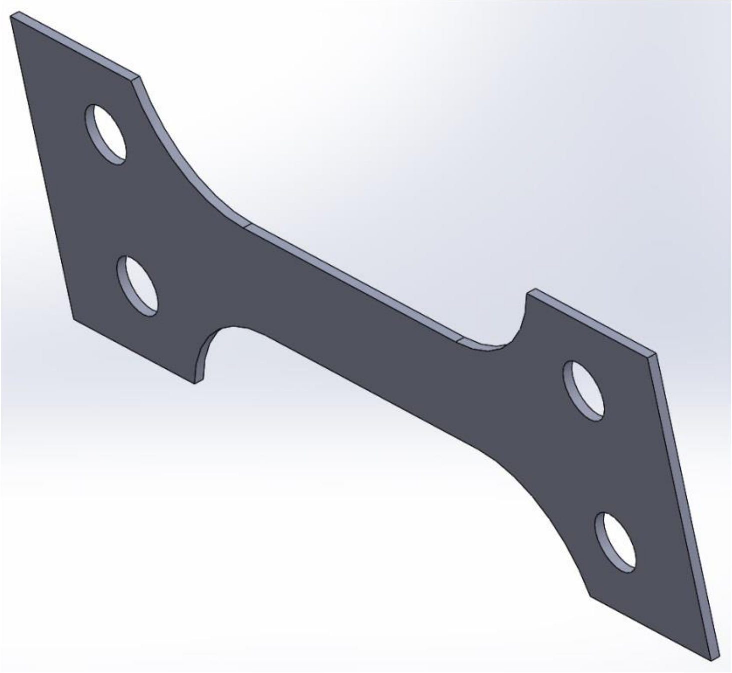

Figure 4-80 Isometric view of the 18mm-width specimen without groove (Courtesy of James Gose and Haocheng Pan).

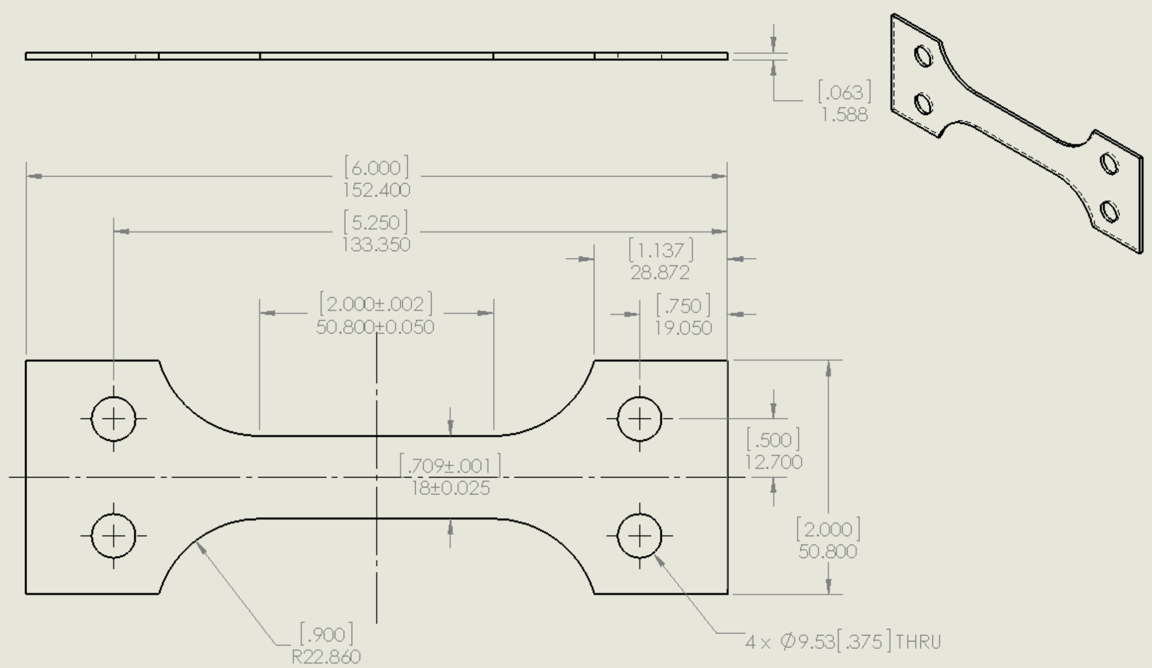

Figure 4-81 Technical drawing of the 18mm-width specimen without groove (Courtesy of James Gose and Haocheng Pan).

4.6.1.1 Test 0

An indentation speed of 0.6 inch/second was applied to the center of the test specimen with 7500 digital images recorded per second. The pixel resolution was approximately 13.7 microns per pixel. Note that the high speed camera and the experimental device were not snychronized in this experiment. A very small lag in the recording might thus be possible.

Frames from the video recording are presented in Figure 4-82, Figure 4-83, Figure 4-84, Figure 4-85, Figure 4-86, Figure 4-87, Figure 4-88, Figure 4-89, Figure 4-90, and Figure 4-91. The vertical direction and the horizontal direction are the longitudinal direction and the width direction of the specimen, respectively. The regions depicted are the exploded views and their dimensions are approximately 1035–1065 pixels by 610–640 pixels. Note that the recording consists of two videos; the first part of the video recording ends at Frame 22253.

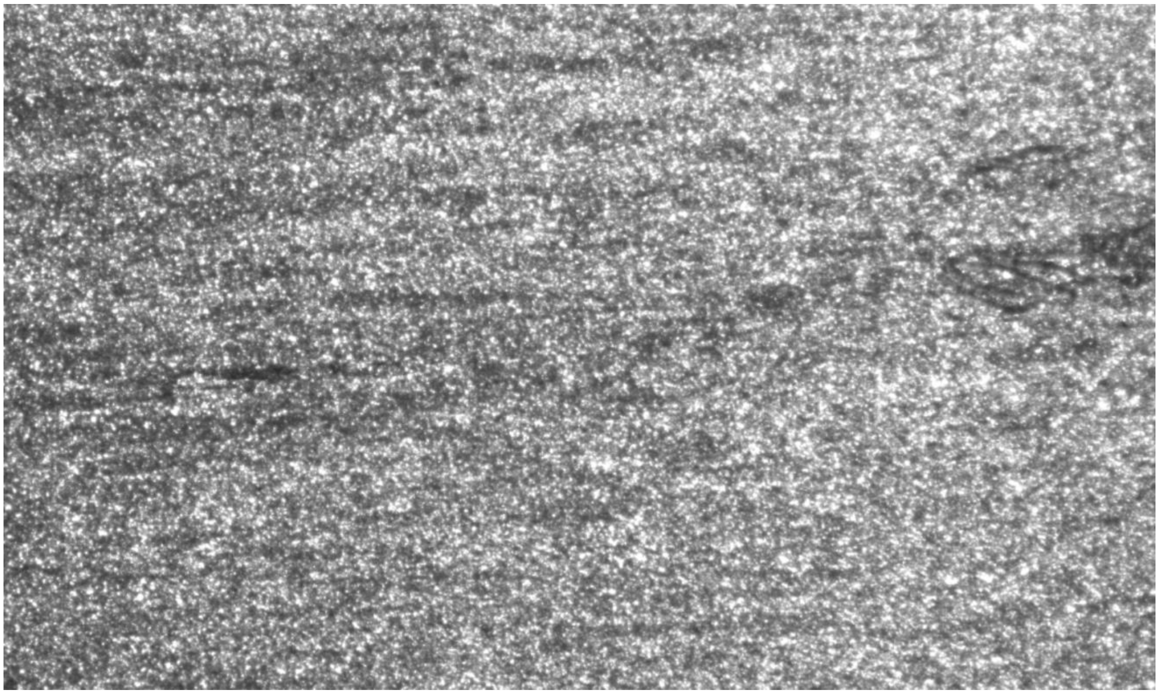

Figure 4-82 Nital etched AH32 steel 18mm-width-specimen without groove at Frame 0; that is, in the undeformed state.

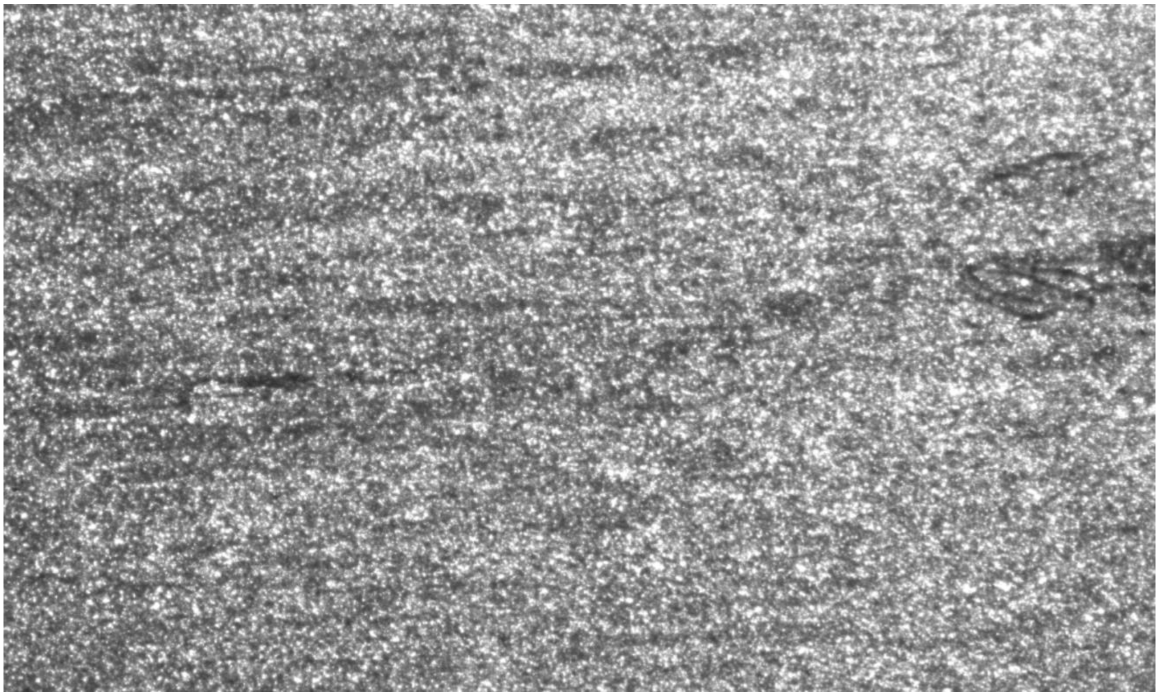

Figure 4-83 Nital etched AH32 steel 18mm-width-specimen without groove at Frame 5000; that is, a 10.160 mm indentation had been applied.

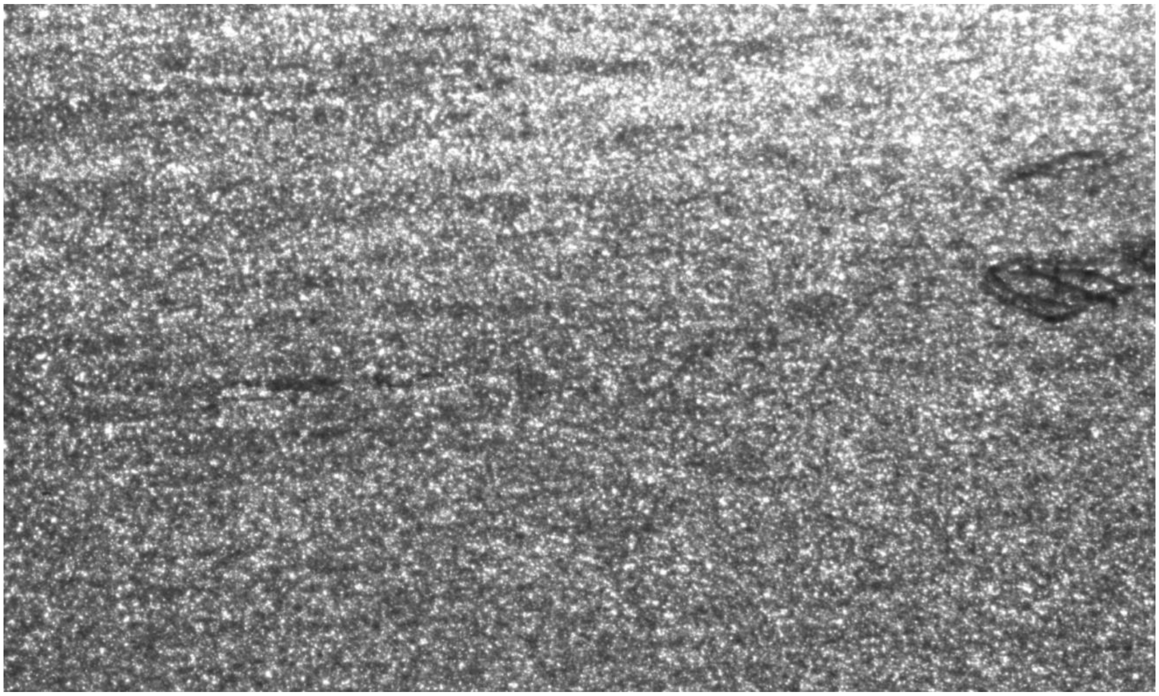

Figure 4-84 Nital etched AH32 steel 18mm-width-specimen without groove at Frame 10000; that is, a 20.320 mm indentation had been applied.

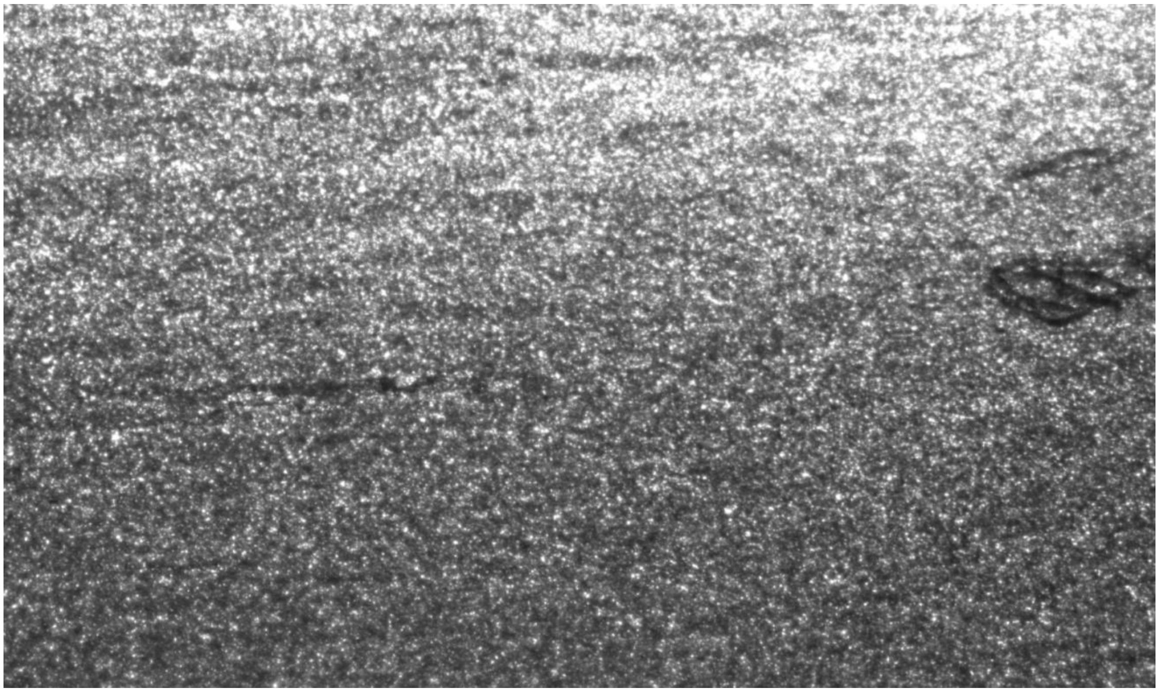

Figure 4-85 Nital etched AH32 steel 18mm-width-specimen without groove at Frame 15000; that is, a 30.480 mm indentation had been applied.

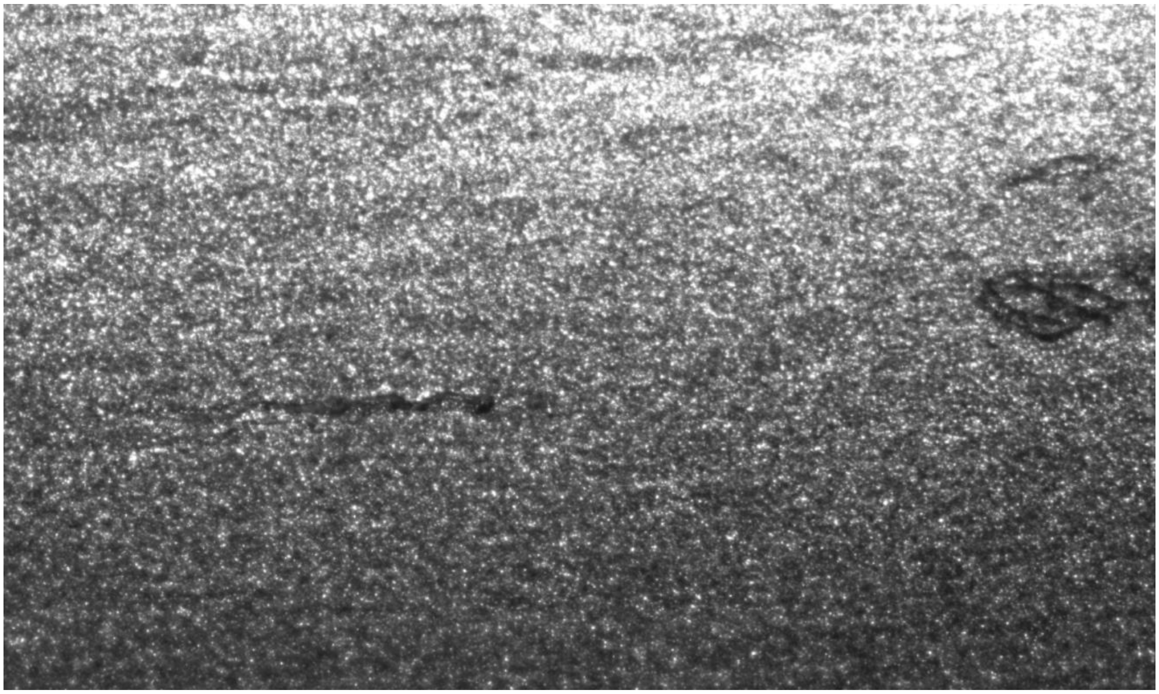

Figure 4-86 Nital etched AH32 steel 18mm-width-specimen without groove at Frame 20000; that is, a 40.640 mm indentation had been applied.

Figure 4-87 Nital etched AH32 steel 18mm-width-specimen without groove at Frame 22250; that is, a 45.212 mm indentation had been applied.

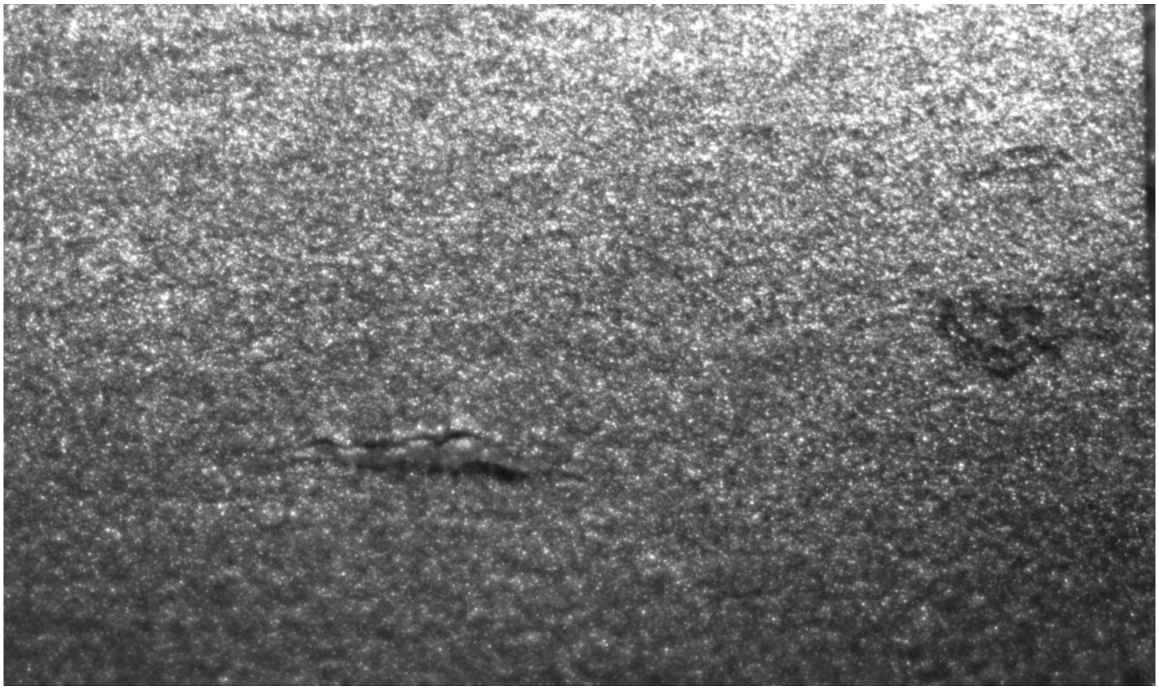

Figure 4-88 Nital etched AH32 steel 18mm-width-specimen without groove at Frame 24250; that is, a 49.276 mm indentation had been applied.

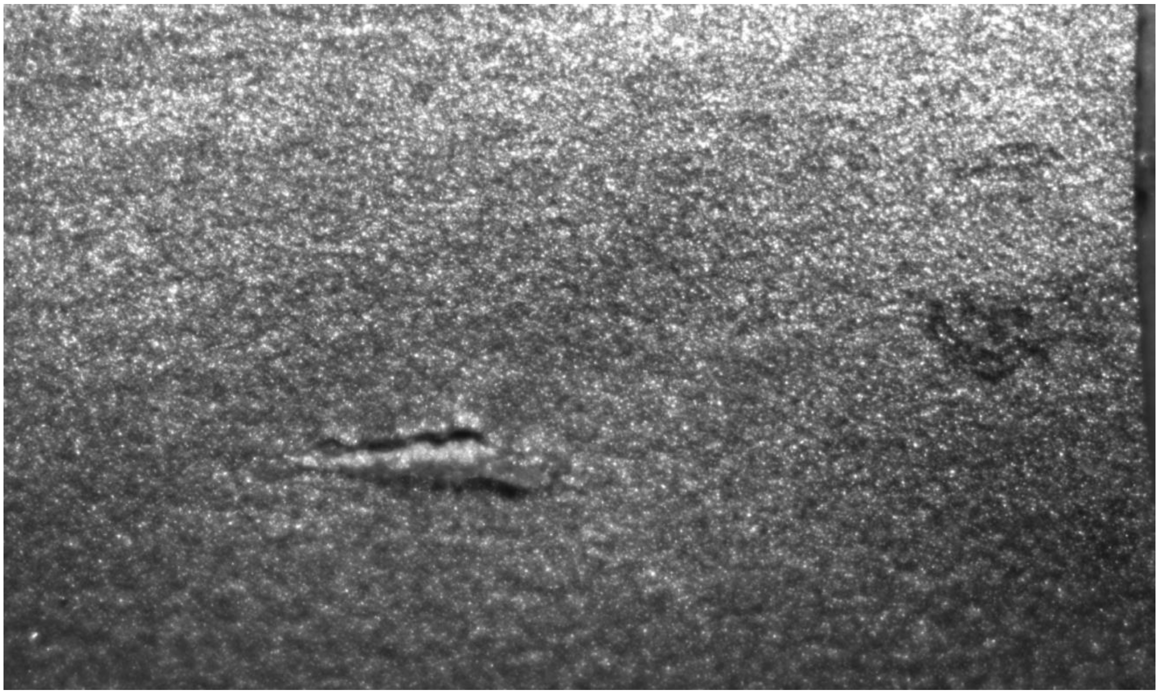

Figure 4-89 Nital etched AH32 steel 18mm-width-specimen without groove at Frame 24520; that is, a 49.825 mm indentation had been applied.

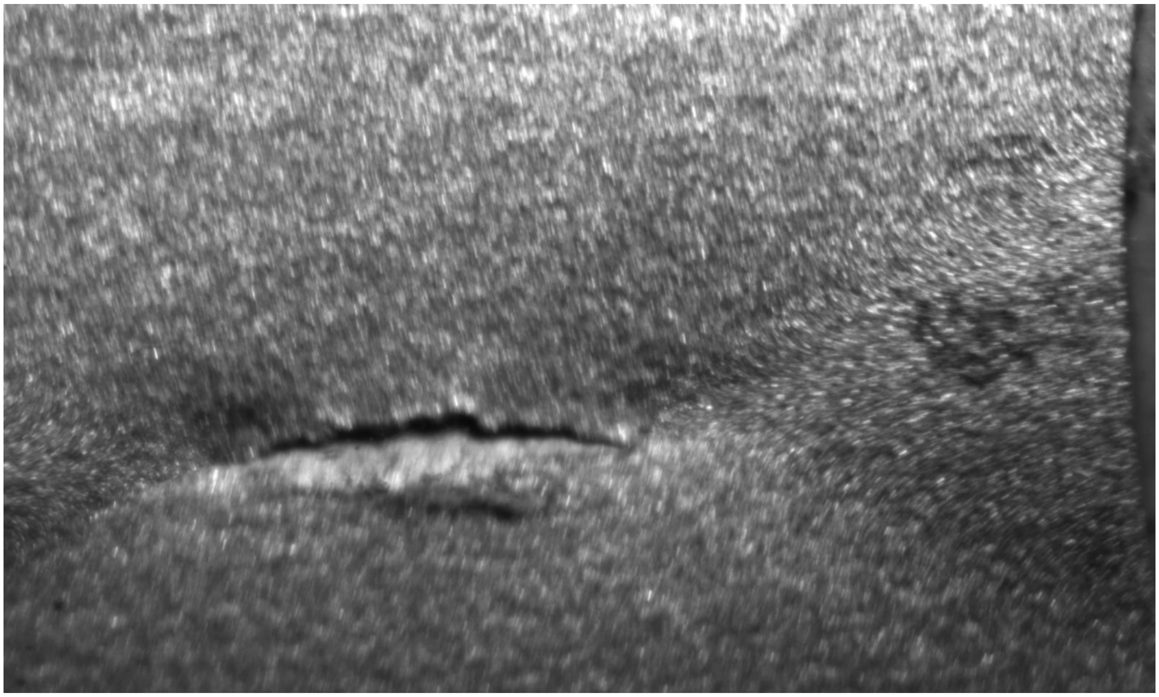

Figure 4-90 Nital etched AH32 steel 18mm-width-specimen without groove at Frame 24526; that is, a 49.837 mm indentation had been applied.

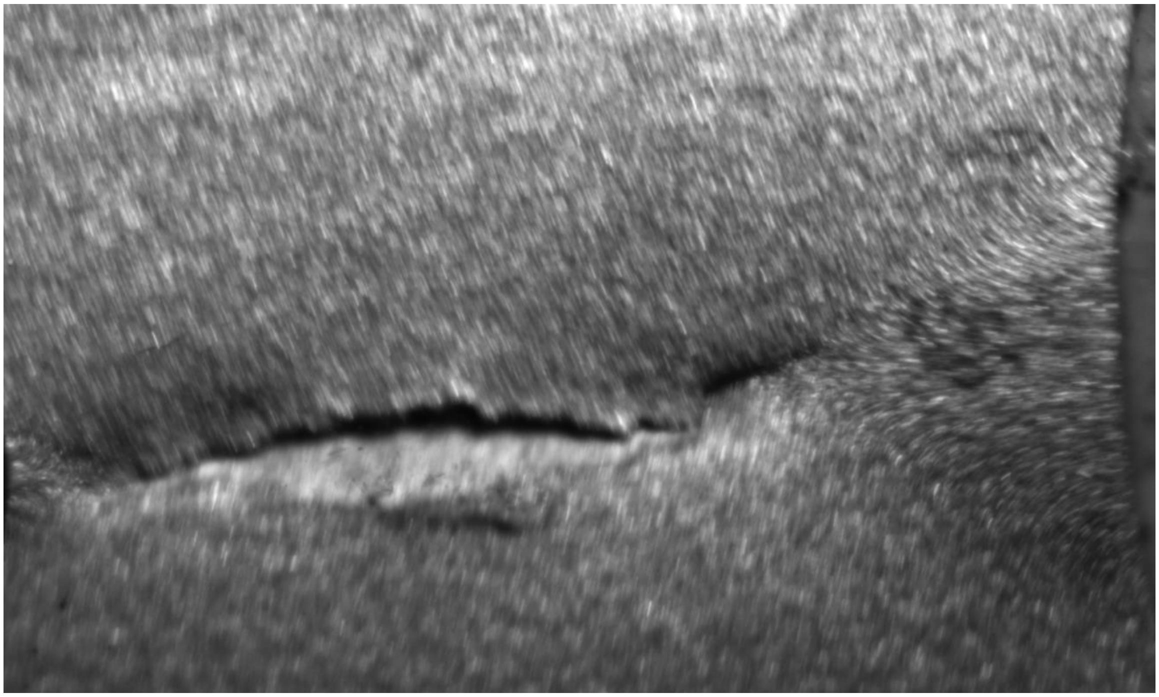

Figure 4-91 Nital etched AH32 steel 18mm-width-specimen without groove at Frame 24527; that is, a 49.839 mm indentation had been applied.

Fracture initiates around Frame 14500; that is, following an approximately 29.464 mm indentation. In fact, the initial crack can clearly be seen at Frame 15000, depicted in

Figure 4-85. Moreover, final stages of the crack propagation are presented in Figure 4-89, Figure 4-90, and Figure 4-91. It is worth noting that shear bands are clearly visible at Frame 24526 (depicted in Figure 4-90) and Frame 24527 (depicted in Figure 4-91).

The evolution of the natural strain and the effective strain within the masked region during cylindrical indentation for different mask sizes are presented in Figure 4-92, Figure 4-93, Figure 4-94, Figure 4-95, Figure 4-96, and Figure 4-97. Note that the graph for the first approach with a 16 pixels by 16 pixels mask is also presented (see Figure 4-92) to show the different qualitative behavior of the effective strain between Frame 2000 and Frame 4000. The reason for this difference is that the first approach may not capture the small changes in the strain field in the calculation of the effective strain due to larger strain increments. Nevertheless, this difference becomes smaller and disappears as the mask sizes are increased (Note that the difference is not visible for masks larger than 64 pixels by 64 pixels). The comparison of the two approaches for all mask sizes is presented in Table 4-5, at the end of this sub-section.

The shear strain remains zero or nearly zero for the larger mask sizes until the initiation of fracture (i.e., Frame 14500), where the analysis was curtailed. However, for smaller mask sizes (which represent more local behavior), shear strain develops at some stages of the experiment. For example, for the 16 pixels by 16 pixels mask, the shear strain nearly progressively increases from the beginning of the experiment and reaches its maximum, which is approximately 0.01, at Frame 9000. Then, it linearly decreases and disappears around Frame 12000. On the other hand, for the 32 pixels by 32 pixels mask, the shear strain develops around Frame 8000. Then, it linearly increases and reaches approximately -0.017 at Frame 13500, after which it remains nearly constant.

Moreover, the absolute value of the transverse strain (ε_{22}) remains less than 0.007 until the initiation of fracture for all mask sizes except the 16 pixels by 16 pixels mask. These small values of the transverse strain and nearly zero shear strains for larger mask sizes may suggest an approximately global plane-strain condition. In fact, this is also in agreement with the average triaxiality value of the corresponding mask sizes, which range between 0.51 and 0.54. Note that the plane-strain assumption in the width-direction reaches a theoretical stress triaxiality value of $1/\sqrt{3} \approx 0.58$.

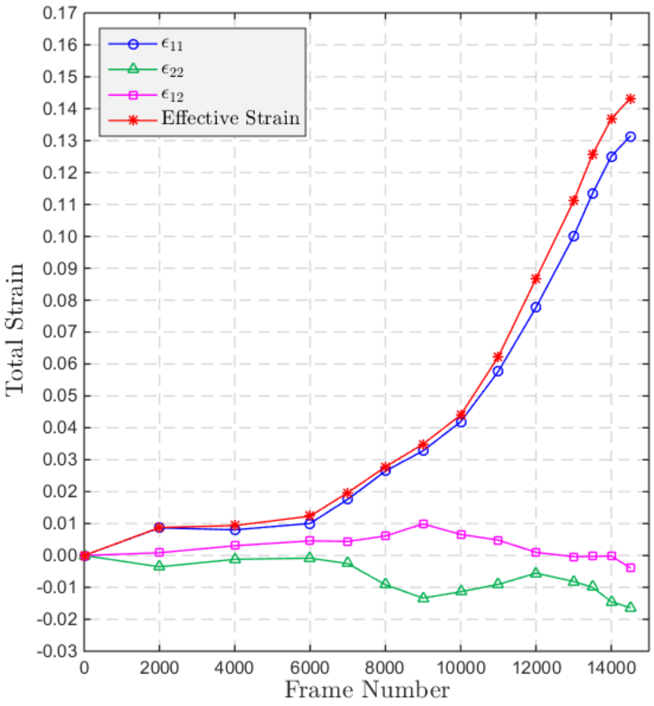

Figure 4-92 Evolution of the natural strain within the masked region during the cylindrical indentation – first approach. Mask size is 16 pixels by 16 pixels (0.219 mm x 0.219 mm).

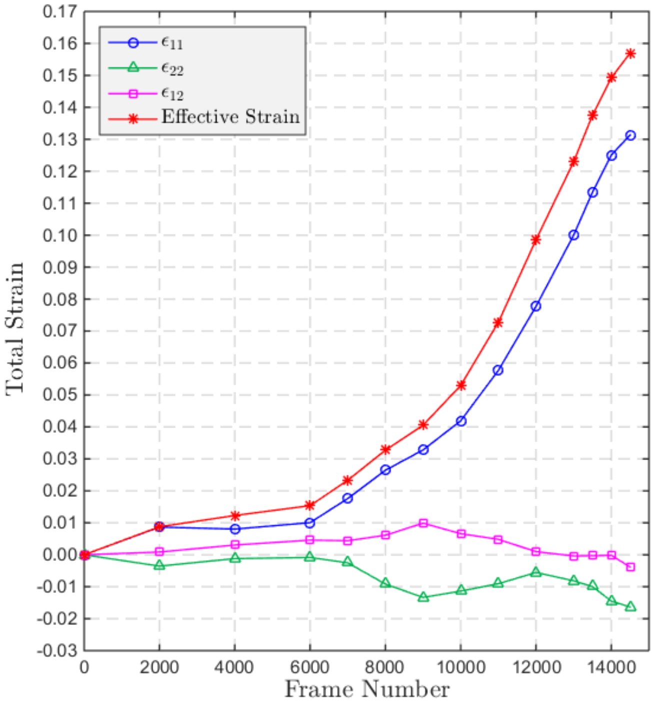

Figure 4-93 Evolution of the natural strain within the masked region during the cylindrical indentation – second approach. Mask size is 16 pixels by 16 pixels (0.219 mm x 0.219 mm).

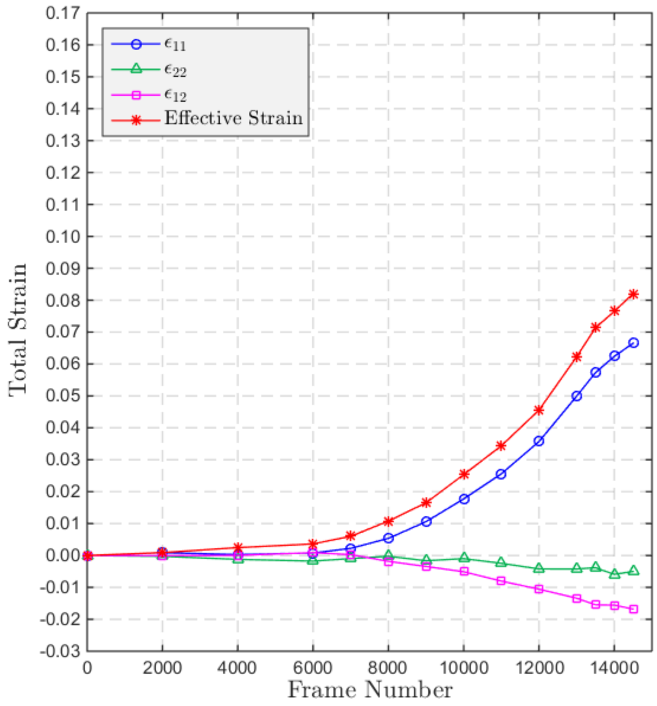

Figure 4-94 Evolution of the natural strain within the masked region during the cylindrical indentation – second approach. Mask size is 32 pixels by 32 pixels (0.438 mm x 0.438 mm).

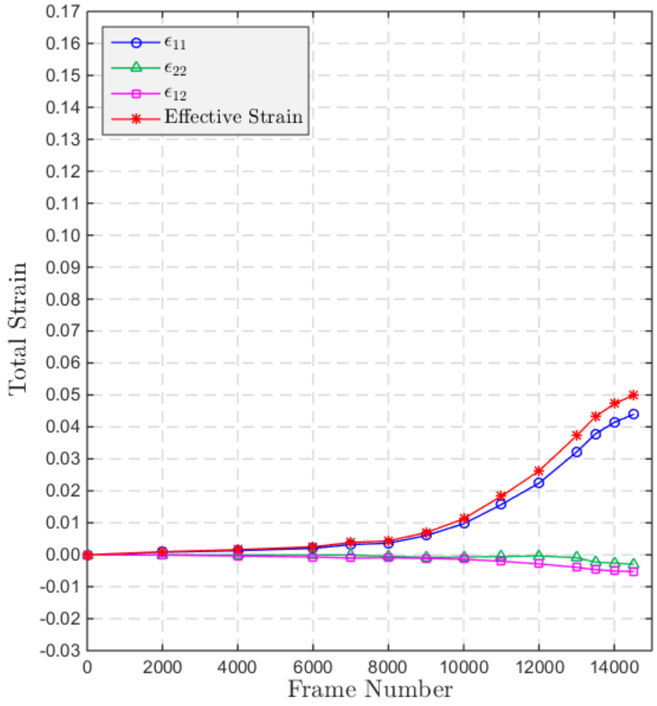

Figure 4-95 Evolution of the natural strain within the masked region during the cylindrical indentation – second approach. Mask size is 64 pixels by 64 pixels (0.877 mm x 0.877 mm).

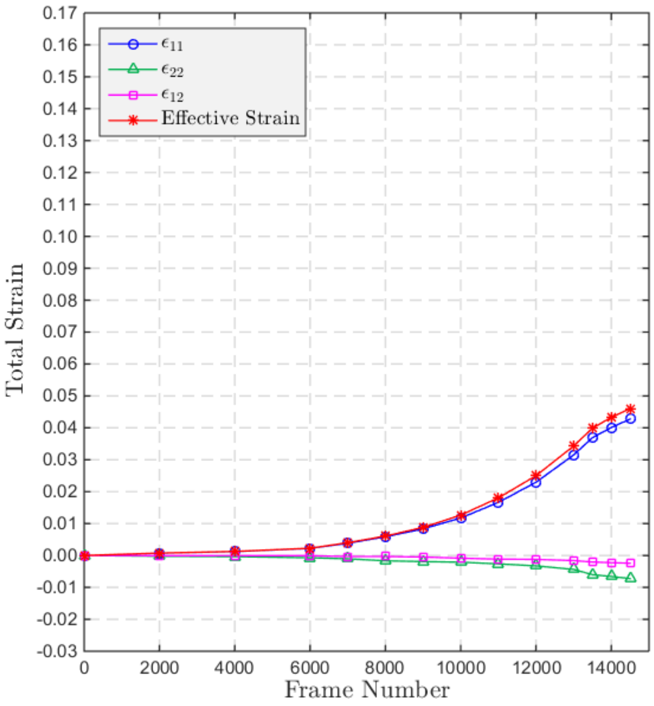

Figure 4-96 Evolution of the natural strain within the masked region during the cylindrical indentation – second approach. Mask size is 128 pixels by 128 pixels (1.754 mm x 1.754 mm).

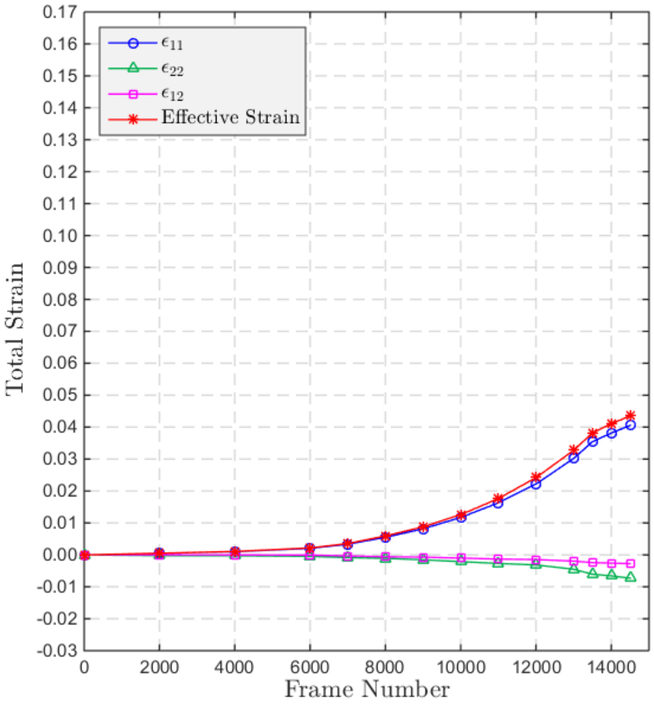

Figure 4-97 Evolution of the natural total strain within the masked region during the cylindrical indentation – second approach. Mask size is 192 pixels by 192 pixels (2.630 mm x 2.630 mm).

The evolution of the true stress (on the left) and the stress triaxiality (on the rigth) within the masked region during cylindrical indentation for different mask sizes are depicted in Figure 4-98, Figure 4-99, Figure 4-100, Figure 4-101, Figure 4-102, Figure 4-103, Figure 4-104, Figure 4-105, Figure 4-106, and Figure 4-107. Note that the state of stress is obtained by assuming that the stress in the longitudinal direction (σ_{11}) remains positive during the entire loading (see Section 4.4.2 for details).

The stress triaxiality at the initiation of the test (i.e., at Frame 2000) varies between 0.35 and 0.57 depending on the mask size. On the other hand, the stress triaxiality at fracture varies between 0.51 and 0.55 for the first approach, whereas it varies between 0.38 and 0.61 for the second approach. In addition, the average stress triaxiality varies between 0.51 and 0.55 for the first approach, while it varies between 0.50 and 0.54 for the second approach. Note that all these variations exhibit no particular order regarding the mask size. Finally, it is interesting to note the instantaneous decrease in the stress triaxiality (as a result of dramatic decreases in normal stresses and increase in shear stress) for the 32 pixels by 32 pixels mask at Frame 6000 as can be seen in Figure 4-101. The author believes that this is caused by the onset of plastic flow (as the plasticity is shear dominated); that is, the region is in the elastic-plastic transition zone. In fact, the true stress-strain curve for different mask sizes, as presented in Figure 4-110, supports this view. Similar behavior being observed for the 64 pixels by 64 pixels at Frame 8000 (see Figure 4-103) demonstrates the expansion/accumulation of plastic flow with time. The reason this behavior is not observed for the 16x16 pixels mask size is that the step increment at the beginning of the test (which was 2000 frames) was sufficiently large such that the plastic flow already starts between Frame 0 and Frame 2000 (see Figure 4-110).

The shear stress is zero or nearly zero for the larger mask sizes (which represent more global behavior) until the initiation of fracture (i.e., Frame 14500), where the analysis was curtailed. On the other hand, it fluctuates for the smaller mask sizes (which represents more local behavior). For instance, it fluctuates between -237 MPa and 205 MPa for the 16 pixels by 16 pixels mask size for the second approach. This fluctuation is between -142 MPa and 207 MPa for the 32 pixels by 32 pixels mask, whereas it is between -117 MPa and 39 MPa for the 64 pixels by 64 pixels mask. Moreover, similar fluctuations are seen in the evolution of the longitudinal stress (σ_{11}) and the transverse stress (σ_{22}) for smaller mask sizes. Nevertheless, the stress state becomes more stable as the mask size is increased.

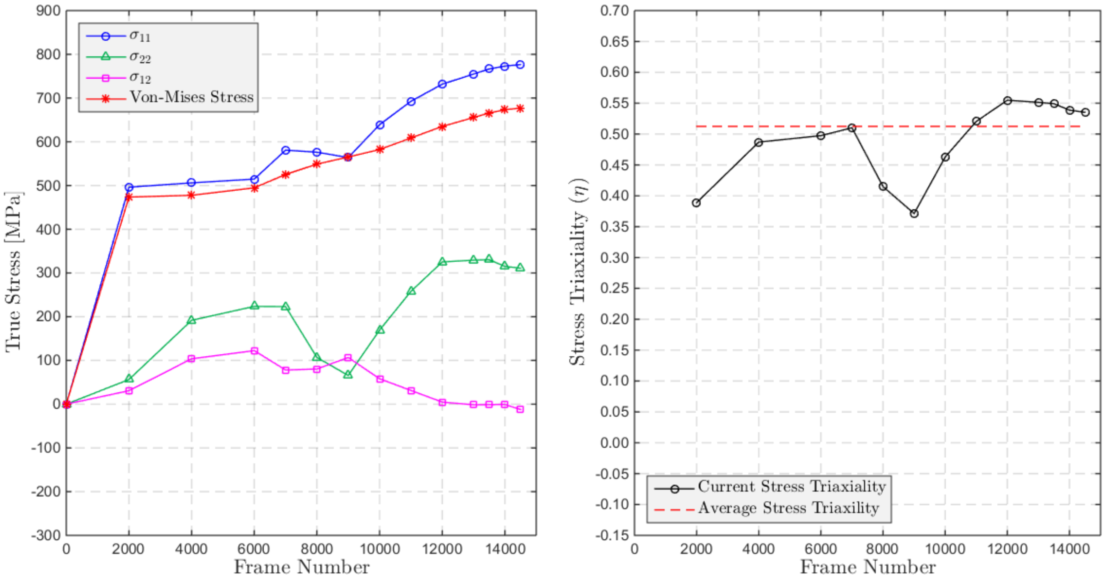

Figure 4-98 Evolution of the true stress (on the left) and the stress triaxiality (on the right) within the masked region during the cylindrical indentation – first approach. Mask size is 16 pixels by 16 pixels (0.219 mm x 0.219 mm).

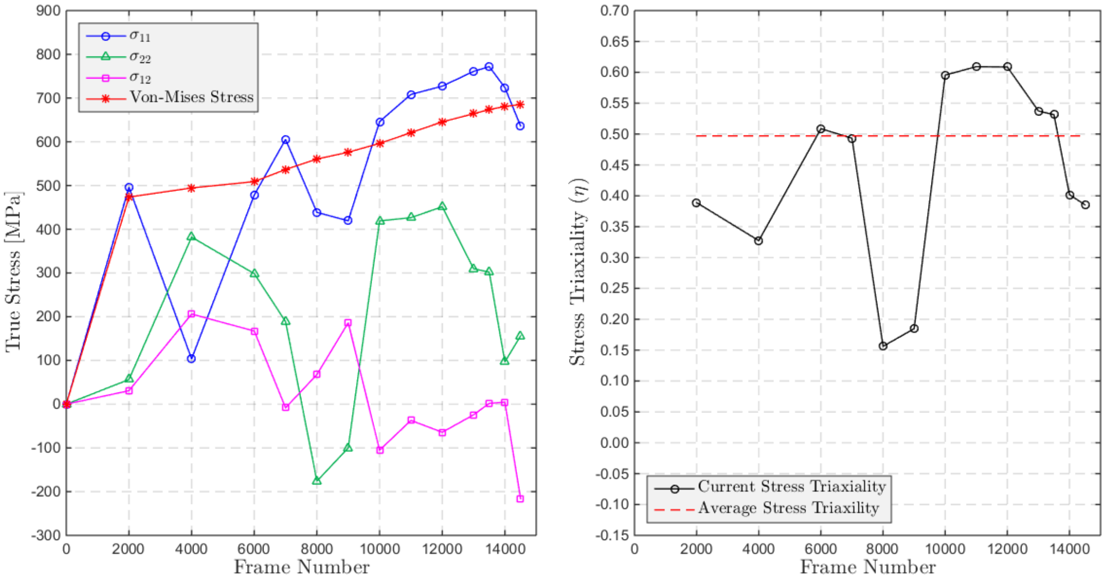

Figure 4-99 Evolution of the true stress (on the left) and the stress triaxiality (on the right) within the masked region during the cylindrical indentation – second approach. Mask size is 16 pixels by 16 pixels (0.219 mm x 0.219 mm).

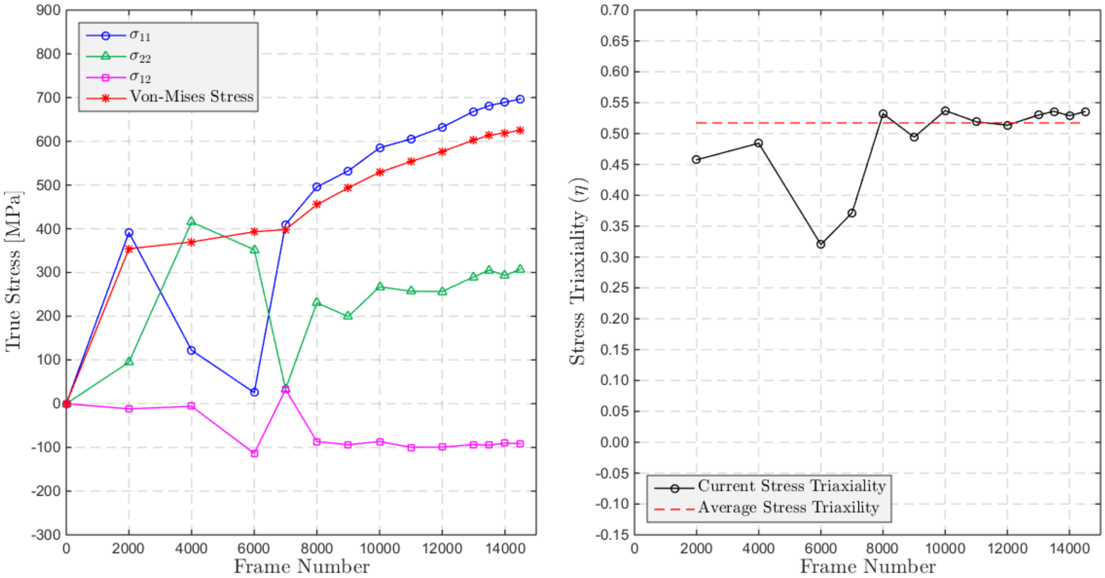

Figure 4-100 Evolution of the true stress (on the left) and the stress triaxiality (on the right) within the masked region during the cylindrical indentation – first approach. Mask size is 32 pixels by 32 pixels (0.438 mm x 0.438 mm).

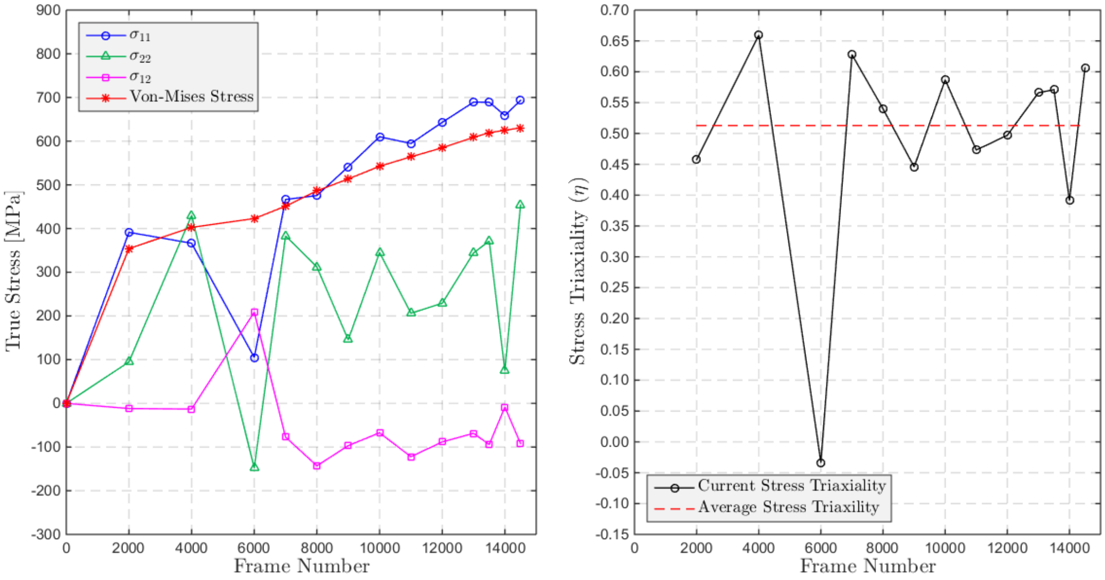

Figure 4-101 Evolution of the true stress (on the left) and the stress triaxiality (on the right) within the masked region during the cylindrical indentation – second approach. Mask size is 32 pixels by 32 pixels (0.438 mm x 0.438 mm).

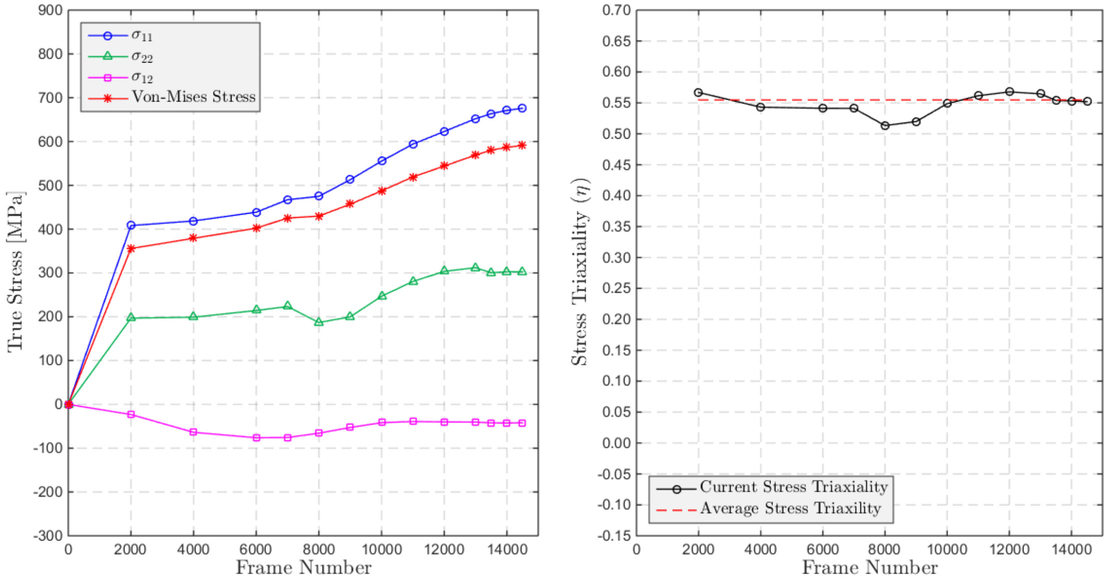

Figure 4-102 Evolution of the true stress (on the left) and the stress triaxiality (on the right) within the masked region during the cylindrical indentation – first approach. Mask size is 64 pixels by 64 pixels (0.877 mm x 0.877 mm).

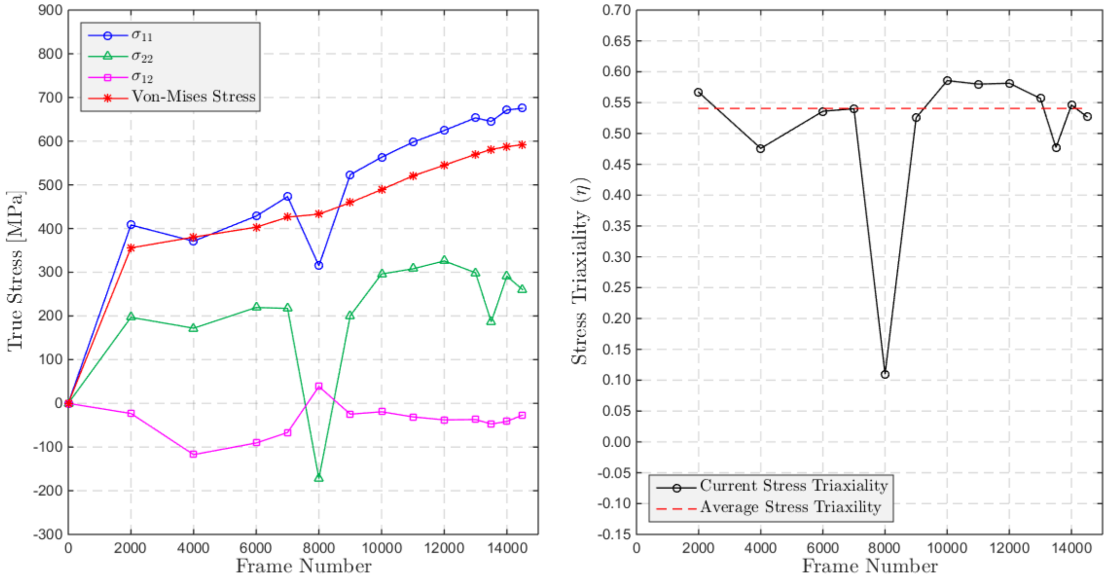

Figure 4-103 Evolution of the true stress (on the left) and the stress triaxiality (on the right) within the masked region during the cylindrical indentation – second approach. Mask size is 64 pixels by 64 pixels (0.877 mm x 0.877 mm).

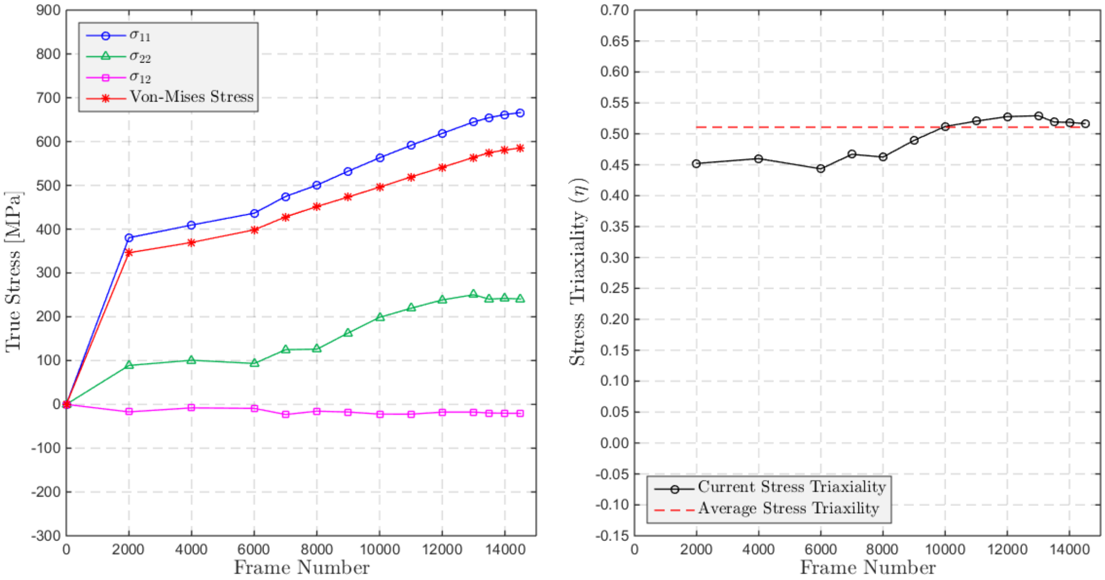

Figure 4-104 Evolution of the true stress (on the left) and the stress triaxiality (on the right) within the masked region during the cylindrical indentation – first approach. Mask size is 128 pixels by 128 pixels (1.754 mm x 1.754 mm).

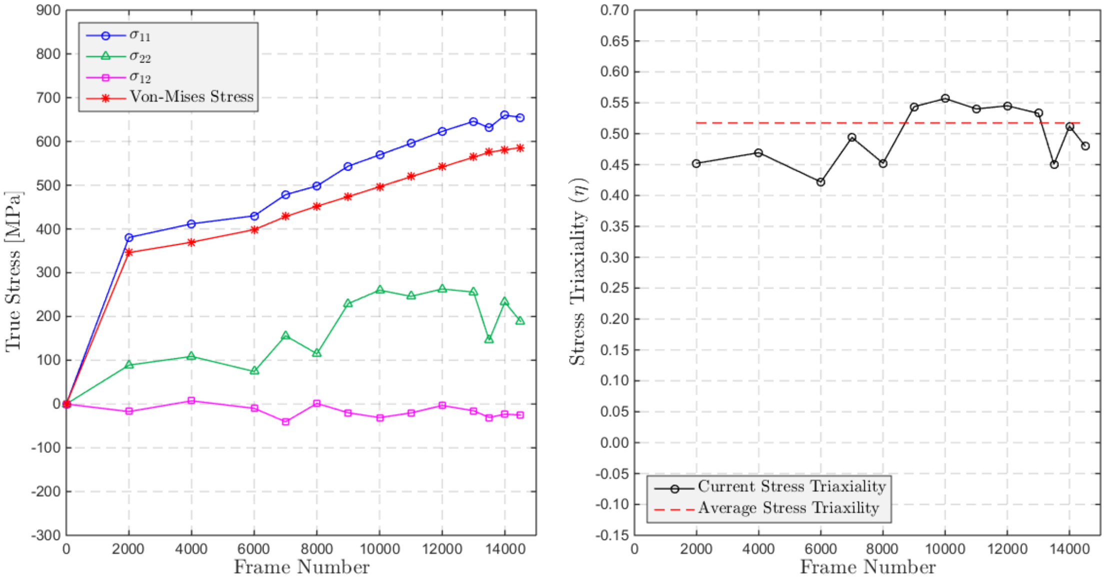

Figure 4-105 Evolution of the true stress (on the left) and the stress triaxiality (on the right) within the masked region during the cylindrical indentation – second approach. Mask size is 128 pixels by 128 pixels (1.754 mm x 1.754 mm).

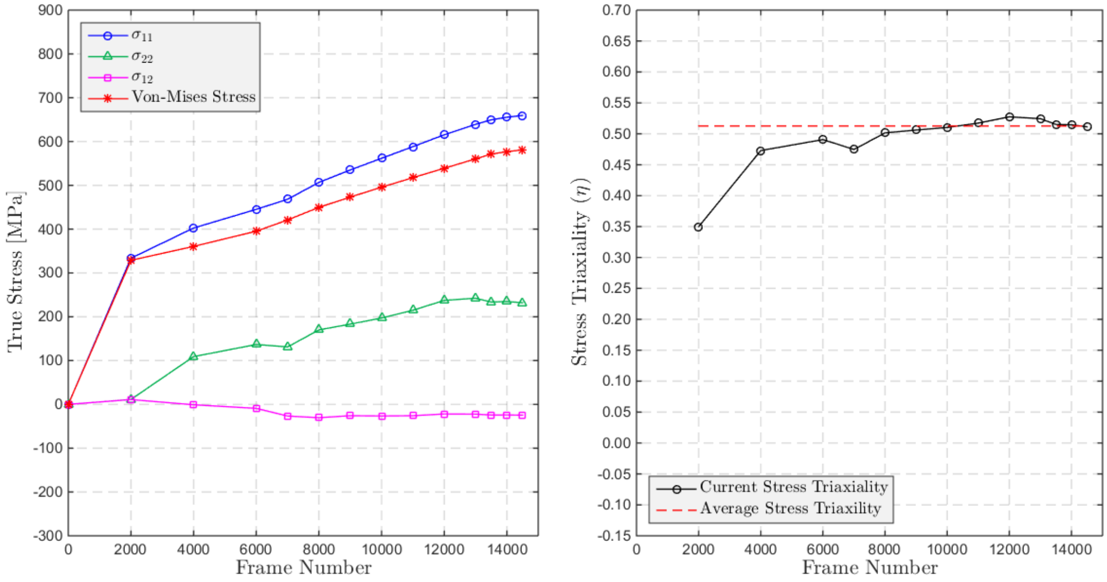

Figure 4-106 Evolution of the true stress (on the left) and the stress triaxiality (on the right) within the masked region during the cylindrical indentation – first approach. Mask size is 192 pixels by 192 pixels (2.630 mm x 2.630 mm).

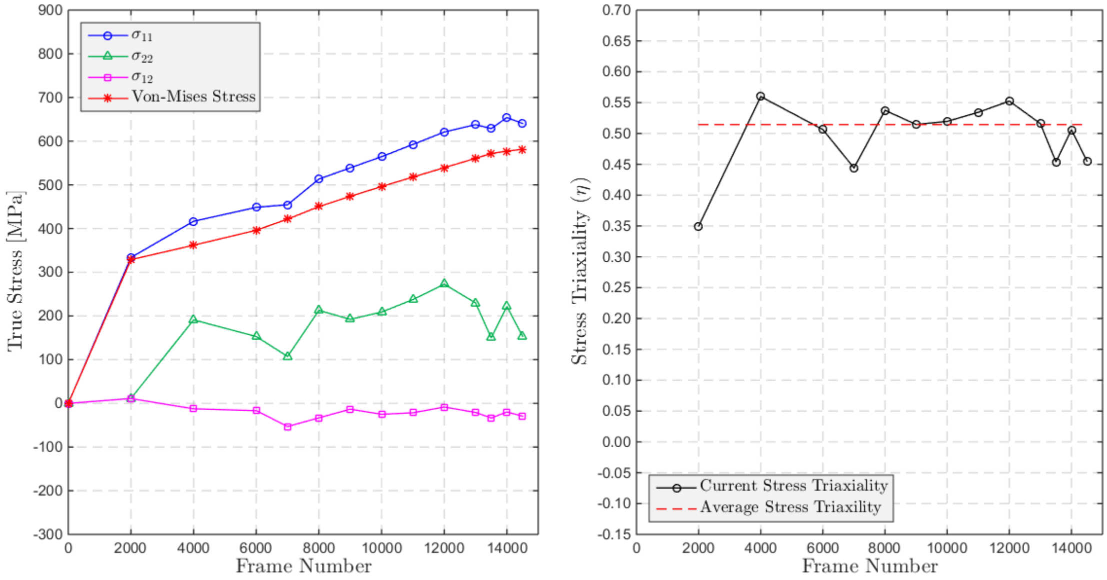

Figure 4-107 Evolution of the true stress (on the left) and the stress triaxiality (on the right) within the masked region during the cylindrical indentation – second approach. Mask size is 192 pixels by 192 pixels (2.630 mm x 2.630 mm).

There are huge stress fluctuations in the second approach at smaller mask sizes, which represent local behavior. Nevertheless, stress fluctuations lose their strength as more global behavior is followed; i.e., as the mask size is increased. Possible reasons that cause these fluctuations are discussed in Section 4.5.1, where the uniaxial test result of the

6mm-width specimen is presented. As discussed and pointed out in Section 4.5.1, the author believes that the stress fluctuations are primarily due to plastic flow localization[52], which occurs at the small scales/mask sizes. The fact that stress deviations die out at larger mask sizes (see Figure 4-105 and Figure 4-107, for example), which are the representations of more global behavior, support this view.

Moreover, the enormous difference between the two approaches, especially at the smaller scales, demonstrates that the loading does not remain proportional[53] at the smaller scales. In other words, if the loading remained proportional, the first and the second approach would have similar, or the same, stress state. From a mathematical point of view, this difference is caused by the instantaneous changes of ψ_1 and ψ_2 (see Equation (4-18), Equation (4-19), Equation (4-26), and Equation (4-28)) in the second approach due to non-proportional loading of the strain history. In addition, the fact that the difference is more pronounced in the smaller mask sizes shows that non-proportional loading is mainly caused by plastic flow localization at small scales. In fact, having small differences (between the two approaches) at larger scales/mask sizes, which are representations of more global behavior, supports this view.

The evolution of the effective strain for the five scales studied from the results of this particular experiment is presented in Figure 4-108. The most prominent feature of the figure from the beginning of the test is the separation of the 16 pixels by 16 pixels mask from the other mask sizes. Moreover, all mask sizes (except the 16 pixels by 16 pixels mask) have the same qualitative behavior and relatively small slopes until Frame 6000, where the 32 pixels by 32 pixels mask starts differing slightly. The reasons for these are discussed in the following pages, where the true stress-strain curves of different mask sizes are presented (see Figure 4-110). However, it is worth noting that these differences are a clear indication of strain localization and that the localization occurs at a scale much smaller than the thickness scale (the thickness of the specimen is 1.588 mm, which corresponds to approximately 116 pixels). In fact, a number of researchers observed grain level strain variations/heterogeneity (see e.g., Raabe et al., 2001; Haltom et al., 2013; Banerjee et al., 2016) in their experimental work and numerical analysis.

---

[52] See Footnote 46.

[53] See Footnote 44.

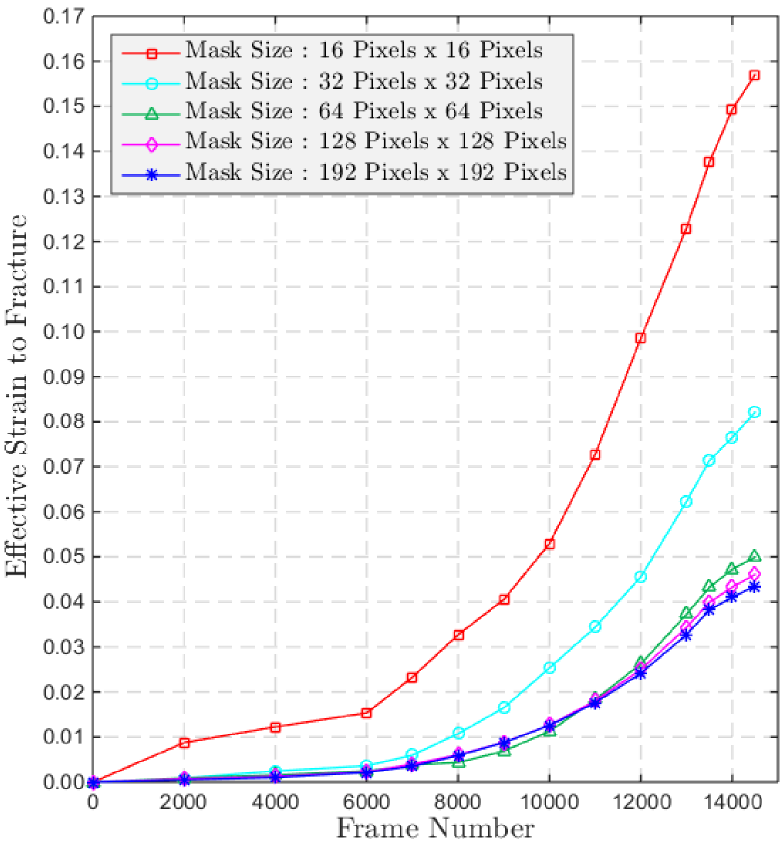

Figure 4-108 Evolution of the effective strain within the masked region the during cylindrical indentation for different mask sizes – second approach. Pixel resolution is approximately 13.7 µm/pixel.

The effect of mask size on failure strain during cylindrical indention can be seen in Figure 4-109. Li & Karr (2009) proposed an analytical relationship for the effect of length scale on the fracture strain (see Equation (4-45)) and the blue solid line shown in the figure is obtained by using this relationship. Note that x represents the length scale, y represents the fracture strain and the constants a and b were determined by a best fit of the experimental results[54]. As can be seen from the figure, there was no sign of convergence of the results as the length scales were reduced.

---

[54] See Footnote 49.

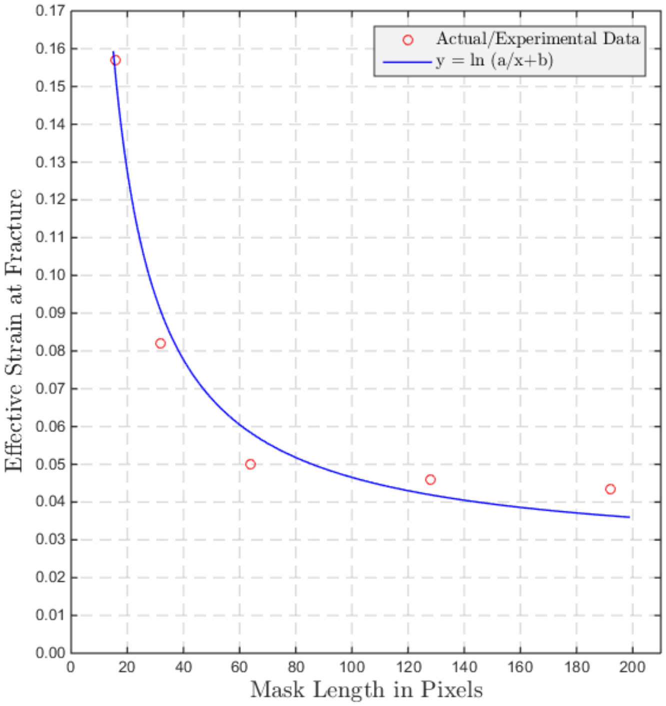

Figure 4-109 Effect of the mask size on failure strain during the cylindrical indention with $y = \ln(a/x + b)$ curve fit – second approach. $a = 2.209$ and $b = 1.026$. Pixel resolution is approximately 13.7 μm/pixel.

The average stress triaxiality (η_{ave}), the stress triaxiality at fracture (η_{frac}), and the effective strain at fracture (ε_{eff}^{f}) for both approaches are summarized in Table 4-5. The effective strain at fracture increases in a non-linear manner as the mask size is decreased, a sign of localization, while the average stress triaxiality or stress triaxiality at fracture exhibits no particular order regarding the mask size. It is worth noting that the effective strain obtained by the 16 pixels by 16 pixels mask size is more than three times as large as the effective strain obtained by the 192 pixels by 192 pixels mask size. Finally, as can be seen from Table 4-5, the maximum difference between the effective strain at fracture for the two different approaches is 8.9%, which occurs on the smallest mask size.

Table 4-5 Summary of the average stress triaxiality (η_{ave}), the stress triaxiality at fracture (η_{frac}), and the effective strain at fracture (ε_{eff}^{f}) for cylindrical indenter experiment of 18mm-width specimen without groove with an indentation speed of 0.6 inch/second.

	Mask size [pixels]	η_{ave}	η_{frac}	ε_{eff}^{f}
First approach	16x16	0.512	0.535	0.143
	32x32	0.517	0.536	0.077
	64x64	0.555	0.552	0.049
	128x128	0.511	0.516	0.046
	192x192	0.513	0.511	0.043
Second approach	16x16	0.497	0.385	0.157
	32x32	0.513	0.606	0.082
	64x64	0.540	0.527	0.050
	128x128	0.517	0.480	0.046
	192x192	0.514	0.455	0.043

Finally, the true stress-strain curves for different mask sizes are presented together in Figure 4-110. Note that the flow rule and the same power-law hardening relationship with the same coefficients (i.e., the strength coefficient of $\Omega = 868.4$ MPa and the hardening exponent of $n = 0.128$) are used here as for the uniaxial tests, presented in Section 4.5, to obtain the components of the stress tensor (see Section 4.4.2 for details) of the DIC analysis. In addition, the stress-strain curve obtained via the MTS machine (represented by dashed lines) is superposed on the same figure for comparison purposes[55]. Solid lines with markers are obtained by the digital image correlation analysis and the last marker of each color represents the fracture initiation point for different mask sizes as the DIC analyses are conducted to the point of fracture initiation. Finally, it is worth noting that as the plastic constitutive and stress-strain relationships that are used (the hardening-law and the flow rule) are independent of a length scale, the effective stress-strain curve is independent of the mask size as well and is as expected.

---

[55] See Footnote 51.

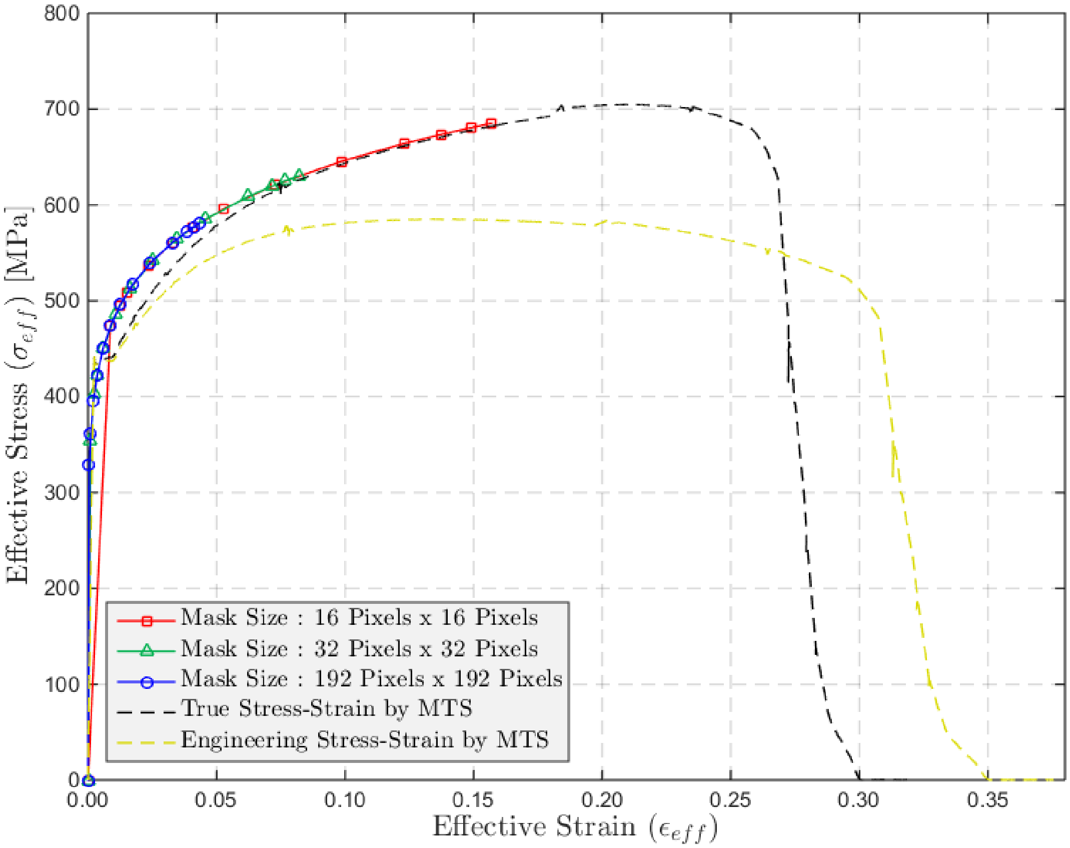

Figure 4-110 True stress-strain curve of the cylindrical indenter test for different mask sizes – second approach. Pixel resolution is approximately 13.7 µm/pixel. Solid lines with markers are obtained by digital image correlation (DIC) analysis while dashed lines are the results from the MTS machine.

It is interesting to note that the 'masked region' is still in the elastic-region until Frame 6000 for the 32 pixels by 32 pixels mask and until Frame 8000 for the 192 pixels by 192 pixels mask. This indicates that all mask sizes except the 16 pixels by 16 pixels mask remain in the elastic-region until Frame 6000. Nevertheless, the step increment at the beginning of the test (which was 2000 frames) was sufficiently large such that the plastic flow starts at a very small scale (i.e., 16 pixels by 16 pixels mask), whereas all other mask sizes are still in the elastic-region. This is the reason that effective strain as a function of frame number for the 16 pixels by 16 pixels mask differs from the others from the beginning of the test (see Figure 4-108). Note that this also causes the 16 pixels by pixels mask to have a different slope (in the true stress-strain curve, presented in Figure 4-110) than the others at the initiation of the experiment. However, they follow the same path immediately thereafter.

4.6.1.2 Test 3

This experiment was a repetition of 'Test 0'. An indentation speed of 0.6 inch/second was applied to the center of the test specimen with 6000 digital images recorded per second. The pixel resolution was approximately 14.0 µm/pixel. Note that the high speed camera and the experimental device were snychronized in this experiment.

Fracture initiates around Frame 21775; that is, following an approximately 55.309 mm indentation. Note that this indentation amount is almost as twice large as the one for Test 0, presented in the previous sub-section. This difference may have been caused by many reasons. One of them can be the difference in the space position of fracture initiation; that is, the fracture may have initiated on the surface of the specimen considered in the previous sub-section, whereas it may have initiated inside the specimen considered in this sub-section and the time until it reaches the surface may cause this difference. Nevertheless, it is worth noting that no fractography has been conducted for either of the specimens; therefore, it is not exactly known whether the fracture initiates on the surface or within. Another reason can be the state of friction at the cylinder/specimen interface; that is, different states of friction may have caused or contribute to this difference as well.

DIC analyses are conducted for four different mask sizes, that is, the 16 pixel by 16 pixel mask (the smallest mask size), the 32 pixel by 32 pixel mask, the 64 pixels by 64 pixels mask, and the 128 pixels by 128 pixels mask, which roughly equals the thickness of the specimen (the thickness of the specimen is 1.588 mm). Results are summarized in Table 4-6.

As can be seen from Table 4-5 and Table 4-6, the fracture strain is much larger in the current experiment (i.e., Test 3) for all mask sizes investigated. This is primarily due to huge difference between the indentation displacements (of the two experiments) at the onset of fracture. The indentation displacement of the current experiment is nearly as twice large as the one obtained for Test 0. On the other hand, the average stress triaxiality and the stress triaxiality at fracture are lower in the current experiment (i.e., Test 3).

Table 4-6 Summary of the average stress triaxiality (η_{ave}), the stress triaxiality at fracture (η_{frac}), and the effective strain at fracture (ε_{eff}^{f}) for cylindrical indenter experiment of 18mm-width specimen without groove with an indentation speed of 0.6 inch/second. This experiment was a repetition of 'Test 0', presented in the previous sub-section.

	Mask size [pixels]	η_{ave}	η_{frac}	ε_{eff}^{f}
First approach	16x16	0.391	0.423	0.616
	32x32	0.424	0.423	0.668
	64x64	0.429	0.419	0.619
	128x128	0.421	0.407	0.597
Second approach	16x16	0.396	0.513	0.689
	32x32	0.405	0.459	0.683
	64x64	0.407	0.452	0.623
	128x128	0.396	0.451	0.602

4.6.1.3 Test 1

An indentation speed of 1.2 inch/second was applied to the center of the test specimen with 7500 digital images recorded per second. The pixel resolution was approximately 13.7 microns per pixel. Note that the high speed camera and the experimental device were not snychronized in this experiment. A very small lag in the recording might thus be possible.

Fracture initiates around Frame 9000; that is, following an approximately 36.576 mm indentation.

DIC analyses are conducted for three different mask sizes, that is, the 16 pixel by 16 pixel mask (the smallest mask size), the 32 pixel by 32 pixel mask, and the 128 pixels by 128 pixels mask, which roughly equals the thickness of the specimen (the thickness of the specimen is 1.588 mm). Results are summarized in Table 4-7.

Table 4-7 Summary of the average stress triaxiality (η_{ave}), the stress triaxiality at fracture (η_{frac}), and the effective strain at fracture (ε_{eff}^{f}) for cylindrical indenter experiment of 18mm-width specimen without groove with an indentation speed of 1.2 inch/second.

	Mask size [pixels]	η_{ave}	η_{frac}	ε_{eff}^{f}
First approach	16x16	0.320	0.501	0.079
	32x32	0.587	0.551	0.077
	128x128	0.492	0.473	0.049
Second approach	16x16	0.515	0.517	0.121
	32x32	0.526	0.413	0.082
	128x128	0.460	0.454	0.049

4.6.1.4 Test 2

An indentation speed of 2.4 inch/second was applied to the center of the test specimen with 7500 digital images recorded per second. The pixel resolution was approximately 14.0 microns per pixel. Note that the high speed camera and the experimental device were not snychronized in this experiment. A very small lag in the recording might thus be possible.

Fracture initiates around Frame 9031; that is, following an approximately 73.404 mm indentation.

DIC analyses are conducted for three different mask sizes, that is, the 16 pixel by 16 pixel mask (the smallest mask size), the 32 pixel by 32 pixel mask, and the 128 pixels by 128 pixels mask, which roughly equals the thickness of the specimen (the thickness of the specimen is 1.588 mm). Results are summarized in Table 4-8.

As can be seen from Table 4-8, fracture strains are huge compared to the results of the other three experiments (see Table 4-5, Table 4-6, and Table 4-7). For example, fracture strain of the current experiment for 128 pixels by 128 pixels mask in the second approach is 27% more than the one obtained for Test 3 and it is more than fifteen times as large as the one obtained for Test 1. One of the reasons for this difference is huge indentation displacement of the current experiment at the onset of fracture (which is approximately

73.404 mm). The indentation displacement is 33% more than the one obtained for Test 3 and as twice large as the one obtained for Test 1.

Table 4-8 Summary of the average stress triaxiality (η_{ave}), the stress triaxiality at fracture (η_{frac}), and the effective strain at fracture (ε_{eff}^{f}) for cylindrical indenter experiment of 18mm-width specimen without groove with an indentation speed of 2.4 inch/second.

	Mask size [pixels]	η_{ave}	η_{frac}	ε_{eff}^{f}
First approach	16x16	0.311	0.493	0.898
	32x32	0.392	0.464	0.806
	128x128	0.408	0.413	0.744
Second approach	16x16	0.393	0.565	1.073
	32x32	0.390	0.519	0.894
	128x128	0.403	0.502	0.763

4.6.2 Analysis of 18mm-Width Specimen with 4mm Groove

The isometric view and technical drawing of the test specimen are depicted in Figure 4-111 and Figure 4-112, respectively.

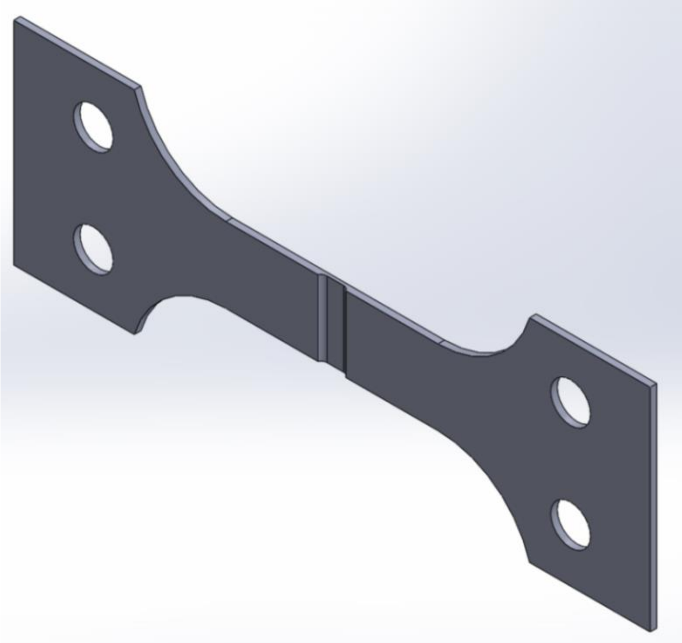

Figure 4-111 Isometric view of the 18mm-width specimen with 4mm groove (Courtesy of James Gose and Haocheng Pan).

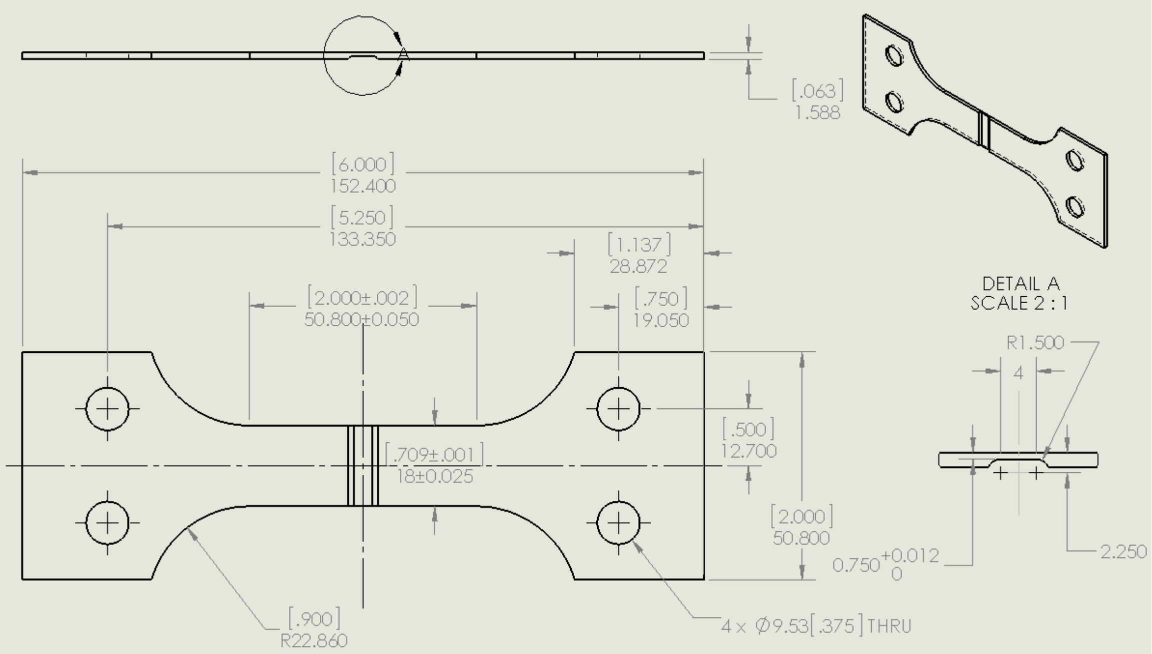

Figure 4-112 Technical drawing of the 18mm-width specimen with 4mm groove (Courtesy of James Gose and Haocheng Pan).

4.6.2.1 Test 1

An indentation speed of 0.6 inch/second was applied to the center of the test specimen with 7500 digital images recorded per second. The pixel resolution was approximately 13.7 microns per pixel. Note that the high speed camera and the experimental device were not snychronized in this experiment. A very small lag in the recording might thus be possible.

Frames from the video recording are presented in Figure 4-113, Figure 4-114, Figure 4-115, Figure 4-116, Figure 4-117, Figure 4-118, Figure 4-119, and Figure 4-120. The vertical direction and the horizontal direction are the longitudinal direction and the width direction of the specimen, respectively. The regions depicted are the exploded views and their dimensions are approximately 1165–1195 pixels by 685–715 pixels.

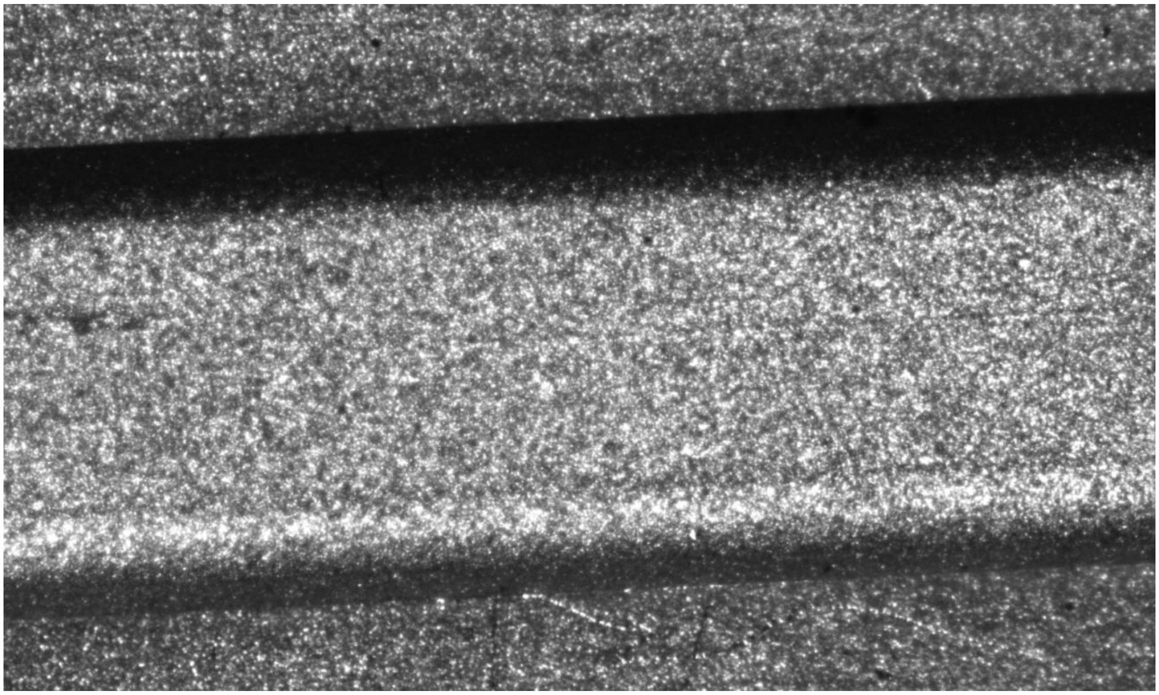

Figure 4-113 Nital etched AH32 steel 18mm-width-specimen with 4mm groove at Frame 0, that is, in the undeformed state.

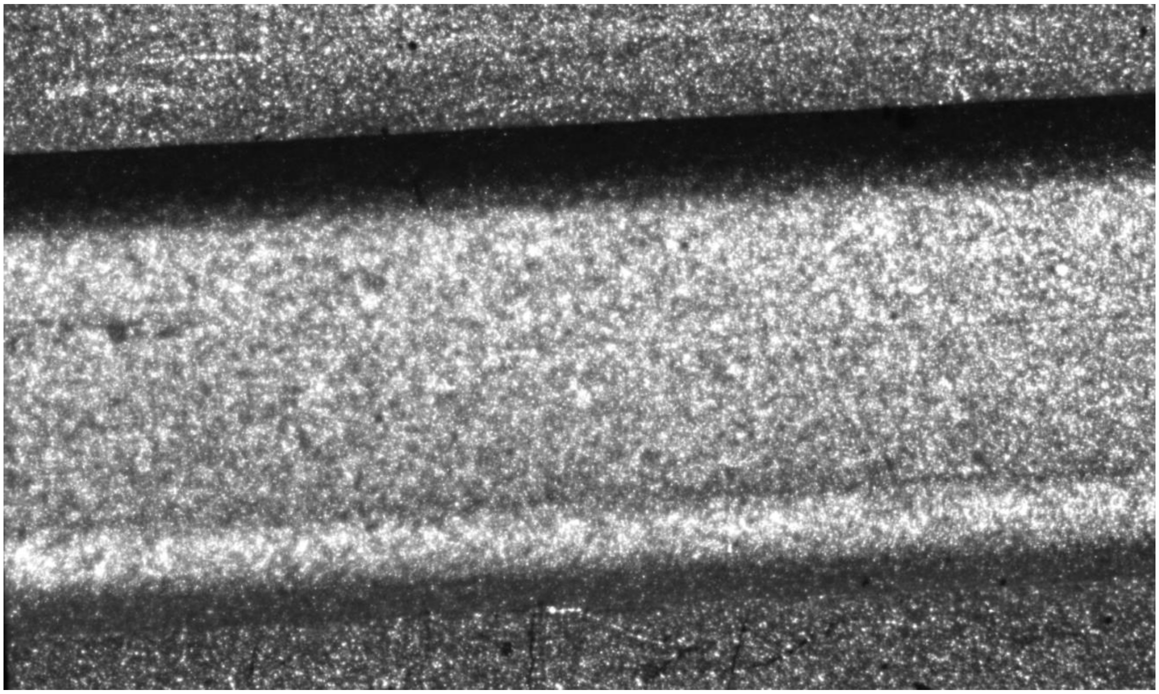

Figure 4-114 Nital etched AH32 steel 18mm-width-specimen with 4mm groove at Frame 7500, that is, a 15.240 mm indentation had been applied.

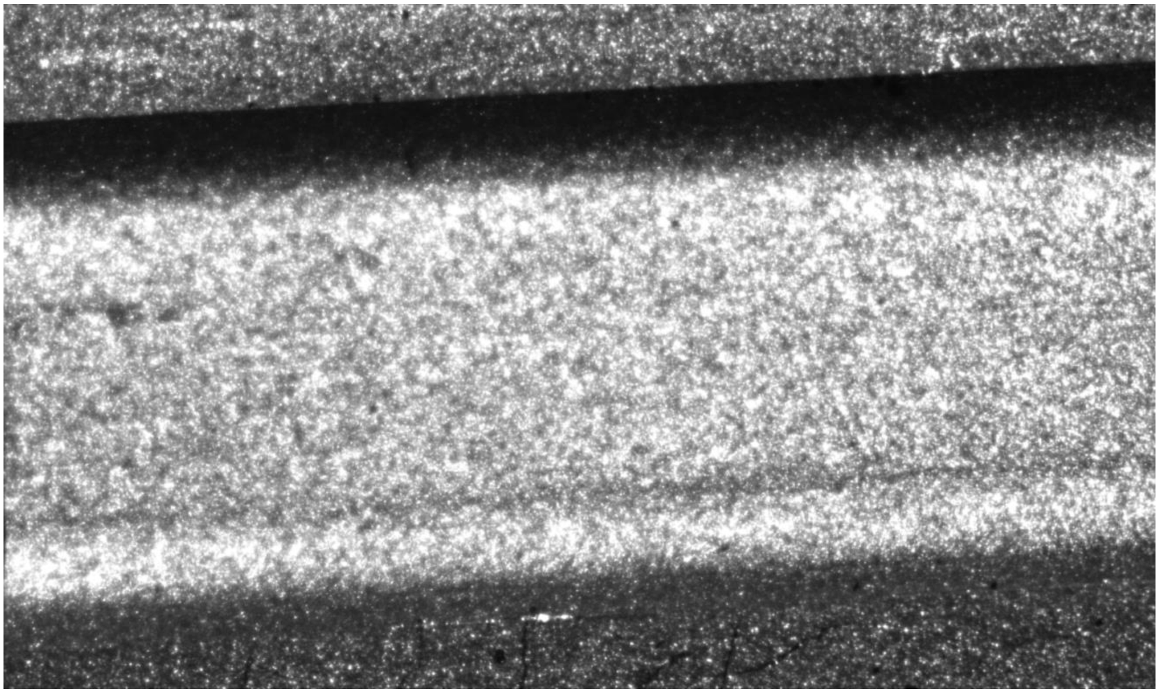

Figure 4-115 Nital etched AH32 steel 18mm-width-specimen with 4mm groove at Frame 13000, that is, a 26.416 mm indentation had been applied.

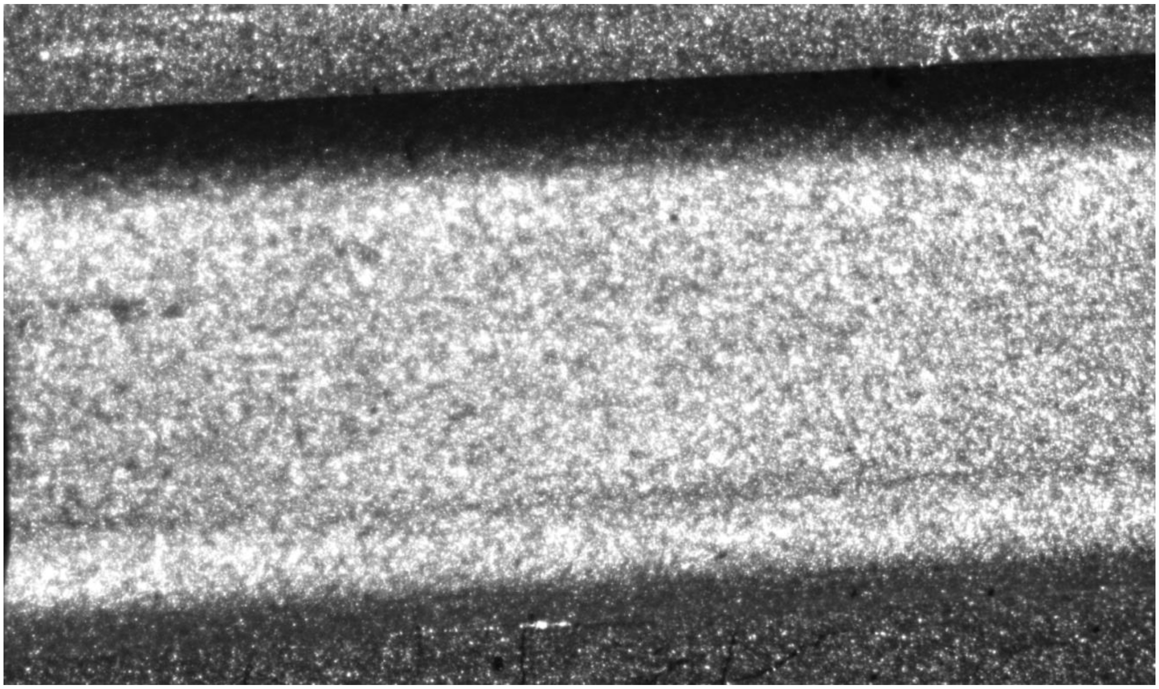

Figure 4-116 Nital etched AH32 steel 18mm-width-specimen with 4mm groove at Frame 13500, that is, a 27.432 mm indentation had been applied.

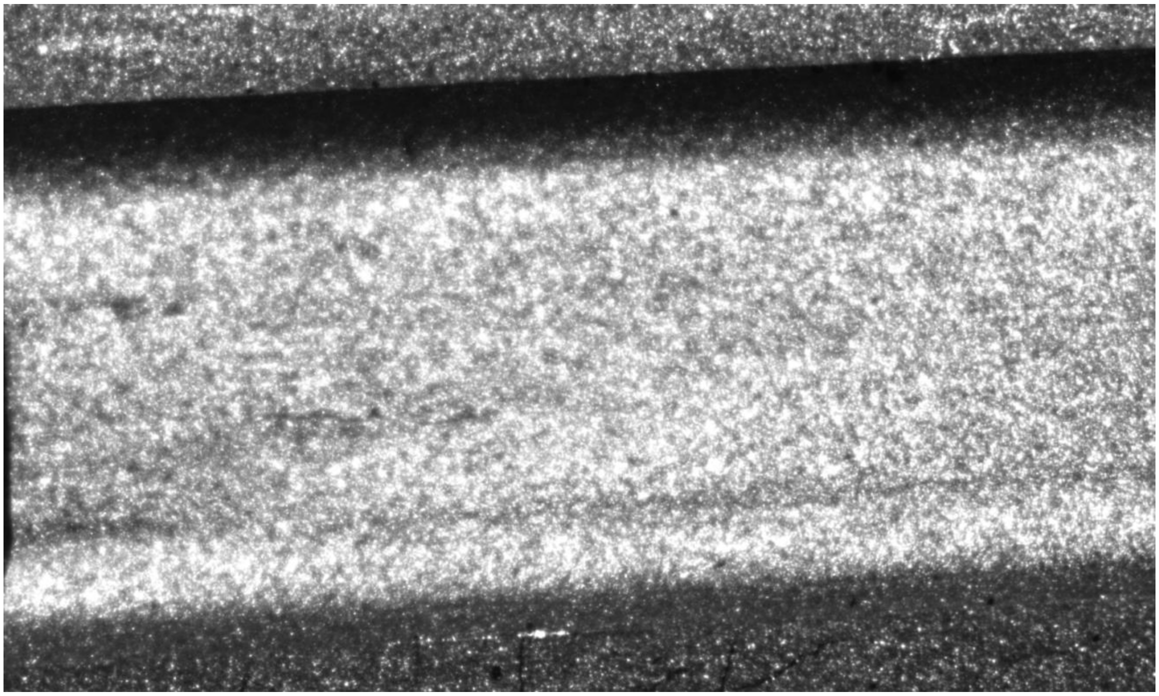

Figure 4-117 Nital etched AH32 steel 18mm-width-specimen with 4mm groove at Frame 13800, that is, a 28.042 mm indentation had been applied.

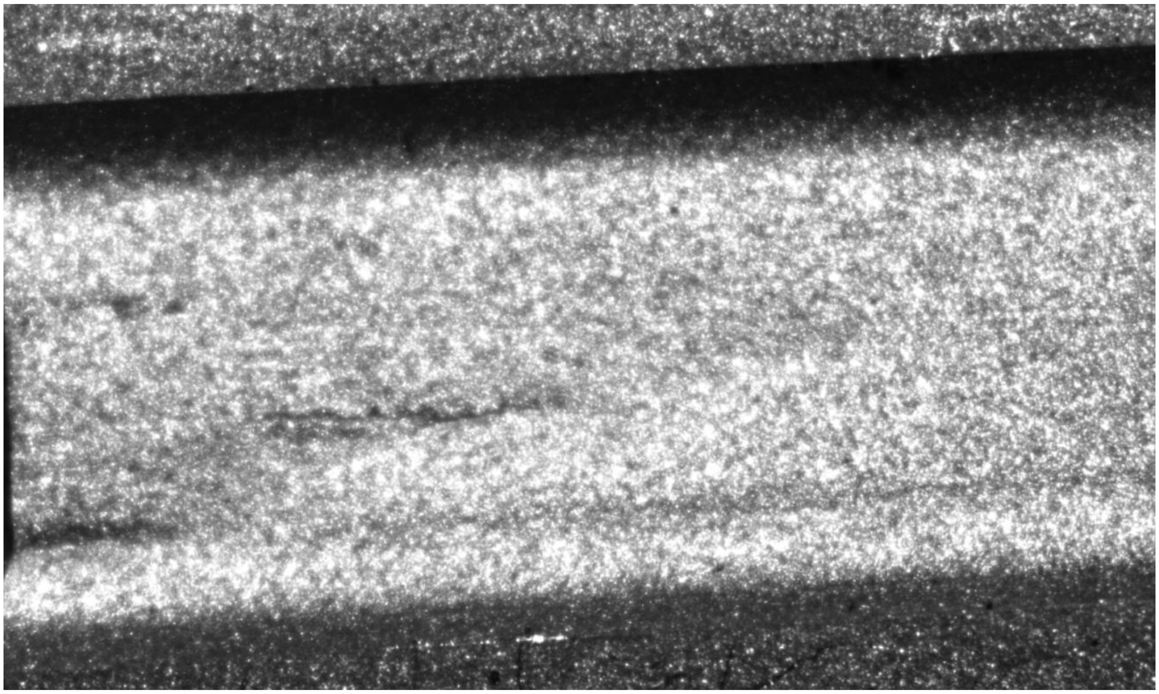

Figure 4-118 Nital etched AH32 steel 18mm-width-specimen with 4mm groove at Frame 13880, that is, a 28.204 mm indentation had been applied.

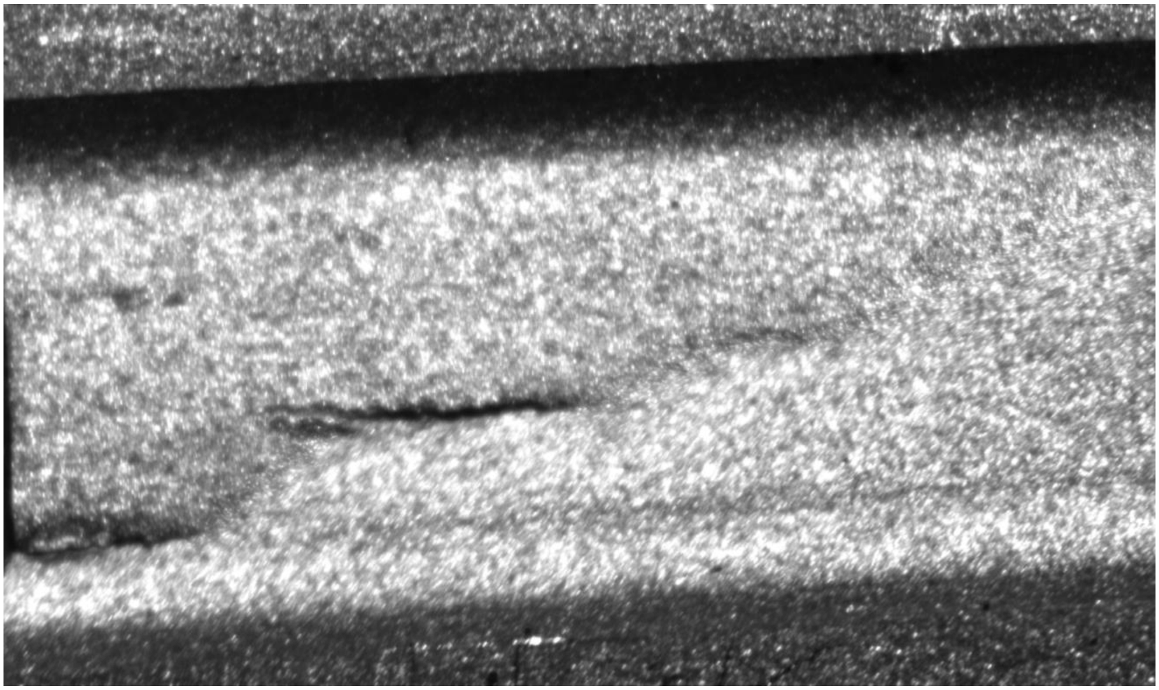

Figure 4-119 Nital etched AH32 steel 18mm-width-specimen with 4mm groove at Frame 13883, that is, a 28.210 mm indentation had been applied.

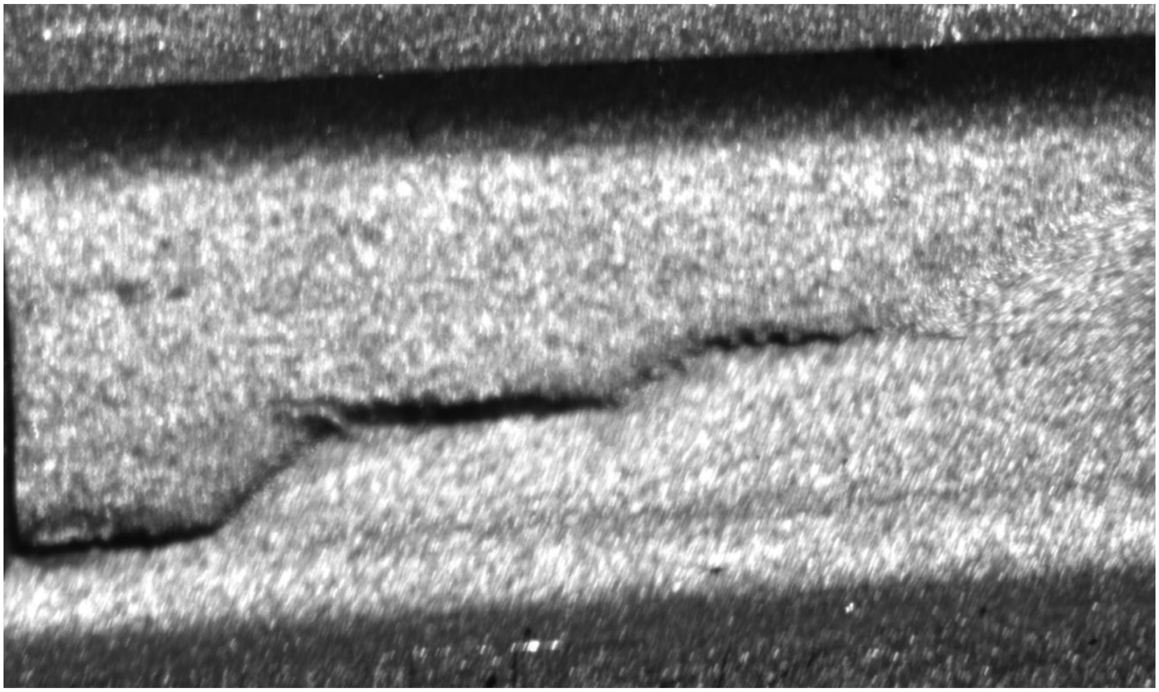

Figure 4-120 Nital etched AH32 steel 18mm-width-specimen with 4mm groove at Frame 13884, that is, a 28.212 mm indentation had been applied.

Fracture initiates around Frame 13250; that is, following an approximately 26.924 mm indentation. In fact, the initial crack can be seen at Frame 13500, depicted in Figure

4-116. Moreover, the final stages of the crack propagation are presented in Figure 4-118, Figure 4-119, and Figure 4-120.

The evolution of the natural strain and the effective strain within the masked region during cylindrical indentation for different mask sizes are presented in Figure 4-121, Figure 4-122, Figure 4-123, Figure 4-124, and Figure 4-125. Note that the graph for the first approach with a 16 pixels by 16 pixels mask is also presented (see Figure 4-121) to show the different qualitative behavior of the effective strain between Frame 2000 and Frame 4000. The reason for this difference is that the first approach is based on the current strain, whereas the second approach is based on the increment in strain. As the current strain components drop to near zero at Frame 4000, the effective strain in the first approach decreases to near zero as well. On the other hand, as there are increments in the strain components from Frame 2000 to Frame 4000 (although these increments are negative), effective strain increases as well. However, this qualitative difference becomes smaller as the mask sizes are increased. The comparison of the two approaches for all mask sizes is presented in Table 4-9, at the end of this sub-section.

The shear strain remains zero or nearly zero for all mask sizes until the later stages of the experiment. On the other hand, shear strain starts developing around Frame 11000 for the 16 pixels by 16 pixels mask, while it starts developing around Frame 12500 and decreases linearly until the initiation of fracture for the 32 pixels by 32 pixels mask. However, the absolute value of the shear strain always remains below 0.01.

The discussion on the evolution of the longitudinal strain (ε_{11}) and the transverse strain (ε_{22}) is presented in the following pages, where a separate figure is presented for each (i.e., Figure 4-134 and Figure 4-135).

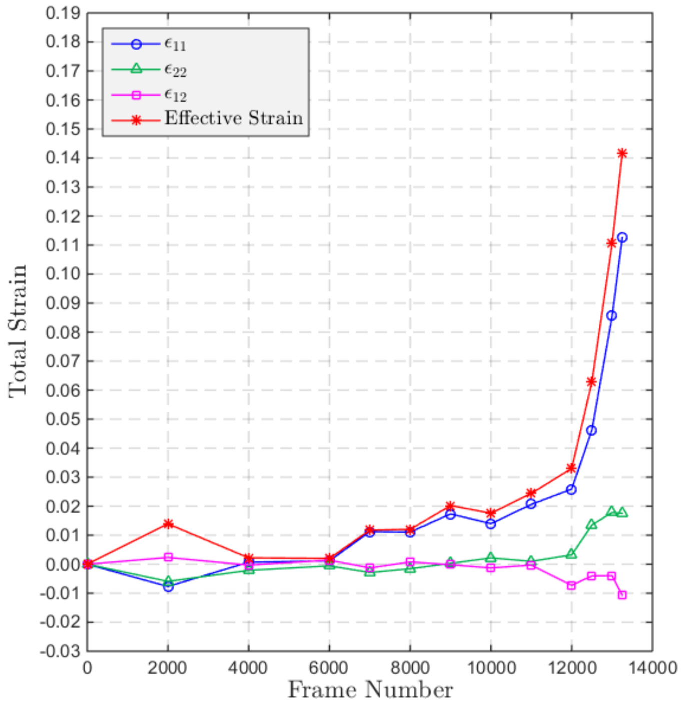

Figure 4-121 Evolution of the natural strain within the masked region during the cylindrical indentation – first approach. Mask size is 16 pixels by 16 pixels (0.219 mm x 0.219 mm).

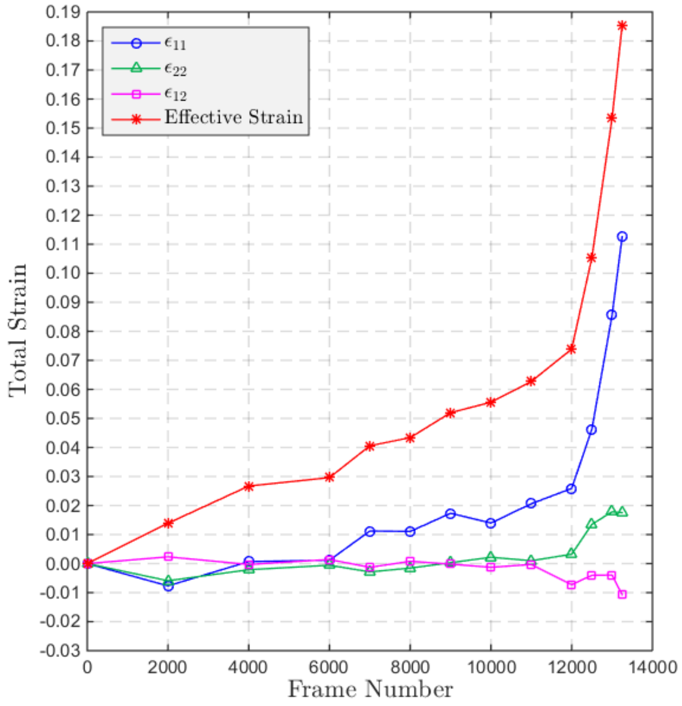

Figure 4-122 Evolution of the natural strain within the masked region during the cylindrical indentation – second approach. Mask size is 16 pixels by 16 pixels (0.219 mm x 0.219 mm).

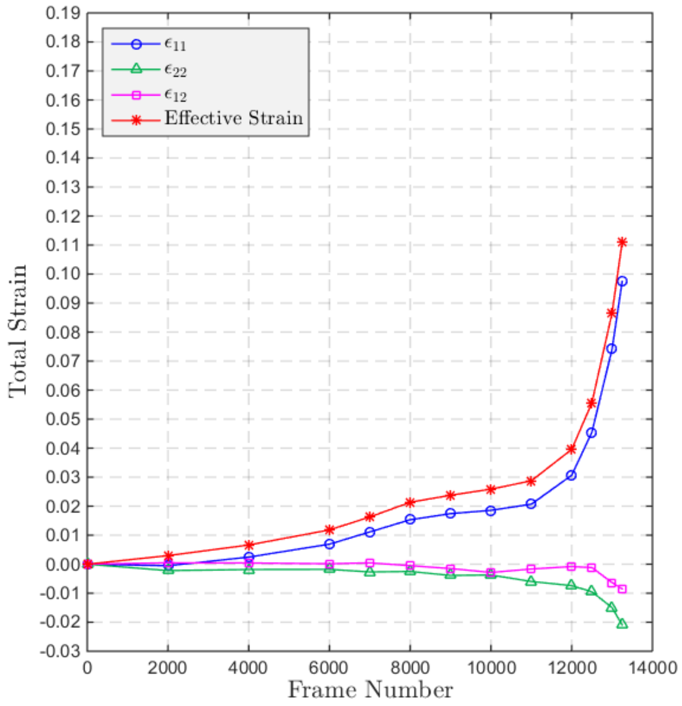

Figure 4-123 Evolution of the natural strain within the masked region during the cylindrical indentation – second approach. Mask size is 32 pixels by 32 pixels (0.438 mm x 0.438 mm).

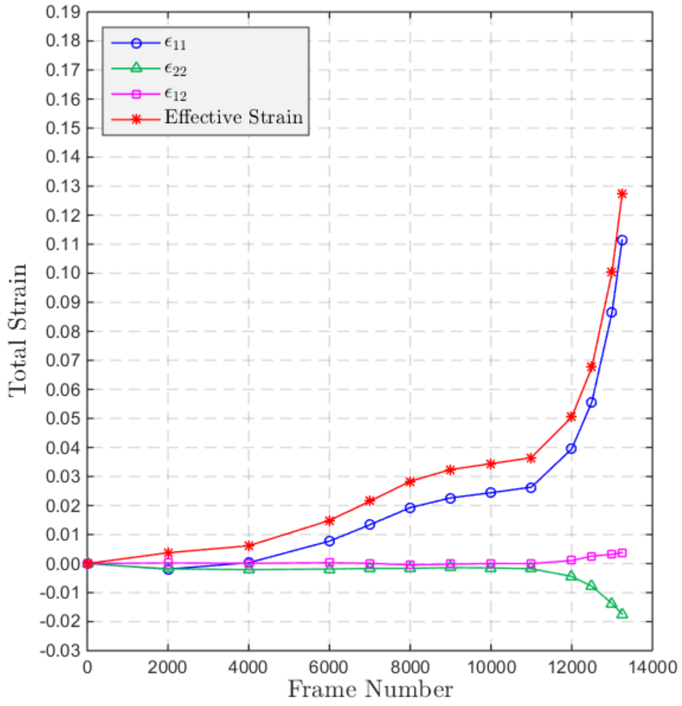

Figure 4-124 Evolution of the natural strain within the masked region during the cylindrical indentation – second approach. Mask size is 64 pixels by 64 pixels (0.877 mm x 0.877 mm).

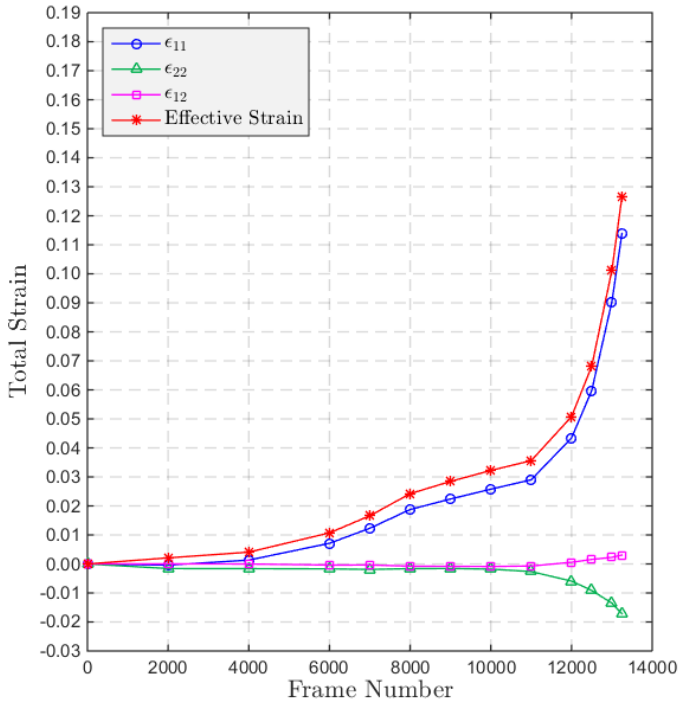

Figure 4-125 Evolution of the natural strain within the masked region during the cylindrical indentation – second approach. Mask size is 128 pixels by 128 pixels (1.754 mm x 1.754 mm).

The evolution of the true stress and the stress triaxiality within the masked region during cylindrical indentation for different mask sizes are depicted in Figure 4-126, Figure 4-127, Figure 4-128, Figure 4-129, Figure 4-130, Figure 4-131, Figure 4-132, and Figure 4-133. Note that the state of stress is obtained by assuming that the stress in the longitudinal direction (σ_{11}) remains positive during the entire loading (see Section 4.4.2 for details).

The stress triaxiality at the initiation of the test (i.e., at Frame 2000) varies between 0.62 and 0.66 depending on the mask size. On the other hand, the stress triaxiality at fracture varies between 0.49 and 0.61 for the first approach, whereas it varies between 0.47 and 0.56 for the second approach. In addition, interestingly, the stress triaxiality at fracture nearly equals the value of the average stress triaxiality. Note that all these variations exhibit no particular order regarding the mask size. Finally, the theoretical stress triaxiality for this experiment is $1/\sqrt{3} \approx 0.58$ assuming a plane-strain condition in the width-direction.

The shear stress is zero or nearly zero for the larger mask sizes (which represent more global behavior) until the initiation of fracture (i.e., Frame 13250), where the analysis was curtailed. On the other hand it fluctuates for the smaller mask sizes (which represents more local behavior). For instance, it fluctuates between -259 MPa and 288 MPa for the 16 pixels by 16 pixels mask size for the second approach. This fluctuation is between -233 MPa and 153 MPa for the 32 pixels by 32 pixels mask. Moreover, similar fluctuations are seen in the evolution of the longitudinal stress (σ_{11}) and the transverse stress (σ_{22}) for smaller mask sizes. Nevertheless, the stress state becomes more stable as the mask size is increased.

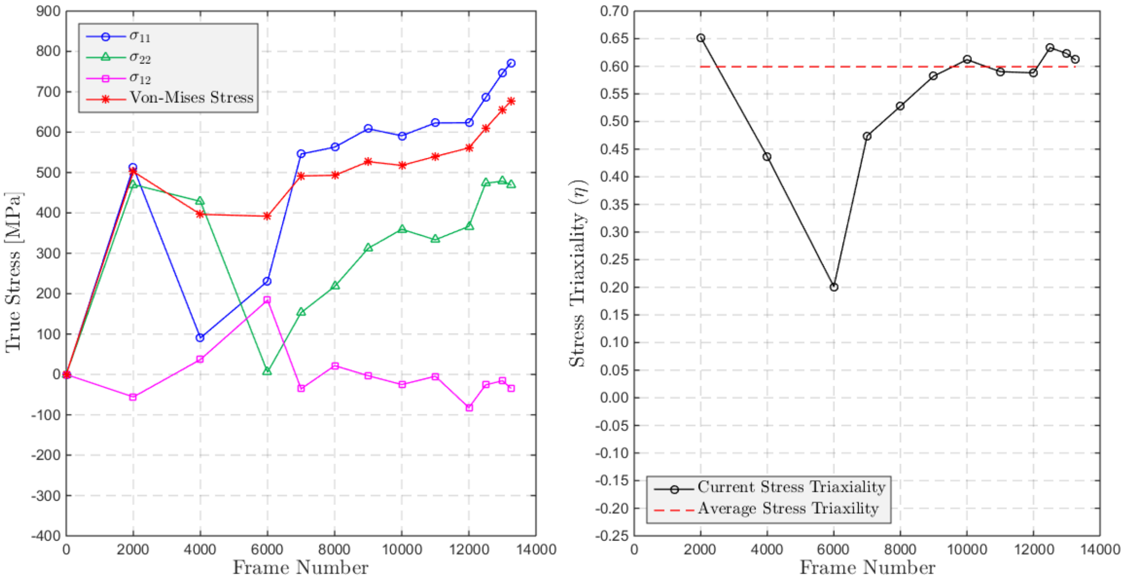

Figure 4-126 Evolution of the true stress (on the left) and the stress triaxiality (on the right) within the masked region during the cylindrical indentation – first approach. Mask size is 16 pixels by 16 pixels (0.219 mm x 0.219 mm).

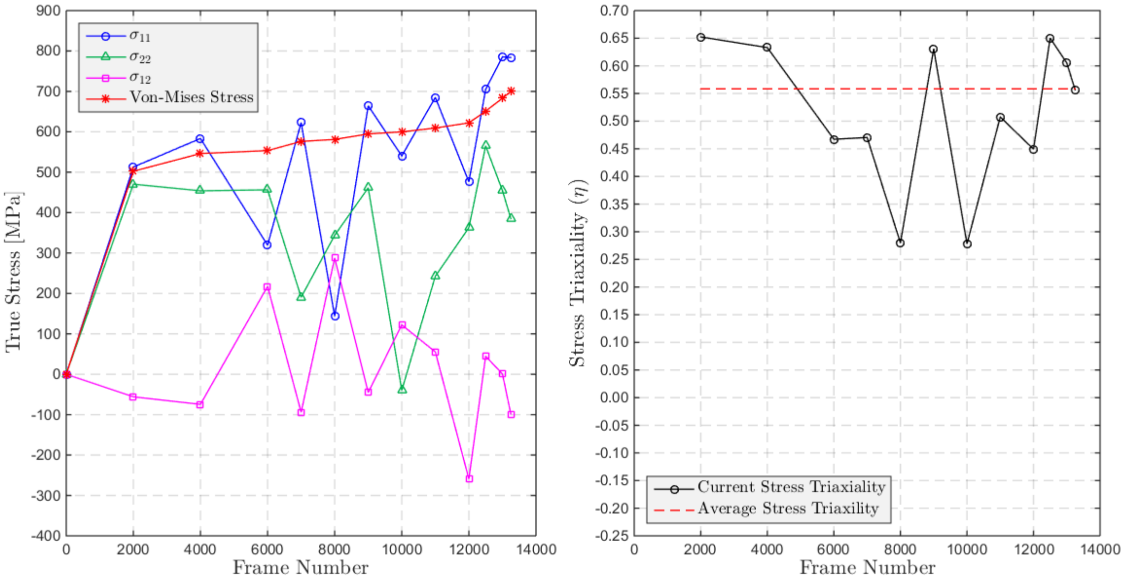

Figure 4-127 Evolution of the true stress (on the left) and the stress triaxiality (on the right) within the masked region during the cylindrical indentation – second approach. Mask size is 16 pixels by 16 pixels (0.219 mm x 0.219 mm).

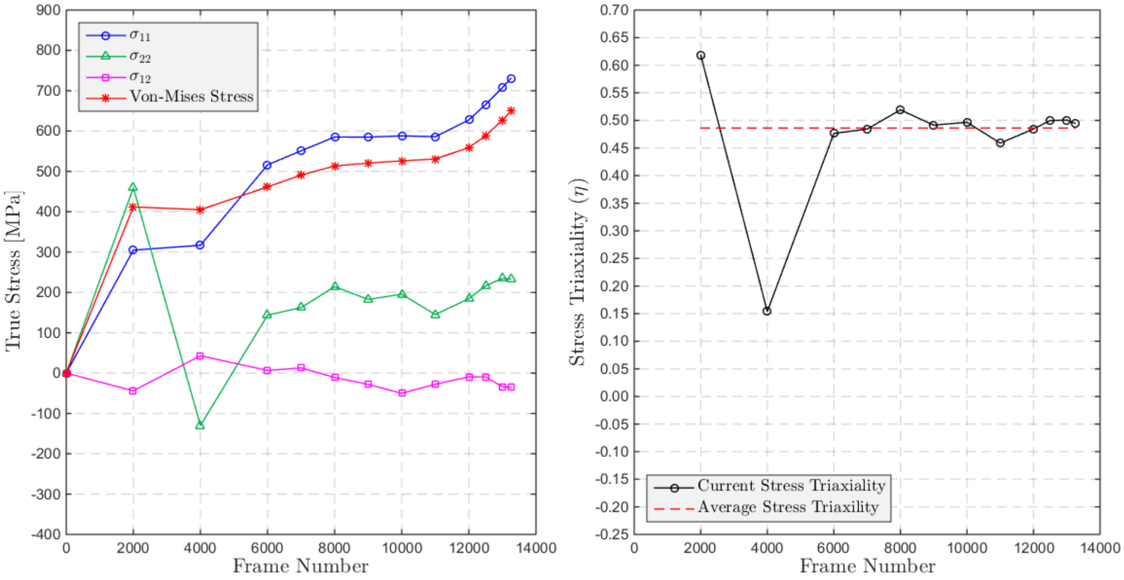

Figure 4-128 Evolution of the true stress (on the left) and the stress triaxiality (on the right) within the masked region during the cylindrical indentation – first approach. Mask size is 32 pixels by 32 pixels (0.438 mm x 0.438 mm).

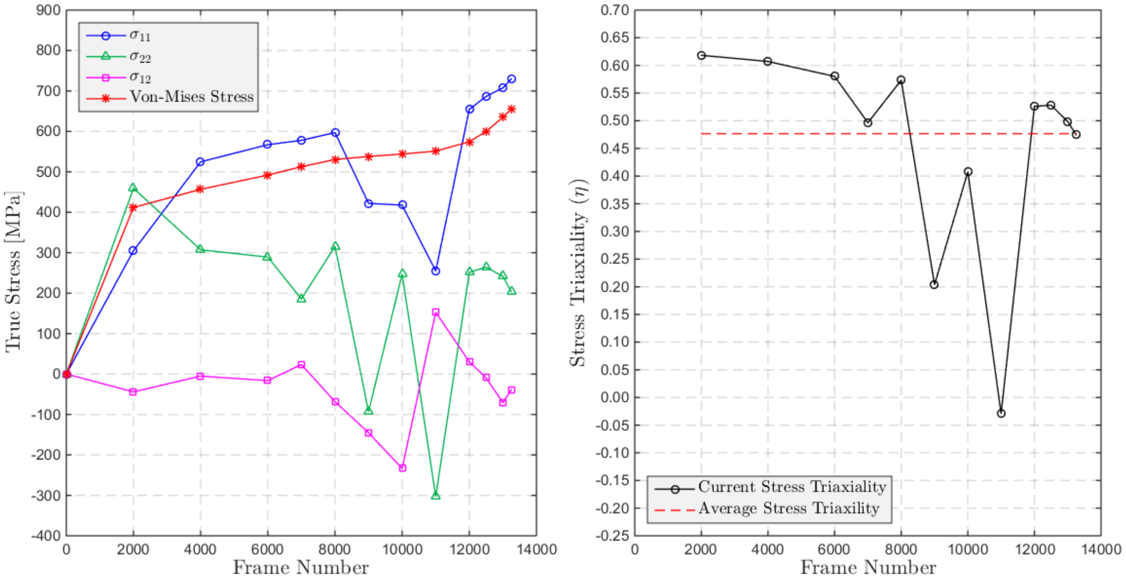

Figure 4-129 Evolution of the true stress (on the left) and the stress triaxiality (on the right) within the masked region during the cylindrical indentation – second approach. Mask size is 32 pixels by 32 pixels (0.438 mm x 0.438 mm).

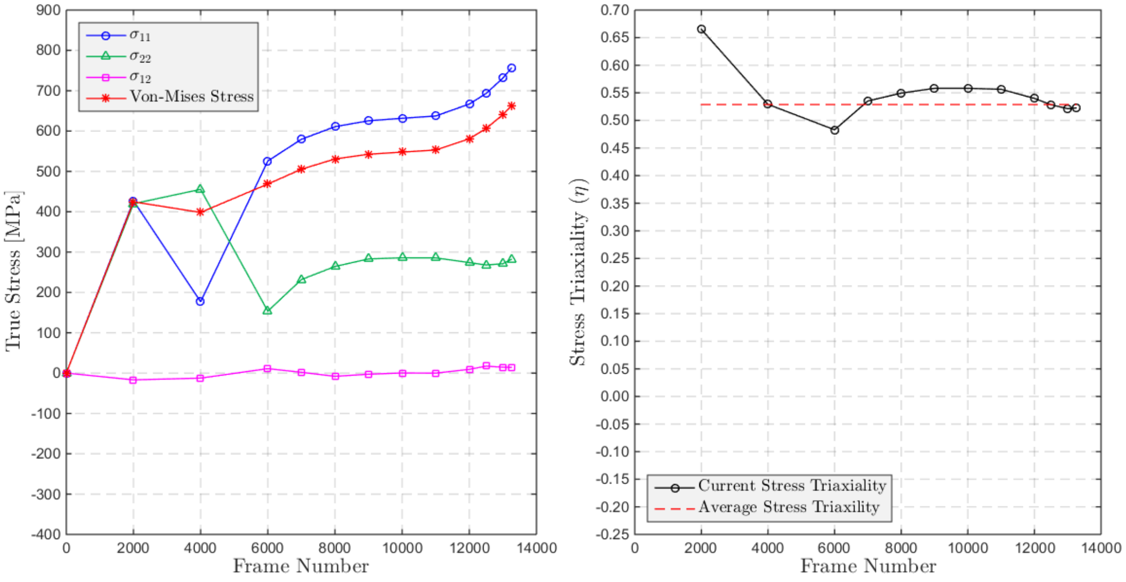

Figure 4-130 Evolution of the true stress (on the left) and the stress triaxiality (on the right) within the masked region during the cylindrical indentation – first approach. Mask size is 64 pixels by 64 pixels (0.877 mm x 0.877 mm).

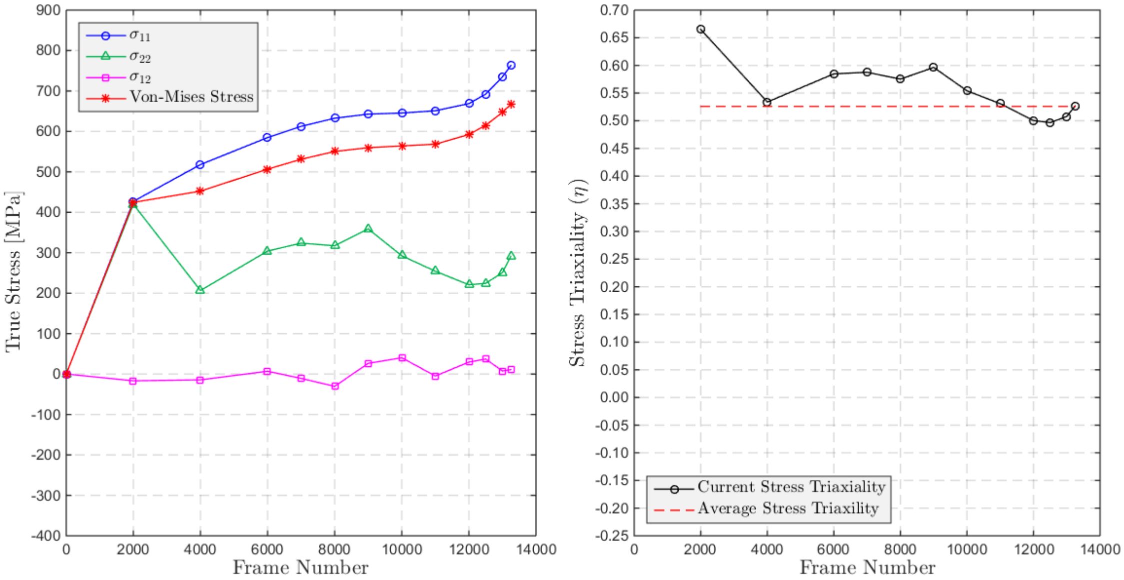

Figure 4-131 Evolution of the true stress (on the left) and the stress triaxiality (on the right) within the masked region during the cylindrical indentation – second approach. Mask size is 64 pixels by 64 pixels (0.877 mm x 0.877 mm).

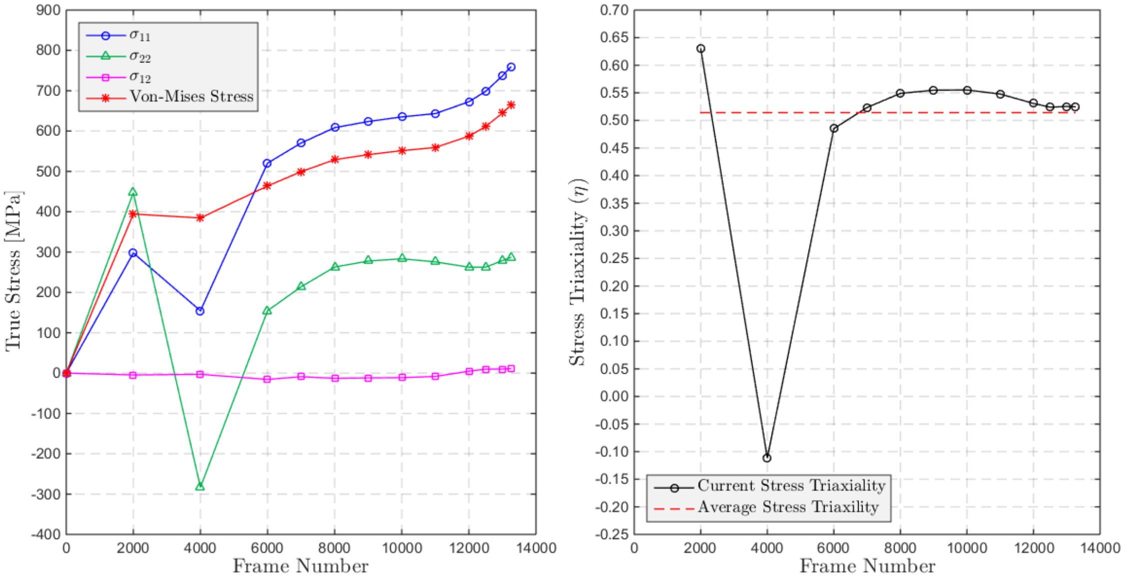

Figure 4-132 Evolution of the true stress (on the left) and the stress triaxiality (on the right) within the masked region during the cylindrical indentation – first approach. Mask size is 128 pixels by 128 pixels (1.754 mm x 1.754 mm).

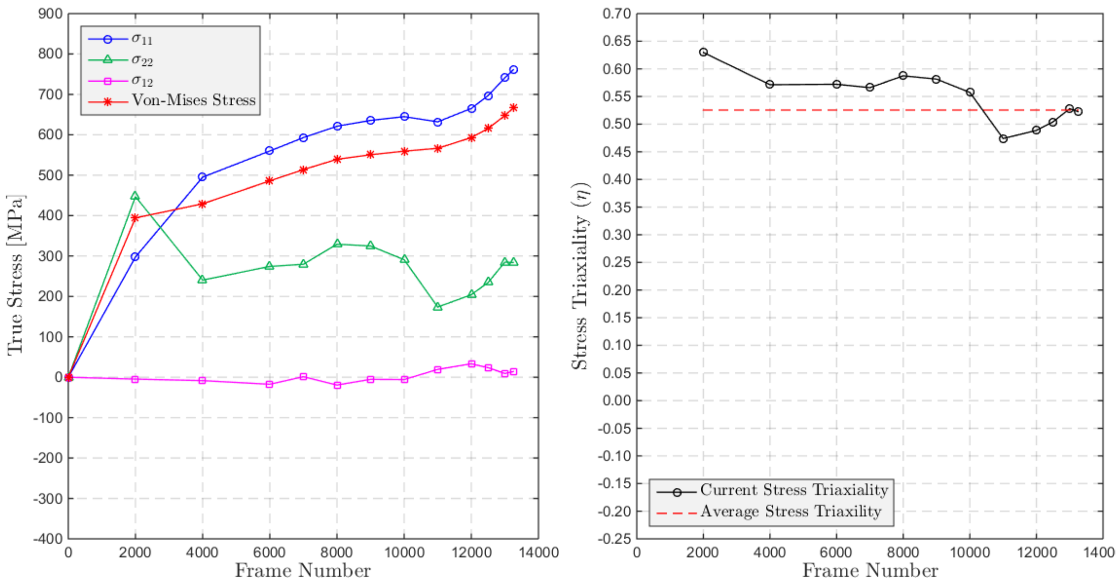

Figure 4-133 Evolution of the true stress (on the left) and the stress triaxiality (on the right) within the masked region during the cylindrical indentation – second approach. Mask size is 128 pixels by 128 pixels (1.754 mm x 1.754 mm).

The most prominent feature of these figures is the huge stress fluctuations (especially in the second approach) at smaller mask sizes, which represents local behavior. Similar fluctuations are observed in the analysis of the cylindrical indenter experiment of the 18mm-width specimen without groove, which is presented in Section 4.6.1. Moreover, possible physical and mathematical reasons that cause these fluctuations are discussed in the same chapter, and in the analysis of the uniaxial test of the 6mm-width specimen, presented in Section 4.5.1. In summary, the author believes that the stress fluctuations are primarily due to plastic flow localization[56] at the small scales/mask sizes. This view is supported by the fact that fluctuations lose their strength as more global behavior is followed; i.e., at larger mask sizes (see Figure 4-133, for example).

Moreover, as discussed in Section 4.6.1 in detail, the enormous difference between the two approaches, especially at the smaller scales, demonstrates that the loading does not remain proportional[57] at the smaller scales and the fact that this difference is more pronounced at the smaller mask sizes shows that non-proportional loading is mainly caused by plastic flow localization at the small scales.

---

[56] See Footnote 46.

[57] See Footnote 44.

The evolution of the longitudinal strain (ε_{11}) and the transverse strain (ε_{22}) for different mask sizes are presented in Figure 4-134 and Figure 4-135, respectively. The longitudinal strains for the 64 pixels by 64 pixels mask and the 128 pixels by 128 pixels mask nearly overlap during the entire loading considered here. Moreover, all mask sizes except the 32 pixels by 32 pixels mask have nearly the same longitudinal strain value at the initiation of fracture (i.e., at Frame 13250). On the other hand, the transverse strain for all mask sizes remains nearly zero until Frame 10000, where it starts developing. As presented in the previous pages, the shear strain is nearly zero until the later stages of the experiment as well. Therefore, the plane-strain condition (in the width-direction) develops and remains until around Frame 10000. This behavior can be expected as the width of the specimen (which is 18 mm) is fairly large compared to the length of the groove (which is 4 mm). However, around Frame 10000, positive transverse strain develops for the 16 pixels by 16 pixels mask, whereas negative transverse strain develops and remains negative for the other mask sizes.

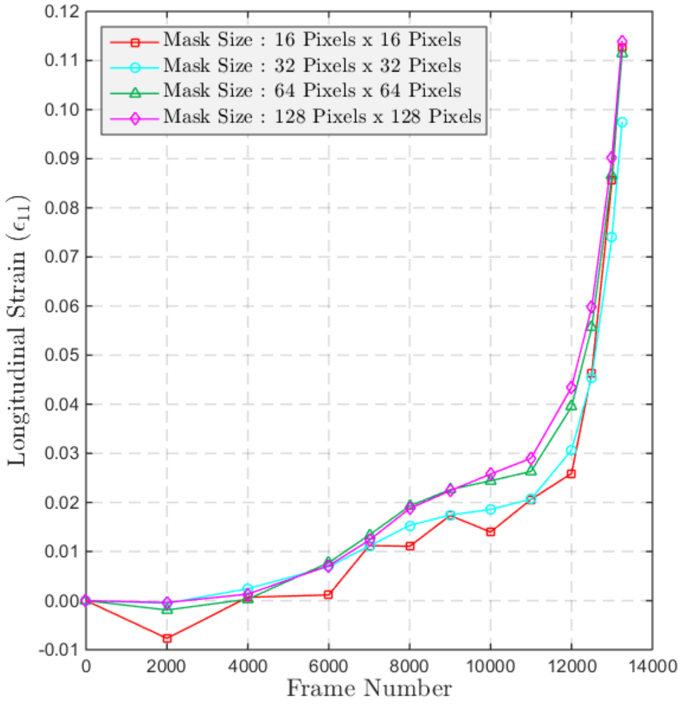

Figure 4-134 Evolution of the longitudinal strain within the masked region during the cylindrical indentation for different mask sizes – second approach. Pixel resolution is approximately 13.7 μm/pixel.

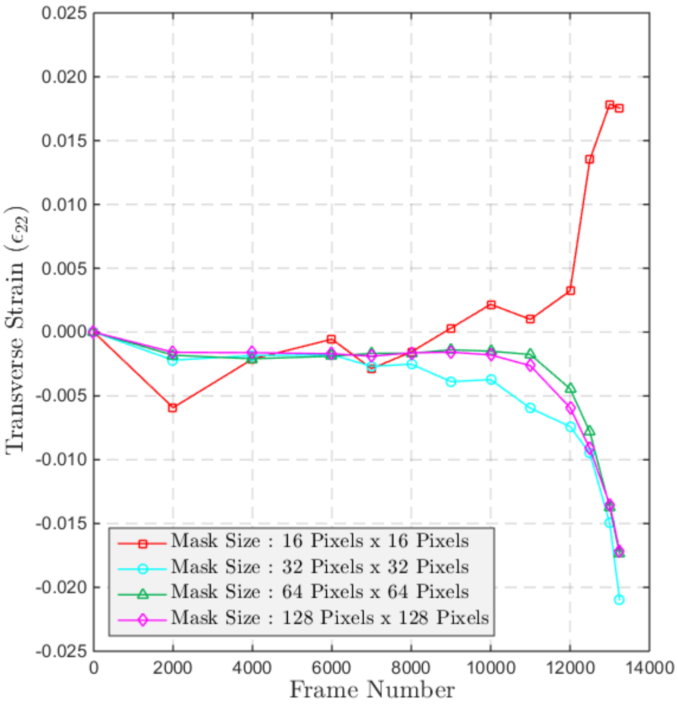

Figure 4-135 Evolution of the transverse strain within the masked region during the cylindrical indentation for different mask sizes – second approach. Pixel resolution is approximately 13.7 µm/pixel.

The evolution of the effective strain for the four scales studied from the results of this particular experiment is presented in Figure 4-136. The most prominent feature of the figure from the beginning of the test is once again the separation of the 16 pixels by 16 pixels mask from the other mask sizes. This separation is a clear indication of strain localization and that the localization occurs at a scale much smaller than the thickness scale (the thickness of the specimen is 1.588 mm, which corresponds to approximately 116 pixels). In fact, as mentioned previously, a number of researchers observed grain level strain variations/heterogeneity (see e.g., Raabe et al., 2001; Haltom et al., 2013; Banerjee et al., 2016) in their experimental work and numerical analysis. Considering that the evolution of the longitudinal strain for all mask sizes does not differ much (see Figure 4-134) and that the development of positive transverse strain in the 16 pixels by 16 pixels mask (see Figure 4-135), one can interpret that the localization is more pronounced along the thickness direction. Moreover, all mask sizes (except the 16 pixels by 16 pixels mask) have the same quantitative behavior and relatively small slopes until Frame 2000. The reason for this is discussed in the following pages, where the true stress-strain curves of different mask sizes are presented (see Figure 4-138). Finally and interestingly, the fracture strain for the 32 pixels by 32 pixels mask is lower than the ones for other two larger masks (i.e., 64 pixels by 64 pixels mask and 128 pixels by 128 pixels mask) with its curve also remaining below them.

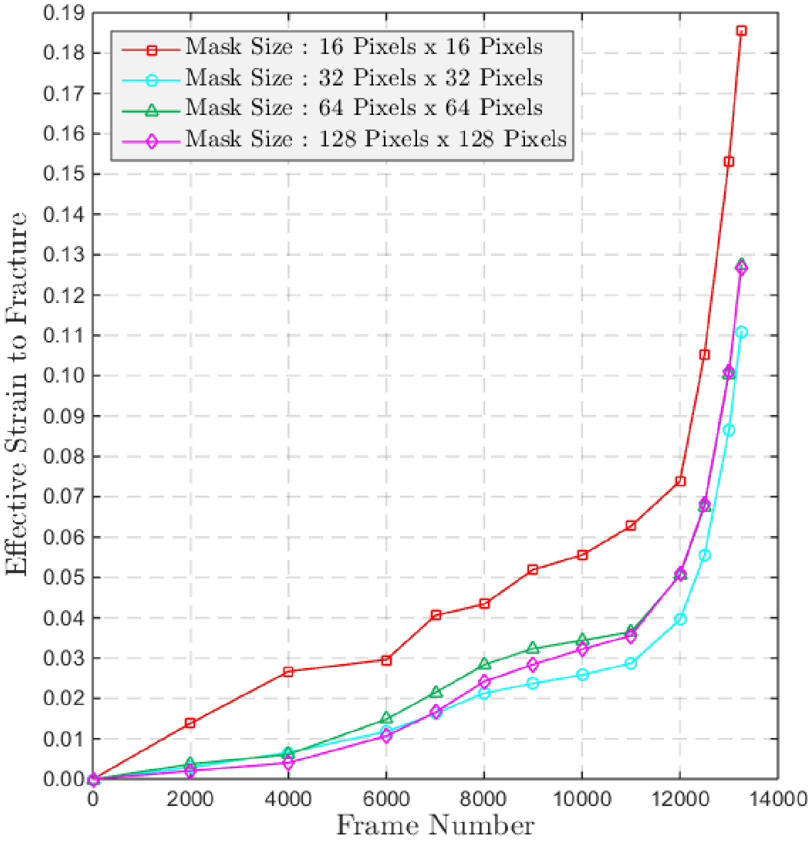

Figure 4-136 Evolution of the effective strain within the masked region during the cylindrical indentation for different mask sizes – second approach. Pixel resolution is approximately 13.7 µm/pixel.

The effect of mask size on failure strain during cylindrical indention can be seen in Figure 4-137. Li & Karr (2009) proposed an analytical relationship for the effect of length scale on the fracture strain (see Equation (4-45)) and the blue solid line shown in the figure is obtained by using this relationship. Again, x represents the length scale, y represents the fracture strain and the constants a and b were determined by a best fit of the experimental results[58]. As can be seen from the figure, there was no sign of convergence of the results as the length scales were reduced.

---

[58] See Footnote 49.

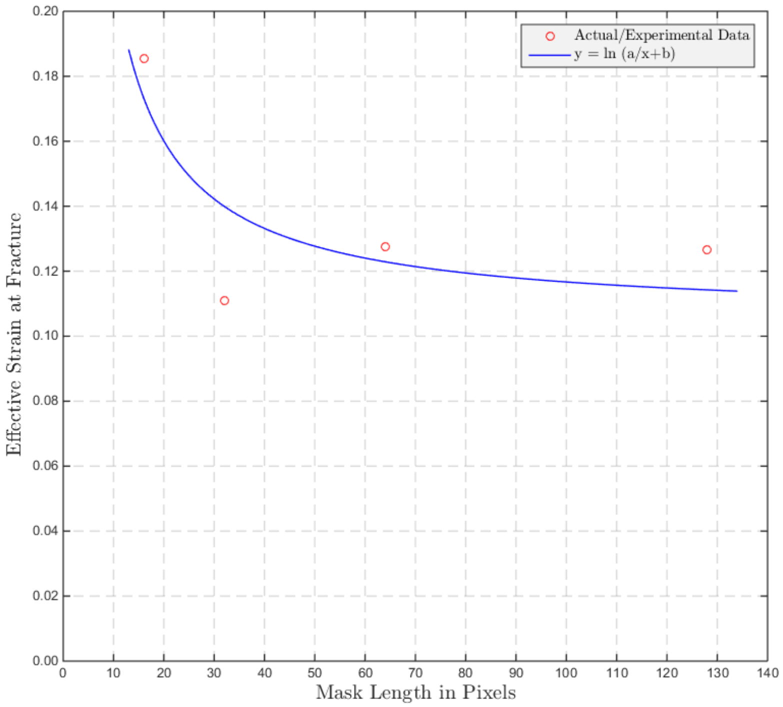

Figure 4-137 Effect of the mask size on failure strain during the cylindrical indention with $y = \ln(a/x + b)$ curve fit – second approach. $a = 1.246$ and $b = 1.111$. Pixel resolution is approximately 13.7 µm/pixel.

The average stress triaxiality (η_{ave}), the stress triaxiality at fracture (η_{frac}), and the effective strain at fracture (ε^{f}_{eff}) for both approaches are summarized in Table 4-9. The effective strain at fracture in the second approach increases as the mask size is decreased (except for the 32 pixels by 32 pixels mask). Moreover, interestingly, the stress triaxiality at fracture nearly equals the value of the average stress triaxiality and it exhibits no particular order regarding the mask size. Finally, as can be seen from Table 4-9, the maximum difference between the effective strain at fracture for the two different approaches is 23.2%, which occurs on the smallest mask size.

Table 4-9 Summary of the average stress triaxiality (η_{ave}), the stress triaxiality at fracture (η_{frac}), and the effective strain at fracture (ε_{eff}^{f}) for the cylindrical indenter experiment of 18mm-width specimen with 4 mm groove with an indentation speed of 0.6 inch/second.

	Mask size [pixels]	η_{ave}	η_{frac}	ε_{eff}^{f}
First approach	16x16	0.599	0.612	0.142
	32x32	0.486	0.495	0.103
	64x64	0.529	0.523	0.120
	128x128	0.514	0.525	0.123
Second approach	16x16	0.558	0.557	0.185
	32x32	0.477	0.475	0.111
	64x64	0.526	0.527	0.127
	128x128	0.525	0.523	0.127

Finally, the true stress-strain curves for different mask sizes are presented together in Figure 4-138. Note that the flow rule and the same power-law hardening relationship with the same coefficients ($\Omega = 868.4$ MPa and $n = 0.128$) are used here as for the cylindrical indenter experiment of the 18mm-width specimen without groove, presented in Section 4.6.1, to obtain the components of the stress tensor (see Section 4.4.2 for details) of the DIC analysis. Solid lines with markers are obtained by the digital image correlation analysis and DIC analyses are conducted to the point of fracture initiation; hence, once again the last marker of each color represents the fracture initiation point for different mask sizes. Dashed lines are the results of the uniaxial test with the MTS machine, which is superposed on the same figure for comparison puropses[59]. Finally, as pointed out in the previous analyses, the effective stress-strain curve is independent of the mask size as a result of using plastic constitutive and stress-strain relationships that are used (the hardening-law and the flow rule) are independent of a length scale.

---

[59] See Footnote 51.

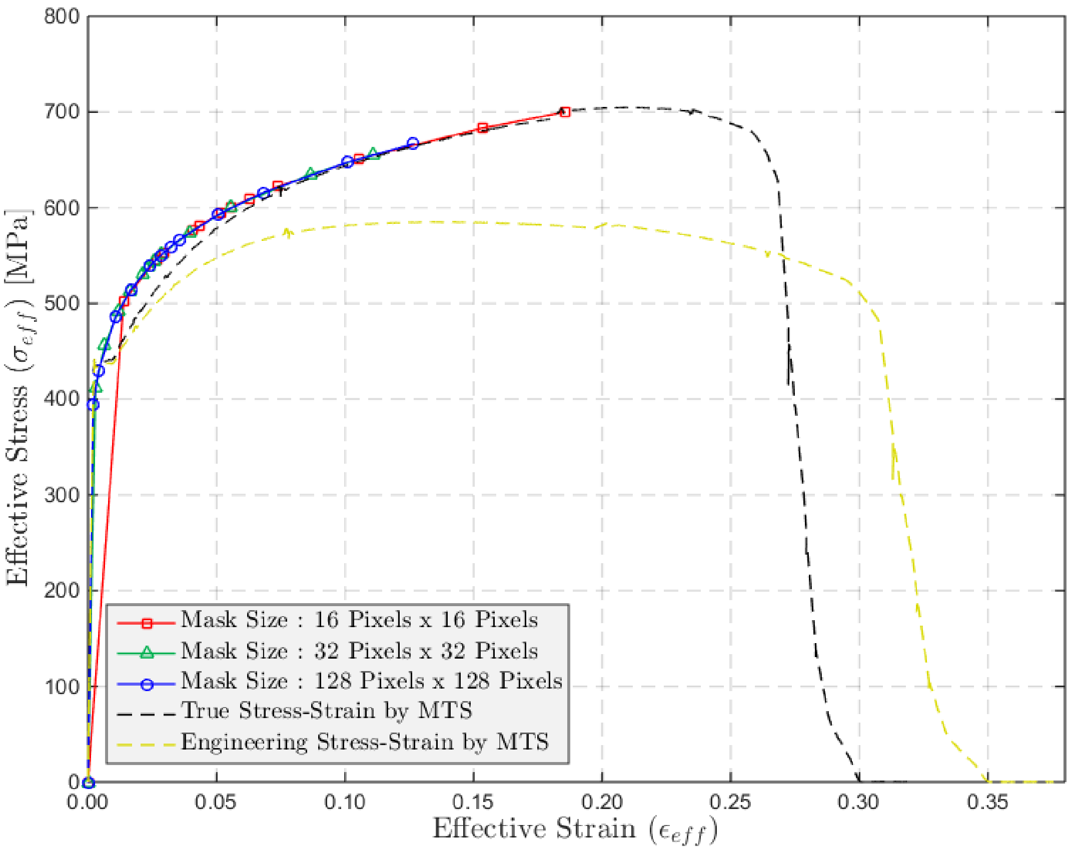

Figure 4-138 True stress-strain curve of the cylindrical indenter test for different mask sizes – second approach. Pixel resolution is approximately 13.7 µm/pixel. Solid lines with markers are obtained by digital image correlation (DIC) analysis while dashed lines are the results from the MTS machine.

It is again interesting to note that the 'masked region' is still in the elastic-region until Frame 2000 for both the 32 pixels by 32 pixels mask and the 128 pixels by 128 pixels mask. This indicates that all mask sizes except the 16 pixels by 16 pixels mask remain in the elastic-region until Frame 2000. Nevertheless, the step increment at the beginning of the test (which was 2000 frames) was sufficiently large such that the plastic flow starts at a very small scale (i.e., 16 pixels by 16 pixels mask), whereas all other mask sizes are still in the elastic-region. This is the reason that effective strain as a function of frame number for the 16 pixels by 16 pixels mask differs from the others from the beginning of the test (see Figure 4-136). Note that this also causes the 16 pixels by pixels mask to have a different slope (in the true stress-strain curve, presented in Figure 4-138) than the others at the initiation of the experiment. However, they follow the same path immediately thereafter.

4.6.2.2 Test 2

An indentation speed of 1.2 inch/second was applied to the center of the test specimen with 6000 digital images recorded per second. The pixel resolution was approximately 14.1 microns per pixel. Note that the high speed camera and the experimental device were snychronized in this experiment.

Fracture initiates around Frame 6650; that is, following an approximately 33.782 mm indentation. Note that this displacement is approximately 25% larger than the one obtained for the low speed test, presented in the previous sub-section.

DIC analyses are conducted for three different mask sizes, that is, the 16 pixel by 16 pixel mask (the smallest mask size), the 32 pixel by 32 pixel mask, and the 128 pixels by 128 pixels mask, which roughly equals the thickness of the specimen (the thickness of the specimen is 1.588 mm). Results are summarized in Table 4-10.

As can be seen from Table 4-9 and Table 4-10, the fracture strain obtained at high strain rate is more than two times as large as the one obtained at the lower strain rate. However, this is not a conclusive trend as more data are required to reach a solid conclusion.

Table 4-10 Summary of the average stress triaxiality (η_{ave}), the stress triaxiality at fracture (η_{frac}), and the effective strain at fracture (ε_{eff}^{f}) for cylindrical indenter experiment of 18mm-width specimen without groove with an indentation speed of 1.2 inch/second.

	Mask size [pixels]	η_{ave}	η_{frac}	ε_{eff}^{f}
First approach	16x16	0.520	0.573	0.456
	32x32	0.541	0.543	0.366
	128x128	0.538	0.544	0.318
Second approach	16x16	0.558	0.597	0.489
	32x32	0.543	0.543	0.367
	128x128	0.539	0.554	0.318

4.7 Results and Discussion

4.7.1 Mask/Mesh Size Dependence

Finite element studies of the mesh size dependence have been conducted previously and discussed widely in the literature. However, the present research is the first study, to our knowledge, that investigates the mesh size dependence through the direct measure of strain via digital image correlation (DIC) analysis.

Although the rate-independent constitutive models may be attributed as the reason for mesh sensitive results or non-convergence behavior as the length scales (i.e., mesh sizes) were reduced (see e.g., Addessio & Johnson, 1993), in the present study, different convergence behaviors (including non-convergence behavior) were obtained for different experiments through a direct measure of strain via DIC analysis. In other words, no stress-strain constitutive models/relations are used in the calculation of strains; strains are calculated through strain-displacement relationships via digital image correlation analysis and the procedure is summarized below.

The strain field is obtained using digital image correlation (DIC) analysis via DaVis LaVision (2015) software. The software calculates the displacement field and it sums the displacement field in a Lagrangian manner such that it provides the total displacement and engineering strain field to the current step. After obtaining the engineering strain field, a property called a 'geometric mask' is applied to extract the data from the region of interest. Strains are calculated to the point of fracture initiation in a backward-stepping manner. Backward-engineering-strains are converted to forward-engineering-strains and natural strains are calculated from the forward-engineering-strains. The details of the calculation are explained in Section 4.4.1. Note that all DIC strain data provided in this work are based on the average strain within the 'masked region'.

Two approaches are used in determination of the effective strain. The first approach is based on the current strain field, while the second approach is based on the incremental strain. The comparison shows that the first approach underestimates the effective strain and may not capture the instantaneous changes/fluctuations in the stress field as it is based on larger strain increments.

The state of stress is obtained using flow rule and power-law hardening relationship with hardening parameters $\Omega = 868.4$ MPa and $n = 0.128$ and these material parameters are used in all analyses.

Table 4-11 Summary of the average stress triaxiality (η_{ave}), the stress triaxiality at fracture (η_{frac}), and the effective strain at fracture (ε_{eff}^{f}) of all uniaxial tests – second approach.

Specimen Type	Test Speed [inch/s]	Pixel Resolution [μm/pixel]	Mask Size [pixels]	η_{ave}	η_{frac}	ε_{eff}^{f}	Corresponding Average Strain Rate [s^{-1}]
6mm-width specimen without groove*	0.20	16.5	16x16	0.364	0.513	0.615	0.513
			32x32	0.375	0.415	0.583	0.486
			64x64	0.364	0.451	0.574	0.478
			128x128	0.365	0.431	0.519	0.433
			192x192	0.363	0.430	0.479	0.399
			1024x256	0.356	0.420	0.229	0.191
6mm-width specimen without groove**	0.40	16.3	16x16	0.371	0.420	0.533	0.955
			32x32	0.344	0.404	0.466	0.835
			128x128	0.354	0.424	0.458	0.820
1in-width specimen with semi-circular groove***	Manual	15.3	16x16	0.369	0.327	0.233	0.126
			32x32	0.521	0.622	0.145	0.078
			64x64	0.519	0.577	0.103	0.056
			128x128	0.530	0.584	0.087	0.047
Shear specimen***	Manual	13.7	16x16	0.024	-0.055	0.549	0.686
			32x32	0.006	-0.001	0.524	0.655
			64x64	0.019	-0.004	0.423	0.529
			128x128	-0.018	0.017	0.321	0.401

* This specimen was obtained by in-house machining of 18mm-width-specimen without groove.
** This specimen was obtained by in-house machining of 1in-width-specimen without groove.
*** These experiments were conducted manually; hence, the test speed may not be constant during the experiment. The strain rates were calculated assuming that the speed was constant.

Table 4-12 Summary of the average stress triaxiality (η_{ave}), the stress triaxiality at fracture (η_{frac}), and the effective strain at fracture (ε_{eff}^{f}) of all cylindrical indenter experiments – second approach.

Specimen Type	Test Speed [inch/s]	Pixel Resolution [µm/pixel]	Mask Size [pixels]	η_{ave}	η_{frac}	ε_{eff}^{f}	Corresponding Average Strain Rate [s^{-1}]
18mm-width specimen without groove (Test 0)	0.60	13.7	16x16	0.497	0.385	0.157	0.081
			32x32	0.513	0.606	0.082	0.042
			64x64	0.540	0.527	0.050	0.026
			128x128	0.517	0.480	0.046	0.024
			192x192	0.514	0.455	0.043	0.022
18mm-width specimen without groove (Test 3)	0.60	14.0	16x16	0.396	0.513	0.689	0.190
			32x32	0.405	0.459	0.683	0.188
			64x64	0.407	0.452	0.623	0.172
			128x128	0.396	0.451	0.602	0.166
18mm-width specimen without groove (Test 1)	1.20	13.7	16x16	0.515	0.517	0.121	0.101
			32x32	0.526	0.413	0.082	0.068
			128x128	0.460	0.454	0.049	0.041
18mm-width specimen without groove (Test 2)	2.40	14.0	16x16	0.393	0.565	1.073	0.891
			32x32	0.390	0.519	0.894	0.742
			128x128	0.403	0.502	0.763	0.634
18mm-width specimen with 4mm groove (Test 1)	0.60	13.7	16x16	0.558	0.557	0.185	0.105
			32x32	0.477	0.475	0.111	0.063
			64x64	0.526	0.527	0.127	0.072
			128x128	0.525	0.523	0.127	0.072
18mm-width specimen with 4mm groove (Test 2)	1.20	14.1	16x16	0.558	0.597	0.489	0.441
			32x32	0.543	0.543	0.367	0.331
			128x128	0.539	0.554	0.318	0.287

The summary of the results of all uniaxial tests and cylindrical indenter experiments are presented in Table 4-11 and Table 4-12, respectively. The strain rates listed are the average strain rates for the test range whereby the strain-to-failure is divided by the time-to-failure. Note that the strain rates at the instant of fracture are much higher.

It is known that the state of stress has a strong influence on the effective failure strain, a measure of ductility. This has been confirmed in numerous investigations including the current experimental study. In addition, we have obtained different mesh convergence behaviors for different experiments. It is believed that strain localization is the main cause of mesh size dependence on fracture strain. As the strain localization depends on the state of stress, it is expected that there will be an effect of mesh size (on fracture strain) for different state of stresses. In other words, mesh convergence behavior is also affected by the state of stress. This has been observed by other researchers, e.g., Barsoum & Faleskog (2007a)[60], Hogström et al. (2009), Walters (2014), and Kõrgesaar & Romanoff (2014).

As a result, care should be exercised in the consideration of establishing a strain-to-failure envelope for a material; that is, both the state of stress and the scale effects should be considered.

4.7.2 Strain Rate Dependence

No conclusive trend is obtained with the current experimental results and more data are required to reach a solid conclusion regarding the fracture sensitivity to strain rate variation.

---

[60] Although they did not point this out explicitly, one can clearly interpret this behavior from Figure 12 of the cited reference. Note that, $\bar{\varepsilon}_{cf}^{p}$ (the effective plastic strain in the center of the notch at failure), shown by dashed lines, may represent the local strain behavior, that is, small/fine mesh size behavior; while $\bar{\varepsilon}_{nf}^{p}$ (the average effective plastic strain over the notch at failure), shown by solid lines, may represent global strain behavior, that is, large/coarse mesh size behavior. In other words, dashed lines (in Figure 12 of the cited reference) would have been parallel (or overlapped) to the solid lines if mesh convergence would not have been affected by the stress triaxiality.

CHAPTER 5

Comparison of Theory and Experimental Results

In this Chapter, the analytical theory of the initiation of ductile fracture, proposed in Chapter 3, is compared to the experimental results for the mild steel presented in Chapter 4.

The comparison of the experimental data and the theoretical results requires a crucial choice of the data points and the coordinate space in which it is presented. Fracture strain as a function of stress triaxiality for three different mask sizes is depicted in Figure 5-1, Figure 5-2, and Figure 5-3. As can be seen from the figures, the experimental data are very scattered. This scattering suggests that the fracture locus may not be accurately represented in the 2D space (stress triaxiality and fracture strain space, for example). Instead, the full state of stress at the initiation of fracture should be considered and the fracture locus should be represented in the 3D space (stress triaxiality, Lode parameter[61], and fracture strain space, for example). Another reason for this scattering is that a small change in toughness stress for Mode I fracture (C_I) results in a huge difference in fracture strain. Figure 5-4 depicts the effective strain to fracture as a function of toughness stress for Mode I fracture for the uniaxial test of the 6mm-width specimen. As can be seen from the figure, increasing toughness stress from 822.6 MPa to 1196.7 MPa (i.e., 45.5% increase) causes a 166.7% increase in fracture strain (i.e., from $\bar{\varepsilon}_f = 0.15$ to $\bar{\varepsilon}_f = 0.40$).

---

[61] Lode parameter is defined as

$$\mathcal{L} = \frac{2\sigma_{II} - \sigma_I - \sigma_{III}}{\sigma_I - \sigma_{III}}$$

where Roman numeral subscripts represent principal stresses with $\sigma_I > \sigma_{II} > \sigma_{III}$. Note that the Lode parameter is not defined for $\sigma_I = \sigma_{III}$, i.e., $\sigma_I = \sigma_{II} = \sigma_{III}$.

It is possible that a fracture may result from the propagation of cracks from within the sample volume. Unfortunately, it is not possible to distinguish this occurrence from cases where fracture initiates on the surface as no fractography is conducted. However, the data from Chapter 4 do offer an indication of the level of expected surface energy by application of the theory presented in Chapter 3. Therefore, all experimental data (with the theoretical results) will be included in the figures presented in this chapter. Nevertheless, the reader should be cautious of evaluating and comparing these data points (with the theory) as any datum point may have a non-surface fracture initiation and/or may be the result of brittle fracture (brittle fracture data points should not be used for comparison as the theory predicts ductile fracture initiation only).

5.1 Toughness Stress Calculation

The toughness stresses C_I and C_{II} are evaluated by using the results of the second approach discussed in Chapter 4, which is based on smaller increments in strain. The toughness stresses are obtained for three different mask sizes, that is, the 16 pixel by 16 pixel mask (the smallest mask), the 32 pixels by 32 pixels mask, and the 128 pixels by 128 pixels mask (the largest mask). The reason for this is discussed and explained in Section 5.1.4.

The pixel resolutions of all experiments are not exactly the same; they range between 13.7 µm and 16.5 µm. Therefore, the actual dimension of a mask size may be different for two different data points. For instance, the actual mask size varies between 0.219 mm and 0.264 mm for 16 pixels, while it varies between 1.754 mm and 2.112 mm for 128 pixels.

Bridgman’s (1945) experiments with pre-strained metal specimens under hydrostatic pressure verified that fracture is history dependent (see Figure 8 of the same reference); that is, the current state of stress and the strain are not the only important parameters. Therefore, the average stress triaxiality was used in the evaluation of C_I and C_{II} rather than the stress triaxiality at fracture because the average stress triaxiality reflects the state of stress history better when the loading does not remain proportional. However, as mentioned in Chapter 3, proportional loading is not required for use of the theory presented there. The general approach for non-proportional loading would be to check the equation of the critical condition throughout the loading history with the critical state being reached when the equation is first satisfied as the loading is applied.

As a practical matter, only one datum point is necessary to calculate a toughness stress. Therefore, the shear mode toughness stress C_{II} is evaluated using the result of the uniaxial test of the shear specimen as we know this is a Mode II fracture. As the theory presented in Chapter 3 provides a necessary condition for fracture initiation, it can be implemented as the lower bound. This lower bound for the opening mode toughness stress C_I is obtained by evaluating the low effective strain to fracture results, and it is shown as a cyan solid curve in Figure 5-1, Figure 5-2, and Figure 5-3. However, as mentioned above, the data are very scattered; hence, a second toughness stress for the opening mode is calculated by evaluating the higher effective strain to fracture results and it is shown as a green solid curve.

5.1.1 16 Pixels by 16 Pixels Mask

Fracture strain as a function of stress triaxiality for the 16 pixels by 16 pixels mask is shown in Figure 5-1. Data points used in the evaluation of a toughness stress are shown as crisscrosses inside the red circles. For instance, the toughness stress $C_I = 909$ MPa and the corresponding cyan solid curve is obtained by considering the best fit of four data points that are shown as cyan crisscrosses. For the 16 pixels by 16 pixels mask, the toughness stress for the shear mode fracture is obtained as $C_{II} = 580$ MPa.

5.1.2 32 Pixels by 32 Pixels Mask

Fracture strain as a function of stress triaxiality for the 32 pixels by 32 pixels mask is presented in Figure 5-2. Again, data points used in the evaluation of a toughness stress are shown as crisscrosses inside the red circles. For example, toughness stress $C_I = 814$ MPa and the corresponding cyan solid curve is obtained by considering the best fit of the four data points that are shown as cyan crisscrosses. For the 32 pixels by 32 pixels mask, the toughness stress for the shear mode fracture is obtained as $C_{II} = 561$ MPa.

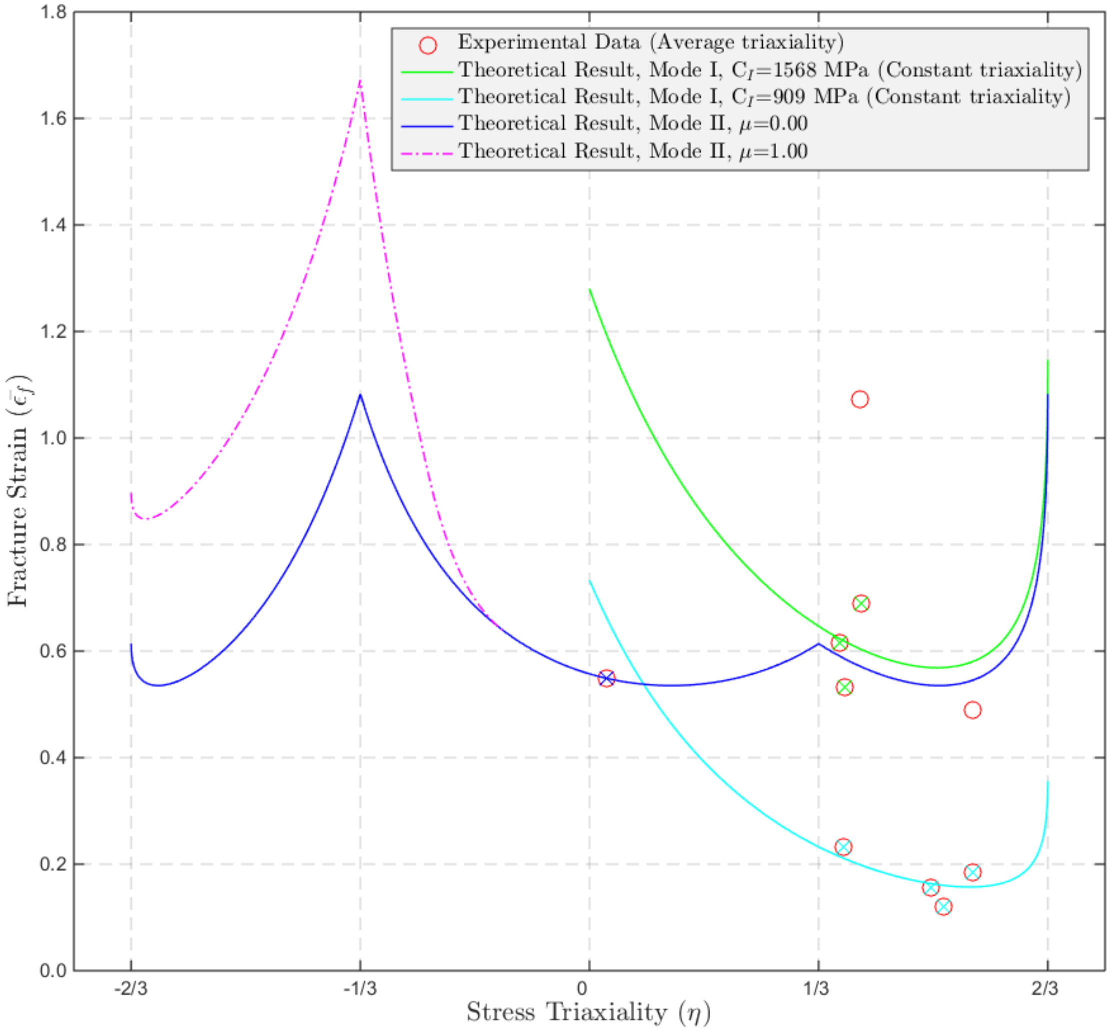

Figure 5-1 Effective strain to fracture versus stress triaxiality for the plane stress condition for the 16 pixels by 16 pixels mask. Two toughness stress results are shown for the opening mode fracture (cyan solid curve and green solid curve), whereas the results of only one toughness stress are presented for the shear mode fracture. For the shear mode fracture, the blue solid curve shows the result for the critical state with no friction on the fracture planes, while the dotted dashed line shows the results of friction occuring on the fracture planes due to compressive normal stresses.

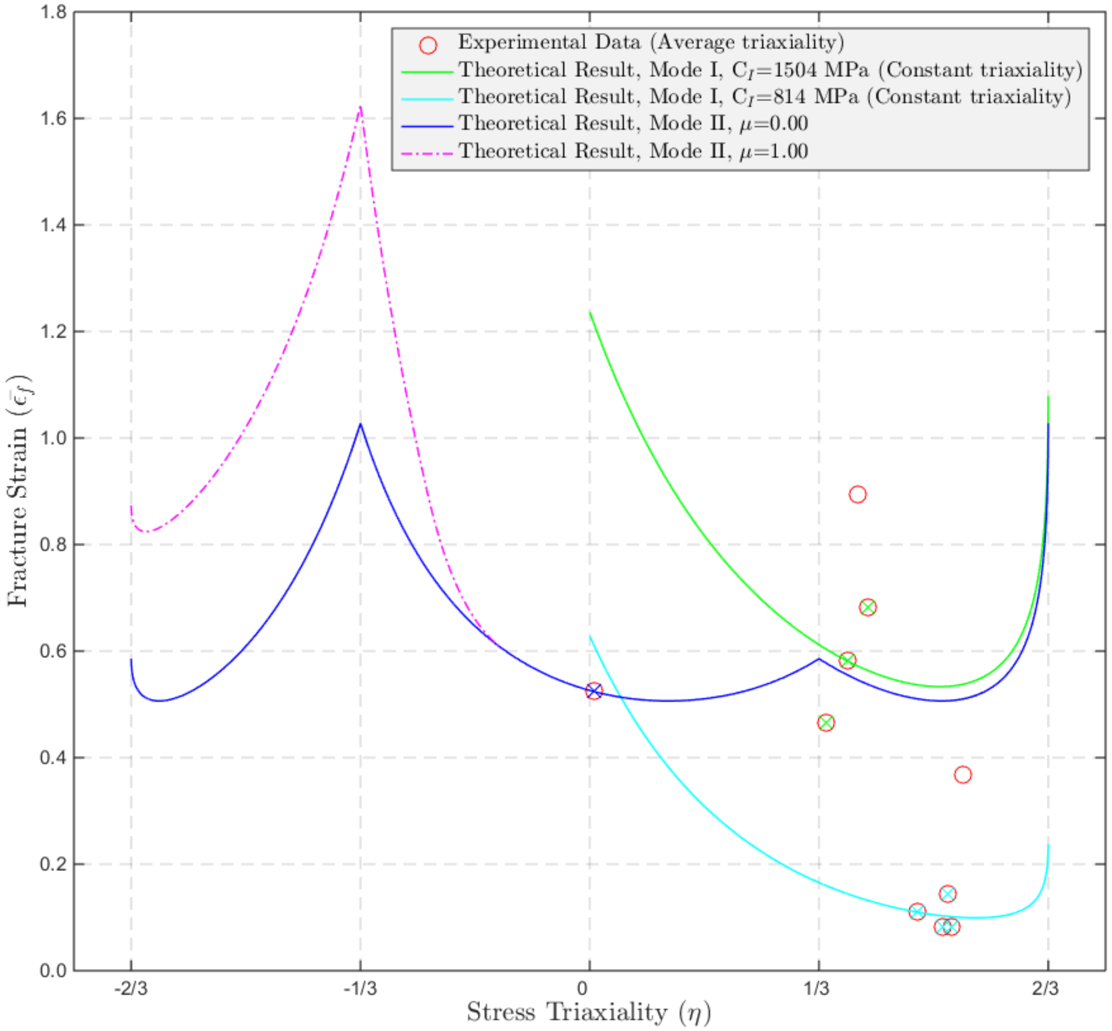

Figure 5-2 Effective strain to fracture versus stress triaxiality for the plane stress condition for the 32 pixels by 32 pixels mask. Two toughness stress results are shown for the opening mode fracture (cyan solid curve and green solid curve), whereas the results of only one toughness stress are presented for the shear mode fracture. For the shear mode fracture, the blue solid curve shows the result for the critical state with no friction on the fracture planes, while the dotted dashed line shows the results of friction occuring on the fracture planes due to compressive normal stresses.

5.1.3 128 Pixels by 128 Pixels Mask

Fracture strain as a function of stress triaxiality for the 128 pixels by 128 pixels mask is depicted in Figure 5-3. Again, data points used in the evaluation of a toughness stress are shown as crisscrosses inside the red circles. For example, toughness stress $C_I = 1405$ MPa and the corresponding green solid curve is obtained by considering the best fit of three data points that are shown as green crisscrosses. For the 128 pixels by 128 pixels mask, the toughness stress for the shear mode fracture is obtained as $C_{II} = 439$ MPa.

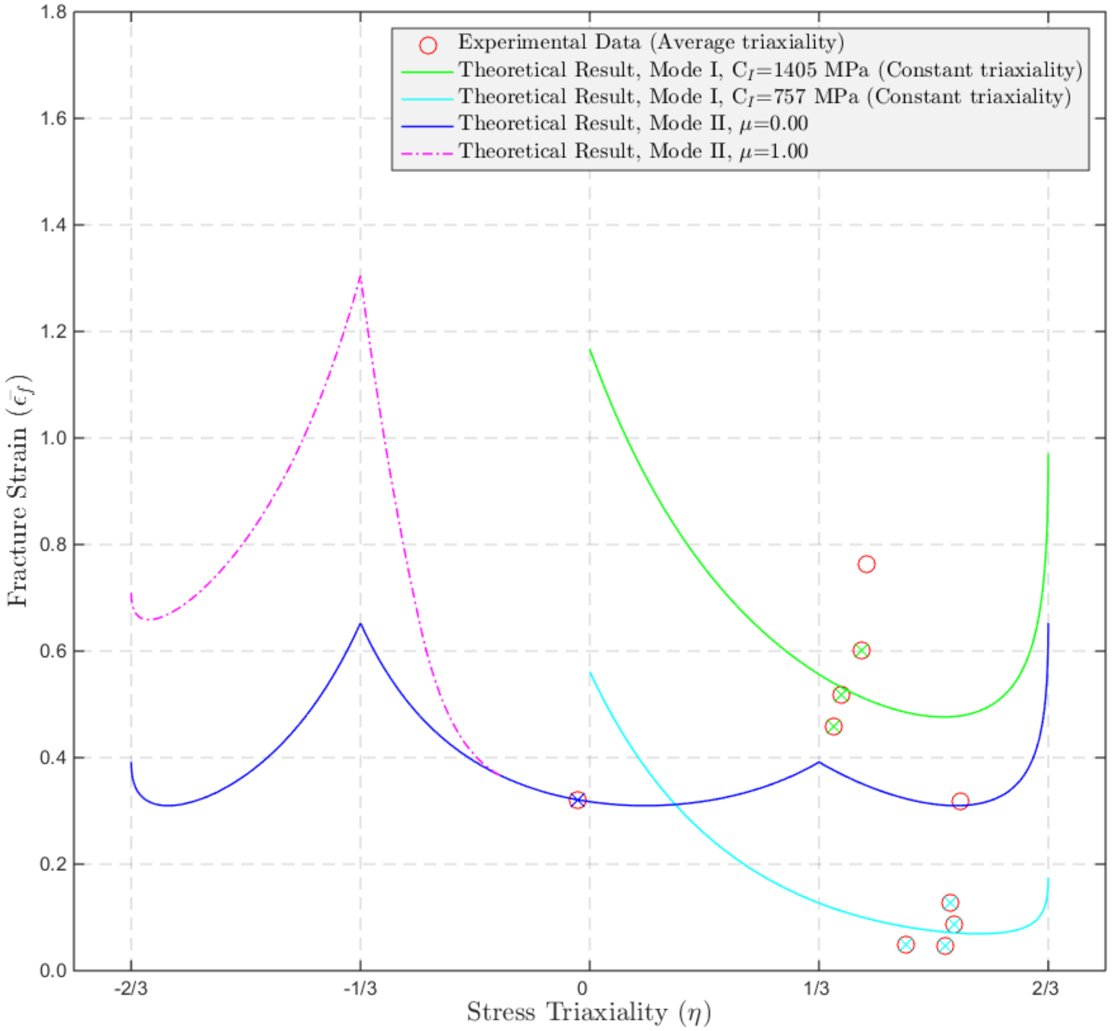

Figure 5-3 Effective strain to fracture versus stress triaxiality for the plane stress condition for the 128 pixels by 128 pixels mask. Two toughness stress results are shown for the opening mode fracture (cyan solid curve and green solid curve), whereas the results of one toughness stress is presented for the shear mode fracture. For the shear mode fracture, the blue solid curve shows the result for the critical state with no friction on the fracture planes, while the dotted dashed line shows the results of friction occuring on the fracture planes due to compressive normal stresses.

5.1.4 Evaluation of Toughness Stresses

As a comparison, we calculate the toughness stress for the opening mode (C_I) by using previously published results relating the conventional energy release rates. Priest et al. (2001) provided fracture toughness (K), the crack-tip opening displacement (CTOD), and the J-integral values for steels used in ship construction, including AH32 steel. The J-integral is reported as being on the order of $J = 0.3$ J/mm^2 and the crack-tip opening displacement (CTOD) is reported on the order of 0.4 mm (see Table 5.5 of the cited reference)[62]. As the J-integral is a way of calculating crack-extension force or strain energy release rate (see Section 2.4), it can be used as an approximation for the surface energy density of a ductile fracture (denoted as Γ) introduced in Chapter 3. Moreover, $l_{I,0}$ is chosen on the order of the crack-tip opening displacement (CTOD) as it generally provides a good estimate for the characteristic length scale[63] (Gao et al., 1998). Therefore, using Equation (3-12) with $\Gamma = 0.3$ J/mm^2 and $l_{I,0} = 0.4$ mm gives a toughness stress of $C_I = 750$ MPa. This is essentially the same order as the lower bounds of C_I presented in Figure 5-1, Figure 5-2, and Figure 5-3.

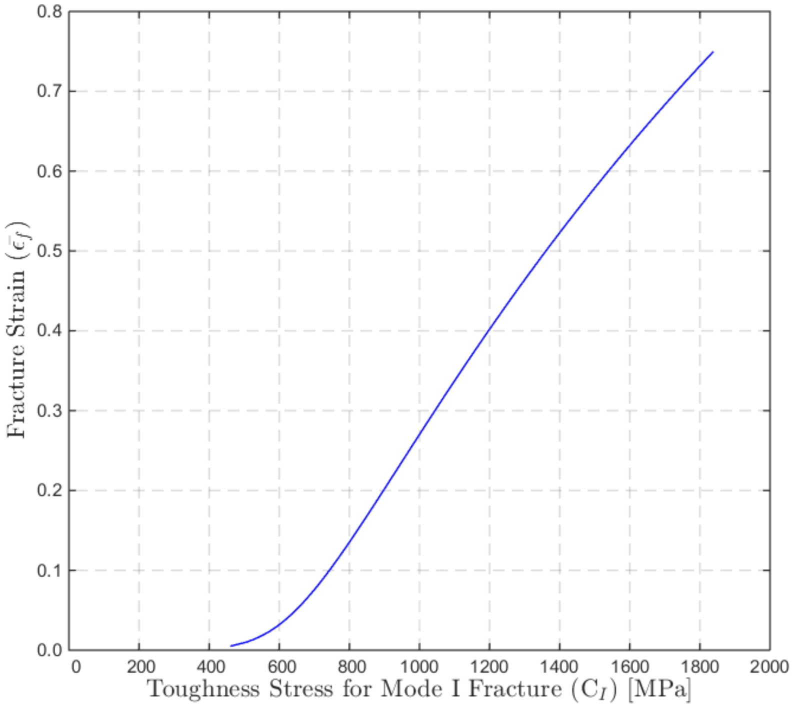

Figure 5-4 Effective strain to fracture versus toughness stress for Mode I fracture for the uniaxial test of the 6mm-width specimen without groove with a test speed of 0.2 inch/second.

---

[62] We use the values denoted as 'i-values' as they represent the value at crack initiation. Moreover, the results of the specimen named as 'AH32N-Y7N10' are used as this is the only AH32 specimen where both the J-integral and crack-tip opening displacement data are reported simultaneously.

[63] “*The layer height, denoted D, introduces a characteristic length scale over which damage occurs and is associated with the mean spacing of the larger, void initiating inclusions ...*

…

The crack tip opening displacement (CTOD) at the initiation of macroscopic tearing, as defined in ASTM E-1290, generally represents a good estimate for the cell height dimension (D)” (p. 762 of Gao et al., 1998).

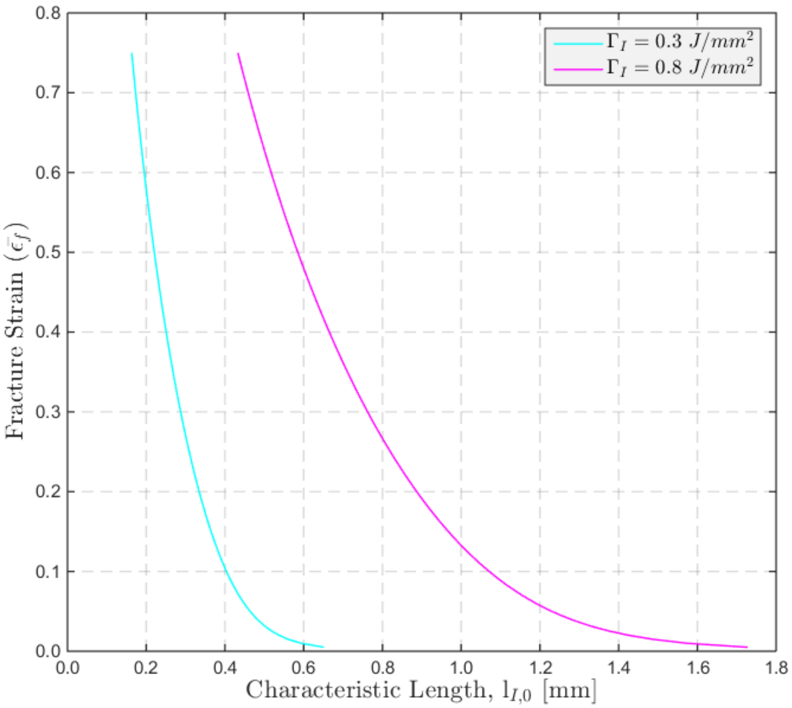

Figure 5-5 Effective strain to fracture versus characteristic length for the uniaxial test of the 6mm-width specimen without groove with a test speed of 0.2 inch/second. Pixel resolution is approximately 16.5 µm/pixel.

For application of the ductile fracture theory (presented in Chapter 3), we suggest the use of a mesh size equal to the characteristic length ($l_{I,0}$) as the theory introduces a micro-structural characteristic length scale and the formulation was derived based on the assumption of a uniform stress field within the volume element. However, here, three different mask sizes were analyzed for the implementation of the theory and the reasons are as follow. As mentioned above, the pixel resolutions of all experiments are not exactly the same; they range between 13.7 µm and 16.5 µm. Hence, the corresponding pixel sizes for the characteristic length of $l_{I,0} = 0.4$ mm range between 24 pixels and 29 pixels. In addition, the characteristic length of $l_{I,0} = 0.4$ mm is an estimate (as it was obtained by assuming that the crack-tip opening displacement, CTOD, generally provides a good estimate for the characteristic length scale) and the fracture strain is extremely sensitive to characteristic length as can be seen from Figure 5-5. Moreover, the limit for the continuum scale for polycrystalline aggregates (e.g., steel, aluminum, etc.) is approximately twenty[64] (Leis et al., 1985; Tegart, 1966); hence, the continuum scale limit ranges between ~100 µm and ~500 µm as the average grain size of AH32 steel ranges from ~5 µm to ~25 µm depending on the cooling process/system used (Zhou et al., 2016). Therefore, the characteristic length lies essentially in the range of 100 µm to 500 µm and the corresponding mask size ranges from 7 pixels to 36 pixels. Hence, the 16 pixels by 16 pixels mask and the 32 pixels by 32 pixels mask are considered appropriate for the application of the ductile failure criterion, presented in Chapter 3. Moreover, we applied the theory on the results of the 128 pixels by 128 pixels mask for comparison purposes. Note that the 128 pixels by 128 pixels mask roughly equals the thickness of the specimens (the thickness of all specimens analyzed is 1.588 mm).

In conclusion, we believe that the toughness stress of ductile fracture C, introduced by Karr & Akçay (2016) and presented in Chapter 3, may be related to the conventional fracture toughness, generally denoted as K_c (see Section 2.3 for details). For example, it may be stated in the following form for the opening mode fracture (i.e., Mode I fracture):

$$C_I \approx \frac{K_{Ic}^2}{E l_{I,0}} \tag{5-1}$$

where E is the modulus of elasticity and $l_{I,0}$ is the micro-structural characteristic length of the material.

---

[64] See Footnote 39 and Footnote 40.

CHAPTER 6

Conclusions and Suggestions for Future Work

6.1 Discussion and Conclusions

The research presented here provides, through combined experimental and analytical studies, a significant contribution to understanding of the evolution of the non-linear stress and strain states leading to ductile fracture. In addition, this study provides key parameters for predicting fracture of ductile materials in general, and thus assists in the guidance of criteria development for materials other than those specifically addressed.

Numerous researches have focused on establishing a criterion for crack propagation (i.e., extension of pre-existing cracks). Moreover, the current criteria for ductile fracture are based on empirical relations and there is presently no generally-accepted criterion for ductile fracture. In Chapter 3, we presented a *closed-form theoretical solution* on the *initiation* of ductile fracture at the continuum scale. This is an extremely important development as crashworthiness assessment, energy absorption capacity and damage survivability depend on the accurate prediction of fracture initiation, which limits the structure's performance.

The ductile fracture theory presented is based on comparison of the energy dissipation rates of the bulk continuum system to the fractured medium. The energy dissipation of the continuum system includes that of plastic work while that of the fractured system includes the surface energy of the crack formation, plastic work, and frictional losses (if any) at the instant of crack initiation. Two mechanisms were considered: Mode I, which accounts for a crack-opening displacement field and Mode II, which accounts for a shear crack initiation. The shear crack was addressed with and without frictional dissipation of the crack surfaces.

The theory presented in Chapter 3 introduces a length scale and a new material constant which we call toughness stress. The toughness stress (C) is defined as the effective surface energy release rate (Γ) divided by the micro-structural characteristic length of the material ($l_{I,0}$). Both the effective surface energy and the characteristic length are material specific. The characteristic length can be associated with averaged spacing of micro-structural inclusions as discussed in Xia & Shih (1995).

An example study of the use of the criterion for a plastic material with power-law hardening is examined and compared with published hybrid experimental-numerical data for an aluminum alloy (see Section 3.4 for details). Although the proper application of the theory requires checking the critical condition equation throughout the loading history with the critical state being reached when the equation is first satisfied as the loading is applied, another method was necessitated. The average stress triaxiality was used for comparison of the aluminum alloy with the theory due to lack of published data of the stress/strain history over the course of loading. We calculated a toughness stress of $C_I = 1081$ MPa for the opening mode fracture and a toughness stress of $C_{II} = 344$ MPa for the shear mode fracture. The agreement of the theory with published hybrid experimental-numerical data for the aluminum alloy are quite good (see Figure 3-2 and Figure 3-4). Moreover, using the energy release rates of aluminum-base alloys (ductile fracture) provided by Hahn et al. (1972), we find a characteristic length for Al 2024 on the order of 10 µm. This is consistent with the micro-structural length scale dominant in aluminum alloys as provided in Table I of Hahn & Rosenfield (1975). The theory is compared to the current experimental results of AH32 steel, a mild steel, as well. We conclude that agreement of the theory with existing experimental results overall is quite good and very encouraging. The AH32 results are presented in Chapter 5 and summarized in the following pages, after the discussion of the experimental results.

The experimental analyses presented in Chapter 4 provides data for validation and verification of fracture models, and provides the data with which to evaluate the constants (i.e., toughness stresses) in the analytical formulation presented in Chapter 3. Moreover, the effects of the state of stress and the element/mask size on the fracture behavior of a mild steel were explored.

Currently, a common, widely used approach to post-process experimental results is to extract stress and strain fields from the corresponding finite element models, that is, hybrid experimental-numerical analysis (see e.g., Bao & Wierzbicki, 2004; Bai & Wierzbicki, 2010; Papasidero et al., 2015). In that approach, both stress and strain depend on the result of the finite element analyses and are not measured during experiments. In the current study, however, *a direct measure of strain* was obtained by digital image correlation analysis (DIC). Strains were obtained by analyzing digital images that were recorded during the experiments with a Phantom v710 high speed camera, via DaVis LaVision (2015) software. The operations that lead to extracting the engineering/nominal strains are shown in Figure 4-12. Strains were calculated to the point of fracture initiation where we define the fracture initiation as the condition when the first visible crack appears in the digital image of the test specimen. After obtaining the engineering strain field, a property called a 'geometric mask' was applied to investigate a specific sub-region of the imaged surface. The natural strains were calculated from the engineering strains. The corresponding state of stress was calculated *directly* (rather than through a numerical simulation) by using the DIC results via the constitutive relationships (i.e., the power-law hardening relationship) and the stress-strain relationships (i.e., the flow rule) for a plane-stress condition. A plane-stress condition develops as the surface (that has been considered in the DIC analysis) is free of stress. We conclude that this method yields a far superior measure of stress and strain fields.

A series of uniaxial tests and cylindrical indenter experiments with various speeds were conducted and presented in Chapter 4. Two different strain increment approaches were applied in the calculation of the effective strain, the state of stress, and the stress triaxiality. In the first approach, the strain increments are from the un-deformed state to the current state, while the values in the second approach were obtained by taking strain increments from the previous state to the current state. Therefore, the only difference between the two approaches is the amount of strain increment considered. These two approaches would lead to similar results for the cases of proportional loading. For the cases of non-proportional loading, however, the use of smaller strain increments (that is, the second approach) is expected to provide more reliable results as the stress-strain relationships (i.e., the flow rule) are based on the linear incremental relationships. The comparison of the two approaches shows that the first approach may underestimate the effective strain and may not capture the instantaneous changes/fluctuations in the stress field as it is based on larger strain increments. The summary of the results of all uniaxial tests and cylindrical indenter experiments are presented in Table 4-11 and Table 4-12, respectively. It is once again clear that the direct measurement techniques are better and more accurate than using simulations for this purpose.

In the uniaxial test of the 6mm-width specimen, both the transverse strain and the longitudinal strain are moderately affected by the mask size and the effect of mask size is more pronounced especially at later stages of the experiment (see Figure 4-40 and Figure 4-41). For example, the strain difference between the smallest and the largest mask size (with respect to the largest mask size) at the initiation of fracture is 22.5% for the transverse strain, whereas it is 26.7% for the longitudinal strain. Thus, having different longitudinal and transverse strains for different mask sizes demonstrates that the strain is not exactly uniform within the neck region at the initiation of fracture. However, the percentages mentioned above are the maximum differences and they are lower in the previous stages of the experiment. Hence, uniform longitudinal strain and/or uniform transverse strain assumptions may be reasonable depending on what stage of the uniaxial test is under consideration.

In addition, the uni-directional stress-strain curve is in fairly good agreement with the effective stress-strain curve in both approaches (see Figure 4-38 and Figure 4-39). Hence, a global uni-directional stress-strain curve may be a fairly good representation of the global effective stress-strain curve, which is a general assumption in obtaining stress-strain curves of materials (through a conventional uniaxial test), when the gauge length is sufficiently large compared to the localization zone. Nevertheless, it is worth noting that there is an increasing difference (as the experiment progresses) between the 1024 pixels by 256 pixels mask and the rest of the mask sizes (see Figure 4-42). This difference (with respect to 1024 pixels by 256 pixels) at the initiation of fracture reaches 109% for the 192 pixels by 192 pixels mask and 168% for the 16 pixels by 16 pixels mask. Therefore, *global strains obtained by a conventional uniaxial test may not represent the actual strains in the localized zone*, as expected.

Moreover, there is fairly good agreement between the hardening part of the MTS uniaxial test result and the DIC analyses (see Figure 4-44). This demonstrates that the power-law hardening relationship with calculated hardening parameters $\Omega = 868.4$ MPa (the strength coefficient) and $n = 0.128$ (the hardening exponent) fits reasonably well for this specific material (i.e., AH32 steel).

Furthermore, huge stress fluctuations in the second approach at smaller mask sizes (which represent local behavior) were observed, particularly in the cylindrical indenter experiments. Nevertheless, stress fluctuations lose their strength as more global behavior is followed; i.e., as the mask size is increased. Hence, as also discussed and pointed out in Chapter 4, the author believes that the *stress fluctuations are primarily due to plastic flow localization* at the small scales/mask sizes. Moreover, the difference of the stress state between the first approach and the second approach can be inferred as the existence of non-proportional loading, and this difference being more pronounced at smaller mask sizes shows that non-proportional loading is mainly caused by plastic flow localization at small scales.

Finite element studies of the mesh size dependence have been conducted previously and discussed widely in the literature. However, the present research is the *first study*, to our knowledge, that investigates the mesh/mask size dependence through the direct measure of strain via DIC analysis. Although the rate-independent constitutive models may be attributed as the reason for mesh sensitive results or non-convergence behavior as the length scales (i.e., mesh size) were reduced (see e.g., Addessio & Johnson, 1993), in the present study, different convergence behaviors (including non-convergence behavior) were obtained for different experiments. It is believed that *strain localization is the main cause of the scale/mask dependence on fracture strain*. In addition, convergence behavior is also affected by the state of stress (Walters, 2014) as the strain localization depends on the state of stress.

On the other hand, as non-proportional loading is mainly the result of plastic flow localization and that the localization is the primary reason for non-convergence behavior, mesh/mask convergence may be obtained under proportional loading. We obtained an indication of convergence for the case of the uniaxial test of the shear specimen where the loading was nearly proportional loading. However, more experimental data are required to reach a solid conclusion for the effect of loading on mesh/mask convergence.

For the higher strain rate experiments, no conclusive trend is observed with the current experimental results. More experimental data are required to reach a solid conclusion and trend, if there is any.

The ductile fracture theory is also compared to the current experimental results of AH32 steel and it is presented in Chapter 5. Although we reported the state of stress and the strain history over the course of loading for AH32 steel (in Chapter 4), the average stress triaxiality was used in the calculation of toughness stresses for comparison purposes and sake of clarity. The toughness stress for the shear mode fracture was evaluated by using the result of the uniaxial test of the shear specimen as we know that it is a shear mode fracture. However, as the data are scattered significantly, two toughness stresses for the opening mode fracture were determined. As the theory presented in Chapter 3 provides a necessary condition for fracture initiation, it can be implemented as the lower bound. Hence, the lower bound toughness stress for the opening mode was calculated by evaluating the low effective strain to failure results. The second one was calculated by evaluating the higher effective strain results.

As discussed in Chapter 5, scattering of the data suggests that the fracture locus may not be accurately represented in the 2D space (stress triaxiality and fracture strain space, for example). Instead, the full state of stress at the initiation of fracture should be considered and the fracture locus should be represented in the 3D space (stress triaxiality, Lode parameter, and fracture strain space, for example). Moreover, another reason for this scattering is that a small change in toughness stress for Mode I fracture (C_I) and/or characteristic length results in huge differences in fracture strain as can be seen from Figure 5-4 and Figure 5-5.

The use of a single characteristic length requires no scale/mesh/mask dependency of strain to failure. However, as pointed out in Karr & Akçay (2016) and in Chapter 3, often times finite element simulations to failure do show mesh size dependency of strain to failure and the critical strains vary with the element size if the finite element results do not converge. Thus, the toughness stresses C_I and C_{II} would also vary with mesh size if one were to use the finite element strains to determine their values. The implication in this case would be the use of a mesh size equal to the characteristic length ($l_{I,0}$) as discussed in Chapter 5.

In the current study, the toughness stresses were calculated for three different mask sizes, which is presented in Chapter 5 (see Figure 5-1, Figure 5-2, and Figure 5-3), to examine their range and sensitivity to scale. Note that fracture strains presented in Chapter 5 were obtained through direct measure of strain via digital image correlation analyses. For the 16 pixels by 16 pixels mask, the lower bound of toughness stress for the opening mode fracture is $C_I = 909$ MPa, while the toughness stress for the shear mode fracture is $C_{II} = 580$ MPa. For the 32 pixels by 32 pixels mask, however, the lower bound of toughness stress for the opening mode fracture is $C_I = 814$ MPa, while the toughness stress for the shear mode fracture is $C_{II} = 561$ MPa. On the other hand, for the 128 pixels by 128 pixels mask, the lower bound of toughness stress for the opening mode fracture is obtained $C_I = 757$ MPa, whereas the toughness stress for the shear mode fracture is obtained as $C_{II} = 439$ MPa. As a comparison, we calculate the toughness stress for the opening mode (C_I) by using previously published results relating the conventional energy release rates. The J-integral and the crack-tip opening displacement for AH32 steel were reported as being on the order of $J = 0.3$ J/mm^2 and $CTOD = 0.4$ mm, respectively (see Table 5.5 of Priest et al., 2001). As the J-integral is a method for the calculating crack-extension force or the strain energy release rate, it can be used as an approximation for the surface energy density of ductile fracture (denoted as Γ). Moreover, the micro-structural characteristic length ($l_{I,0}$) was chosen on the order of the crack-tip opening displacement (CTOD) as it generally provides a good estimate for the characteristic length scale (Gao et al., 1998). Using Equation (3-12) with $\Gamma = 0.3$ J/mm^2 and $l_{I,0} = 0.4$ mm gives a toughness stress of $C_I = 750$ MPa. This is essentially the same order as the lower bounds of C_I presented in Figure 5-1, Figure 5-2, and Figure 5-3. In conclusion, we believe that the toughness stress of ductile fracture C, introduced by Karr & Akçay (2016) and presented in Chapter 3, may be related to the conventional fracture toughness, generally denoted as K_c (see Chapter 2.3 for details). This relation for Mode I fracture, for example, can be written in the form of Equation (5-1).

6.2 Suggestions for Future Work

The mixed-mode fracture, in which one should consider the change in energy dissipation from tensile and shear stress states simultaneously, is not addressed in the ductile fracture theory presented in Chapter 3. A future study would be to consider further the mixed failure mode of the material in an effort to understand the effects of combined tensile and shear stress states. Moreover, the applications of the theory, presented in Section 3.4 and Chapter 5, consider the application of the model to only a non-porous material. As also mentioned by Karr & Akçay (2016), a further refinement of the theory would be the application of Gurson's model or variations of it to account for void growth in the parent material as the growth and/or coalescence of micro-voids may be considered as fracture initiation at the macro/continuum scale, where the proposed theory can be applied. In addition, the average stress triaxiality is used in the example applications for comparison purposes and sake of clarity. However, as mentioned previously, the proper application of the theory requires checking the equation of the critical condition throughout the loading history with the critical state being reached when the equation is first satisfied as the loading is applied. This application would be another avenue of continuing the study as there could presumably be a different effective strain to failure if the actual stress and strain history was used during loading.

The experimental analyses presented in Chapter 4 are based on 2D-DIC analyses; that is, only the surface strain components are obtained. The strain in the thickness direction was obtained using incompressibility. A further study to obtain the exact value of the strain in the thickness direction would be the application of 3D-DIC (also called Stereo DIC). The application of incompressibility can also be validated in this manner.

As mentioned previously, the fracture initiation is defined as the condition when the first visible crack appears in the digital image of the test specimen. The initiation of fracture has been established by observing the digital images of the test specimen as the continuum scale is the subject of interest. In other words, the establishment of fracture initiation relies on human judgment. Scale effects (the size of the initial crack, for example) affect the establishment of fracture initiation as well. Therefore, a standardized and computerized automation of this establishment would accelerate the process and may provide more reliable results.

A mask/mesh convergence study was conducted through the direct measure of strain via DIC analysis. As mentioned in the conclusions of Section 6.1, different convergence behaviors were obtained for various experiments. We obtained a non-convergence behavior for the cases of cylindrical indenter experiments, where the loading at smaller scales/masks was non-proportional; whereas an indication of convergence was obtained for the case of the uniaxial test of the shear specimen, where the loading was nearly proportional. However, further experimental investigation of the effect of loading condition on mask/mesh convergence is a necessary point of future study.

As mentioned previously, no conclusive trend was obtained for the higher strain rate experiments with the current experimental results. Hence, performing more high-speed experiments should be a consideration of a future study.

Finally, as mentioned in Chapter 5, the experimental data are very scattered and this scattering suggests that the fracture locus may not be accurately represented in 2D space (stress triaxiality and fracture strain space, for example). Moreover, all experiments except the lowest speed cylindrical indenter experiment were performed once; that is, repeatability of the results was not verified. Thus, a continuing study would be the repetition of the experiments with the fracture locus represented in 3D space (stress triaxiality, Lode parameter, and fracture strain space, for example). In this manner, statistical data on the variability of the fracture strengths can be established.

References

References

Addessio, F. L., & Johnson, J. N. (1993). Rate-dependent ductile failure model. *Journal of Applied Physics*, *74*(3), 1640–1648.

Bai, Y., & Wierzbicki, T. (2010). Application of extended Mohr–Coulomb criterion to ductile fracture. *International Journal of Fracture*, *161*(1), 1–20.

Banerjee, S., Dasgupta, T., Mukherjee, S., Shome, M., Chakraborti, P. C., & Saha, S. K. (2016). Digital image correlation for grain scale strain measurement in interstitial free high strength steel. *Materials Science and Technology*, DOI: 10.1179/1743284715Y.0000000075.

Bao, Y., & Wierzbicki, T. (2004). On fracture locus in the equivalent strain and stress triaxiality space. *International Journal of Mechanical Sciences*,*46*(1), 81–98.

Barsoum, I., & Faleskog, J. (2007a). Rupture mechanisms in combined tension and shear—experiments. *International Journal of Solids and Structures*, *44*(6), 1768–1786.

Barsoum, I., & Faleskog, J. (2007b). Rupture mechanisms in combined tension and shear—Micromechanics. *International Journal of Solids and Structures*, *44*(17), 5481-5498.

Baskes, M. I., & Ortiz, M. (2015). Scaling laws in the ductile fracture of metallic crystals. *Journal of Applied Mechanics*, *82*(7), 071003-1–071003-5.

Bažant, Z. P. (2000). Size effect. *International Journal of Solids and Structures*, *37*(1), 69–80.

Berg, C. A. (1962). The motion of cracks in plane viscous deformation. In *Proceedings of the fourth US national congress of applied mechanics, Berkeley, June 18-21, 1962,* 885–892. American Society of Mechanical Engineers: New York.

Besson, J. (2010). Continuum models of ductile fracture: a review. *International Journal of Damage Mechanics*, *19*(1), 3–52.

Bridgman, P. W. (1945). Effects of high hydrostatic pressure on the plastic properties of metals. *Reviews of Modern Physics*, *17*(1), 3–14.

Bridgman, P. W. (1964). *Studies in large plastic flow and fracture*. Harvard University Press: Cambridge.

Cotterell, B. (2002). The past, present, and future of fracture mechanics. *Engineering Fracture Mechanics*, *69*(5), 533–553.

DaVis LaVision, 2015. *Version 8.2.2*, LaVision GmbH, Göttingen, Germany.

de Borst, R. (2001). Some recent issues in computational failure mechanics. *International Journal for Numerical Methods in Engineering*, *52*(1-2), 63–95.

Desai, C. S., & Siriwardane, H. J. (1984). *Constitutive laws for engineering materials with emphasis on geologic materials*. Prentice-Hall: New Jersey.

Dieter, G. E. (1986). *Mechanical metallurgy.* McGraw-Hill: New York.

Erdogan, F. (2000). Fracture mechanics. *International Journal of Solids and Structures*, *37*(1-2), 171–183.

Gao, X., Faleskog, J., Shih, C. F., & Dodds, R. H. (1998). Ductile tearing in part-through cracks: Experiments and cell-model predictions. *Engineering Fracture Mechanics*, *59*(6), 761–777.

Garrison, W. M., & Moody, N. R. (1987). Ductile fracture. *Journal of Physics and Chemistry of Solids*, *48*(11), 1035–1074.

Griffith, A. A. (1921). The phenomena of rupture and flow in solids. *Philosophical Transactions of the Royal Society of London, Series A*, *221*, 163–198.

Gullerud, A. S., Gao, X., Dodds, R. H., & Haj-Ali, R. (2000). Simulation of ductile crack growth using computational cells: Numerical aspects. *Engineering Fracture Mechanics*, *66*(1), 65–92.

Gurson, A. L. (1977). Continuum theory of ductile rupture by void nucleation and growth: Part I—Yield criteria and flow rules for porous ductile media. *Journal of Engineering Materials and Technology*, *99*(1), 2–15.

Hahn, G. T., Kanninen, M. F., & Rosenfield, A. R. (1972). Fracture toughness of materials. *Annual Review of Materials Science*, *2*(1), 381–404.

Hahn, G. T., & Rosenfield, A. R. (1975). Metallurgical factors affecting fracture toughness of aluminum alloys. *Metallurgical Transactions A*, *6*(4), 653–668.

Haltom, S. S., Kyriakides, S., & Ravi-Chandar, K. (2013). Ductile failure under combined shear and tension. *International Journal of Solids and Structures*, *50*(10), 1507–1522.

Hancock, J. W., & Mackenzie, A. C. (1976). On the mechanisms of ductile failure in high-strength steels subjected to multi-axial stress-states. *Journal of the Mechanics and Physics of Solids*, *24*(2), 147–169.

Hart, E. W. (1967). Theory of the tensile test. *Acta Metallurgica*, *15*(2), 351–355.

Hill, R. (2009). *The mathematical theory of plasticity*. Oxford University Press: New York.

Hogström, P., Ringsberg, J. W., & Johnson, E. (2009). An experimental and numerical study of the effects of length scale and strain state on the necking and fracture behaviours in sheet metals. *International Journal of Impact Engineering*, *36*(10), 1194–1203.

Irwin, G. R. (1948). Fracture dynamics. In *Fracturing of metals: A seminar on the fracturing of metals held during the twenty-ninth national metal congress and exposition, Chicago, October 18-24, 1947*, 147–166. American Society for Metals: Cleveland.

Irwin, G. R. (1957). Analysis of stresses and strains near the end of a crack traversing a plate. *Journal of Applied Mechanics*, 24, 361–364.

Irwin, G. R. (1960). Fracture mechanics. In *Structural mechanics: Proceedings of the first symposium on naval structural mechanics, Stanford, August 11-14, 1958*, 557–594. Pergamon Press: New York.

Jia, J., Dong, Z., Yuan, J., & Han, T. (2013). Study on mechanical properties of AH32 opened plate. *Advanced Materials Research*, *631-632*, 354–357.

Jin, H., Lu, W. Y., & Korellis, J. (2008). Micro-scale deformation measurement using the digital image correlation technique and scanning electron microscope imaging. *The Journal of Strain Analysis for Engineering Design*, *43*(8), 719–728.

Johnson, G. R. (1979). Dynamic response of axisymmetric solids subjected to impact and spin. *AIAA Journal*, *17*(9), 975–979.

Johnson, G. R., & Cook, W. H. (1985). Fracture characteristics of three metals subjected to various strains, strain rates, temperatures and pressures. *Engineering Fracture Mechanics*, *21*(1), 31–48.

Karr, D.G., & Akçay, F.A. (2016). A criterion for ductile fracture based on continuum modeling of energy release rates. *International Journal of Fracture*, *197*(2), 201–212.

Kõrgesaar, M., & Romanoff, J. (2014). Influence of mesh size, stress triaxiality and damage induced softening on ductile fracture of large-scale shell structures. *Marine Structures*, *38*, 1–17.

Lava, P., Van Paepegem, W., Coppieters, S., De Baere, I., Wang, Y., & Debruyne, D. (2013). Impact of lens distortions on strain measurements obtained with 2D digital image correlation. *Optics and Lasers in Engineering*, *51*(5), 576–584.

Leis, B. J., Ahmad, J., & Kanninen, M. F. (1985). Effect of local stress state on the growth of short cracks. In *Multiaxial fatigue: Proceedings of the international symposium on biaxial/multiaxial fatigue, San Francisco, December 15-17, 1982*, 314–339. American Society for Testing and Materials: Philadelphia.

Li, Y., & Karr, D. G. (2009). Prediction of ductile fracture in tension by bifurcation, localization, and imperfection analyses. *International Journal of Plasticity*, *25*(6), 1128–1153.

Malvern, L. E. (1969). *Introduction to the mechanics of continuous medium*. Prentice-Hall: New Jersey.

McClintock, F. A. (1968). A criterion for ductile fracture by the growth of holes. *Journal of Applied Mechanics*, *35*(2), 363–371.

Mirza, M. S., Barton, D. C., & Church, P. (1996). The effect of stress triaxiality and strain-rate on the fracture characteristics of ductile metals. *Journal of materials science*, *31*(2), 453–461.

Nahshon, K., & Hutchinson, J. W. (2008). Modification of the Gurson model for shear failure. *European Journal of Mechanics-A/Solids*, *27*(1), 1–17.

Needleman, A. (1972). Void growth in an elastic-plastic medium. *Journal of Applied Mechanics*, *39*(4), 964–970.

Needleman, A., & Tvergaard, V. (1984). An analysis of ductile rupture in notched bars. *Journal of the Mechanics and Physics of Solids*, *32*(6), 461–490.

Orowan, E. (1945). Notch brittleness and the strength of metals. Transactions of the Institution of Engineers and Shipbuilders in Scotland, *89*, 165–215.

Orowan, E. (1949). Fracture and strength of solids. *Reports on Progress in Physics*, *12*, 185–232.

Pan, B., Qian, K., Xie, H., & Asundi, A. (2009). Two-dimensional digital image correlation for in-plane displacement and strain measurement: a review. *Measurement Science and Technology*, *20*(6), 1–17.

Papasidero, J., Doquet, V., & Mohr, D. (2014). Determination of the effect of stress state on the onset of ductile fracture through tension-torsion experiments. *Experimental Mechanics*, *54*(2), 137–151.

Papasidero, J., Doquet, V., & Mohr, D. (2015). Ductile fracture of aluminum 2024-T351 under proportional and non-proportional multi-axial loading: Bao–Wierzbicki results revisited. *International Journal of Solids and Structures*, *69-70*, 459–474.

Priest, A. H., Mannsfeld, A., Langenberg, P., Ausejo, I., Azpiazu, W., Greisen, Z., Bédaton, F. (2001). *Steel selection criteria for fracture avoidance in welded ships* (EUR 20048 En). Office for Official Publications of the European Communities: Luxembourg.

Raabe, D., Sachtleber, M., Zhao, Z., Roters, F., & Zaefferer, S. (2001). Micromechanical and macromechanical effects in grain scale polycrystal plasticity experimentation and simulation. *Acta Materialia*, *49*(17), 3433–3441.

Rice, J. R. (1968). A path independent integral and the approximate analysis of strain concentration by notches and cracks. *Journal of Applied Mechanics*, *35*(2), 379–386.

Rice, J. R., & Tracey, D. M. (1969). On the ductile enlargement of voids in triaxial stress fields*. *Journal of the Mechanics and Physics of Solids*, *17*(3), 201–217.

Sutton, M. A., Yan, J. H., Tiwari, V., Schreier, H. W., & Orteu, J. J. (2008). The effect of out-of-plane motion on 2D and 3D digital image correlation measurements. *Optics and Lasers in Engineering*, *46*(10), 746-757.

Tegart, W. J. McG. (1966). *Elements of mechanical metallurgy*. MacMillan: New York.

Tvergaard, V. (1981). Influence of voids on shear band instabilities under plane strain conditions. *International Journal of Fracture*, *17*(4), 389–407.

Walters, C. L. (2014). Framework for adjusting for both stress triaxiality and mesh size effect for failure of metals in shell structures. *International Journal of Crashworthiness*, *19*(1), 1–12.

Westergaard, H. M. (1939). Bearing pressures and cracks. *Journal of Applied Mechanics*, *6*, A-49–A-53.

Wierzbicki, T., Bao, Y., Lee, Y. W., & Bai, Y. (2005). Calibration and evaluation of seven fracture models. *International Journal of Mechanical Sciences*, *47*(4), 719–743.

Wineman, A. (2010). *Thermo-mechanics of solid continua* (Coursepack). Dollar Bill Copying: Ann Arbor.

Xia, L., & Shih, C. F. (1995). Ductile crack growth–I. A numerical study using computational cells with microstructurally-based length scales. *Journal of the Mechanics and Physics of Solids*, *43*(2), 233–259.

Zhou, C., Ye, Q., Yan, L. (2016). Effect of ultra-fast cooling on microstructure and properties of high strength steel for shipbuilding. In *Proceedings of the HSLA Steels 2015, microalloying 2015 & offshore engineering steels 2015, Hangzhou, November 11-13, 2015*, 1179–1185. New Jersey: Wiley.

Zhu, F., Bai, P., Zhang, J., Lei, D., & He, X. (2015). Measurement of true stress–strain curves and evolution of plastic zone of low carbon steel under uniaxial tension using digital image correlation. *Optics and Lasers in Engineering*, *65*, 81–88.